Charged Hadron Transverse Momentum Spectra in Au+Au and d+Au Collisions at 200 GeV per Nucleon Pair

by

Jay Lawrence Kane

Submitted to the Department of Physics
in partial fulfillment of the requirements for the degree of

Doctor of Philosophy

at the

MASSACHUSETTS INSTITUTE OF TECHNOLOGY

April 2005 [June 2005]

Author .....
Department of Physics
April 28, 2005

Certified by .....
Gunther Roland
Associate Professor
Thesis Supervisor

Accepted by .....
Thomas Greytak
Associate Department Head for Education

Charged Hadron Transverse Momentum Spectra in Au+Au and d+Au Collisions at 200 GeV per Nucleon Pair

by

Jay Lawrence Kane

Submitted to the Department of Physics
on April 28, 2005, in partial fulfillment of the
requirements for the degree of
Doctor of Philosophy

Abstract

The Relativistic Heavy Ion Collider (RHIC) collides Au ions at a center of mass energy of 200 GeV per nucleon pair, which produces the most energetic collisions yet seen in the laboratory. RHIC has also collided proton beams and deuteron+gold beams. By studying these collisions important information about hadronic matter under extreme conditions and quantum chromodynamics (QCD) can be collected.

One of the predictions of QCD is that at very high energy densities the quarks and gluons within hadrons will become deconfined and form a Quark-Gluon Plasma (QGP). These densities are thought to be achievable with Au+Au collisions at RHIC energies. Another prediction theorizes that before the collision, the very high energies of the nuclei will create a condensate of the low momentum gluons within the nuclei before any collisions occur. This condensate is termed the Color Glass Condensate (CGC). Both of these predictions can be tested by studying the transverse momentum, p_T, spectra of charged hadrons produced in the heavy ion collisions. This thesis presents data on p_T spectra collected using the PHOBOS detector at RHIC. PHOBOS is capable of measuring a wide range of momenta using a silicon based double armed spectrometer located in a strong magnetic field.

The results show a strong suppression of a factor of 4 - 5 in the nuclear modification factor, R_{AA} at high p_T as predicted in a QGP. This suppression is absent in d+Au collisions, where R_{dA} has a value consistent with unity from mid to high p_T. A QGP is not expected to form from d+Au collisions, so no suppression would be expected. When R_{dA} is calculated for different rapidities, a suppression is seen as the rapidity in the deuteron fragmentation region increases. This has been predicted to be seen if a CGC does form in the colliding nuclei.

Thesis Supervisor: Gunther Roland
Title: Associate Professor

Contents

1 Theory **11**

1.1 The Quark Model 11

1.2 QED and QCD 13

1.2.1 The QED Lagrangian 13

1.2.2 The QCD Lagrangian 14

1.3 Properties of QCD 16

1.4 Quark-Gluon Plasma and the QCD Phase Diagram 24

1.5 Color Glass Condensate 27

1.6 Heavy Ion Collisions 29

1.7 p_T Spectra 31

1.7.1 d+Au Spectra 32

2 PHOBOS Detector **35**

2.1 Overview 35

2.2 Beam Pipe 37

2.3 Silicon Detectors 37

2.3.1 Sensor Design and Testing 37

2.3.2 4π Multiplicity Array 39

2.3.3 Vertex Detector 41

2.3.4 Spectrometer 42

2.4 Magnet 42

2.5 Trigger System 44

2.5.1 Paddle Counters 44

2.5.2 Cerenkov counters 45
2.5.3 Zero Degree Calorimeters 46
2.5.4 Spectrometer Trigger 47
2.6 Proton Calorimeter 48
2.7 Time of Flight 50
2.7.1 Time-Zero Counters 50
2.8 Readout Electronics and Data Acquisition 51
2.8.1 PHOBOS Trigger 51
2.8.2 VA Chip 51
2.8.3 Front-End Controller 54
2.8.4 Data Concentrator 56
2.8.5 Data Acquisition 56
2.9 PHOBOS Coordinates 56
2.10 RHIC 57
2.10.1 Tandem Van de Graaff 57
2.10.2 Booster 58
2.10.3 Alternating Gradient Synchrotron 58
2.10.4 Relativistic Heavy Ion Collider 58

3 Data Processing **61**
3.1 Signal Processing 61
3.1.1 Pedestal Correction 61
3.1.2 Noise Correction 62
3.1.3 Gain Calibration 62
3.1.4 Hit Merging 64
3.2 Event Selection 64
3.2.1 Au+Au Event Selection 64
3.2.2 d+Au Event Selection 67
3.2.3 Au+Au Centrality Determination 69
3.2.4 d+Au Centrality Determination 73

3.3 Vertexing 77
3.3.1 ZVertex 77
3.3.2 OctagonVertex 78
3.3.3 OctMainVertex 78
3.3.4 SpecVertexSpecPN 79
3.3.5 SpecMainVertex 79
3.3.6 PaddleVertex 80
3.3.7 RMSSelVertex 80
3.3.8 OctDeVertex 83

4 Tracking **85**
4.1 PR01 Au+Au Tracking 85
4.1.1 Straight Line Tracking 85
4.1.2 Curved Tracking 87
4.1.3 d+Au Tracking 90
4.2 Track Cuts 92
4.3 Tracking Efficiency and Momentum Resolution 94

5 Corrections **97**
5.1 Acceptance and Efficiency Correction 97
5.1.1 SpecToF Correction 106
5.2 Momentum Resolution and Bin Width Correction 106
5.3 Feeddown Correction 111
5.3.1 Au+Au Correction 111
5.3.2 d+Au Correction 111
5.4 Ghost Correction 114
5.4.1 Au+Au Correction 114
5.4.2 d+Au Correction 115
5.5 Dead Channel Map Correction 116
5.6 OctDeVtx Resolution Event Normalization Correction 118
5.7 Centrality Dependence of the Efficiency 120

6 Data Analysis and Results **121**

6.1 Event Selection 121

6.2 Track Cuts 122

6.3 Assembling the Spectra 123

6.3.1 Histogramming Spectra 123

6.3.2 Final Corrections 127

6.4 UA1 Reference Spectra 128

6.4.1 UA1 Correction 128

6.4.2 UA1 Fit Function 129

6.5 Centrality Dependence of the Spectra 131

6.5.1 Au+Au Results 131

6.5.2 d+Au Results 134

6.5.3 Systematic Errors 139

6.5.4 Au+Au and d+Au Centrality Dependence Discussion 142

6.6 Pseudorapidity Dependence of the Spectra 156

6.6.1 d+Au Versus η Results 156

6.6.2 d+Au Versus η Discussion 157

7 Conclusions **163**

A Tables of Data A **167**

A.1 Au+Au Invariant Yields 167

A.2 R_{AA} Data 167

A.3 $R_{AA}^{N_{part}}$ Data 167

B Data Tables B **185**

B.1 $R_{CP}^{N_{part}}$ Data 185

B.2 $R_{CP}^{N_{coll}}$ Data 185

B.3 d+Au Invariant Yields Data 185

C Data Tables C **203**

C.1 R_{dAu} Data 203

C.2 R_{dAu} vs N_{coll} Data 203
C.3 R_{dA} as a Function of η 203
C.4 R_{dAu} vs η Data 203

Chapter 1

Theory

1.1 The Quark Model

The last half of the 20th century saw great strides in particle physics. As detector and accelerator technology advanced many new particles were discovered. As the list of known particles grew, it became apparent that physicists' knowledge of "fundamental" particles was incomplete.

Similar to Mendeleev's postulation of the periodic table, Murray Gell-Mann and Ne'eman [1] [2] proposed a hierarchy for these new particles and the known nucleons, which Gell-Mann termed "The Eight-Fold Way". This theory describes hadrons, which are particles that feel the strong force. There are two types of hadrons: mesons and baryons. In the Eight-Fold Way model the mesons and baryons are grouped into geometrical arrays, called multiplets, based on their properties, such as charge, strangeness, and total spin. The spin-$\frac{1}{2}$ baryons are arrayed in an octet and the spin-$\frac{3}{2}$ baryons are arrayed in a decuplet. The mesons were arrayed in an octet also. Later, more mesons that were discovered were arranged in nonets.

In 1964 Gell-Mann and Zweig [3] theorized that these mesons and baryons are in turn made up of smaller constituent, which were named quarks. Although originally there were three different kinds, or flavors, of quarks postulated, there are now known to be six. These quarks are spin-$\frac{1}{2}$ and have a fractional charge, in relation to the charge of the electron and the proton. Baryons are made up of three quarks and

Flavor	Charge	Mass/c^2
up	$+\frac{2}{3}$	1-5 MeV
down	$-\frac{1}{3}$	3-9 MeV
strange	$-\frac{1}{3}$	75-170 MeV
charm	$+\frac{2}{3}$	1.15-1.35 GeV
bottom	$-\frac{1}{3}$	4.0-4.4 GeV
top	$+\frac{2}{3}$	174 GeV

Table 1.1: Charges and masses for the six flavors of quarks [4].

mesons are made up of a quark and an antiquark. The different flavors of quarks and some of their properties are shown in Table 1.1.

The quark model was not accepted immediately. One problem was that free quarks had never been observed, and detecting them should be easy to do because of their unique fractional charge. The reason free quarks have never been seen is discussed in Section 1.3. Another issue was the Δ^{++} particle, which is a spin-$\frac{3}{2}$, charge +2 baryon. In the quark model, the Δ^{++} particle consists of three up quarks with spins in the same direction. This violates the Pauli exclusion principle, since all of the fermions are in the same state. To circumvent this problem, it was proposed that there was another quantity associated with quarks, termed "color" [5]. Each quark can be one of three colors: red, green, or blue, and the antiquarks can be antired, antigreen, or antiblue. With this additional quantum number, the Δ^{++} particle consists of three up quarks, with each one a different color. Now the Pauli exclusion principle is no longer violated since the different colored quarks are in different states. The further significance of this color quantum number will be discussed in the following sections.

In 1960's and 1970's the deep inelastic experiment carried out at SLAC and MIT collided electrons with protons [6], [7], [8], [9]. It was shown that the protons are in fact made up of three spin-$\frac{1}{2}$ particles, interpreted to be the quarks postulated by Gell-Mann. Although this was a help to the quark model, free quarks had still never been seen. The reason for this involves fundamental differences between the properties of the strong force and the electromagnetic force which are discussed in the following sections.

1.2 QED and QCD

Quantum electrodynamics (QED) and quantum chromodynamics (QCD) are the theories that describe the electromagnetic force and the strong force respectively. Although the two theories share many similarities, there are also important differences that lead to new and novel effects for the strong force.

1.2.1 The QED Lagrangian

QED describes the interactions of Dirac fermions with photons. The basic Lagrangian for a free Dirac particle is given by

$$\mathcal{L} = i\bar{\psi}\gamma^{\mu}\partial_{\mu}\psi - m^2\bar{\psi}\psi. \tag{1.1}$$

ψ is the wave function of the Dirac fermion, γ^{μ} are the Dirac matrices, and m is the mass of the fermion. The first term is the kinetic energy term and the second term is the mass term of the fermion. This Lagrangian is invariant under phase, or gauge, transformations, which can be seen by substituting $\psi \rightarrow \psi e^{i\theta}$. θ in this case is a constant, and this gauge transformation represents a shift in the wave function of the Dirac particle. But what happens if θ is a not a constant, but a function of the position 4-vector x^{μ}, $\theta = \theta(x)$? This is called a local gauge transformation. What happens is the Lagrangian is no longer invariant because now there is a term that involves the derivative of θ. If local gauge invariance is to hold, the QED Lagrangian must be modified. The derivative is replaced by the covariant derivative D_{μ}:

$$\mathcal{D}_{\mu} = \partial_{\mu} + eA_{\mu} \tag{1.2}$$

A_{μ} is a vector field that transforms as:

$$A_{\mu} \rightarrow A_{\mu} + \frac{1}{e}\partial_{\mu}\theta \tag{1.3}$$

The Lagrangian now becomes:

$$\mathcal{L} = i\bar{\psi}\gamma^{\mu}\partial_{\mu}\psi - m^2\bar{\psi}\psi - e\bar{\psi}\gamma^{\mu}\psi A_{\mu} \tag{1.4}$$

Now there is an extra term (the last term) that involves the new gauge field which couples to the Dirac particles, just as the photon does. Indeed, this gauge field is the photon field. So enforcing local gauge invariance requires the photon field to exist and to couple with the Dirac particles. However, the above Lagrangian for electromagnetism is not yet complete. It also requires the kinetic energy term of the electromagnetic field:

$$\mathcal{L} = i\bar{\psi}\gamma^{\mu}\partial_{\mu}\psi - m^2\bar{\psi}\psi - e\bar{\psi}\gamma^{\mu}\psi A_{\mu} - \frac{1}{16\pi}F^{\mu\nu}F_{\mu\nu} \tag{1.5}$$

where

$$F^{\mu\nu} = \partial^{\mu}A^{\nu} - \partial^{\nu}A^{\mu} \tag{1.6}$$

The $F^{\mu\nu}$ tensor is itself separately gauge invariant, as can readily be seen by substituting in the gauge transformed field A_{μ} from Equation 1.3:

$$F^{\mu\nu} = \partial^{\mu}A^{\nu} + \frac{1}{e}\partial^{\mu}\partial^{\nu}\theta - \partial^{\nu}A^{\mu} - \frac{1}{e}\partial^{\nu}\partial^{\mu}\theta = F^{\mu\nu} \tag{1.7}$$

1.2.2 The QCD Lagrangian

The strong force, like the electromagnetic force, is one of the fundamental forces of nature. The only fundamental Dirac fermions that feel the strong force are the quarks. While the electric force is a U(1) gauge force, the strong force was postulated to be SU(3). This implies that instead of one fundamental charge and anticharge, there will be three charges and three anticharges for the quarks and antiquarks. These charges and anticharges are called red, blue, green, antired, antiblue, and antigreen, and is the same color quantum number that was postulated to explain how the Δ^{++} particle could exist in the quark model.

The Lagrangian for a quark without interactions is

$$\mathcal{L} = i\bar{\psi}_i\gamma^\mu\partial_\mu\psi_i - m\bar{\psi}_i\psi_i \tag{1.8}$$

where the ψ_i represents the three possible colors of the quark.

Again, this Lagrangian is invariant under a global gauge transformation, but not a local gauge transformation. Since there are three color quark fields, it is necessary to look at an SU(3) local gauge transformation:

$$\psi(x) \rightarrow e^{i\alpha_a T_a}\psi(x) \tag{1.9}$$

The T_a are a set of eight linearly independent traceless matrices (here they are equal to $\lambda_a/2$, where λ_a are the eight Gell-Mann matrices) and the α_a are the group parameters. Again, the derivative of α_a spoils the gauge invariance since

$$\psi(x) \rightarrow (1 + i\alpha_a T_a)\psi(x)\partial_\mu \rightarrow (1 + i\alpha_a T_a)\partial_\mu + ieT_a\partial_\mu\alpha_\mu \tag{1.10}$$

so the derivative is replaced with a covariant derivative:

$$\mathcal{D}_\mu = \partial_\mu + igT_a G^a_\mu \tag{1.11}$$

Again, enforcing gauge invariance has led to the introduction of a gauge field G^a_μ. The difference here from QED is that now there are eight of these gauge fields. They transform under a gauge transformation as:

$$G^a_\mu \rightarrow G_\mu a - \frac{1}{g}\partial_\mu\alpha_a - f_{abc}\alpha_b G^c_\mu \tag{1.12}$$

The f_{abc} are the structure constants of the SU(3) group. Adding in the kinetic energy term for the gauge fields gives the final QCD Lagrangian:

$$\mathcal{L} = \bar{\psi}(i\gamma^\mu\partial_\mu - m) - g\bar{\psi}\gamma^\mu T_a\psi G^a_\mu - \frac{1}{4}G^a_{\mu\nu}G^{\mu\nu}_a \tag{1.13}$$

where

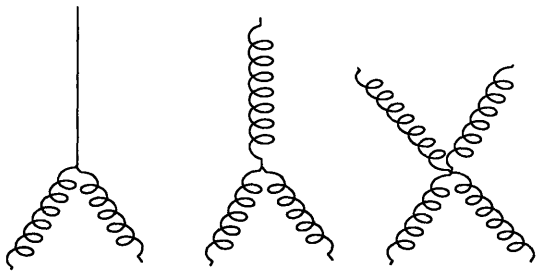

Figure 1-1: Vertices for quark-quark-gluon, 3-gluon, and 4-gluon interactions.

$$G^a_{\mu\nu} = \partial_\mu G^a_\nu - \partial_\nu G^a_\mu - g f_{abc} G^b_\mu G^c_\nu \tag{1.14}$$

In QED, the requirement of local gauge invariance led to the requirement of the photon to couple to the Dirac particles. In QCD, the gauge invariance for the colored quarks has led to the introduction of eight gauge fields which couple to the quarks. These gauge fields are the gluons, the carriers of the strong force. The extra term in the kinetic energy term of the gluon fields has an interesting effect. It leads to self-interactions of the gluons, which means that the gluons themselves also carry color. This is absent in QED, as the photon has zero charge and they do not interact to first order. In particular, there is, in addition to the quark-quark-gluon interaction (or vertex), a three gluon vertex and a four gluon vertex, as shown in Figure 1-1. The importance of this gluon self-interaction will be discussed below.

1.3 Properties of QCD

The electric charge of an electron measured in a laboratory is not constant as a function of distance to the electron. In fact, the measured charge is quite different from the true, or bare, charge of the electron. In a simple electron-electron interaction the Feynman diagram is shown in Figure 1-2.

However, there are higher order corrections to this diagram. For example, the mediating photon can briefly split into an electron-positron pair, and they can then

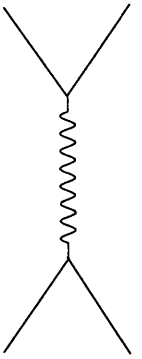

Figure 1-2: Two electrons interacting via the exchange of a virtual photon.

annihilate into a photon, as shown in Figure 1-3. It is also possible to have more than one electron-positron loop. Indeed, any amount is possible, but the probability decreases as the number of loops increases. If the corrections these loops induce are included in calculating the electric coupling strength between two electrons (or any two fermions), one finds that the electron's charge, or the QED coupling constant α, is not constant. It depends on the momentum transfer q between the interacting electrons:

$$\alpha(q^2) = \frac{\alpha_0}{1 - \frac{\alpha_0}{3\pi} \ln \frac{q^2}{m^2}} (|q^2| \gg m^2) \tag{1.15}$$

with $\alpha_0 = \epsilon_0/4\pi$, where e_0 is the bare charge of the electron. Since this effective charge is a function of q^2 this means the measured charge is a function of distance to the electron (or any other charged particle). Physically, this can be understood as a polarization of the vacuum. While the electron sits in the vacuum, particle-antiparticle pairs are continually formed and annihilated in the vacuum. The charge of the electron will polarize these pairs and pull the opposite charges closer, thereby screening its charge, much the same as an open charge can be Debye screened within a medium. While equation (1.15) holds for large momentum transfers, or interactions at very small distances, α becomes constant as interaction distances increase. As the momentum transfer $|q^2| < m^2$, α becomes q^2-independent, and approaches the familiar value of 1/137.

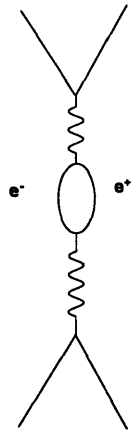

Figure 1-3: Two electrons interacting via the exchange of a virtual photon, and the photon briefly splits into an electron-positron pair

In QCD there is a similar process. For example, the basic Feynman diagram for the strong interaction of two quarks can have a loop in the gluon propagator. Now, however, there is an important difference. Earlier it was shown that the gluon interacts with other gluons, which means that in addition to the quark-antiquark loops there can also be purely gluonic loops (Figure 1-4). The corrections from these loops in the Feynman diagrams can be corrected for analogously to the case in QED. While quark loops in the gluon propagator will work to screen the color charge in the same way, the purely gluonic loops actually have the opposite effect. This leads to an "antiscreening" effect for the strong force. Indeed, this important result led to the awarding of the Nobel Prize for physics in 2004 for the authors Wilczek, Gross, and Politzer [10], [11]. As the distance to the open color charge decreases, the coupling strength actually decreases also. For the strong force, the coupling "constant" α is given by equation (1.16).

$$\alpha(q^2) = \frac{12\pi}{(11n - 2f)\ln(\frac{q^2}{\Lambda^2_{QCD}})}(|q^2| \gg \Lambda^2_{QCD}) \tag{1.16}$$

Λ_{QCD} is the QCD scale parameter, which has a value between 100 and 500 MeV [12], n is the number of quark colors, and f is the number of quark flavors. It should be noted here that this formula only holds for large momentum transfers. In the

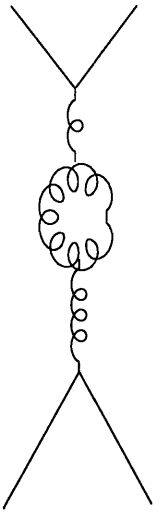

Figure 1-4: Two quarks interacting via the exchange of a virtual gluon, which in turn has a gluon bubble, which is a result of the fact that gluons are self-interacting.

limit where $|q^2| \ll \Lambda^2_{QCD}$, $\alpha(q^2)$ is not well defined. This is due to the confining characteristics of QCD: at large interaction distances, free quarks cannot exist, and therefore the strong interaction between them at large distances is not defined.

A big difference between QED and QCD is that as q^2 increases, or as the distance gets smaller, α actually decreases. This means that the closer we get to the color charge the smaller the coupling constant becomes, which is the opposite of what happens in the case of electromagnetism. This is known as *asymptotic freedom* [13], [14], [10], [11]. The strength of the coupling constant as a function of distance is shown in Figure 1-5 [15].

Quarks interacting at small distances can be treated perturbatively, while as the quarks become separated by large distances the strong coupling constant α_s rises logarithmically, and perturbative methods are no longer possible. This also leads to the phenomenon of *confinement*, which states that free quarks cannot exist in nature. More specifically bare color charges cannot exist in nature, so all colored objects, quarks and gluons, must be bound into states such that the overall color combinations are "white", such as red + blue + green, or any color and its corresponding anticolor. (Actually, only color *singlets* are allowed in nature, but the effect is to disallow bare color). Therefore, in Gell-Mann's quark model the mesons are a quark

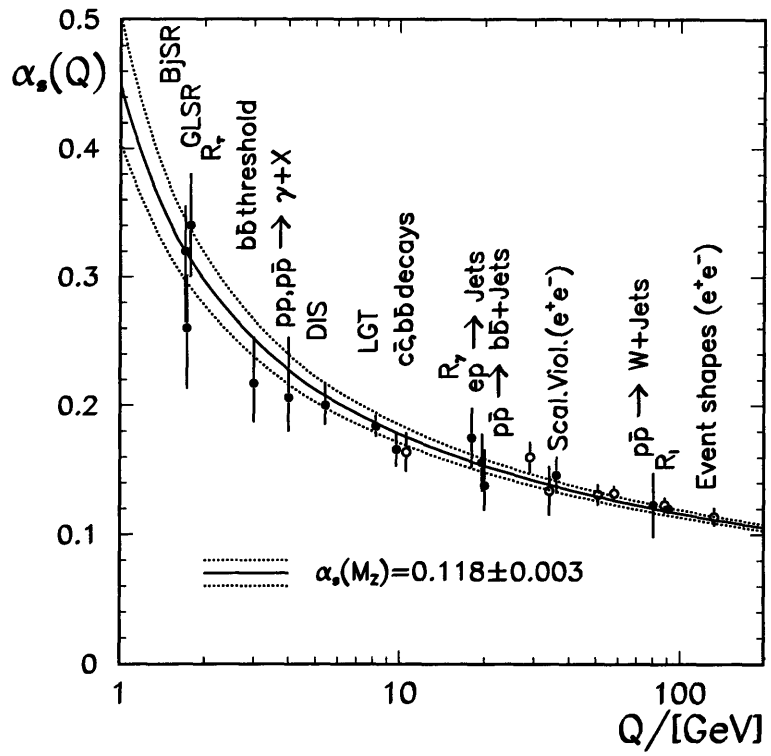

Figure 1-5: The strength of the running coupling constant α_s as a function of momentum transfer. The points are gathered from many different experiments, and are compared to theoretical prediction (lines). Figure is taken from [15].

and an antiquark with the corresponding anticolor, and a baryon is three quarks with colors red, green, and blue.

Consider the case of a quark and an antiquark bound together. As long as they are close, the strong force will be relatively weak. Now assume that there is some mechanism by which the quarks are being pulled apart. As they get farther and farther away, the self-interacting effect of the gluons serves to increase the energy in the strong field between the quarks. At small distances the strong force potential is proportional to 1/r, as in the Coulomb force. However, there is a linear term in the potential, $U \sim kr$, that dominates as the distance increases. This linearity in the potential creates an (approximate) constant force between the quarks and an increase in the energy of the field between the quarks as their distance apart increases. As the quark-antiquark pair becomes separated the strong force field lines take on a tube shaped form between the two quarks. Finally, the strong field between the quarks has enough energy to create another quark-antiquark pair, and the original two quarks pair off with the new quark-anitquark pair. Instead of separating the two quarks we have merely created new quarks without ever freeing them. This situation is illustrated in Figure 1-6. This is similar to breaking a bar magnet, which does not leave two isolated magnetic monopoles, but rather two complete magnets, each with a north and south pole.

At high energies, the strong coupling constant α_s becomes small and perturbative techniques can be used in calculations. Otherwise, α_s is too large and perturbative techniques cannot be used. In this regime, a technique called *lattice QCD* has been developed [16]. A spacetime grid of points, separated by a distance a, is constructed. The parameters of volume, temperature, and baryon chemical potential μ_B are input. These parameters and the Feynman path integral are used to calculate the partition function $\mathcal{Z}$ in the limit the the spacing $a \to 0$ and the number of spacetime points goes to infinity. The partition function is then used to calculate quantities such as pressure and energy density of the system. The results of such calculations are shown in Figures 1-7 and 1-8 [17].

These lattice calculations predict a phase transition in a hadronic system as the

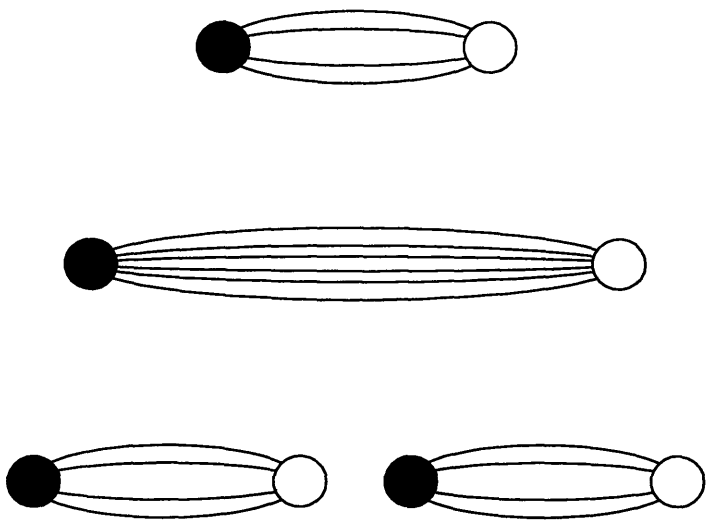

Figure 1-6: Illustration of a quark and antiquark separating. The strong force field lines form a tube shape, and as they get farther apart the energy in the strong force field increases. Eventually, there is enough energy in the field to create another quark/antiquark pair and now there are two mesons. The original quark and antiquark are never freed.

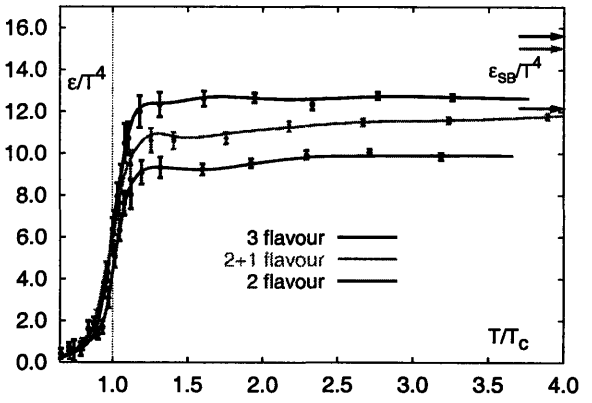

Figure 1-7: Energy density as a function of temperature for a hadronic system. At the critical temperature T_c there is a rapid rise in the energy density, corresponding to the expected phase transition. From [17].

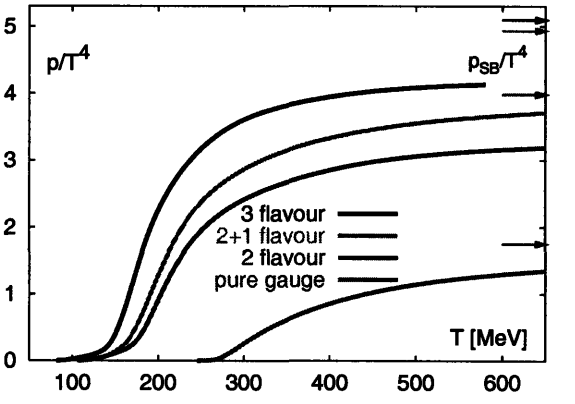

Figure 1-8: Pressure of a hadronic system as a function of temperature. At a temperature of about 170 MeV there is a rapid rise. This is similar to the rise in energy density seen in Figure 1-7. From [17].

temperature increases. Figure 1-7 shows a steep rise in the energy density at around $T_c = 170$ MeV. There is a corresponding rise in the pressure at the same temperature, but the rise is not as steep.

1.4 Quark-Gluon Plasma and the QCD Phase Diagram

The phase transition predicted by lattice calculations is a result of a large increase in the number of degrees of freedom of the system [18]. Before the phase transition the system consists of a gas of hadrons, which is made up mostly of the three pions π^+, π^-, and π^0. The phase transition is a result of the quarks and gluons inside the hadrons becoming *deconfined*, which means they are no longer bound inside colorless hadrons. In the hadron gas phase the number of degrees of freedom are the number of hadrons that exist, which is dominated by the three pions. After the quarks and gluons become deconfined, the color, spin, and helicity degrees of freedom are available. The degrees of freedom grow from $\sim$ 3 to 40 - 50 in the temperature range of (1-3)T_c [18]. This deconfined state is called a Quark-Gluon Plasma.

An important result from QCD and deconfinement has effects on *chiral symmetry*, which involves the helicity of particles. The helicity is the projection of the particle's spin along the direction of its momentum:

$$h = \frac{\vec{S} \cdot \vec{P}}{|\vec{p}|}. \tag{1.17}$$

$\vec{S}$ is the particle's spin and $\vec{p}$ is the momentum. Massless fermions will travel at the speed of light, and the helicity will either be $+\frac{1}{2}$ or $-\frac{1}{2}$. Particles with helicity $+\frac{1}{2}$ are called right- handed are particles with helicity $-\frac{1}{2}$ are left-handed. For massless fermions, these right- and left-handed states are eigenstates. If the particles were massive, however, this ceases to be the case. The reason for this is simple: a massive particle must travel with a speed less than the speed of light c. It is therefore possible to boost into a frame that has a speed greater than that of the particle. In this frame, the helicity of the particle will flip because the sign of $\vec{p}$ will change while the sign of $\vec{S}$ will not.

The QCD Lagrangian for a massless quark, as seen in Equations 1.8 and 1.11, is

$$\mathcal{L} = \bar{\psi}\gamma^{\mu}\mathcal{D}_{\mu}\psi \tag{1.18}$$

with the kinetic gluon field omitted. For very light u and d quarks the mass term can be neglected. With no mass term, this Lagrangian can be separated into left- and right-handed components of the spinor $\psi = \psi_L + \psi_R$. The addition of the mass term, however, spoils the chiral symmetry of the massless Lagrangian:

$$\mathcal{L} = \bar{\psi}(\gamma^{\mu}\mathcal{D}_{\mu} - m)\psi \tag{1.19}$$

This Lagrangian can no longer be separated into left- and right-handed components due to this mass term.

Since the quarks do have mass, QCD is not absolutely chirally symmetric. However, the light u and d quarks can be thought to obtain a mass through *spontaneous chiral symmetry breaking.* The reason for this is that quarks, due to the strength of the strong force, can interact with the vacuum by virtue of their strong interactions with $q\bar{q}$ pairs that form. Pairs of quarks and antiquarks exhibit high attractive interactions due to the inherent strength of the strong force. With small u and d masses, it therefore becomes energetically favorable to create quark-antiquark pairs [19]. These pairs must have zero total angular momentum and linear momentum, and therefore a net "chiral charge". The vacuum expectation value has been calculated with lattice QCD to be:

$$\langle 0|\bar{\psi}\psi|0\rangle = \langle 0|\bar{\psi}_L\psi_R + \bar{\psi}_R\psi_L|0\rangle = (250MeV)^3. \tag{1.20}$$

The addition of the mass term introduces the term which introduces the non-zero expectation value with the vacuum. This *quark condensate* $\langle q\bar{q}\rangle$ can cause a quark to flip its helicity, and thus acquire a mass. The Lagrangian for massless quarks is chirally symmetric, but the vacuum interaction causes a spontaneous breaking of this chiral symmetry. The Goldstone bosons associated with this spontaneous symmetry breaking are the three lightest mesons: the pions.

An interesting feature of the quark gluon plasma is that it is expected to approx-

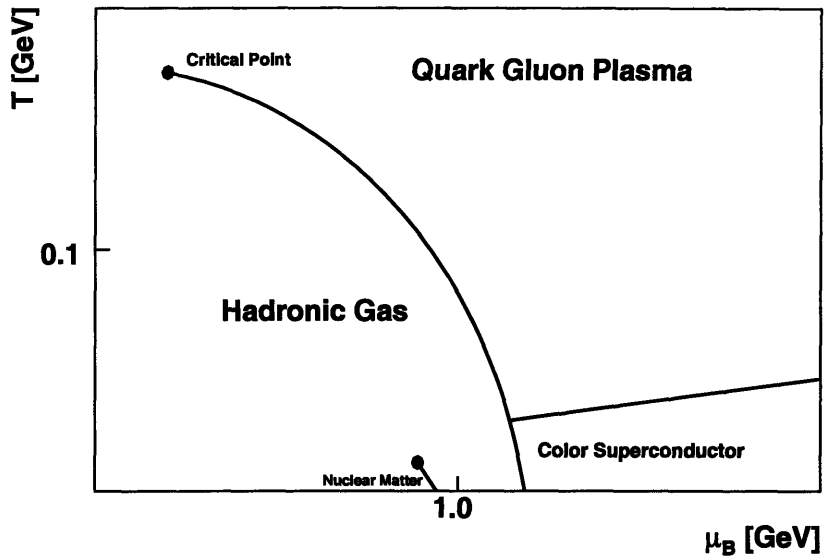

Figure 1-9: QCD phase diagram as discussed in the text.

imately restore chiral symmetry. To create the QGP high energy density is required. This high energy density can create many $q\bar{q}$ pairs (and gluons), and this high color density will screen the color charge for other quarks. The vacuum interaction will then reduce to zero, and chiral symmetry will be approximately restored.

In lower temperature regimes, but greater than T_c, the system is expected to be in a deconfined state, but the energies are low enough such that the constituents are still strongly interacting. This state is referred to as a sQGP, for strongly interacting QGP. At temperatures high above T_c the α_s becomes smaller and the constituents in the system interact very weakly. This state is called a wQGP, for weakly interacting QGP.

The different regimes of hadronic matter are shown in the QCD Phase Diagram, shown in Figure 1-9. The X-axis is the baryochemical potential μ_B (or the density of the matter) and the Y-axis is temperature. Normal nuclear matter exists at low temperatures near $\mu_B = 940$ MeV (the mass of the nucleons). At higher temperatures there is a hadron gas, and as the temperature is increased still more, there is a phase transition to the quark-gluon plasma.

At high densities and lower temperatures (lower right of the QCD phase diagram)

another form of matter is thought to exist which is called a color superconductor (discussed in [20]). In this state quarks form Cooper pairs with each other forming a superconductor of color, in much the same way electric superconductors form.

The critical point, as shown in figure 1-9, is also thought to exist, but not yet verified. The transition line separating the hadronic gas phase and the QGP phase is a first order transition. This transition is characterized by a sudden change from one phase to another. The lattice calculation seen in Figure 1-7 was carried out at $\mu_B = 0$, and shows a continuous transition between the hadron gas and QGP phases. This corresponds to the y-axis of the QCD phase diagram. This implies that at some point the first-order transition line must end before it reaches $\mu_B = 0$. The endpoint of a first order transition line is a second order critical point.

The universe was thought to exist in a deconfined hadronic phase for the first microsecond after the Big Bang. Some cores of neutron stars are thought to consist of quarks that exist in a deconfined state [21], but this has not yet been observed.

The best way to study the behavior of matter under these extreme conditions is through heavy ion collisions. Heavy nuclei are accelerated and collided, creating a hot dense region that may form a quark-gluon plasma. Studying p_T spectra can give information about the state of the matter produced in such a heavy ion collision. In 1982 Bjorken predicted a relative suppression in the p_T spectra in the presence of a deconfined medium [22]. This will be discussed further in Section 1.8. This QGP will form after a collision, and hence is termed a "final state". There has also been an initial state that has been predicted, called the Color Glass Condensate, which is also thought to effect the p_T spectra from heavy ion collisions.

1.5 Color Glass Condensate

While the QGP is a final state, which is formed after the collision, there can also be initial states, which exist before the collision occurs. In this thesis, the data from the p_T spectra of the PHOBOS experiment will be compared to the predictions of the parton saturation, or the Color Glass Condensate (CGC) model, as well as the

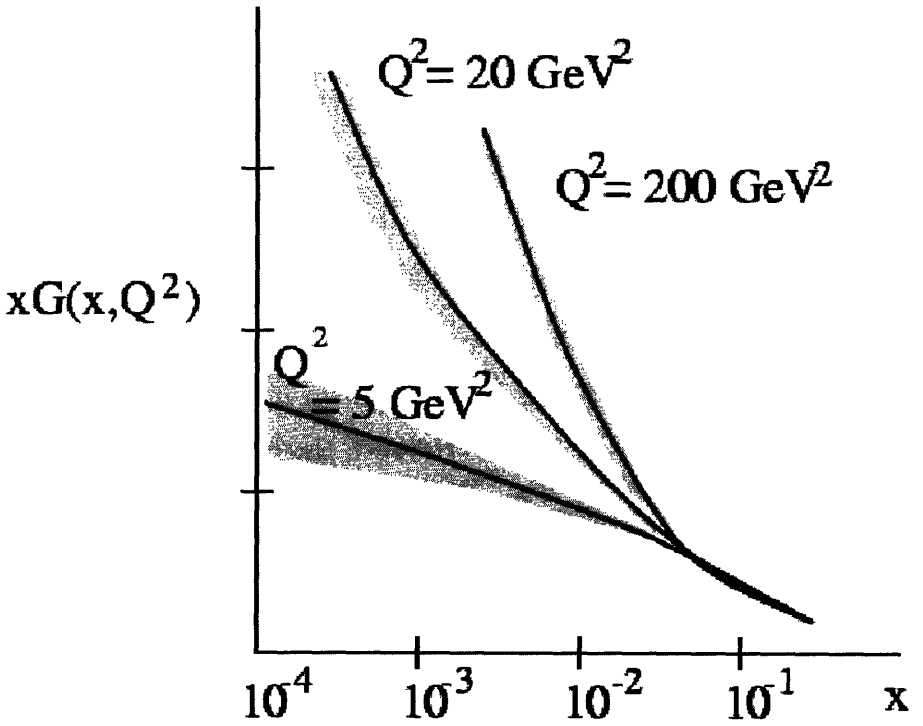

Figure 1-10: Gluon distributions from [23]

predictions from effects of the QGP.

The ZEUS experiment at HERA reported experimental results in the gluon density distribution, G(x,Q^2), as the beam energy of a hadron increases [23]. Q^2 is the momentum transfer scale at which the parton saturation sets in (see below). Figure 1-10 shows the rise in the gluon density as a function of x, the fractional momentum of the gluon with respect to the hadron's momentum. This rise in the gluon density with decreasing x is due to the self- interaction nature of the gluons, and was predicted to rise rapidly with log(1/x) [24]. This is caused by single gluons splitting into two gluons (the basic three gluon vertex seen in Figure 1-1) and enhancing the number of gluons with lower momenta [25], [26].

This gluon emission is not the only gluonic process that can occur. There is a competing process that stops the divergent rise in the gluon density from gluon emission. Just as one gluon can emit two gluons, two gluons can recombine into a single gluon. This process was predicted to kick in at very small x [27] and counteract the emission process. The rates of these processes depend on the density of gluons. The

emission rate is proportional to the density and the recombination rate is proportional to the square of the density [28]. The emission process increases the gluon density, but once the density is high enough, the recombination process will take over and effectively saturate the gluon density within the hadron or nucleus. This description of the emission and recombination processes is not a process that occurs as a function of time, it should be noted. The particular rates of emission and recombination depend on the momentum scale at which this is viewed.

The QCD phase that is reached when this saturation occurs is called the Color Glass Condensate. The reasons for this name are [18] [28]:

1): The gluons, which are the saturated particles, carry color.

2): The number of gluons at low x is high, and these are produced mostly from high x gluons. These high x gluons have a large time dilation, and therefore evolve very slowly with respect to natural time scales. This slow evolution with time is a property of a glass.

3): The density of gluons has increased and saturated, and the density is highest for low momentum gluons. The wavefunctions for these gluons will overlap and become coherent, and the occupancy of the low quantum states will be high. This is similar to a Bose condensate and shares some of its properties.

This state is a description of the wave function of the gluons in the nucleus, and is present regardless of beam energy. However, in the case of d+Au collisions, as the beam energy increaes the cross section for partons interacting with low momentum gluons increases as well, in much the same way that the structure of the atom can be revealed by increasing the probe's energy.

1.6 Heavy Ion Collisions

In heavy ion collisions it is important to quantify how head-on a collision is, i.e. the collision *centrality* (Figure 1-11). The impact parameter b is shown in the figure, and is the distance between the centers of the two nuclei. Although the impact parameter is a perfectly good quantity to use to denote centrality, it is more useful to quantify

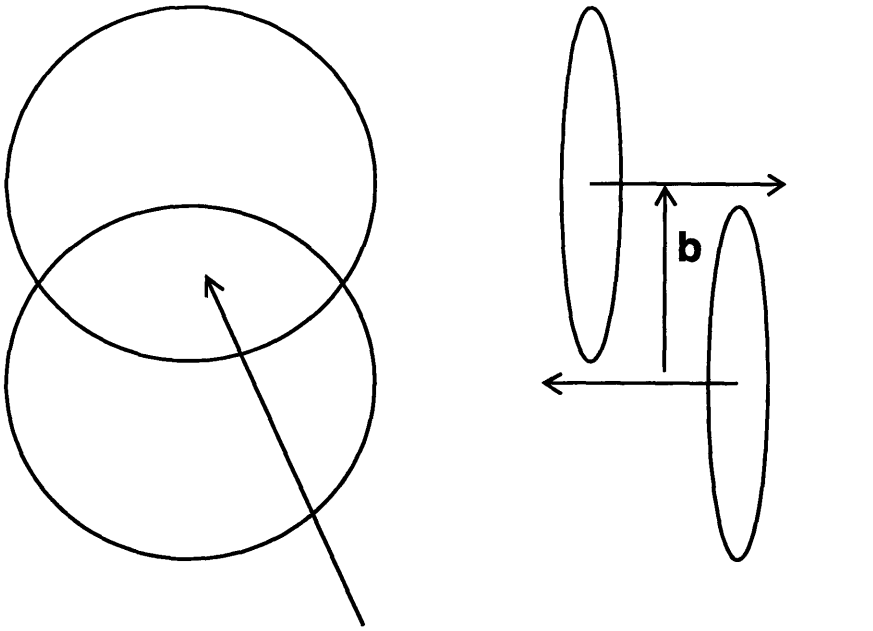

Figure 1-11: Illustration of a heavy ion collision. The illustration on the left shows a collision looking down the Z-axis, or in the beam direction. The illustration on the right shows the collision side view. The two nuclei are Lorentz contracted.

the centrality in terms of the number of interacting nucleons, which is called the number of participants, or N_{part}. A nucleon that undergoes a collision with another nucleon is considered a participant. Another quantity related to N_{part} is the number of binary collisions N_{coll}, which is the total number of nucleon-nucleon collisions that occur. Since nucleons can undergo more than one collision, N_{coll} is greater than or equal to N_{part}. Nucleon-nucleon interactions that occur in the heavy ion collision are generally classified into two broad categories: hard and soft collisions. Hard collisions are parton collisions with a large momentum transfer. Soft collisions are parton collisions with smaller momentum transfers. The generally accepted cutoff between the two is a momentum transfer of 2 GeV/c [29].

After the heavy ion collision, there are both elastic and inelastic interactions

between the particles produced. As the system expands the inelastic processes end and the particle species content is set. This is called *chemical freezout.* As the system continues to expand, all interactions of the particles cease, which is known as *kinetic freezout.* After this, the momentum distribution of the particles is set.

1.7 p_T Spectra

Studying the p_T spectra offers an opportunity to probe the state of matter that exists in heavy ion collisions. If a quark-gluon plasma is created, it is termed a "final state" effect because it comes into existence after the initial collisions occur. Hard processes that involve large momentum transfers involve short range interactions and occur very early in the nucleus-nucleus collision. These hard scatterings produce most of the high p_T particles, which come from the hadron jets as the scattered parton fragments. Because these hard scatterings generally occur early in the collision, the high p_T particles that result from them will have to traverse the medium that is created in the collision before reaching the detector. This is of interest, and one of the foci of this thesis because it has been theorized that high energy partons will quickly lose energy as they traverse a deconfined medium [30]. The dominant mechanism of this energy loss is gluon bremstrahlung radiation, which arises from the interactions of the parton with the color charges in the medium. The amount of energy loss is thought to scale with the square of the path length through the medium:

$$\frac{dE}{dx} \sim L^2 \tag{1.21}$$

This energy loss is calculated to be 1-3 GeV/fm. [31]. This effect of high energy partons losing energy is termed *jet quenching.*

After the kinetic freezout the p_T invariant yield distribution will have an exponential shape for the majority of the particles (particles with $p_T < 2$ GeV, which make up $\sim$ 99.9% of the particles produced in the collision). This is due to the particles reaching thermalization, and results in the familiar Maxwell-Boltzmann distribution. The high p_T particles, or jets, have a power law distribution, which dominates the

exponential distribution at high p_T. The soft particle production is thought to scale with the number of participants in the collision. Since hard processes can result from any binary collision, the yield at high p_T is expected to scale with the number of binary collisions N_{coll} in the absence of medium effects.

By comparing the high p_T spectra in Au+Au collisions with the corresponding spectra in d+Au, p+p, and A+A collisions at lower energies, we can examine the effects this medium has on the spectra and compare with theoretical models. Since the size of the collision region in the d+Au and p+p systems is much smaller they are not expected to create an extended deconfined region with which high p_T particles can interact and be appreciably effected by.

The way different collision systems are compared is with the *nuclear modification factors*, denoted by R. This thesis will investigate several different scaling scenarios. Two of these are scaling with both N_{part} and N_{coll} with respect to p+p, and a third is scaling with N_{part} with respect to peripheral heavy ion collisions. The nuclear modification factors compare the spectra of either Au+Au or d+Au with the spectra of p+p collisions at the same energy, with a weight of either N_{coll} or with the number of participant pairs $N_{part}/2$:

$$R_{AB}^{N_{part}} = \frac{d^2N_{AB}/dp_Td\eta}{\langle N_{part}/2\rangle d^2N_{pp}/dp_Td\eta} \tag{1.22}$$

$$R_{AB} = \frac{d^2N_{AB}/dp_Td\eta}{\langle N_{coll}\rangle d^2N_{pp}/dp_Td\eta} \tag{1.23}$$

The scaling with respect to the peripheral collisions is denoted $R_{CP}^{N_{part}}$, where C and P denote central and peripheral respectively:

$$R_{CP}^{N_{part}} = \frac{\langle N_{part}\rangle_P d^2N_C/dp_Td\eta}{\langle N_{part}\rangle_C d^2N_P/dp_Td\eta} \tag{1.24}$$

1.7.1 d+Au Spectra

Previous results [32] have shown that in p+A collisions, scaled by N_{coll}, there is an enhancement in the yield of high p_T particles with respect to p+p collisions. In other

words, the nuclear modification factor R_{pA} is greater than unity for $p_T > 2\text{GeV/c}$. This has been termed the *Cronin effect.* One explanation for this effect is the p_T broadening from multiple interactions [33]. The high p_T particles are assumed to be produced from hard scatterings. The final p_T from such a process is sensitive to the initial p_T of the interacting partons [33]. However, in a p+A or d+A collision particles can undergo multiple collisions. After each collision, the p_T of the particle becomes "broadened". In other words, each collision can give the particle a kick in the transverse direction. If the initial p_T distribution is taken to be a gaussian, each multiple scattering will in effect widen the gaussian distribution [34]. These two effects, sensitivity of the final p_T after a collision to the initial parton p_T and the broadening of the p_T distribution, serve to increase the yield in p+A and d+A collisions at high p_T relative to p+p collisions.

The effect of parton saturation can be studied with d+Au collisions. Since parton saturation is also thought to cause a decrease in the nuclear modification factor as a function of centrality [35], it can be used in conjunction with Au+Au data to help disentangle whether effects in the yields are due to initial or final state effects, since final state effects are not expected to effect the d+Au yields.

In addition to the centrality dependence of the d+Au spectra, the η dependence of the nuclear modification factor has been predicted to be sensitive to the effects of the Color Glass Condensate. The quantum evolution of the gluons, in which there is a sharp increase in the low-x gluons accessible at high beam energies, actually leads to a suppression in gluon production after a p+A or d+A collision. This suppression is a function of energy, or rapidity, and is suppressed relative to p+p collisions scaled by N_{coll}, which are not expected to produce a CGC. This suppression should be evident in the nuclear modification factor R_{dA} [36, 37, 38], which should show a decrease as the rapidity increases. As an example, R_{pA} has been calculated to be, at very high energies, to be [36]:

$$R_{pA} \sim A^{-0.2} e^{-1.0\alpha_s y} \tag{1.25}$$

which clearly shows the decrease with rapidity. The saturation scale Q_s is not yet known, and at what energies these effects will set in at has not been predicted. Therefore, equation (1.25) merely illustrates the suppressive effect with rapidity that the quantum evolution of the low-x gluons is thought to have in particle production relative to a system without the CGC.

Chapter 2

PHOBOS Detector

2.1 Overview

The PHOBOS detector sits in the 10 o'clock region in the Relativistic Heavy Ion Collider at Brookhaven National Laboratory. Data has been collected at $\sqrt{s} = 19.6$, 62.4 56, 130, and 200 GeV for Au+Au collisions and d+Au collisions at 200 GeV, and p+p collisions at 200 GeV. In this thesis the 200 GeV Au+Au data is referred to as the PR01 data, as it was collected in 2001, and the d+Au data is referred to as the PR03 data. PHOBOS was designed with several principles in mind: to cover as large a range in pseudorapidity as possible, to cover a large range in p_T, and to operate at a high trigger rate. The large range in η and p_T made it possible for PHOBOS to study a broad range of physics topics. Also, the high trigger rate would allow a search for rare events containing interesting new physics results.

Since some of the physics goals for PHOBOS were modified between the PR01 and the PR03 data runs, there were some modifications to the detectors. Most notable are the addition of the spectrometer trigger (SpecTrig) and the moving of the Time of Flight walls. These will be discussed in more detail in Sections 2.5 and 2.7. The detector layouts for the two runs are shown Figures 2-1 and 2-2.

The main elements of the detector are the two arm spectrometer, the 4π multiplicity detector, the vertex detector, the time of flight counters, and the trigger and centrality detectors.

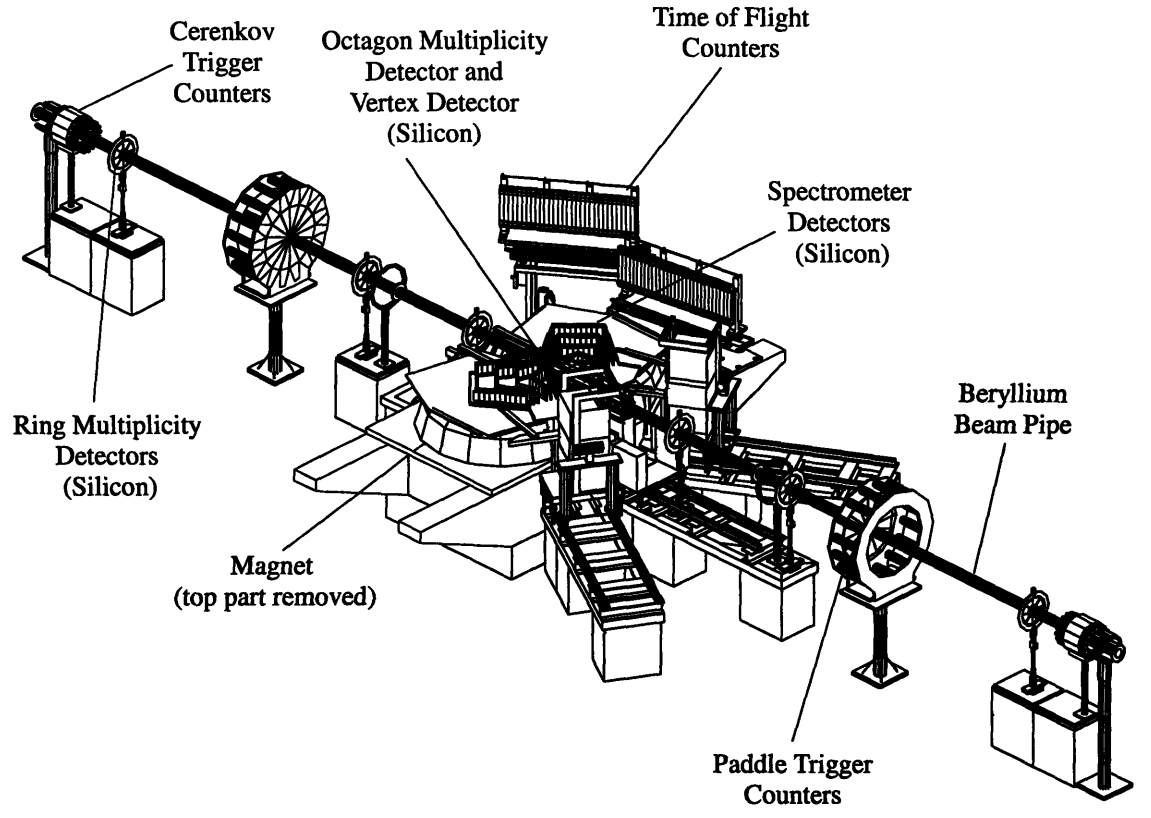

Figure 2-1: The PHOBOS detector for the PR01 Au+Au run.

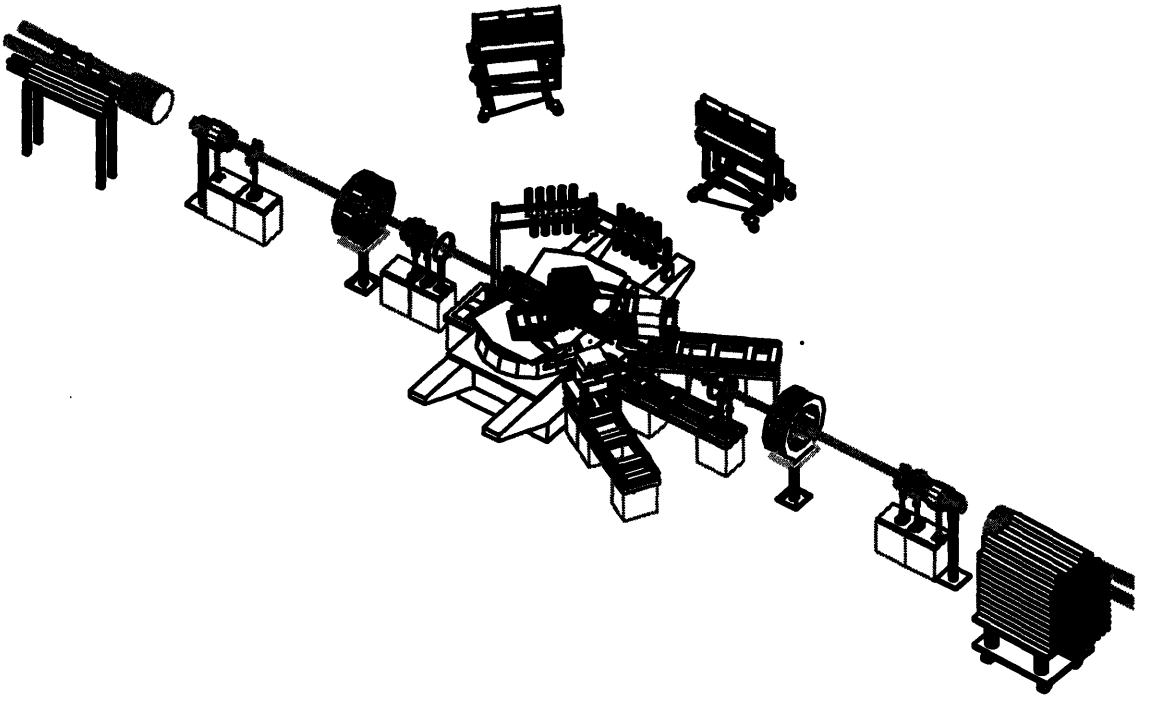

Figure 2-2: The PHOBOS detector for the PR03 d+Au run.

2.2 Beam Pipe

The beam pipe is made of three segments of beryllium tubing coated in an epoxy. Since beryllium is a low Z element it greatly reduces background and secondary particles scattering from its nuclei. The beam pipe is 12 m long in total, and is divided into three 4 m sections. The beam pipe has a diameter of 76 mm and is 1 mm thick.

2.3 Silicon Detectors

The spectrometer, 4π multiplicity detector, and the vertex detector all consist of silicon pad detectors [39]. These silicon detectors are used for a variety of tasks in the PHOBOS physics programs. Their basic designs are described here.

2.3.1 Sensor Design and Testing

The sensors were made by the Miracle Technology Co. and the National Central University in Taiwan [40]. There are nine different wafer designs for the silicon pad detectors used for the different silicon detectors, four of which are shown in Figure 2-3. The wafers vary in thickness between 300 and 340 μm. All of the wafer designs are single sided and signals are AC-coupled to an oxide nitride oxide (ONO) coupling capacitor and the first metal layer. There are two metal layers, with another ONO layer on top of the second layer to carry signals from the pads to the bonding areas at the edge where the chips are located. The junctions are biased by $5M\Omega$ polysilicon resistors.

After the sensors were diced and initially inspected at NCU further tests were carried out at the Massachusetts Institute of Technology and the University of Illinois at Chicago. A probe station was used to carry out the following tests: 1) The leakage current was measured as a function of bias voltage on the active area and guard ring separately. To pass the test the sensors were required to have less than 5 μA current for the active area for vertex and spectrometer sensors, and 10 μA for octagon and

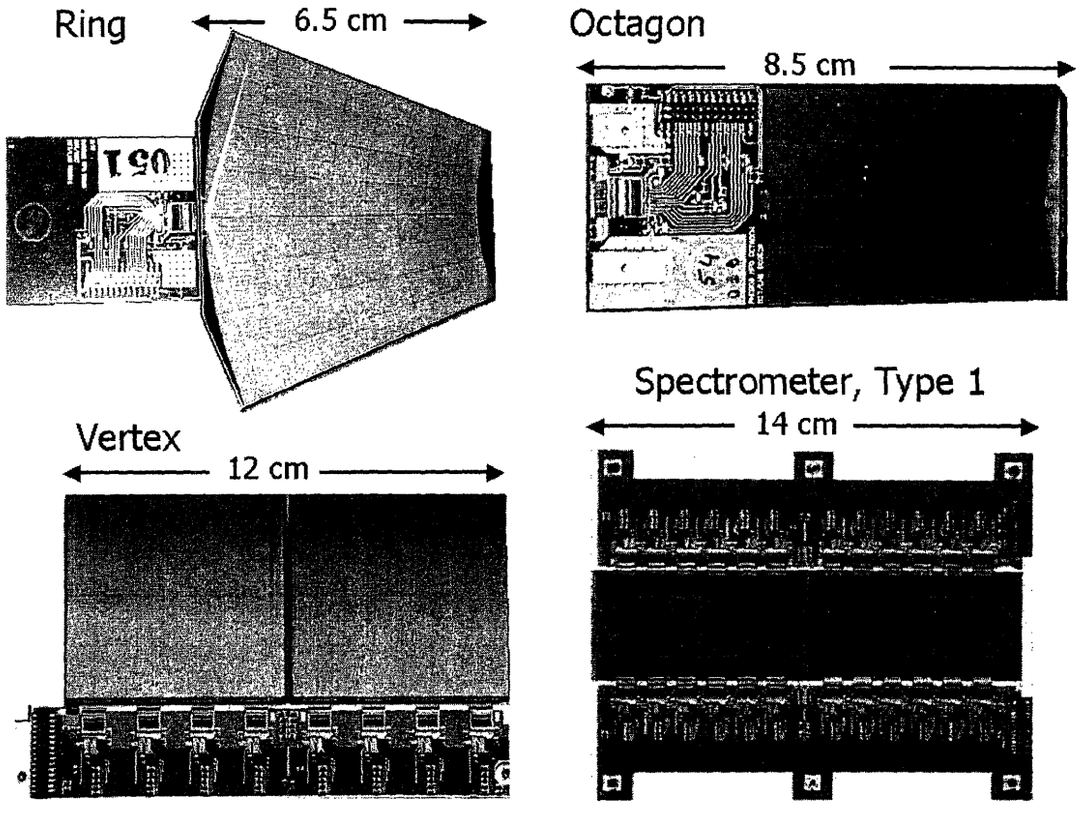

Figure 2-3: Four Silicon modules used in PHOBOS. Clockwise from top left: a sensor from the ring counters, a sensor from the octagon barrel, sensors from the vertex detector, and two sensors from one of the first four planes of the spectrometer.

Detector System	Sensor Type	Active Area (mm^2)	Number of Pads	Pad Size (mm^2)
Spectrometer	1	70.000 x 22	70 x 22	1.000 x 1.0
	2	42.700 x 30	100 x 5	0.427 x 6.0
	3	42.688 x 60	64 x 8	0.667 x 7.5
	4	42.688 x 60	64 x 4	0.667 x 15.0
	5	42.688 x 76	64 x 4	0.667 x 19.0
Multiplicity	Octagon	34.880 x 81.280	30 x 4	2.708 x 8.710
	Ring	3200	64	20 - 105
Vertex	Inner	60.584 x 48.180	4 x 256	0.473 x 12.035
	Outer	60.584 x 48.180	2 x 256	0.473 x 24.070

Table 2.1: Characteristics for the different silicon sensors in the PHOBOS detectors

ring sensors. 2) The depletion voltage as a function of bias voltage, which was found by measuring the capacitance of a *pn* junction with a guard ring, had to be less than 70 V. 3) The polysilicon resistor values were measured, and had to be between 1 and 10 MΩ. 4) There could be no more than 3% broken channels.

Once the sensors were tested they could be assembled into modules. A module consists of one to four silicon sensors mounted onto a hybrid. A hybrid is a mounting board that the silicon sensors and the preamplifier chips and readout circuitry are attached to. There are 13 separate hybrid designs for the silicon detectors. In the case of the spectrometer and vertex detectors the hybrid is made of ceramic. For the octagon and ring detectors the hybrid is a multilayer printed circuit board. After the chips were tested they were glued onto the hybrid with a conductive glue, and then the silicon sensors were glued to the hybrid using a special gluing station. Following this the sensors and the chips were electrically connected with micro wire bonds at MIT and by the Silicon-detector group at Fermi National Accelerator Laboratory. Table 2.1 summarizes the characteristics of the different silicon detectors.

2.3.2 4π Multiplicity Array

The 4π multiplicity array consists of the octagon and six sets of ring counters. Combined these give a single layer of silicon detectors that cover 2π in ϕ and $|\eta| < 5.4$.

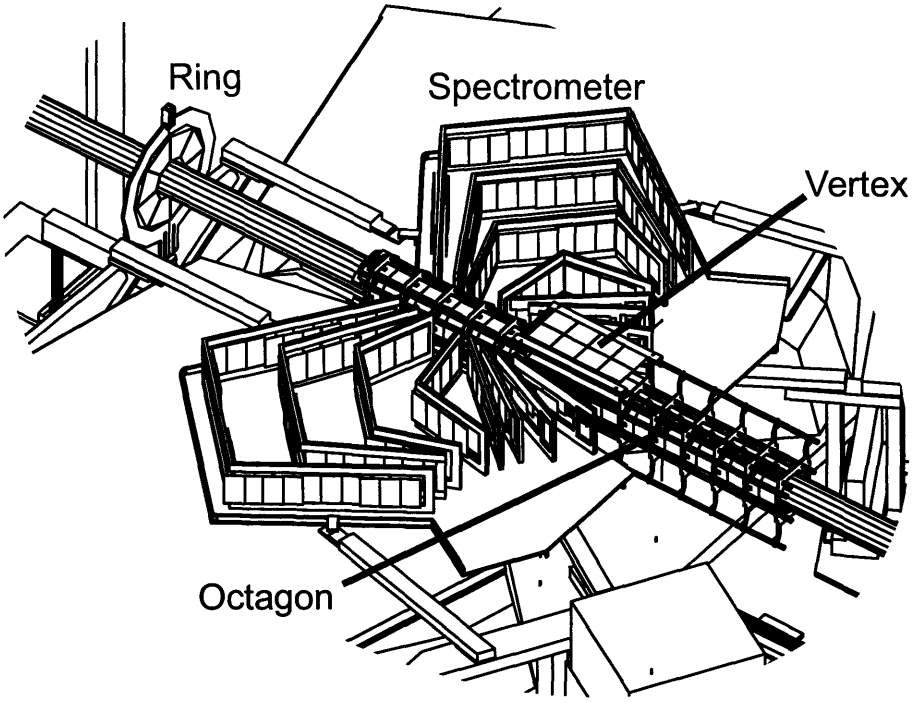

Figure 2-4: The Octagon, Ring, Vertex, and Spectrometer detectors.

Octagon

The octagon detector is barrel shaped and octagonal in cross section and surrounds the beam pipe. It is 1.10 m long and 90 mm in diameter (face to face). There are 92 silicon pad wafers in total, each one being 84 mm by 36 mm and are divided into four rows of 30 pads each. Octagon modules consist of one wafer attached to a printed circuit board hybrid. Each pad of the octagon covers between 0.06 and 0.005 units of rapidity, from midrapidity to the edges. The total pseudorapidity coverage of the octagon is $|\eta| < 3.2$. There are four holes in the octagon acceptance resulting from sensors being removed in front of the spectrometer arms and the vertex detector.

The octagon and associated electronics is supported with an aluminum frame, which includes tubes through which water flows to cool the electronics. The low density of the frame permits less background from scattering.

Rings

The rings form the high η region of the multiplicity array. They extend the coverage of the multiplicity detector to $|\eta| < 5.4$. There are are six sets of ring counters in total, placed around the beam pipe at distances of 1.13, 2.35, and 5.05 m from the nominal interaction point. The rings are disks with an octagonal shape and consist of eight silicon wafers each. Like the octagon, the ring modules consist of a single silicon wafer attached to a printed circuit board hybrid. Each wafer has 64 trapezoidal pads, varying in size from 3.8 mm x 5.1 mm at the inner radii to 10.2 x 10.2 mm at the outer radii. The inner and outer radii are 100 mm and 220 mm.

The support structures for the rings consist of carbon fiber frames. This low Z material allows for low backgrounds from particles coming from a collision. The rings are in turn encased in a light sealed aluminum box.

2.3.3 Vertex Detector

The vertex detector consists of two sets of silicon detectors above and below the nominal interaction point. Each set has two layers which are mounted on the octagon frame over two of the holes in the octagon. The vertex detector was designed to determine the collision position along the z-axis (along the beam line) to an accuracy of better than 0.2 mm. This is done by identifying two hit tracks in the inner and outer detectors which point to the collision location, or vertex. To get a high resolution in the vertex position, the pads of the inner and outer sensors of the vertex detector are finely segmented perpendicular to the z-direction (see Table 2.1). The inner vertex detectors are made up of two modules, each having two silicon sensors. The outer vertex detectors consist of four modules of two silicon sensors each. The vertex detector extends from $\pm$ 10 cm from the nominal interaction region. The inner vertex detector covers $|\eta| < 1.54$ and the outer vertex detector $\eta < 0.92$ for collisions at $z = 0$. The azimuthal coverage is $\Delta\phi = 42.7$.

2.3.4 Spectrometer

The spectrometer consists of two arms, one on each side of the beam pipe. They are partially situated in a 2 T magnetic field, and each arm is made up of 16 layers of silicon sensors. Eight aluminum water cooled frames support the silicon, with two layers per frame. These are mounted on a carbon-epoxy material base plate. The nonconductive nature of this material minimizes vibrations caused by eddy currents caused by the magnet. Of all the silicon detectors the spectrometer has the most variety of different types of silicon sensors used. The modules in the spectrometer have between two and four sensors each. There are a total of five different kinds of sensors used, as shown in Table 2.1, with 137 sensors and 42 modules total in each arm.

The first six layers are in an essentially field-free region, while the back 10 layers are in a 2 T magnetic field. The size of the pixels varies in the spectrometer to allow for greater track momentum resolution while at the same time keeping the total number of channels low. The first four layers contain type 1 sensors, which have the largest width at 1 mm. After these layers the magnetic field increases, and the pad width decreases in order to have a better momentum resolution. The pad height also increases to reduce the total number of channels.

2.4 Magnet

The PHOBOS magnet is a double dipole magnet that was designed at MIT and built by Danfysik in Denmark. The beam pipe runs through the middle of the magnet, with the two dipoles on opposite sides of the beam line. The magnet provides a field in the vertical (y) direction for the spectrometer, with one side having a positive field and the other side a negative field. This field allows for momentum measurements with the spectrometer. The total current provided is 3600 A. Figure 2-6 shows the measured vertical field with respect to the spectrometer. The horizontal components B_x and B_z are less than 0.05 T.

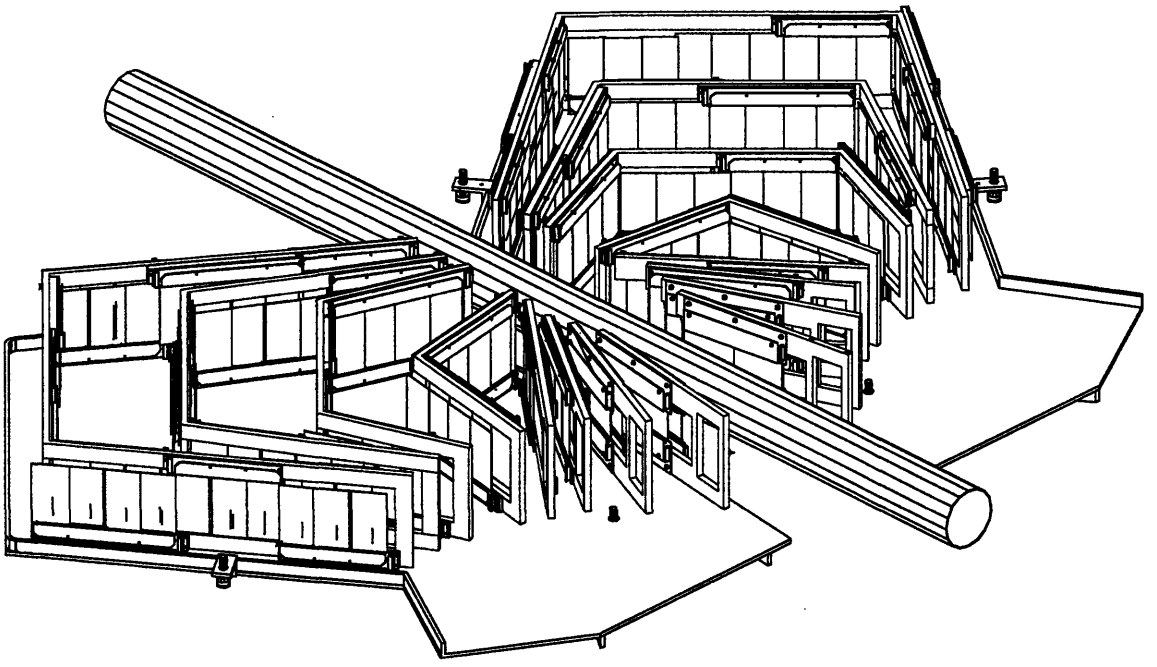

Figure 2-5: The PHOBOS Spectrometer

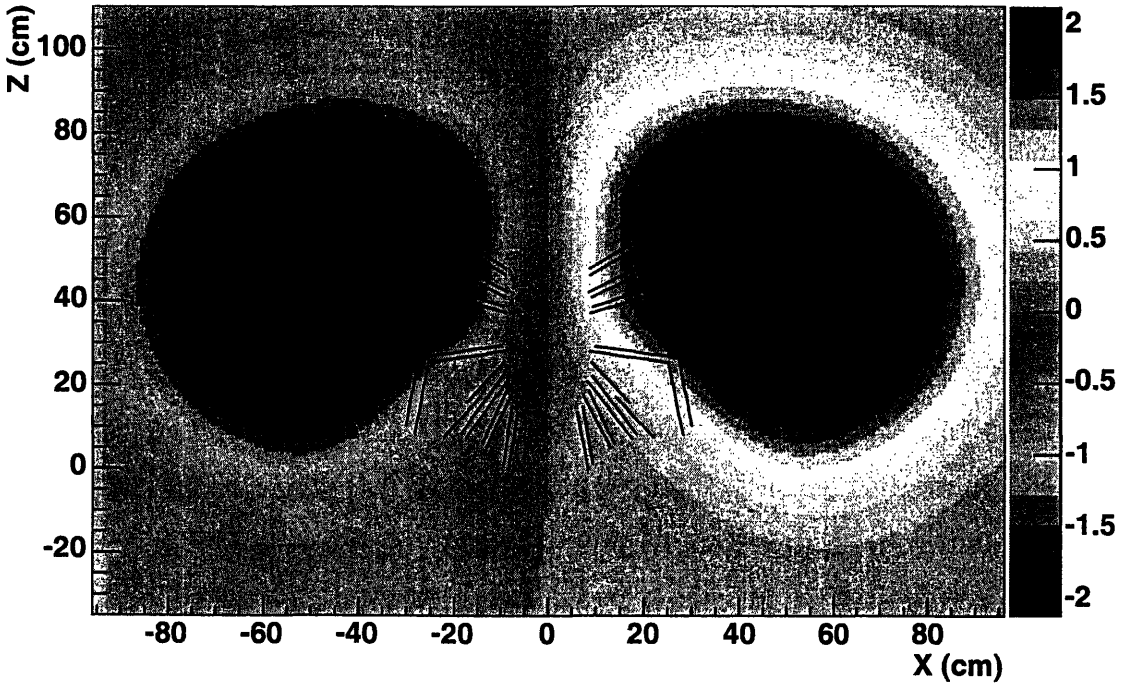

Figure 2-6: The magnetic field strength as it varies over the spectrometer.

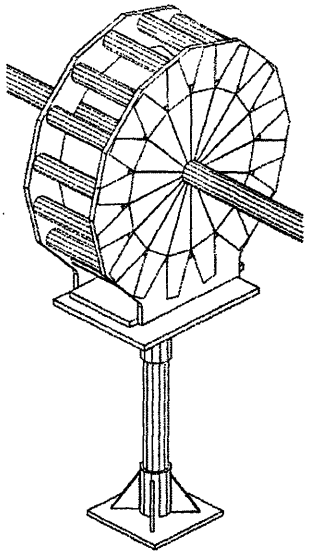

Figure 2-7: One of the set of paddle counters

2.5 Trigger System

2.5.1 Paddle Counters

The paddle counters [41], shown in Figure 2-7, consist of two arrays of BC-400 plastic scintillators located along the beam pipe at $z = \pm 3.21$ m from the interaction region. Each array is situated perpendicular to the beam pipe and is made up of 16 separate paddles with an active length of 18.6 cm. Each scintillator is attached to a BC-800 light guide which reflects light by a 45^o mirror into a photomultiplier tube. The phototube itself is encased in a magnetic mu-metal shielding. The active area of the paddles covers the pseudorapidity region $3 < |\eta| < 4.5$. The distance from the beam pipe to the inner edge of the active region is 7 cm and to the outer edge is 25.6 cm.

The paddles are the primary trigger detectors in PHOBOS. By measuring the time difference between signals in the positive paddles (PP) and negative paddles (PN) background events such as beam-gas interactions scattering upstream or downstream of the detectors can be reduced. This will be discussed in Chapter 3. The paddles have a time resolution of about 1 ns per paddle. Also, by measuring the amount of energy deposited in the paddles the centrality of the collision can be determined for Au+Au collisions. This will be discussed in greater detail in Chapter 3.

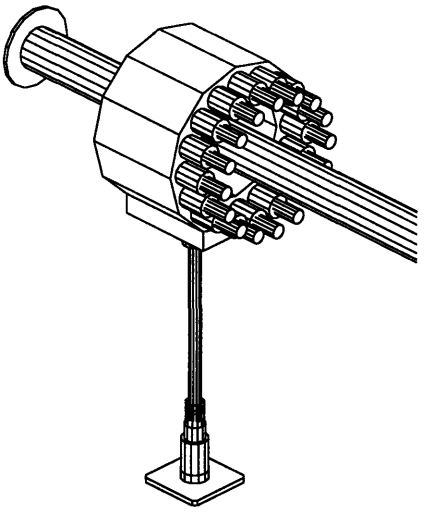

Figure 2-8: The Cerenkov counters and part of the beryllium beam pipe

2.5.2 Cerenkov counters

The Cerenkov counters [42], shown in Figure 2-8 provide an online vertex determination for the trigger system. Because the z position of the collision vertex can vary by a large amount, exceeding the acceptance of the spectrometer, the Cerenkov counters can reduce the spread in this position for events written to tape. They consist of two sets of 16 radiators positioned at ± 5.5 m. Each set of 16 radiators forms a ring around the beam pipe. The pseudorapidity coverage of these detectors is $4.5 < |\eta| < 4.7$, which is 37% covered by the active area of the counters. The center of the radiators is 8.57 cm from the beryllium beam pipe.

The radiators are made of BC-800 acrylic. Each cylindrical radiator has a length of 4.0 cm and a diameter of 2.5 cm. A hybrid photomultiplier tube assembly is attached to the end of each radiator, and each tube is inside a 2 mm mu-metal magnetic shield. The Cerenkov counters can provide an online vertex position to an accuracy of 4 cm. The timing resolution is between 350 to 400 ps for the individual counters, and the signal is available for the trigger in a time of 650 ns.

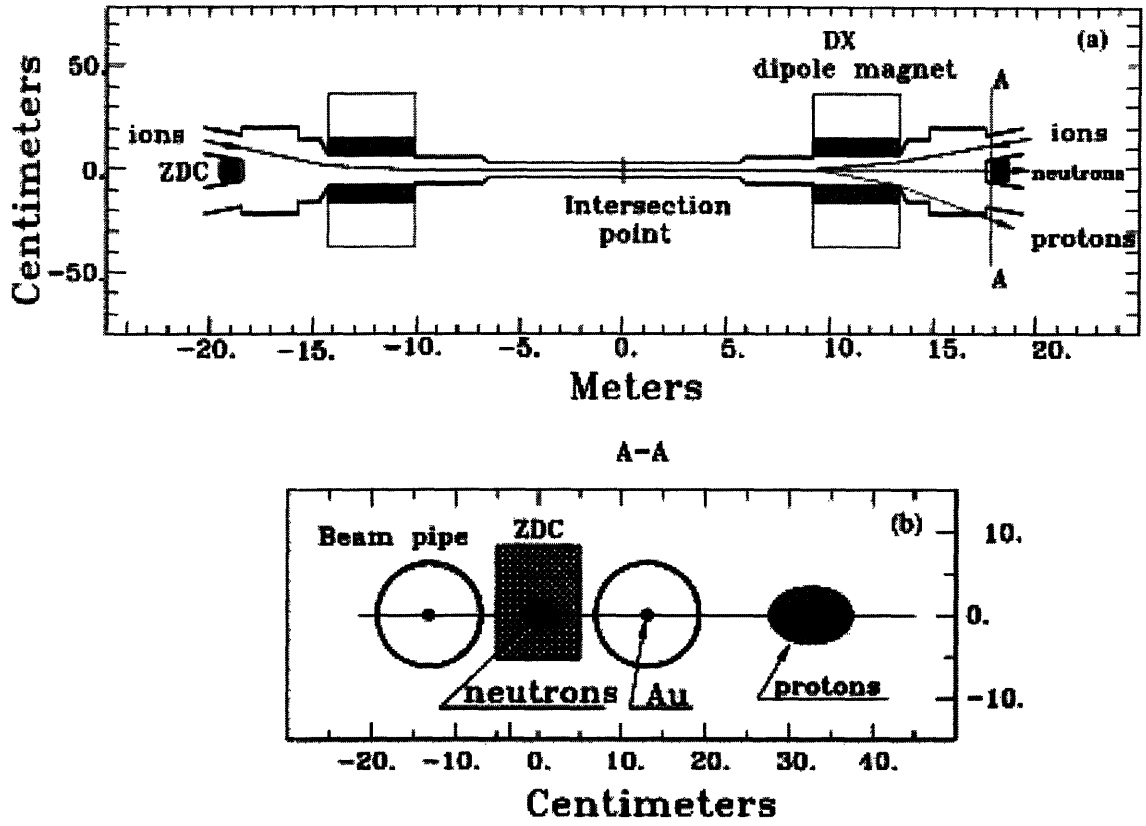

Figure 2-9: Position of the ZDC calorimeters in relation to PHOBOS and RHIC. The top figure shows a top view of the position of the ZDC's, with the interaction point being the position of PHOBOS. The bottom figure shows the view looking down the beam pipe. In this view, the DX dipole magnets shown in the top figure have separated the two beams into two different beam pipes. These DX magnets will sweep spectator protons out of the path of the ZDC's, leaving just the neutrons to hit the ZDC's.

2.5.3 Zero Degree Calorimeters

The Zero Degree Calorimeters (ZDC's) [43] are a set of trigger counters used by all four experiments at RHIC. The purpose of these calorimeters is to detect spectator neutrons from the collisions and measure the energy they deposit. PHOBOS has two ZDC's at $z = \pm 18.5$ m. They are located along the single beam line, but after the DX magnets separate the beam into the separate two beams, as shown in Figure 2-9. The DX magnets bend spectator protons away from the ZDC's, leaving the neutrons to hit the detector.

Each ZDC consists of three separate calorimeters placed end to end along the z-

axis. Each calorimeter is made of layers 5 mm thick tungsten plates, with 20 ribbons of 0.5 mm diameter optical fiber between the plates. There are 22 plates for each calorimeter and 4200 optical fibers. These optical fibers are then pointed toward a Hamamatsu R329-2 photomultiplier tube, with a 0.5 mm gap between the fibers and the PMT.

Neutrons traversing the tungsten create hadronic showers, and these in turn radiate Cerenkov light in the optical fibers, which is then then carried to the PMT. The tungsten plates are angled at 45^o relative to the beam to optimize the signal transmitted by the fibers. The energy deposited in the ZDC's can be used as an event trigger and as a centrality determination. Except for very peripheral collisions, there is an anti-correlation between the energy deposited in the ZDC's and the centrality. This will be discussed further in Chapter 3.

2.5.4 Spectrometer Trigger

The Spectrometer Trigger (SpecTrig) is a specialized detector installed for the d+Au run. In a low multiplicity environment it is used to trigger on rare events with high p_T tracks. The details of the triggering can be found in Section 3.2.

There are two SpecTrig detectors, B and C, located at 45^o and 90^o to the beam axis, between the spectrometer and the ToF walls. Each wall consists of 10 separate BC-408 plastic scintillator paddles from Saint-Gobain Crystals & Detectors. The scintillator paddle units consist of the active detector paddle, which is rectangular with a length of 11 cm and a width of 7.24 cm, and the light guide. The thickness of the scintillator is 0.5 cm. Glued to this scintillator is a trapezoidal light guide 15 cm long which tapers to a width of 4.4 cm. The scintillator plastic is wrapped in foil to reflect light. This light guide is then glued to a photo-multiplier tube with BC-600 optical cement. These PMT's are model number XP2212 from Amperex electronics and are from the E850 experiment at the AGS. The setup is then wrapped in black tape to block out light. The PMT is encased in an iron tube 2 mm thick which serves as a magnetic shield.

For long term stability testing purposes, an LED testing unit was constructed and installed for each SpecTrig wall. The fiber optic cables were cut to length and the ends were finely sanded to create a smooth flat surface. One end of the cable was then epoxied to a 3 cm by 2 cm piece of plastic. The piece of plastic had a groove machined down one face that the cable was epoxied into. This serves as a holder for the optic cable. These units were then epoxied onto the circular base of each scintillator unit such that the end of the cable pointed into the base, and hence into the PMT.

The other end of the cables were then run into a light tight aluminum box affixed to the aluminum frame of the SpecTrig. Inside the box, the ends of the cables, which have also been sanded, are pointed at a blue LED light situated at one end of the box. The ends of these cables were threaded into a plastic crossbar in the center of the box and circling a magnifying glass held in place by the crossbar. At the other end of the box, and at the focal point of the magnifying glass, is a photo diode.

The LED is hooked up to a voltage supply, and when turned on emits light that is picked up by the optic cables in the aluminum box and sent to the other end and into the PMT's. The photo diode also picks up light from the LED, and the signal from it is used to monitor the stability of the LED over time. Once the intensity of the LED is accounted for, the signals from the PMT's can be monitored for long term stability.

2.6 Proton Calorimeter

The proton calorimeter (PCal) was designed after the PR01 run and installed for the PR03 d+Au run. The PCal consists of two detectors close to the beam pipe next to the ZDC's. The positive PCal (the detector on the positive z-side) is an array of modules eight wide by ten high, and the negative PCal is two modules wide and two modules high. Their main purpose is to detect spectator protons from the collision. Since they sit next to the ZDC's and beyond the DX magnets, the protons that do not participate in the collision will be bent by the DX magnets and into the PCal,

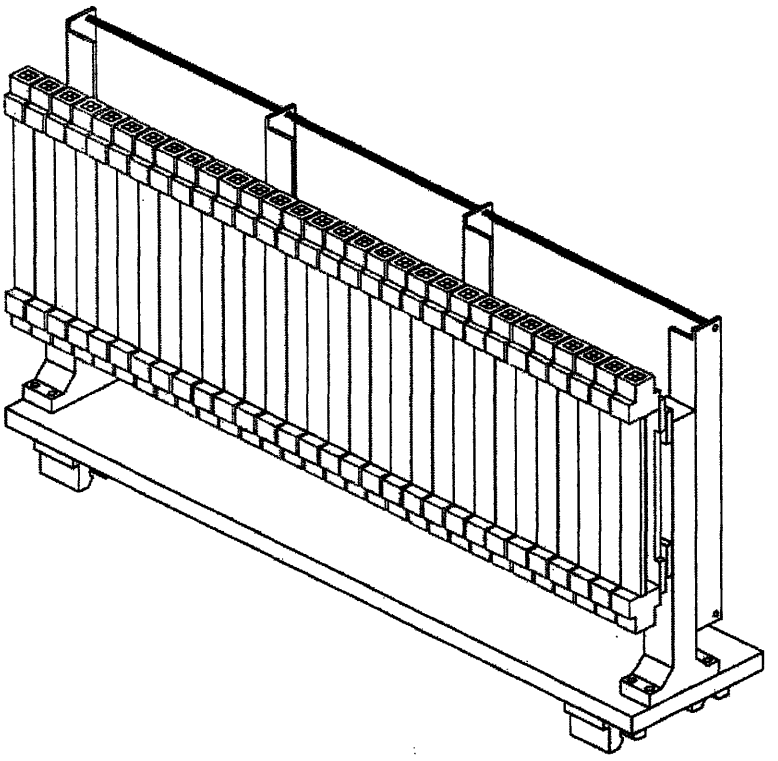

Figure 2-10: One of the ToF walls

while the spectator neutrons continue straight and hit the ZDC's. The PCal thus provides a complementary energy measurement to the ZDC's that can be used to study centrality. Since the negative PCal sits on the deuteron fragmentation side, it is expected to record at most one proton, and therefore is much smaller. Two sets of concrete shielding between the interaction region and the PCal protect it from particles from the collision that are not spectators.

The PCal modules are made of lead absorber sandwiched with plastic scintillator. The scintillator fibers have a diameter of 1 mm and are sandwiched at 0.213 cm intervals. The modules have a 10 cm square cross section and are 117 cm long. The scintillating fibers end in a light guide, which is 42 cm long. At the end of the light guide photomultiplier tubes are glued.

2.7 Time of Flight

The purpose of the time of flight detector is to provide particle identification at high p_T, beyond the capabilities of the spectrometer. The time of flight consists of two separate parts: wall TB and wall TC. Wall TB sits behind the negative spectrometer arm at a 45^o angle from the beam axis. Wall TC is also behind the negative spectrometer arm, but at an angle 90^o to the beam axis. For the d+Au run both walls were moved to distances of 5.4 m for wall TB and 3.9 m for wall TC in order to increase the p_T range for identifying particles. One of the ToF walls is shown in Figure 2-10

Each wall consists of 120 Bicron BC404 scintillator of height 20 cm and width 0.8 cm. Attached to the top and bottom of each scintillator is a photomultiplier (Hamamastsu R5900) with a fast rise time of 1.8 ns and a high gain of 1×10^6. The two photomultipliers can be used to measure the vertical position of a hit in the scintillator by measuring the time difference between signals on the top and bottom tubes. The resolution for this position measurement is 1.0 cm.

2.7.1 Time-Zero Counters

The time-zero detectors, or T0's, are needed to measure the actual time of flight of particles that hit the ToF. These consist of two sets of Cerenkov detectors located at $z = \pm 5.2$ m for the Au+Au run and $z = 5.2$ and $z = 2.5$ m for the d+Au run. The T0 in the deuteron fragmentation direction was moved close to increase the acceptance. Each Cerenkov radiator is made from Bicron BC800 and is 25 mm long and 50 mm in diameter. These are attached to a 50 mm diameter photomultiplier tube (Hamamatsu model R2083). For the Au+Au run there were four tubes per side and centered on a circle of radius 15.1 cm. For the d+Au run there were 10 tubes per side. The T0's provide a timing signal used by the ToF to measure the flight time for particles hitting it.

Similar to the Cerenkov detectors, the T0's can also be used to determine the vertex position of a collision online. The details of this triggering will be discussed in

2.8 Readout Electronics and Data Acquisition

2.8.1 PHOBOS Trigger

To collect data from actual heavy ion collisions event information must be analyzed quickly so that the data collected in all the detectors can be stored and written to disk (for a general reference see [44]).

Signals from the ToF and the trigger detectors are sent to VME modules in a FASTBUS crate in the counting house. This information is used to determine whether or not an event has occurred, and hence whether to process and store the data taken in the silicon detectors. The Level 0, or L0, trigger, signifies a possible event. The L0 trigger is given by signals from the paddle counters called *PP*PN(wide)*. This requires both paddles to be hit, and for the time difference of the two hits to be less than 38 ns. This puts the collision in the interaction region of the detector.

The Level 1, or L1, trigger tells the DAQ to readout the event and process the event. This is usually given by more accurate vertex information. Figures 2-11 and 2-12 show schematic diagrams of the trigger logic for the PR01 run and the SpecTrig logic from the PR03 run.

2.8.2 VA Chip

To read out the signals from the silicon a commercial integrated circuit is used, which is called a VA chip. These chips are glued on the same hybrids as the silicon sensors with micro-wire bonds. They have a bussed differential analog readout which allows them to be connected together to increase the number of readout channels. Since there are nine different silicon wafer designs with varying number of channels, this feature becomes important. The chips have a range of 100 times the energy of a minimizing ionizing particle.

A schematic of the VA chip is shown in Figure 2-13. The current from the silicon

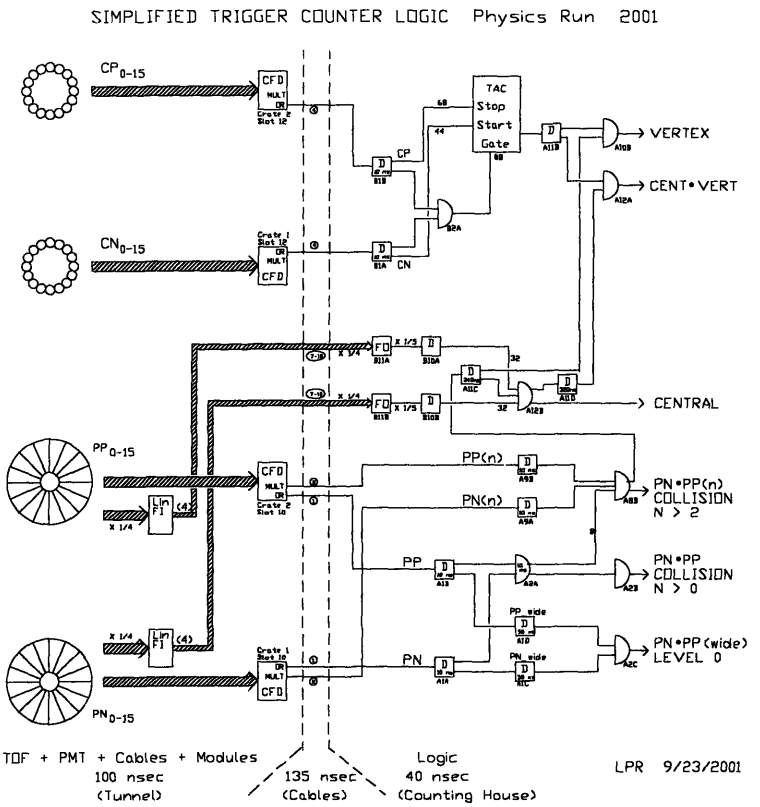

Figure 2-11: Trigger logic for PR01

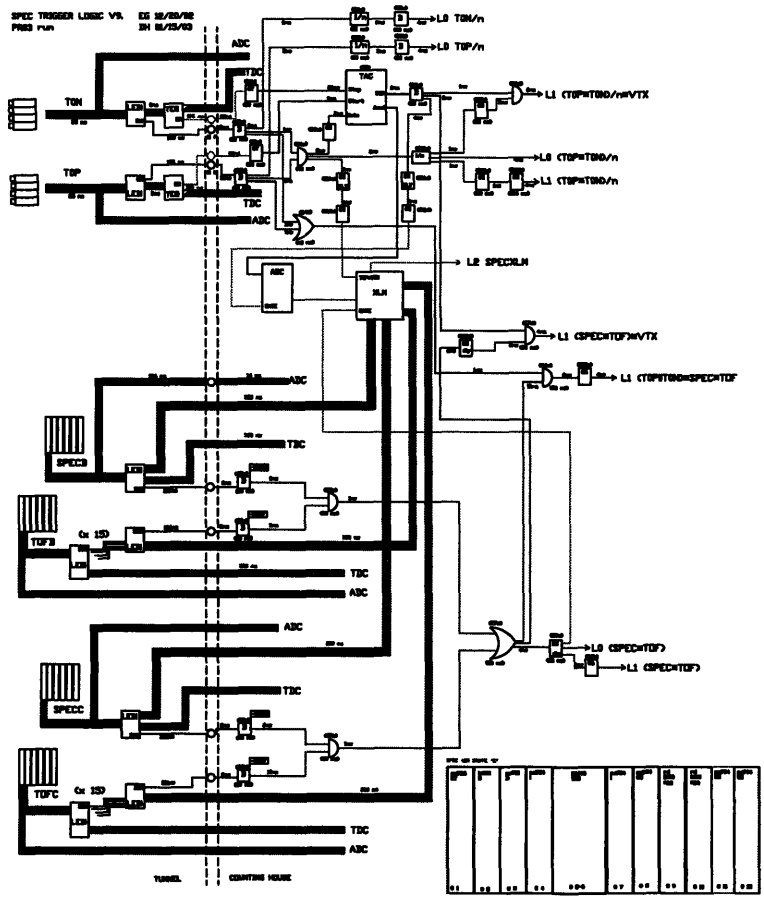

Figure 2-12: Trigger logic for the SpecTrig used in PR03

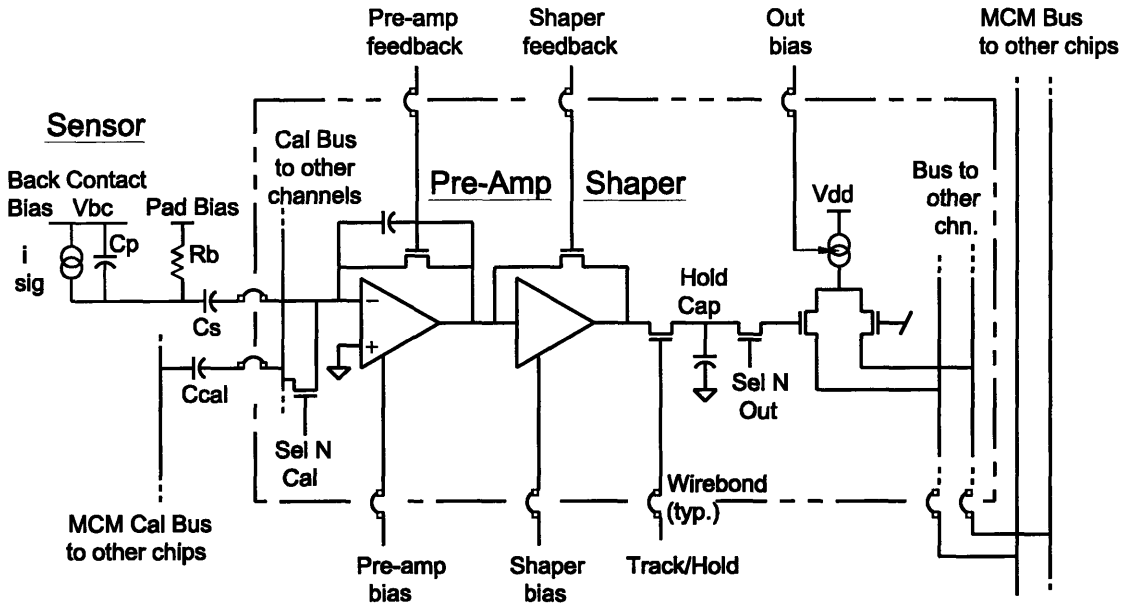

Figure 2-13: Schematic drawing of the VA chip

is first integrated by the pre-amplifier with a nominal time of 100 ns and 50 ns decay onto a 10 pF capacitor. After the the pre-amplifier is the shaping stage, which has a time of 1.1 μs set, and after this is the track-and-hold stage.

2.8.3 Front-End Controller

Controlling and reading out the silicon detectors is carried out by modules that make up the Front-End Controller, or FEC. These modules are located about 2 m from the detector. The silicon modules are connected to the FEC modules by flex cables. These cables are composed of a 30 conductor flat cable core and laminated copper foils on both surfaces for the power rails and ground. These cables provide good shielding and voltage drops for the load currents. Each FEC has four ports, and each silicon module is connected to one or two ports on the FEC. These ports provide, via the flex cables, the bias voltages for the silicon and bias and control signals for the VA chips. They also provide temperature monitoring. The bias voltages are generated from a 0 to 200 V regulator for the silicon and a 0 to 2 V regulator for the VA chips.

Each port on the FEC can allow 1472 channels, which are evenly split into two

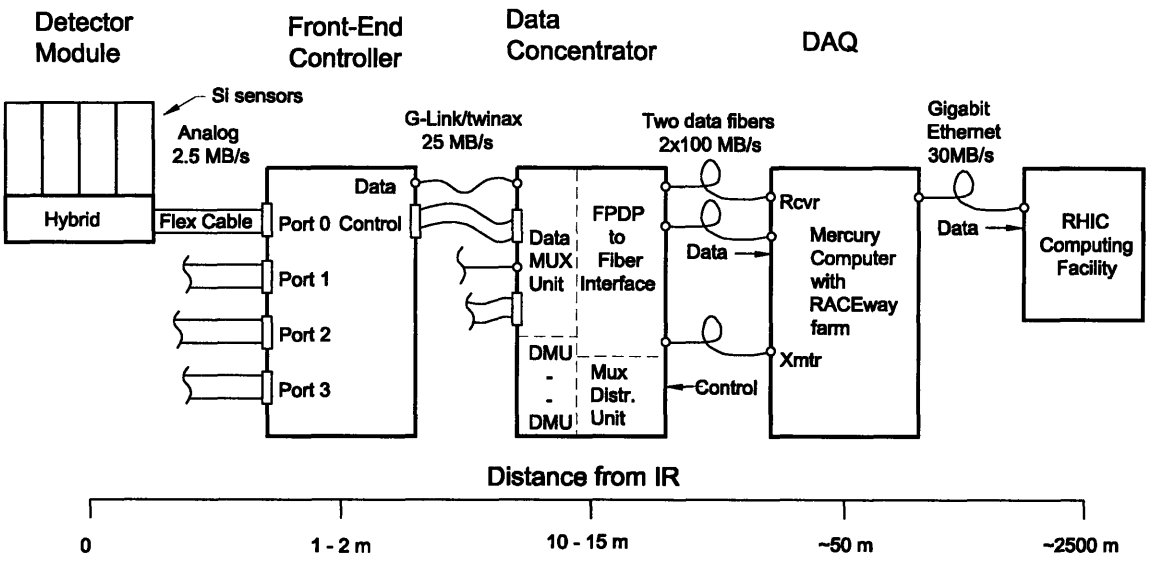

Figure 2-14: Electronics system for reading data from the silicon detectors

strings. Each string provides a differential analog signal and a digital signal. The string circuit on the FEC signal board in turn has a differential receiver for the string's analog signal, which is then digitized with an ADC. This then goes to the FIFO, which can store two events of data.

The FEC uses a field programmable array (FPGA) to control its various functions and modes of operation, which are Set-up, Test, Calibration, and Run. The FPGA boots from a programmable read-only memory chip (PROM), which contains information about the ports, such as bias voltages for the sensors and VA chips and the number of channels per string.

For data taking the FEC's are set to Run mode. In Run mode the FEC waits for an L1d signal, which is a 1.1 μs delayed first level event trigger (L1). Once it receives this signal it sends a "Hold" signal to the VA chips, which causes them to capture the peak of the analog signal from the silicon. Then when it receives the L2 signal it reads out the strings, digitizes them, and sends the data to the data concentrator via a G-link interface over twin coaxial cable.

2.8.4 Data Concentrator

The data concentrator controls the data going in and coming from the FEC's. It consists of three types of modules: the Data Multiplexing Unit (DMU), the Multiplexor Distributor Controller (MDC), and the FPDP/Fiber Interface (FFI). The DMU is connected to the FEC's via G-Link, which can transmit data at 25 MB/s. The FEC's transmit the data to the DMU's in parallel. The DMU's also transmit the trigger information to the FEC's. The data is then stored in a FIFO.

The MDC controls the data concentrator. It multiplexes the data from the DMU to a bus using the FPDP protocol, which are then received by the FFI. The FFI then serializes the data and streams them to the counting house.

2.8.5 Data Acquisition

The data from the silicon is sent to the counting house over two fiber optic wires at 100 MB/s. They are sent to a Mercury RACEway farm and distributed between 24 PowerPC-750 CPU's. Each CPU is dedicated to processing a certain portion of the event. When it is done it sends a compressed buffer to an UltraSPARC VME computer, which builds the events from the input of all the CPU's. Upon completion of the transfer to the UltraSPARC host, it constructs a ROOT object containing the event information, including the data from the FASTBUS trigger crate. It then transfers the data to the RHIC Computing Facility (RCF) over Gigabit Ethernet.

2.9 PHOBOS Coordinates

In the PHOBOS coordinate system, Z lies along the beam direction, and Y lies in the vertical direction (with positive pointing downward). The X direction is then transverse with Y and Z to make the system right-handed. In spherical coordinates, θ is the angle to the beam axis, and ϕ is the azimuthal angle, measured as the angle to the Y = 0 plane. The pseudorapidity, η, is defined as $\eta = -ln(tan(\theta/2))$.

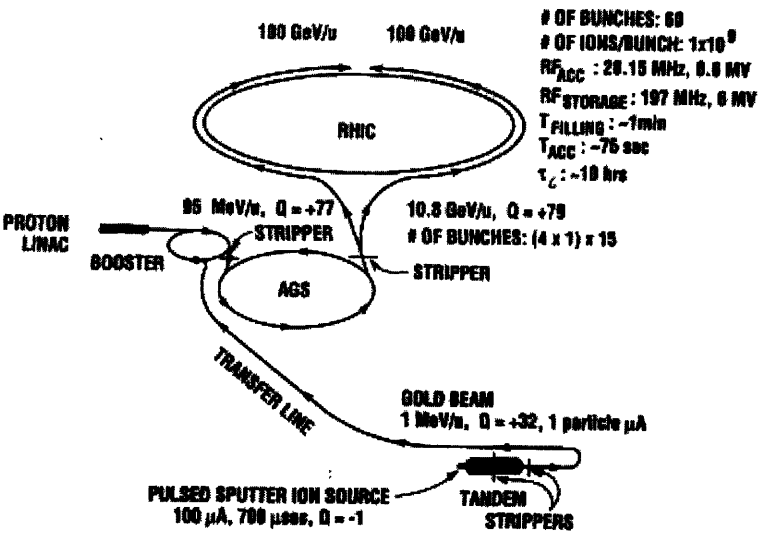

Figure 2-15: RHIC facility.

2.10 RHIC

The Relativistic Heavy Ion Collider [45] was first conceived in 1983, and construction began in 1991. The collider consists of two beam rings in a tunnel with a circumference of 3.8 km. The RHIC tunnel was actually originally built for the ISABELLE project. RHIC was also designed to use existing hadron accelerators, the Tandem Van de Graaff, the Alternating Gradient Synchrotron (AGS), and the Booster, to inject beam into the collider rings.

2.10.1 Tandem Van de Graaff

The first link in the injector chain is the Tandem Van de Graaff, which starts with negatively charged gold ions from its pulsed sputter ion source. There are two stages where the gold ions are stripped of some of their electrons with a foil. Upon leaving the Tandem Van de Graaff they have a charge of +32 and have been accelerated to an energy of 1 MeV/A.

2.10.2 Booster

After the Van de Graaff the gold ions are selected based on their charge using bending magnets and sent down the transfer line and to the Booster. Here they are further accelerated to 95 MeV/A. As the ions exit the Booster for the AGS they are stripped of all but two electrons, thus acquiring a charge of +77.

2.10.3 Alternating Gradient Synchrotron

Gold ions leave the Booster and enter the AGS for the final acceleration up to the injection energy into RHIC of 10.8 GeV/A. The ions are injected into the AGS at 24 bunches, and are then debunched and rebunched into four bunches. These four bunches are then injected into RHIC at 10.8 GeV/A. In the AGS-to-RHIC transfer line the gold ions are stripped of their last two electrons.

2.10.4 Relativistic Heavy Ion Collider

Once the ions are injected into the RHIC ring from the AGS they can be accelerated up to their final energy. This acceleration and the storage of the beam is accomplished with two RF systems. One, which operates at 28 MHz, captures the bunches from the AGS and accelerates them to the final collision energy. The other RF, which operates at 197 MHz, provides a small collision vertex region for the four detectors.

The two counter rotating beams in RHIC are labeled the blue and yellow rings, which are concentric and lie at the same vertical level. The collider consists of six curved arc sections, which are 356 m long each, and six straight insertion sections, which are 277 m long each. The collisions occur at the center of the insertion sections. The arc sections contain series of dipole, quadrupole, and sextupole magnets. In the insertion sections, a pair of dipole magnets (DX and D0, located 10 m and 23 m from the collision point) steer the beams into a common beam pipe for collisions.

The maximum energy for Au+Au collisions RHIC is designed for is $\sqrt{s_{NN}} = 200$ GeV. It can also operate at lower energies, and has delivered Au+Au collisions at $\sqrt{s_{NN}} = 19.6$, 56, 62.4, and 130 GeV in addition to 200 GeV. It can also accelerate

different species, such as deuterons and protons. The maximum energy for $p + p$ collisions is $\sqrt{s_{NN}} = 500$ GeV.

Chapter 3

Data Processing

3.1 Signal Processing

Once the ADC silicon signals are received they must be converted to a usable form for analysis. The raw signals need to be corrected for pedestals and noise before signals from hits can be meaningfully interpreted as deposited energy.

3.1.1 Pedestal Correction

In general, when a silicon pad receives no hits, i.e. there is no particle traversing it and depositing energy, the ADC output is still nonzero. This is due to leakage currents and general noise in the electronics. This nonzero output signal when there are no hits in the pad is called the pedestal. Studies have shown that the pedestals for the pads can change often enough that they need to be calculated for every run.

Ideally a special run would be taken while there is no activity in RHIC, and the signals recorded in each pad would be its pedestal. However, this requires RHIC to be down, and there is not enough of this downtime. This procedure was used early on, but as RHIC's uptime improved a new method was needed. At the beginning of each run the ADC signals from the first 200 events of each pad are averaged. Next, the first 300 events are run over with the average from the previous iteration subtracted from the signal. Only signal differences of $< \pm 100$ ADC units are used to remove

pads with a real signal. These signal differences are histogrammed, and the bin with the highest population is taken to be the pedestal. The top histogram in Figure 3-1 shows the pedestals calculated for one Au+Au run.

3.1.2 Noise Correction

There are two types of noise that must be corrected: common mode noise and random noise. Noise from effects in the electronics causes fluctuations around the pedestal. Common mode noise is noise that affects all pads for a given chip and random noise is noise affecting just one pad. Common mode noise (CMN) is corrected for event by event. After subtracting the pedestal, the ADC signal is histogrammed for each pad and each chip, leaving out large signals indicative of a hit pad. The histogram bin with the highest content is taken to be the CMN, and this value is subtracted from the signal in all pads connected to that particular chip. The middle histogram in Figure 3-1 shows the common mode noise for one Au+Au run.

Random noise is corrected after both the pedestals and the CMN is subtracted from the signal. The signals for each pad are histogrammed for 300 events, and the root mean square of the distribution is the random noise, which is then subtracted from the signal in the pad. Figure 3-1, bottom panel shows the random noise associated with each chip in a given sensor.

3.1.3 Gain Calibration

Once the pedestals and noise have been subtracted, the ADC signals in the pad must be related to the amount of energy deposited by a particle.

This was done using special calibration runs while there was no beam. It was determined that the calibrations were stable with time, and these calibration runs were only taken every few weeks. A known amount of charge from a digital to analog converter (DAC) is sent into each pad, and the corresponding ADC signal is measured. These two values are plotted against each other for each chip, which is called the gain calibration curve. This curve is linear, and only deviates at very high input charges.

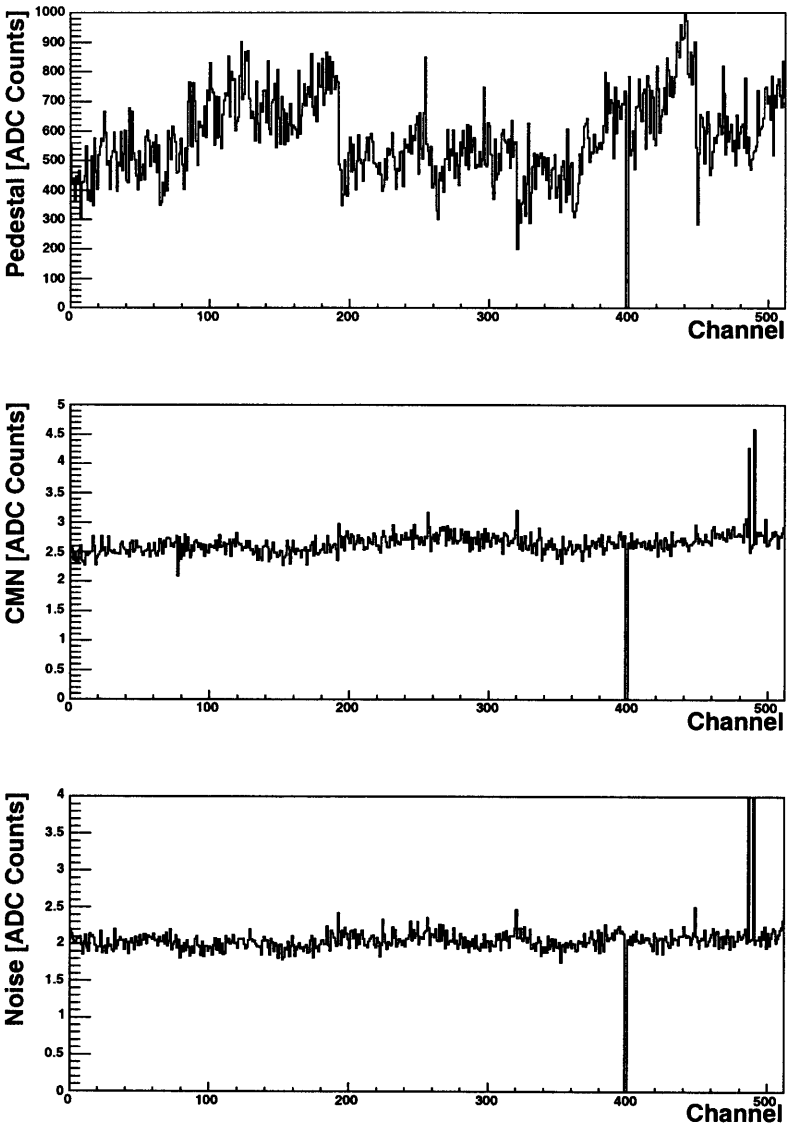

Figure 3-1: The top figure shows the pedestals for the chips of a given spectrometer sensor. The middle histogram shows the common mode noise (CMN), and the bottom figure shows the random noise.

The slope of this line gives the energy per ADC unit, which is 2.1 keV.

3.1.4 Hit Merging

Because particles most often do not hit the silicon perpendicularly, they have a chance of hitting more than one pad. Particles hitting at shallow angles can strike a number of pads before leaving the active area. A procedure is used, called merging, where signals from multiple hit pads are merged and considered as a single hit.

During the data processing the silicon hits are analyzed. For a given hit, the pads adjacent to it in the local X direction are checked for a signal. If the signal in the adjacent pad is greater than 0.15 MIP (minimum ionizing particle), its energy is summed with the previous pad's energy. This process is continued until a pad fails the energy cut. If the total energy is greater than 0.5 MIP, the cluster of hit pads is counted as a single hit, with a location determined by a weighted average with the energy of each hit pad. Because, in the spectrometer, the Y segmentation of the silicon is very large, except in the first four planes, this process is only carried out in the X direction for those sensors.

3.2 Event Selection

Actual heavy ion collisions must be distinguished from other events that leave hits in the detectors. Ions in the beam can interact with gas in the beam pipe, which could then leave hits in the silicon and the paddle trigger detectors. Therefore, processes were developed for the Au+Au and d+Au data to sift these background events out from the true heavy ion collisions.

3.2.1 Au+Au Event Selection

The main detectors used in the event selection for the Au+Au data are the plastic paddle counters and the ZDC's. Figure 3-2 shows the time difference Δt of signals in the two sets of paddle counters. If a collision occurs in the interaction region of

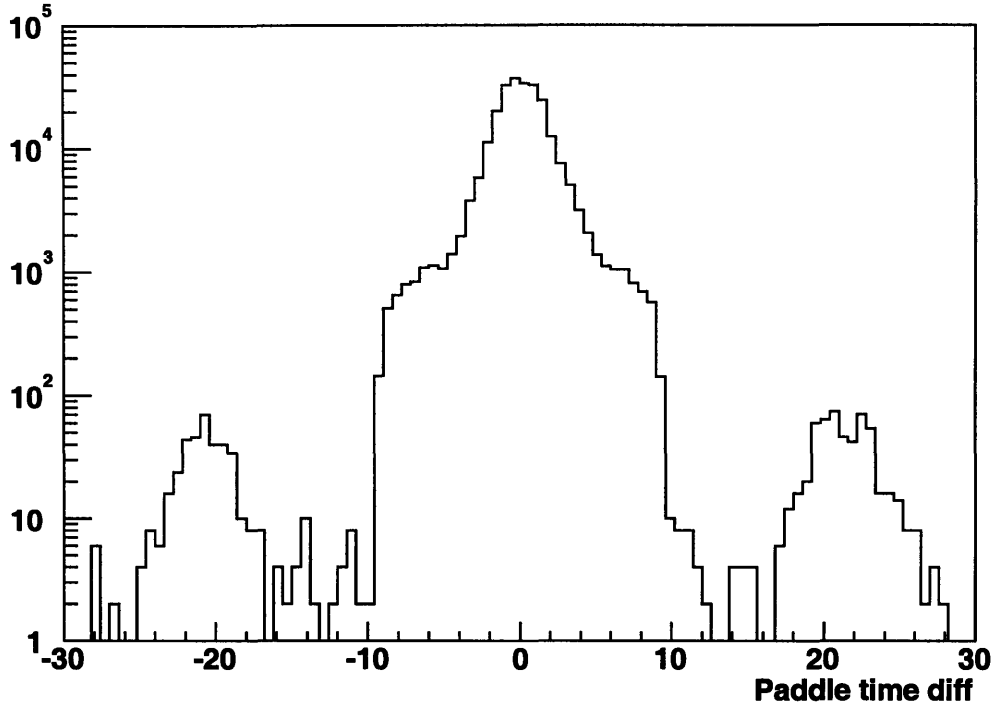

Figure 3-2: A plot showing the difference in paddle timing signals for data in Au+Au collisions. The central peak corresponds to collisions that occur in the interaction region.

PHOBOS, it will be between the positive and negative paddles. These make up the central peak shown in Figure 3-2. There are two other peaks that sit at about ± 21 ns. These are background signals mostly caused by interactions of the beam with gas in the beam pipe. Since these can occur anywhere, the outside peaks are caused by particles hitting one set of paddles and then the other set, with a time difference of about 21 ns, which is the time it takes a particle moving at $\sim$ speed of light to travel the distance that separates the two sets of paddles.

By applying a cut of $|\Delta t_{paddle}| < 4$ ns we can remove most of the background events. However, in some cases background events can survive this cut. This can occur when there are two beam gas events that together provide the necessary timing signal in the paddle counters, for example. A further timing cut is placed on the ZDC signals to account for these events. Figure 3-3 shows the time difference in the negative ZDC versus the positive ZDC. The triangle is the region that is accepted by

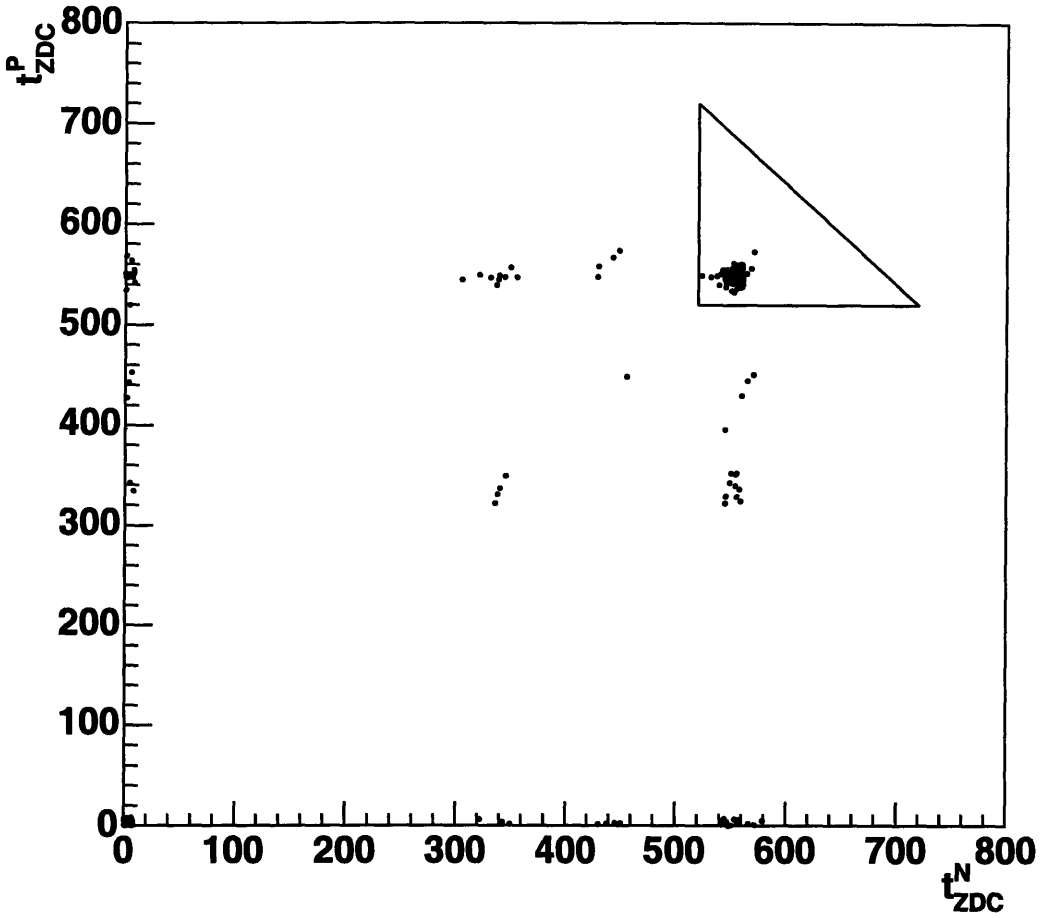

Figure 3-3: The negative ZDC timing signal versus the positive ZDC timing signal. These are used to make further event cuts. The enclosed triangle region are the events that pass the cuts.

the event cuts: $t^N_{ZDC} > 520$ ns, $t^P_{ZDC} > 520$ ns, and $t^N_{ZDC} + t^P_{ZDC} < 1240$ ns.

Applying these ZDC cuts to all events can remove a case of interesting collision events. For very central events there are no spectator neutrons, and therefore there will be no signal in the ZDC's. For this reason if the energy deposited in both paddle counters is high the event will be accepted regardless of the ZDC signal. The truncated mean of each paddle signal must be greater than 1500 for this criteria to be met. The event cuts are summarized in table 3.1.

Δt_{paddle}	$\lvert t_N - t_P \rvert < 4ns$
t^P_{ZDC}	$t^P_{ZDC} > 520ns$
t^N_{ZDC}	$t^N_{ZDC} > 520ns$
t^{sum}_{ZDC}	$t^P_{ZDC} + t^N_{ZDC} < 1240ns$
IsCollision	(Δt_{paddle} AND t^P_{ZDC} AND t^N_{ZDC} AND t^{sum}_{ZDC}) Paddle Signal > 1500

Table 3.1: The event cuts for Au+Au events, which involve paddle timing and energy deposition and ZDC timing cuts.

3.2.2 d+Au Event Selection

The event selection for the d+Au data has some of the same features as the Au+Au, but there are four differently triggered data sets used in the analysis presented here: MinBias, dAVertex, Peripheral, and SpecToF.

MinBias Event Selection

The MinBias portion of the data set accounts for 29 million triggered events. The event trigger is similar to that used in the Au+Au data for the paddles. In the d+Au MinBias, both paddles must fire, and the time difference Δt of the paddles firing follows the same acceptance as the Au+Au.

Once the data is collected, there are further event selection cuts that must be made. For the MinBias data set the following cuts are made: First, a cut on AllT0Diagonal is applied. This is essentially to further ensure that only events in the central region are used. The AllT0Diagonal cut is a timing cut placed on the timing difference seen in the signals received from hit T0 counters. This timing difference gives a position of the event vertex in the same way the timing difference in the paddles does. The main advantage is that the T0's have a better resolution. Due to debunched beam in the accelerator there were many events that were outside of the usable region for the spectra analysis. Next, a cut on OctDeT0 is made which checks that the T0Vertex and OctDeVtx agree to within 25 cm. Finally, pileup events are rejected, which means that there are no other events in the paddles before or after a collision is read out.

dAVertex Event Selection

The dAVertex trigger uses the T0 timing window rather than the paddles. The resolution is higher in the T0's, so they can provide a more accurate online vertex determination.

After the triggering, the event selection for the dAVertex data is the same as for the MinBias data. There is also the requirement that both paddles fire, which is already satisfied in the MinBias data because of the trigger requirements.

Peripheral Event Selection

The Peripheral data set is a special subset of the dAVertex data. The trigger and event selection are identical except for one condition: the number of paddles hit cannot exceed eight. Because of the low efficiency for triggering on low centrality events, this data set greatly increased the number of peripheral events.

SpecToF Event Selection

As discussed in Sections 2.5 and 2.7, the Spectrometer Trigger and Time of Flight walls can combine to enhance the number of high p_T tracks collected in d+Au and p+p collisions. The SpecTrig walls and the ToF walls are both connected to the XLM (Xilinx Logic Module). The XLM receives information about which channels in these detectors have been hit. Using a previously loaded tracking program, it performs a rudimentary tracking procedure using the fired channels in the detectors. It then determines if a straight line fit between the fired channels of the two detectors points back to the usable vertex region, $v_z < \pm 10$. If it does, the event is accepted. Since high p_T tracks will travel in an approximate straight line through the magnetic field, this provides an online trigger for accepting events with a high p_T track.

After the triggering, the offline event selection is identical to the dAVertex event selection.

3.2.3 Au+Au Centrality Determination

The centrality of a collision is a measure of how head-on the ions collide, as shown in Figure 1-11. The impact parameter, as shown, is the distance between the centers of the two nuclei. Another way of quantifying the centrality is by the number of participants, N_{part}, which is the number of nucleons that interact with other nucleons in the collision.

Since the actual impact parameter and N_{part} cannot be measured directly we must use a Monte Carlo simulation to determine these quantities. For Au+Au data the paddle counters that were used for the trigger and event selection are also used for centrality determination. Figure 3-4 shows the energy spectrum of both sets of paddle counters. In particular, the truncated mean of the energy signal in the paddles is used, which is the average of the 12 lowest paddle signals from each set of the paddle counters. The truncated mean is used to counter the long tails in the Landau distribution from background hits with high incident angles. Figure 3-5 shows the correlation between the truncated mean paddle signal in MC (Hijing) events and the N_{part} value calculated from a Glauber [46] model. The monotonic relation between these variables make the paddle counters suitable for calculating the centrality.

Before these paddle signals can be used to determine centrality, the efficiency of the detector must be understood. The signal from the paddles in data is compared to the signal from Monte Carlo runs. Figure 3-6 shows the number of paddles hit for both data and Monte Carlo. The number of events triggered with low centrality, particularly under 10 paddles hit, is much less in the data than the MC. This is assumed to be from acceptance and inefficiency effects in the detector. There is a central plateau region where the two distributions agree with each other, where the number of paddles hit varies between about 16 and 23 (the distributions have been normalized by their integral between these two points).

Since the paddle signal will be divided up into different percentages of the total cross section, and the data shows that the lower end of this paddle signal is missing, this must be taken into account when determining the centrality bins. The comparison

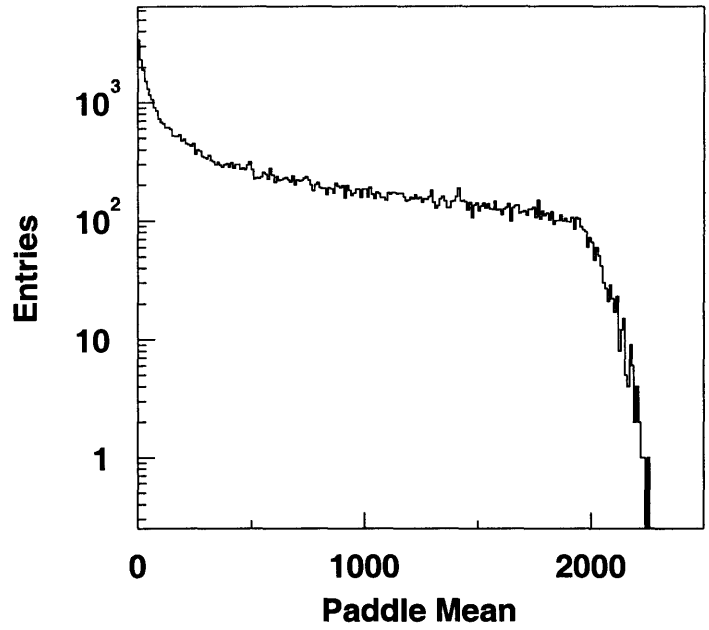

Figure 3-4: Average energy deposited in the paddle detectors. This average is calculated from the 12 lowest signals from each paddle.

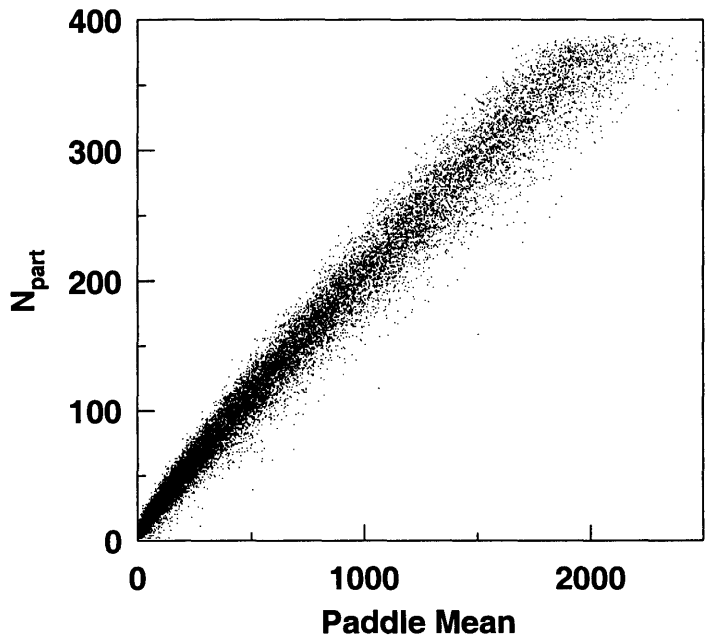

Figure 3-5: Truncated mean paddle signal in Monte Carlo versus N_{part} calculated from the Glauber model.

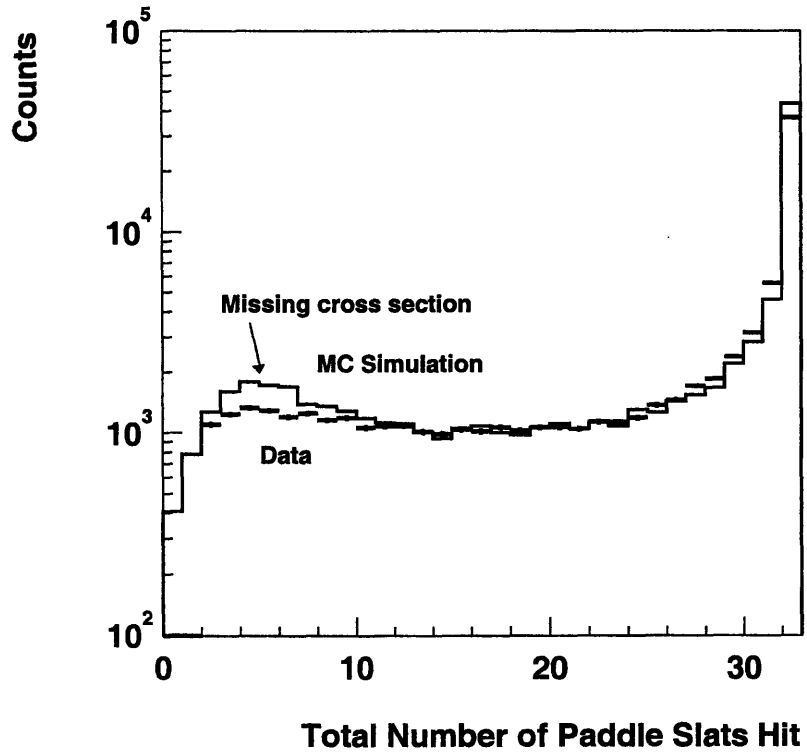

Figure 3-6: Comparison of the number of paddles hit for data and MC. In the central region, between about 16 and 23 paddles hit, there is good agreement. When the number of paddles hit is low (low centrality) the data falls well short of MC. This is assumed to be due to low efficiencies in the detectors at these low centralities.

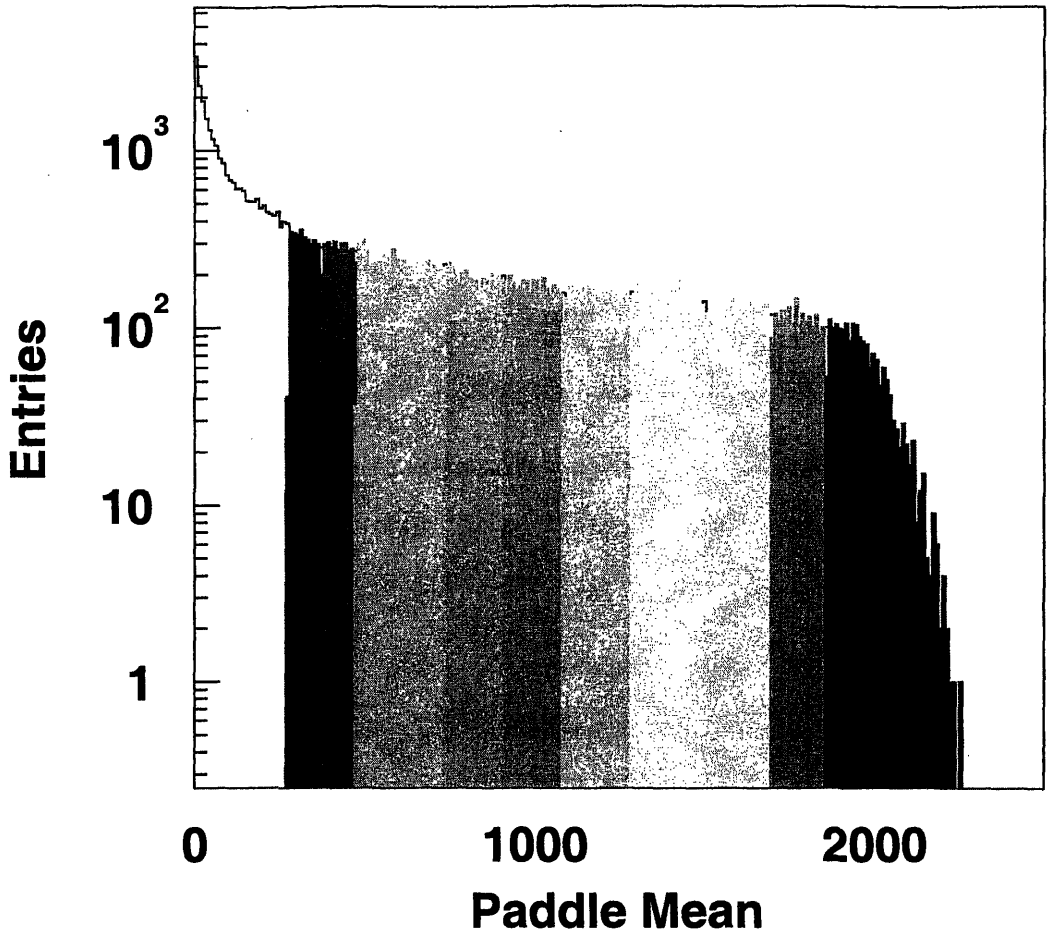

Figure 3-7: Paddle signal divided up into percentages of the total cross section. Although 17 bins in total were calculated, this plot shows only the top 11, which were used in the data analysis.

between data and MC is made between these two distributions, and the efficiency is calculated to be $88\% \pm 3\%$.

Once this inefficiency is accounted for the distribution is cut up into 17 different centrality bins, as shown in Figure 3-7. For example, the most central bin consists of 3% of the total (efficiency corrected) events in the paddle signal distribution. Table 3.2 shows the Glauber calculated values for N_{part} and N_{coll}.

A correlation can be seen between the paddle signal and the energy deposited in the ZDC's. Since the ZDC's measure the energy of the spectator neutrons, we see a

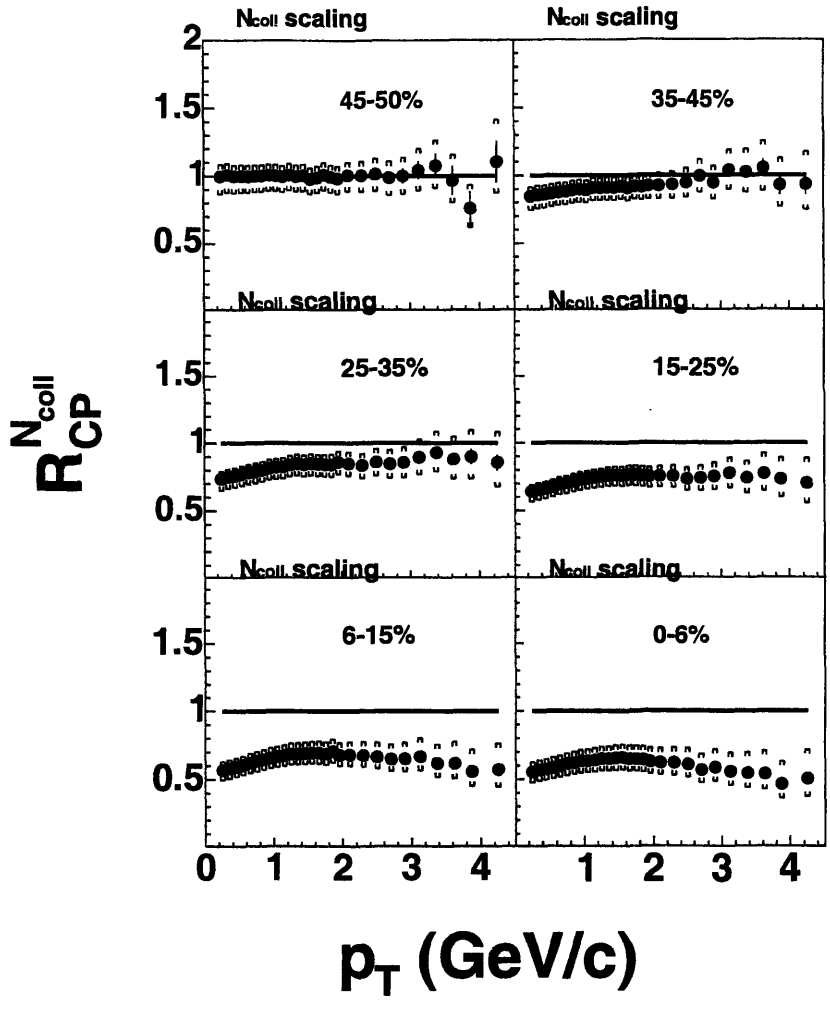

Figure 6-13: $R_{CP}^{N_{coll}}$ as a function of p_T for the six centrality bins. Each centrality bin has been weighted by its N_{coll} value and divided by a fit to the most peripheral bin. The top left panel, which is the most peripheral bin, has been divided by a fit to itself, which shows the quality of the fit.

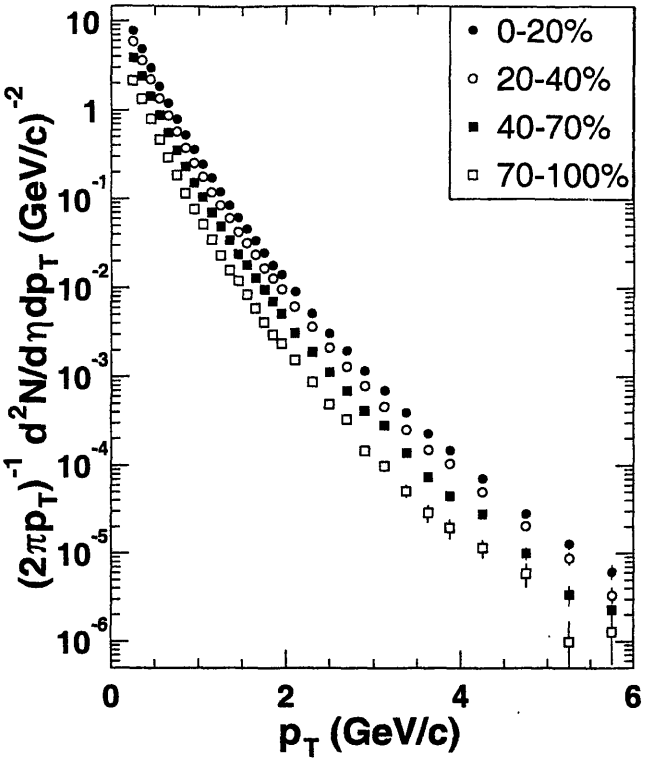

Figure 6-14: d+Au $\frac{1}{2\pi p_T}\frac{d^2N}{dp_T d\eta}$ distributions for the four centrality bins.

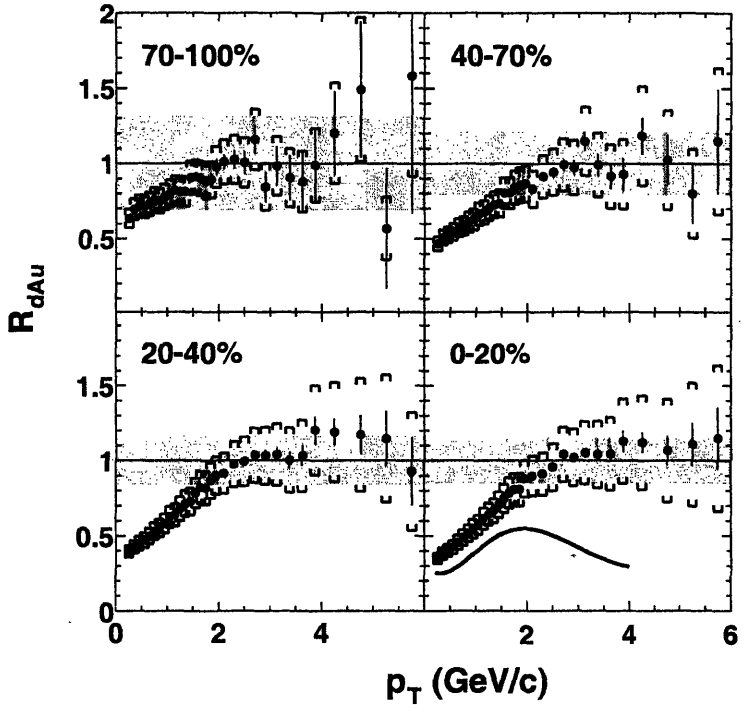

Figure 6-15: Nuclear modification factor R_{dAu} for the four centrality bins. The gray bands show the overall scale error.

% Cross Section	Bin Number	N_{part}
0-3	17	358 ± 5
3-6	16	331 ± 2
6-10	15	298 ± 3
10-15	14	256 ± 3
15-20	13	217 ± 4
20-25	12	183 ± 5
25-30	11	152 ± 5
30-35	10	124 ± 5
35-40	9	103 ± 5
40-45	8	83 ± 5
45-50	7	65 ± 4

Table 3.2: Percentage cross section, bin number, and N_{part} values for the centrality bins used in this analysis.

lower signal from the more central events, since there are fewer spectator neutrons. Figure 3-8 shows the paddle signal versus the ZDC signal. The ZDC signal decreases monotonically with the paddle signal, except at very peripheral collisions. This is due to the spectator neutrons still being within the nucleus, and the whole nucleus gets swept out by the DX magnets.

3.2.4 d+Au Centrality Determination

In d+Au collisions the paddles are not the best detector to determine the centrality. Studies have shown that the Monte Carlo and data spectrum of hit paddles do not match well, and there is no apparent monotonic relationship between the paddle signal and N_{part} as was seen in Au+Au collisions. Furthermore, since there are only 16 paddles dividing these up into centrality bins is courser with the low multiplicity environment seen in d+Au collisions.

A much more useful correlation is seen in the total energy deposited in all six silicon ring counters. Figure 3-9 shows the total energy in the rings versus N_{part}. Although the distribution is wider, there is a smooth monotonic rise. Since the rings are out of the acceptance region used in this analysis, there is no auto-correlation between the centrality determination and the data used itself.

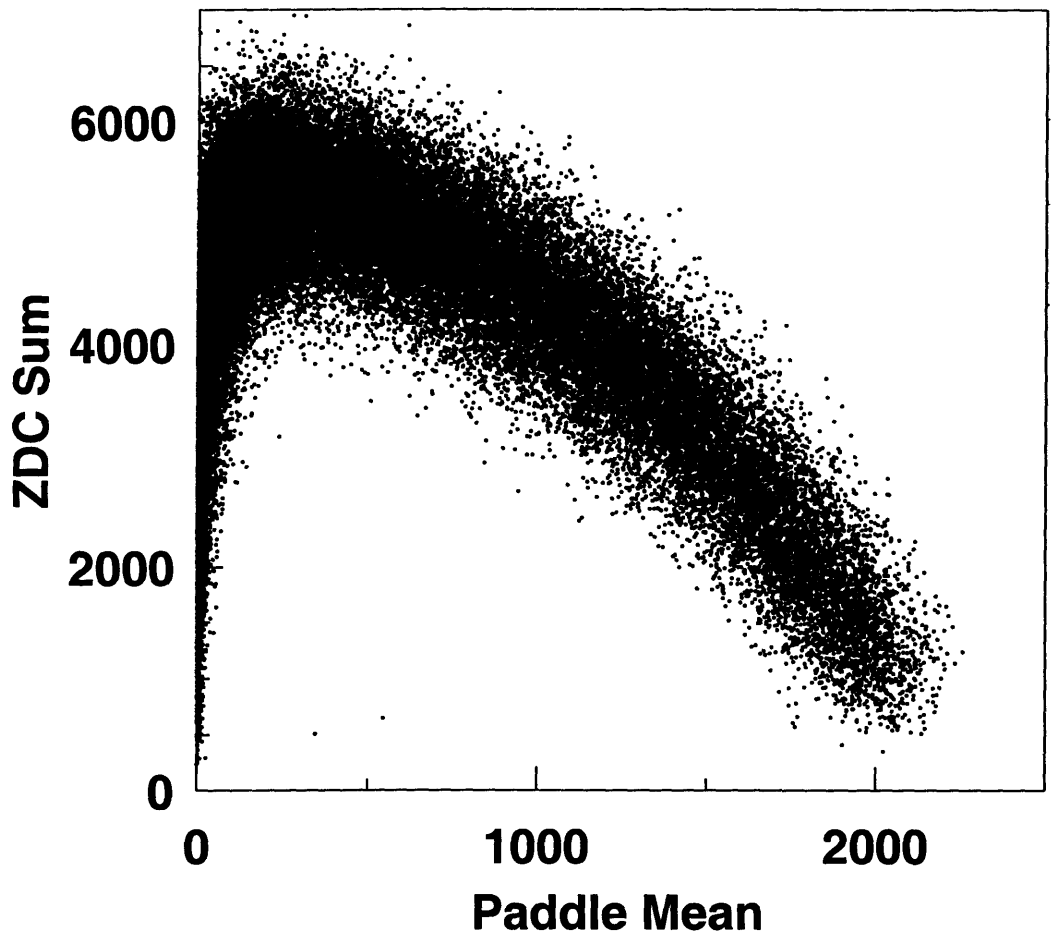

Figure 3-8: Paddle signal vs the signal from the ZDC's.

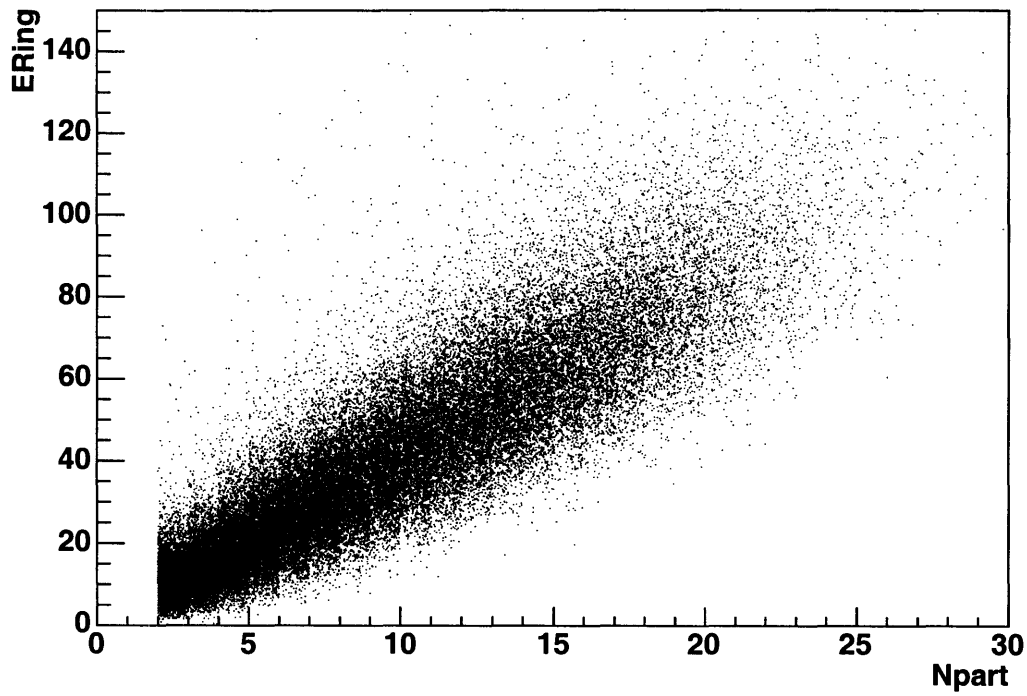

Figure 3-9: Energy deposited in the six silicon ring counters for MC events versus N_{part} calculated with the Glauber model. The vertical structure seen is a histogramming effect with the quantized N_{part} values.

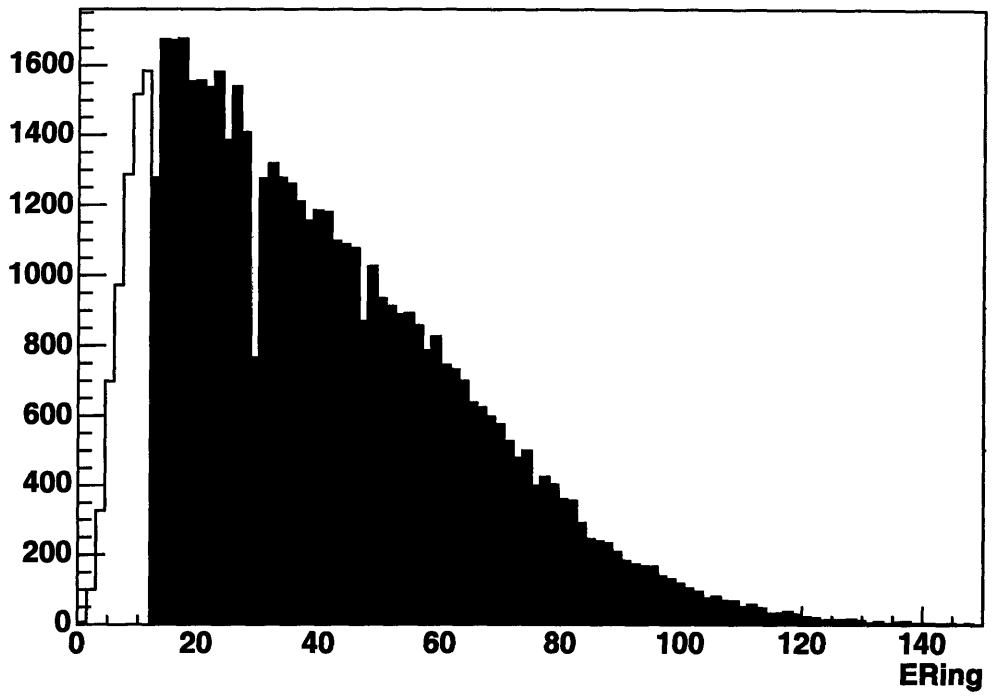

Figure 3-10: Energy spectrum for the ring counters, divided into the four centrality bins. This is for monte carlo events that go through the same event selection procedure as the data.

The same basic method used for Au+Au is also used for d+Au. The MC that goes through the event triggering does not actually match the data. To get the two distributions to match a correction factor of $0.005 * E^2_{Ring}$ is added to the MC spectrum. This does not affect the centrality determination.

The true MC, with no bias or triggering, is divided into four centrality bins, corresponding to $0-20\%$, $20-40\%$, $40-70\%$, and $70-100\%$ of the total cross section. Next, this true distribution is compared to the event triggered MC distribution to determine the overall efficiency and the efficiency of each centrality bin. With these efficiencies, the cuts are extracted from the data itself. Table 3.3 shows the calculated N_{part} and N_{coll} values for these four centrality bins as well as the efficiencies of the event selection. Figure 3-10 shows the ERing energy spectrum with the four centrality bin divisions.

% Cross Section	Bin Number	N_{part}	N_{coll}	Efficiency
0-20	3	15.5 ± 1.0	14.6 ± 0.9	82%
20-40	2	10.9 ± 0.9	9.7 ± 0.8	73%
40-70	1	6.7 ± 0.9	5.4 ± 0.8	49%
70-100	0	3.3 ± 0.7	2.2 ± 0.6	14%

Table 3.3: Percentage cross section, bin number, N_{part}, and N_{coll} values for the centrality bins used in this analysis and the efficiency of the event selection.

3.3 Vertexing

There are several different methods for determining the event vertex using different parts of the PHOBOS detector. Since these detectors were designed for different acceptances and different purposes, their efficiencies and effective ranges vary. For the Au+Au data a combination of these different methods is used, and the results from the different detectors are averaged depending on the position of the vertex. For the d+Au data only one method of vertexing is used.

3.3.1 ZVertex

The ZVertex is found by using the vertex detector. Due to the pixel size of the silicon detectors, as described in Section 2.3, the vertex detector has a high resolution in the Z direction, but less so in the X and Y direction.

The first step in the algorithm is to find clusters of hits in the four silicon planes of the vertex detector. These clusters are adjacent pixels that have registered hits. Once the number of pixels in the cluster is known a range in the Z position of the vertex can be estimated (this range is large). This is done for all clusters, and the probability of the vertex location is histogrammed. This same procedure is carried out for the Y direction also.

Once the clusters are found in each layer of silicon one cluster from the inner layer is connected by a straight line to each cluster in the outer layer. Where this line crosses the beam axis, assuming $Y = 0$, is the predicted vertex for these two clusters. This is carried out for all cluster combinations, for the top, bottom, and top

+ bottom sections of the vertex detector. These Z positions are histogrammed, and the actual vertex will have a peak above the background noise of random unassociated combinations of clusters.

3.3.2 OctagonVertex

The OctagonVertex uses clusters similar to the ZVertex algorithm, although no rudimentary tracking can be used since the octagon consists of a single layer of silicon. Clusters of hit pads are identified, and the Z range of possible vertex positions is determined by combining the number of pads hit with the Z position of the cluster. This range of possible Z vertex positions is quite large, and the probability distribution is triangular in shape, with the middle of the distribution being the most likely position. These probability distributions are then summed over all clusters into the probability histogram. The probability histogram is then used to find the vertex. A region is identified where the probability is greater than a set value between 60 and 95%, and the vertex can be set three different ways: 1) the maximum in the region, 2) mean Z weighted by the height of the histogram in the range, or 3) the middle of the range.

3.3.3 OctMainVertex

OctMainVertex is another algorithm for finding the vertex using the octagon. This only supplies information for the Z-position. All hits in the octagon are looped over, and those that have an energy deposition between 0.5 and 2 MiPs have their Z-positions histogrammed. The cuts in energy are used to reduce the effects of high-angle hits, noise, and background. Once the histogram is filled a gaussian function is fit to it, and the OctMainVertex Z-position is set to the mean value of the function. The resolution is low ($\sim$ 10 cm), but the range can extend from $|Z| < 60$ cm, which covers the whole range of the octagon.

3.3.4 SpecVertexSpecPN

In addition to the vertex detector and the octagon, the spectrometer can also be used for vertex determination. The first spectrometer vertex finder discussed is called SpecVertexSpecPN, and it uses tracklets to locate the vertex. A tracklet is a piece of a found track that uses only part of the spectrometer. In this algorithm the first six layers are used.

The algorithm starts by looking at straight line candidates in the first four layers of the spectrometer. Three hit combinations are made in these layers and a straight line is fit to them. If the χ^2 of the fit is greater than 10^{-8} then that tracklet is accepted for the next step. Once these tracklets are found the missing hit is attempted to be found. If a hit lies within a cone of 0.02 from the line fit, then it is added to the tracklet.

It is likely that ghost tracklets can arise from different tracklets sharing hits. For this reason the tracklet pairs are checked for shared hits, and the one with the lowest probability is discarded. The track is then extended from the fourth to the sixth layers, using the same stepping algorithm with the same cuts.

To find the Z-position of the vertex each tracklet's extrapolated minimum transverse distance to the Z-axis is histogrammed, and tracklets that are more than 3 cm away from the maximum of this histogram are rejected. Using the surviving tracklets, the Z-position of the vertex is found by minimizing the total calculated Z-positions of all tracklets. Using this method, all three coordinates of the vertex can be calculated.

3.3.5 SpecMainVertex

This algorithm uses the same idea as SpecVertexSpecPN of finding tracklets in the spectrometer, but the process is different. First, tracklet candidates are constructed using all possible two hit combinations in the first and fourth layers. Tracklets that are more than 2.5 cm from the beam orbit are rejected. Hits in the other layers, up to the sixth, are iterated over layer by layer. If a hit has a residual (distance along the plane of the sensor to the straight line fit) of less than 0.2 cm that hit is added

to the tracklet, and a new straight line is fitted after each added hit. Each tracklet must have at least three hits. The tracklets are then checked for shared hits, and, as in the SpecVertexSpecPN, the track with the higher probability is kept and the other is rejected.

Next, all surviving tracklets' vertex positions are compared by extrapolating back to the beam orbit. If the positions of the two vertices differ by less than 0.4 cm, then the three coordinates midway between the two vertices are separately histogrammed. The average of each of the three histograms are the coordinates of the vertex.

3.3.6 PaddleVertex

The timing difference between when the paddles fire is used in the event trigger, as the timing difference gives an approximate location of where the collision takes place. For this reason, it can obviously be used to determine the Z-position of the vertex, albeit with a rather poor resolution of about 15 cm. Because the resolution is so low, it is rarely used in data analysis. However, the efficiency is high, even at low centralities, and the Z range is large. Therefore, it can be used as a cross-check with other vertexing methods.

3.3.7 RMSSelVertex

The resolutions and ranges for the various algorithms varies. It is clear that all the algorithms have advantages and disadvantages. For example, ZVertex is very precise in determining the Z-coordinate, but not in the X-coordinate. Others lose efficiency at low centralities. The octagon vertices, while having a lower resolution, have a greater range in the Z direction than the ZVertex and the spectrometer vertices.

Due to these differences, a combination of the different vertices is usually used to construct a single vertex with the maximum accuracy for all three coordinates. This combination of vertices is called RMSSelVertex. A study was done using MonteCarlo runs to determine which vertex is the most accurate for the X, Y, and Z directions at different Z-ranges and centrality bins. In the MC data the vertex was

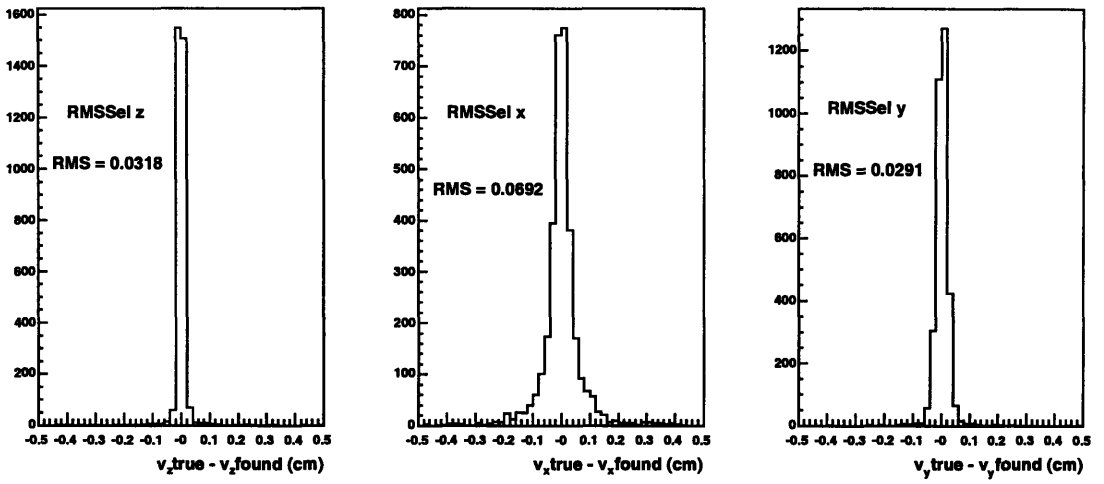

Figure 3-11: Vertex resolution for RMSSelVertex. These results are from MC and are averaged over centrality and vertex position.

reconstructed using each of the different algorithms for each coordinate in a range of vertices and centralities. These reconstructed vertices were then compared to the true MC vertex to determine which one is the most accurate for the given event class. This information is then stored in a file and when the data is processed, the event centrality and approximate Z-coordinate is input and the best vertex algorithm is then chosen for each vertex coordinate. These three numbers are then assigned to the new RMSSelVertex, which is then added to the event.

The octagon vertices have poor resolution compared to the others. Their advantage lies in their large range in Z. However, in this analysis only vertices between $-10 < v_z < 10$ are used, which is in the range of ZVertex and the spectrometer vertices. Therefore, only these three vertices will enter in the Au+Au analysis.

Figure 3-11 shows the distributions of true vertex positions minus found vertex positions for RMSSelVertex for the three coordinates. These are averaged over centrality and vertex position.

Figure 3-12 shows the resolution of the Z coordinate of the vertex position for the spectrometer vertices, and vertex vertex, and the octagon vertex. The low resolution of the octagon vertex is readily apparent.

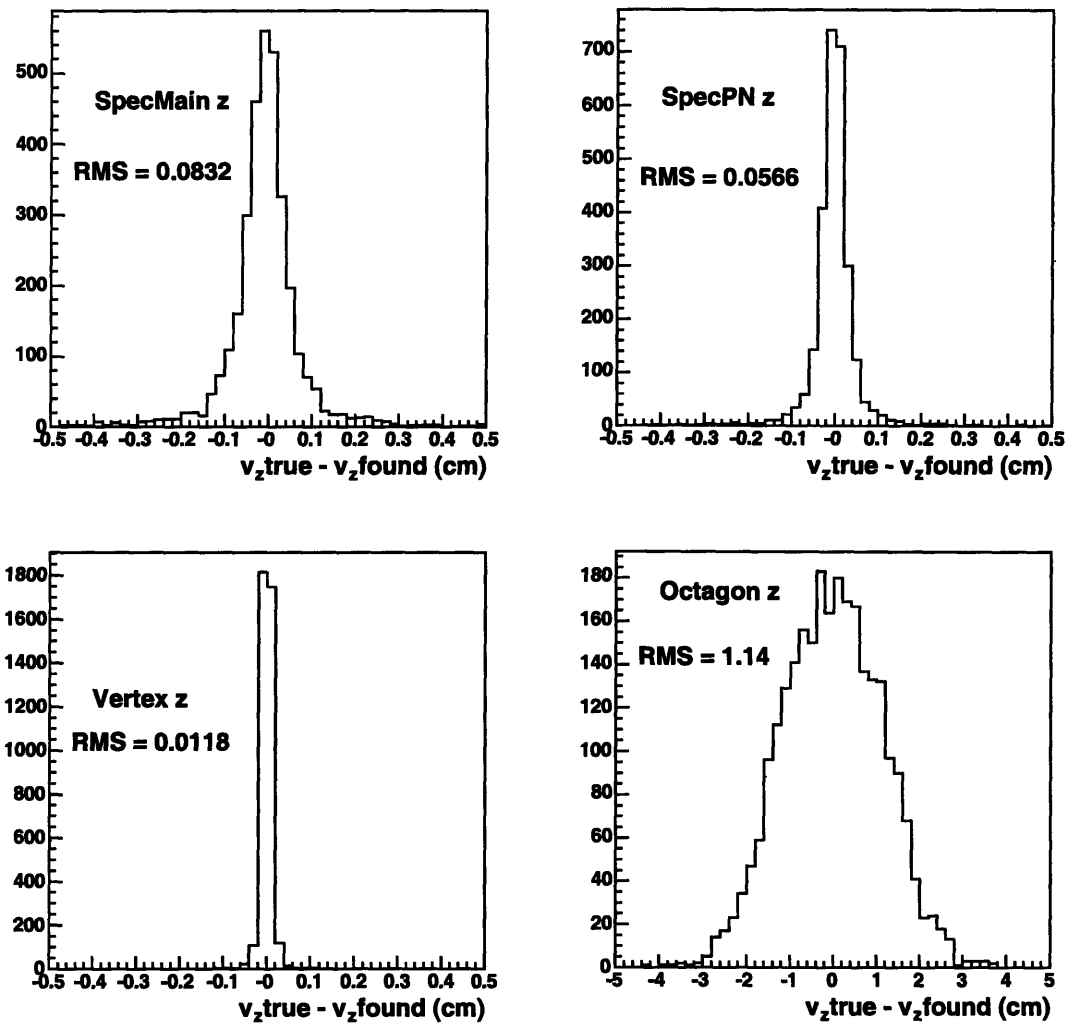

Figure 3-12: Resolutions for the spectrometer vertices, the vertex vertex, and the octagon vertex, all for the Z coordinate.

3.3.8 OctDeVertex

The efficiency of RMSSelVertex decreases drastically at low centralities. This is due to the low multiplicity environment seen in those events. In d+Au collisions, the N_{part} values correspond to these low centralities in Au+Au collisions. Therefore, the efficiency of RMSSelVertex for d+Au collisions is rather poor.

Since the vertex efficiencies and resolutions used for the Au+Au data are low, another vertexing algorithm, called OctDeVtx, was developed for the d+Au data. OctDeVtx is similar to the octagon vertices described above, except that it uses the energy deposition to determine the Z-position of the vertex. As the angle of a particle traversing a silicon pad increases, so does the energy it deposits in the detector. This angle can be translated into a Z-coordinate for the origin of the track. Hits are determined by a threshold energy deposited in a pad. However, as the angle changes so does the minimum energy needed to define a hit. The Z-position of the vertex is then found by maximizing the number of hits with this varying threshold.

The resolution of OctDeVtx is dependent on centrality, and ranges from 0.8 to 1.3 cm. Figures 3-13 show the resolution per centrality bin for Monte Carlo. Although this resolution is an improvement, it will still lead to corrections in the data. This is discussed in Section 5.6.

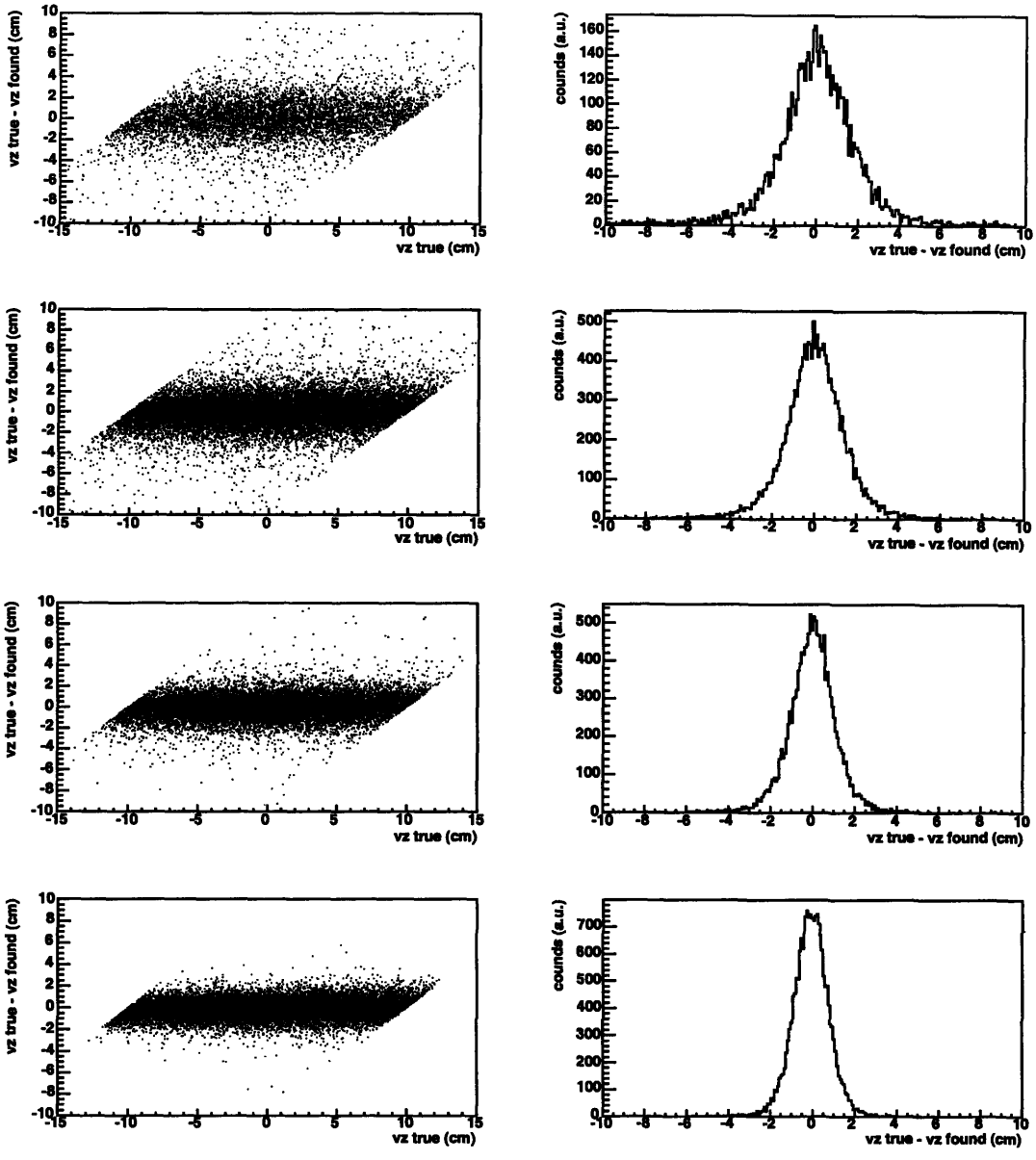

Figure 3-13: Resolutions for OctDeVtx by centrality bin for MC. The most most peripheral is the top row and the most central is the bottom row. The plots on the left show the true vertex versus the difference in the true and found vertex. The plots on the right show the difference in true and found vertices.

Chapter 4

Tracking

There are two main components to the tracking algorithm: the straight line tracking and the curved tracking. Since the magnetic field is small in the first six layers of the spectrometer we employ straight line tracking in this region. There are two slightly different tracking algorithms for the PR01 and PR03 data sets.

4.1 PR01 Au+Au Tracking

4.1.1 Straight Line Tracking

The first step in the tracking procedure is to identify straight line candidates in the first six layers of the spectrometer, which requires the z-coordinate of the event vertex. The straight line tracking module is designed to take the vertex name as one of the input parameters. For PR01 RMSSelVertex was used (see Chapter 3). The module then iterates overall hits in the first layer used, which is another input parameter, but is always set to Layer 0 in this analysis. For each hit in Layer 0, the module then iterates over all hits in the next layer and calculates the difference in the θ and ϕ angles between these hits. The θ angle is defined as the angle between the beam axis and a line from the vertex to the hit position. The ϕ angle is the azimuthal angle in spherical coordinates.

These two quantities, $\Delta\theta$ and $\Delta\phi$ are then compared to limits that are hard

Layer	0	1	2	3	4
Max $\Delta\theta$	0.012	0.010	0.008	0.007	0.004
Max $\Delta\phi$	0.025	0.025	0.025	0.045	0.065

Table 4.1: Maximum angle differences for hits in adjacent layers of the spectrometer to be considered as track candidates. Layer refers to the starting layer when comparing two hits from consecutive layers.

coded in the module. If $\Delta\theta$ and $\Delta\phi$ are less than these limits then a track candidate is constructed with these two hits and stored. Each layer has a defined $\Delta\theta$ and $\Delta\phi$ which was determined by calculating the residuals from straight line fits with known tracks. These values are shown in Table 4.1.

After the set of track candidates is assembled the procedure is carried out again, this time comparing the last hit of each track to each hit in the next layer. $\Delta\theta$ and $\Delta\phi$ are compared to the corresponding values in Table 4.1, and if the hit passes that hit is added to the list of hits for the track candidate. If more than one hit in the following layer is found to pass the angle cuts, a separate track is made for each of the hits. It is possible for the hits of a track to miss a layer, as this algorithm will check for a matching hit two layers ahead if it doesn't find one in the next layer.

After each new layer is complete a straight line is fit to existing tracks. The fit is carried out separately in the XZ and YZ planes. In the YZ plane the fit is only carried out in the first four layers. The momentum direction and the χ^2 straight line fit probability is stored in the track. If the track's probability is greater than 0.0005 the track is kept. Also, the track is discarded if there are fewer hits than the number of layers minus one. Finally, the tracks are compared to each other for shared hits. If tracks are found to share hits, then only the track with the greater probability is retained.

4.1.2 Curved Tracking

Reconstruction

The curved tracking algorithm is more complicated than the straight tracking. The layers used in the spectrometer for the curved tracking are layers 8 to 15. Layers 6 and 7 are not used due to their small overlapping region with each other and the other layers. Since the magnetic field is not uniform as was seen in Section 2.4, the trajectories of the tracks will not be simple circles. For this reason angular variables are extracted from track candidates and compared using a Hough transform to known tracks. These known tracks are MC generated tracks which are swum through the PHOBOS spectrometer within the usable z_{vtx} range. These tracks are then used to generate the Hough tables, which store information of hits of adjacent layers. The angle Θ, which is the polar angle from the event vertex to the hit and the angle the two hits make with Θ are stored for each track. With the known event vertex position, these two quantities for the hit positions uniquely define a track. For each of these pairs of hits, and for all the tracks these two angles are associated with the track's momentum p and its polar angle θ.

The procedure starts with the hits in the spectrometer. Every hit in the first layer of the curved tracking, layer 8, is compared to every hit in the following layer, layer 9. Then, two angles are extracted from these two hits. These angles are then used to obtain values of 1/p and θ that a track starting from the known event vertex would make. 1/p and θ come from the Hough tables, which are filled using the known simulated embedded tracks described above. The two hit combinations are called Hough sticks.

This procedure is repeated for each available layer pair in the spectrometer, with the first layer in each further iteration being the last layer in the previous iteration. Because some layers do not extend for the whole spectrometer (Figure 4-1), the layer pairs used are dependent on whether the track is in the central part of the spectrometer or the outer wing. Table 4.2 lists the layer pairs that are used in the tracking algorithm.

Spectrometer region	Layers used
Center	(8,9) (9,10) (10,12) (12,13) (13,14)
Outer wing	(8,9) (9,10) (10,12) (12,14) (14,15)

Table 4.2: Layer pairs used in the Hough stick finding algorithm for the different parts of the spectrometer. Due to the spectrometer design, not all layers are present in the two sections used.

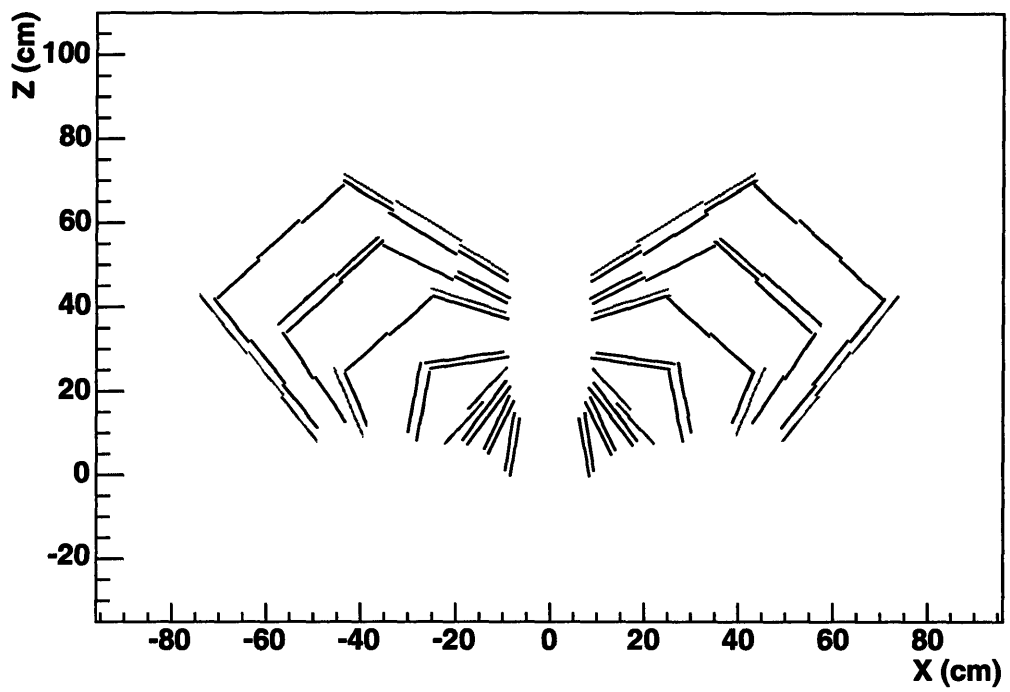

Figure 4-1: Spectrometer layers used for the different sections of the tracking. The layers drawn in black are used in both the central and outer wing algorithms, the red layers are not used in either, the blue layer is used just in the central region, and the green layer is used just in the outer wing section.

Each pair of Hough sticks in adjacent layer-pairs are compared for their momentum and angular values to see if they agree. If they do, the two Hough sticks are combined, and the next iteration is carried out. Once all of these Hough sticks are created they are assembled into Hough chains, which consist of five Hough sticks each (for each layer pair). Finally, the whole set of chains is checked and quality cuts are made on the χ^2, mean dE/dx, and the y-coordinates of the hits on the chain.

Joining Tracks

The next step in the process is to join the straight track segments to the curved track segments. The straight tracks are iterated over and each one is compared to each curved track by checking three quantities between them. First a straight line fit is done in the y direction between the hits of the two segments. Since there is a very small field in the XZ direction there should be little curvature. The χ^2 of this fit must be less than 5.0. Secondly there must be $\Delta\theta < 0.015$ between the straight segment and the curved segment. Lastly, the difference in the mean dE/dx of the two segments must be less than 0.8. If these criteria are met the two segments are joined into a single track. In the outer wing, the χ^2 and $\Delta\theta$ values must be less than 3 and 0.03 respectively, while the dE/dx cut remains unchanged.

Momentum Reconstruction

After the tracks have been joined the momentum and quality parameters must be determined. As seen before, the magnetic field is not uniform, and therefore the momentum cannot be determined using analytic fits to the trajectory. First, pions are simulated and swum through the magnetic field. To calculate the trajectory we integrate using a Runge-Kutta integration method. This must be done using step sizes. Ideally, the step sizes should be as small as possible, but this increases the computing time. The step sizes that are used are 10 cm in the central part of the spectrometer and 2.5+p cm in the wing section. The step size is half this size when the field gradient is high, 1 T/5cm. This trajectory is what we would expect if the detector effects of pixelization and multiple scattering were absent.

To include the detector effects we calculate the deviations of the hits of the track from the ideal trajectory. Pions are again simulated and are thrown through the detector, with the effects of pixelization and multiple scattering included. For each hit the track residual of this hit from the ideal trajectory is found by taking the three closest step points of the trajectory and fitting a circle to these points. The residual is the distance of the hit to the circle.

Now the covariance matrices are generated, which are used to calculate the χ^2 of the track. The deviations in the XZ and YZ planes (δxz and δyz) as calculated above are used. Covariance matrices $\mathbf{V_{qz}}$ are calculated for the XZ and YZ directions separately.

The χ^2 is given by

$$\chi^2 = \delta\mathbf{xz}^{\mathbf{t}}\mathbf{V}_{\mathbf{xz}}^{-\mathbf{1}} + \delta\mathbf{yz}^{\mathbf{t}}\mathbf{V}_{\mathbf{yz}}^{-\mathbf{1}} \tag{4.1}$$

Finally, to find the best track parameters, which are $(1/p, \theta_0, \phi_0, y_0, z_0)$ (y_0 and z_0 are the y and z coordinates at x = 0) a simplex minimization procedure of the χ^2 is used.

Track Selection

The final step in the tracking is to check tracks for shared hits. If two tracks share several hits, there is a high probability that only one real track exists, and the other is a ghost using part of the real track. All track pairs are compared, and if they are found to share more than two hits, the track with the higher probability is kept and the other track is discarded.

As an example, Figure 4-2 shows a Monte Carlo event after the tracking has been run.

4.1.3 d+Au Tracking

The algorithm used for the d+Au tracking is similar to that used for the Au+Au tracking described above. However, the biggest difference comes from the fact that

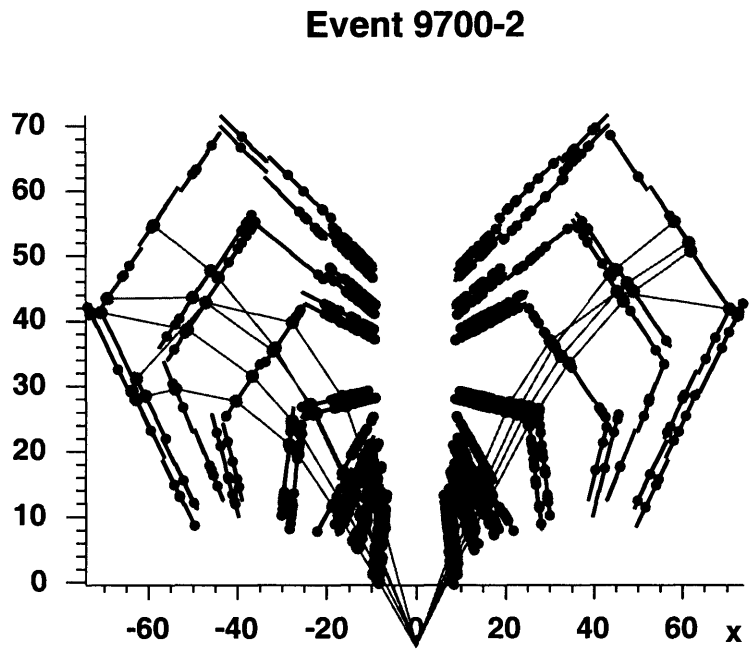

Figure 4-2: Monte Carlo Au+Au event with the tracking run on it. The hits are drawn on the spectrometer with the track hits connected to show the found tracks.

the vertexing in d+Au events is much less accurate than in Au+Au events (as seen in Section 3.3, the resolution of OctDeVtx varies from 0.8 to 1.3 cm, depending on the centrality) and both the straight tracking and curved tracking algorithms described for Au+Au rely on an event vertex. For this reason, both algorithms have been changed to circumvent this.

d+Au Straight Tracking

Instead of starting with the event vertex, the straight tracking just uses hits in the first six layers of the spectrometer. In fact, the algorithm for constructing straight track candidates is the same as that used for the SpecVertexSpecPN vertex finder (Section 3.3.4).

d+Au Curved Tracking

Since the curved tracking algorithm also depends on the location of the event vertex, this must be changed also. For the d+Au data set, each straight track is looped over. For each loop, the one straight track is treated as the only straight track in the event. It is then checked with each Hough chain found. The event vertex is taken as the extrapolation of the straight track back to the beam orbit. This procedure is repeated for each straight track. Once all candidates are assembled, track checking is performed in the same manner as the Au+Au tracking.

Figure 4-3 shows the results of the tracking run on a d+Au Monte Carlo event.

4.2 Track Cuts

There are two more cuts applied to the tracks that are not included in the tracking algorithm. These cuts are made in the track trees after the tracking has been run on the data. The distance of closest approach, or dca, must be less than 0.35 cm for the Au+Au data and 0.4 cm for the d+Au data. The *dca* is the distance the track extrapolates back to the event vertex. This cut is applied to reduce the number of secondary and feeddown tracks. The second track cut is the probability of the found

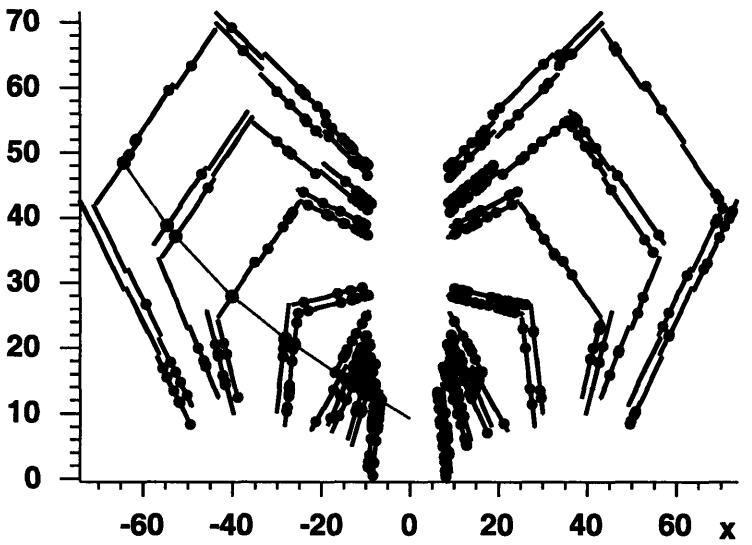

Figure 4-3: Monte Carlo d+Au event with the tracking run on it. The hits are drawn on the spectrometer with the track hits connected to show the found tracks.

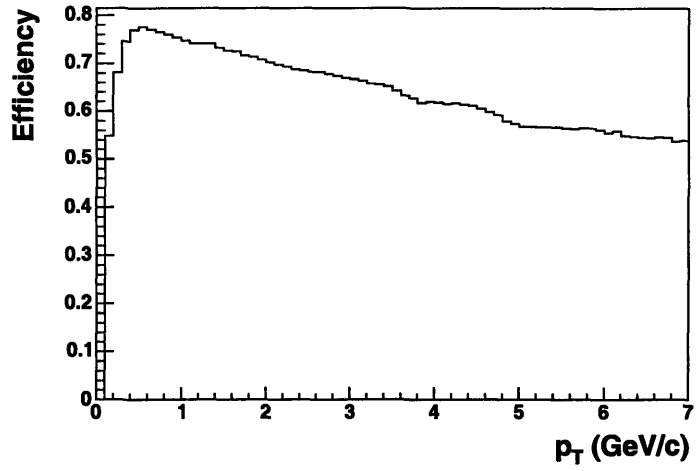

Figure 4-4: Tracking efficiency for single MC tracks. This efficiency has the track cuts $prob > 0.04$ and $dca < 0.35$ applied.

tracks must be greater than 0.04. These cuts will be discussed later in Section 6.2, and are used in both the data analysis and the corrections that are applied to the data.

4.3 Tracking Efficiency and Momentum Resolution

The tracking efficiency is found by embedding MC tracks with known parameters into empty events, running the tracking algorithm over the events, and comparing the output to the input tracks. For more details, see Section 5.1. Figure 4-4 shows the tracking efficiencies as a function of p_T. These tracks have the same cuts of dca > 0.35 (0.4 for d+Au tracking) and prob > 0.04 that are applied to the data. Figure 4-5 shows the momentum resolution as a function of p_T. The resolution is obviously finite, and must be corrected for, which will be discussed in Section 5.2. Finally, the geometrical acceptances of the tracking in the spectrometer and the SpecToF are shown in Figures 4-6 and 4-7 respectively.

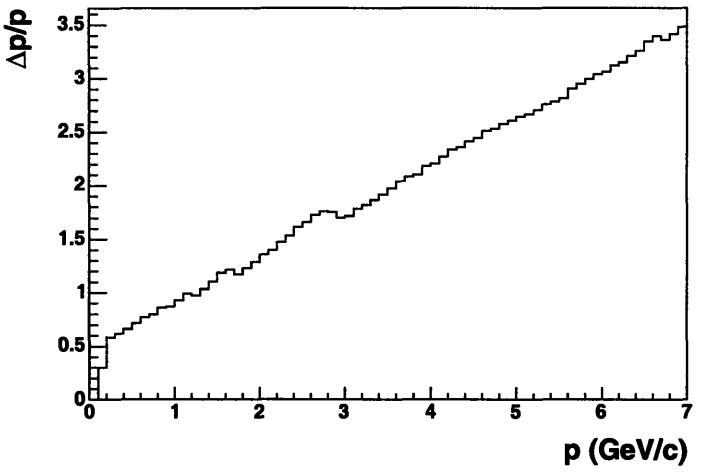

Figure 4-5: Tracking momentum resolution for the PR01 Au+Au tracking.

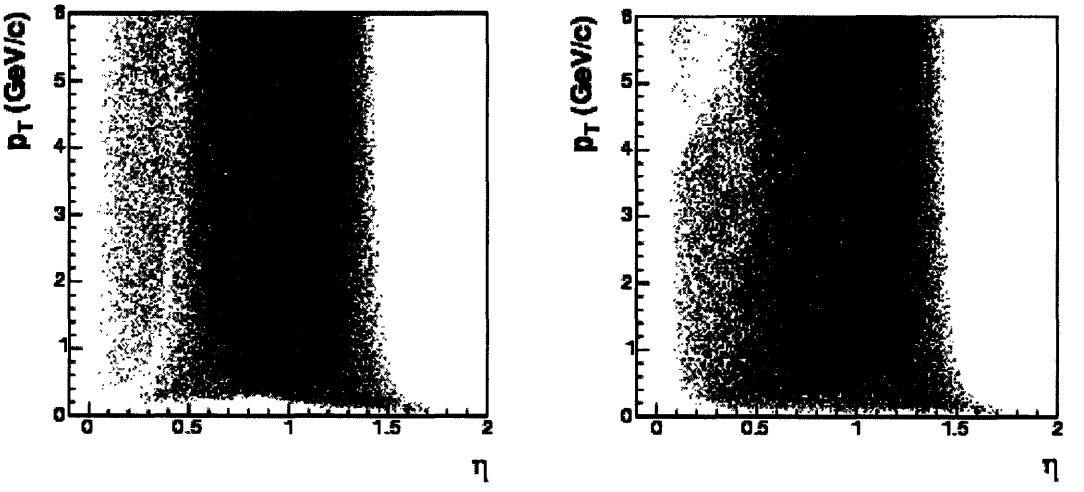

Figure 4-6: The acceptance of the tracking within the spectrometer as a function of p_T and η.

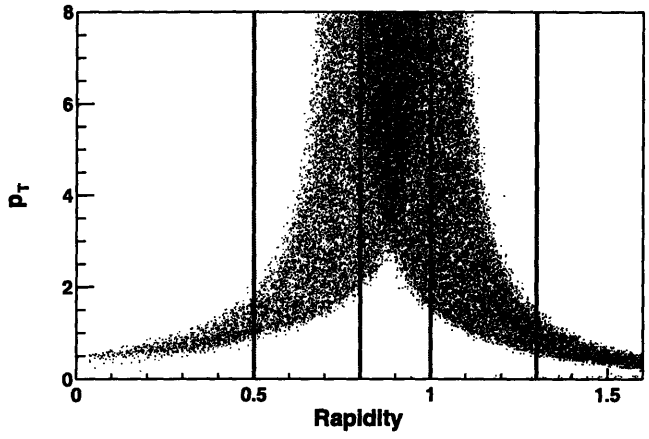

Figure 4-7: The acceptance of the tracking within the spectrometer and the ToF wall as a function of p_T and η.

Chapter 5

Corrections

To obtain the final charged hadron spectrum, corrections must be applied to the raw data. These corrections are the acceptance and efficiency correction, momentum resolution correction, secondary and feeddown correction, ghost correction, dead channel map correction, occupancy correction (for the Au+ Au data only), and for the d+Au data, the vertex flowing correction.

5.1 Acceptance and Efficiency Correction

The acceptance and efficiency correction is determined using a Monte Carlo simulation. The PHOBOS detector is simulated with GEANT, and simulated tracks are sent through the spectrometer. These simulated tracks were created with flat distributions in the following ranges: $0.1 < p_T < 8.0$, $0.0 < \eta < 1.5$, $-15 < v_z < 10$, and $-0.2 < \phi < 0.2$. These quantities were generated randomly for each track. The original, or true values, were written to ROOT trees. After the track is sent through the spectrometer, the hits are recorded, stored in a container, and then the tracking algorithm is run over the event. If a track is reconstructed, the reconstructed values are recorded in the same tree as the true values. It should be emphasized here that if a track is reconstructed, the true p_T is histogrammed for *both* found and reconstructed histograms. The reason for this is the p_T distribution of created tracks is flat, and thus is not a realistic distribution. Since the momentum resolution of the tracking is

finite, there will be some flowing between p_T bins. The effect this has depends on the relative number of entries between bins. Thus, if a momentum resolution correction is folded into this correction, the created tracks must have a realistic distribution. Since it is known that p_T spectra follow a general power law shape, in order to have reasonable statistics at high p_T it would require computing resources far beyond the scope of this experiment. Thus, the resolution correction is done separately, which will be discussed in Section 5.2.

To determine the correction functions, the p_T values of all created tracks are histogrammed. If a track was reconstructed, the p_T value of that track is put into another histogram. The found track must also pass the same track cuts as the data, namely $dca < 0.35$ and $prob > 0.04$. Furthermore, only tracks with $0.2 < \eta < 1.4$, for both true and found tracks are accepted. Once all of the events have been run over, the found track histogram is divided by the true track histogram. The resulting histogram is the combined acceptance and efficiency of the tracking and spectrometer as a function of p_T.

These corrections are done separately for the two bending directions, one that bends towards the beampipe and the other that bends into the outer wing. Furthermore, the correction functions are done separately for five different vertex bins for each bending direction. These vertex bins are in 5 cm increments of v_z: $-15 < v_z < -10$, $-10 < v_z < -5$, $-5 < v_z < 0$, $0 < v_z < 5$, and $5 < v_z < 10$. The corrections in the region $-15 < v_z < -10$ were found to be unstable and were excluded from these analyses. This reduces the η dependency of the acceptance and efficiency correction, since the variation of the vertex distribution can vary depending on the accelerator's performance.

The vertex binning is the same for the pseudorapidity dependence spectra of the d+Au data, but the acceptance for all three η bins does not cover the entire v_z region. For this reason, the v_z bins shown in Table 5.1 are used for the three different η bins.

After the 10 correction histograms are made, functions are fit to them. The histograms and the functional fits are shown in Figures 5-1 and 5-2, and the analytical functions are shown in Tables 5.2 and 5.3. The functions fit to the d+Au correction

η range	Vertex range (cm)
$0.2 < \eta < 0.6$	0 to 10
$0.6 < \eta < 1.0$	-10 to 5
$1.0 < \eta < 1.4$	-10 to 5

Table 5.1: Vertex ranges for the three different η bins.

Vertex Range	Function
$-15 < v_z < -10$	$0.13 * (1 - 1.23e^{-1.0p_T}) + (-0.47p_T + 0.12p_T^2 - 0.0098p_T^3)$
$-10 < v - z < -5$	$0.083 * (1 - 2.75e^{-3.83p_T}) + (0.048p_T - 0.0040p_T^2 - 0.000063p_T^3)$
$-5 < v_z < 0$	$0.13 * (1 - 2.64e^{-4.40p_T}) + (0.016p_T + 0.016p_T^2 + 0.0015p_T^3)$
$0 < v_z < 5$	$0.14 * (1 - 2.55e^{-4.50p_T}) + (-0.0.031p_T + 0.0051p_T^2 - 0.00071p_T^3)$
$5 < v_z < 10$	$0.085 * (1 - 4.65e^{-7.50p_T}) + (0.023p_T - 0.013p_T^2 - 0.00081p_T^3)$

Table 5.2: Acceptance/efficiency correction functions for the Au+Au tracking divided into 5 cm wide event vertex bins. These functions correspond to particles bending toward the beam pipe, or away from the outer wing. These have a much smaller acceptance at low p_T due to the fact that the low momentum particles will bend out of the accepted region of the spectrometer.

histograms are shown in Tables 5.4 and 5.5.

The η dependent spectra have different vertex ranges and η ranges, and therefore the acceptances will be different from the spectra that utilize the whole range in v_z. Because of this, separate acceptance/efficiency functions must be determined for each η bin. The η ranges used for the created and found tracks that go into the correction histograms are, instead of $0.2 < \eta < 1.4$ used for the Au+Au and other d+Au data, the same η ranges used in the analyzed spectra: $0.2 < \eta < 0.6$, $0.6 < \eta < 1.0$, and

$-15 < v_z < -10$	$0.05(1 - 1.54e^{-18.47p_T}) + (0.14p_T - 0.076p_T^2 + 0.0047p_T^3)$
$-10 < v_z < -5$	$0.87(1 + 5.08e^{-3.14p_T}) + (0.19p_T - 0.12p_T^2 + 0.040p_T^3 - 0.0065p_T^4 + 0.00040p_T^5)$
$-5 < v_z < 0$	$0.18(1 + 4.33e^{-3.04p_T})(1.35p_T - 0.95p_T^2 + 0.31p_T^3 - 0.046p_T^4 + 0.0027p_T^5)$
$0 < v_z < 5$	$0.29(1 + 2.64e^{-2.57p_T})(0.98p_T - 0.65p_T^2 + 0.20p_T^3 - 0.028p_T^4 + 0.0016p_T^5)$
$5 < v_z < 10$	$0.67(1 + 50.16e^{-1.15p_T})(0.016p_T - 0.015p_T^2 + 0.010p_T^3 - 0.0023p_T^4 + 0.00015p_T^5)$

Table 5.3: Acceptance/efficiency correction functions for the Au+Au tracking divided into 5 cm wide event vertex bins. These functions are for the particles that bend away from the beam pipe and into the outer wing. This gives a higher acceptance at low p_T.

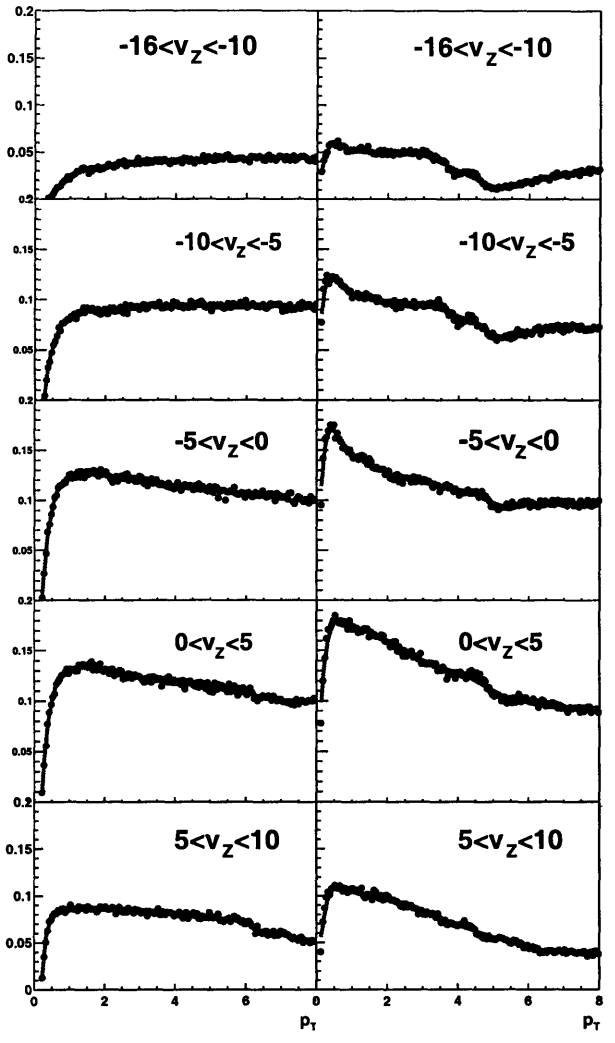

Figure 5-1: Acceptance and efficiency corrections for the Au+Au data. The left column is the correction functions for the charge/polarity combination of tracks bending toward the beam pipe, and the right hand side is the corrections for tracks that bend into the wing.

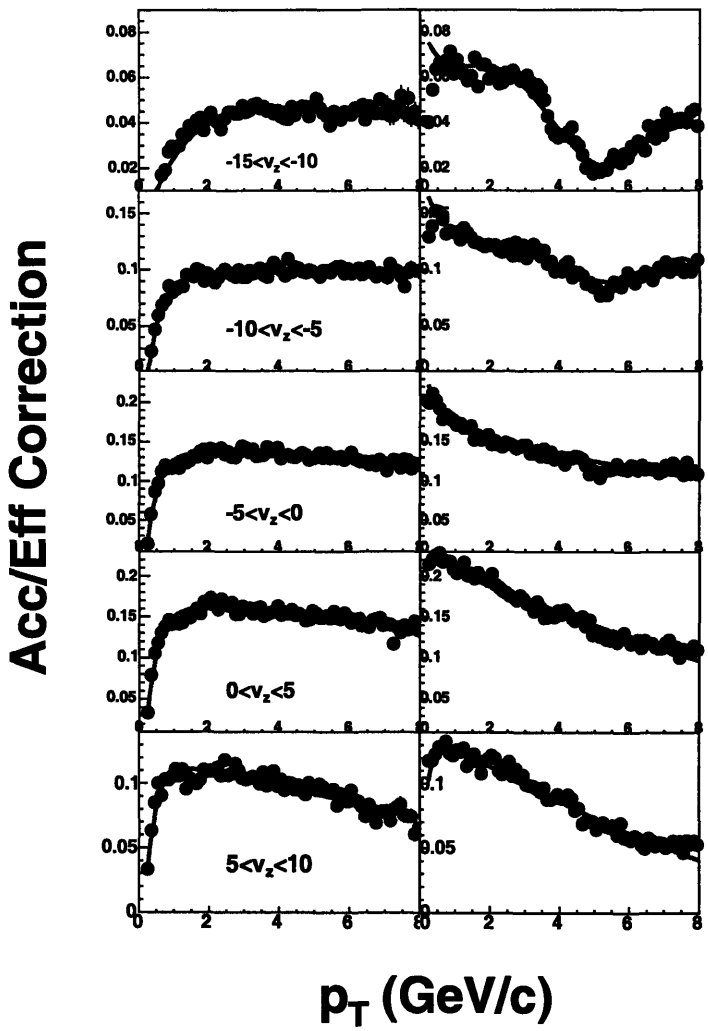

Figure 5-2: Acceptance and efficiency corrections for the d+Au data. The left column is the correction functions for the charge/polarity combination of tracks bending toward the beam pipe, and the right hand side is the corrections for tracks that bend into the wing.

Vertex Range	Function
$-15 < v_z < -10$	$0.055 * (1 - 1.25e^{-0.84p_T})(1 - 0.028p_T)$
$-10 < v - z < -5$	$0.095 * (1 - 2.03e^{-2.94p_T})(1 + 0.0058p_T)$
$-5 < v_z < 0$	$0.14 * (1 - 1.89e^{-3.16p_T})(1 - 0.013p_T)$
$0 < v_z < 5$	$0.17 * (1 - 1.67e^{-2.97p_T})(1 - 0.021p_T)$
$5 < v_z < 10$	$0.12 * (1 - 1.69e^{-3.39p_T})(1 - 0.048p_T)$

Table 5.4: Acceptance/efficiency correction histograms and functions for the d+Au tracking divided into 5 cm wide event vertex bins. These functions correspond to particles bending toward the beam pipe, or away from the outer wing. These have a much smaller acceptance at low p_T due to the fact that the low momentum particles will bend out of the accepted region of the spectrometer.

$-15 < v_z < -10$	$0.085 - 0.049p_T + 0.043p_T^2 - 0.016p_T^3 + 0.0024p_T^4 - 0.00012p_T^5$
$-10 < v_z < -5$	$0.19 - 0.10p_T + 0.065p_T^2 - 0.020p_T^3 + 0.0027p_T^4 - 0.00013p_T^5$
$-5 < v_z < 0$	$3.85(1 - 0.96e^{0.0011p_T})(1 - 0.027p_T) + 0.015/p_T$
$0 < v_z < 5$	$8.53(1 - 0.97e^{0.0012p_T})(1 - 0.044p_T) + 0.0027/p_T$
$5 < v_z < 10$	$7.65(1 - 0.98e^{0.0012p_T})(1 - 0.059p_T) + 0.011/p_T$

Table 5.5: Acceptance/efficiency correction histograms and functions for the d+Au tracking divided into 5 cm wide event vertex bins. These functions are for the particles that bend away from the beam pipe and into the outer wing. This gives a higher acceptance at low p_T.

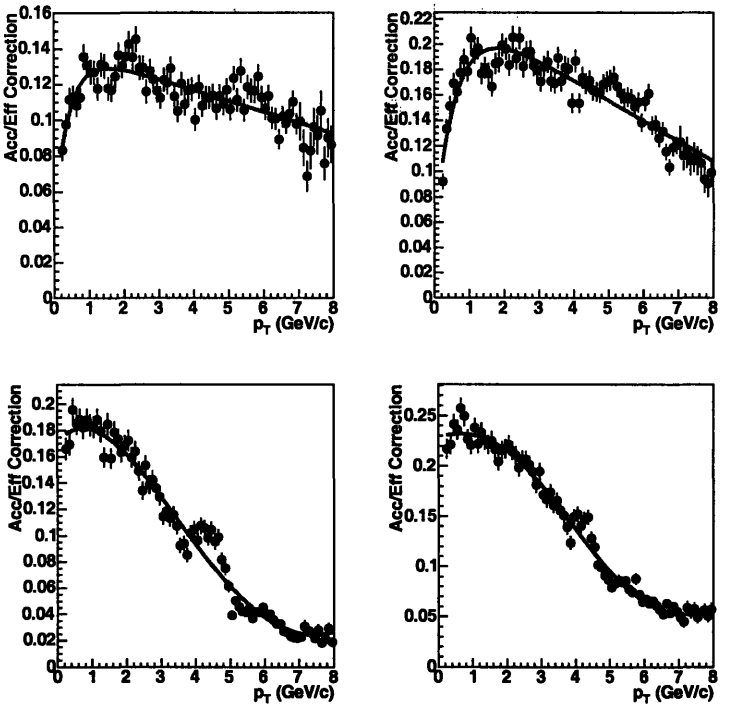

Figure 5-3: Acceptance/efficiency corrections for the η binned d+Au data. The η range for these corrections is $0.2 < \eta < 0.6$. The top row is for tracks bending toward the beam pipe and the bottom row is for tracks bending away from the beam pipe. The columns are for the vertex ranges, from left to right, $0 < v_z < 5$ and $5 < v_z < 10$.

$1.0 < \eta < 0.4$. These are shown in Figures 5-3, 5-4, and 5-5. The analytical forms of the functions used to fit these histograms are shown in Tables 5.6, 5.7, and 5.8.

As the data is being run over, the p_T and v_z values of the track are read from the tree, and the appropriate correction function is evaluated at the p_T value of the track. The value of the function at this point is then used to divide the histogram entry.

It should be noted that the overall scale of these corrections is dependent on the acceptance part of the correction. This in turn depends on the ϕ range the embedded tracks are generated in, since the η range of the spectra is fixed. Since the tracks are generated in a region $-0.2 < \phi < 0.2$ around each spectrometer arm, there is a further multiplicative correction of $2\pi/0.8$.

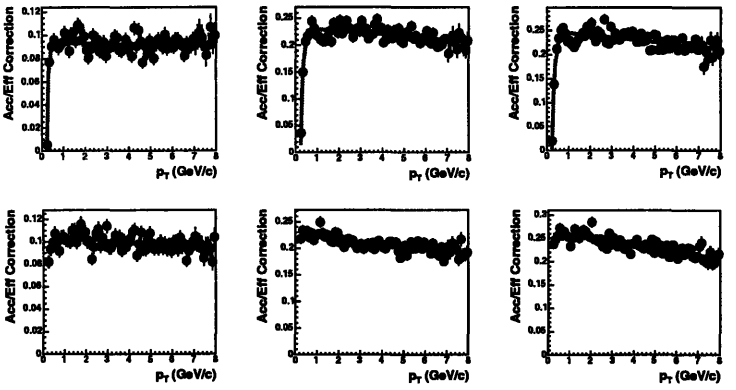

Figure 5-4: Acceptance/efficiency corrections for the η binned d+Au data. The η range for these corrections is $0.6 < \eta < 1.0$. The top row is for tracks bending toward the beam pipe, in the vertex ranges $0 < v_z < 5$ and $5 < v_z < 10$ respectively. The bottom row is for tracks bending away from the beam pipe.

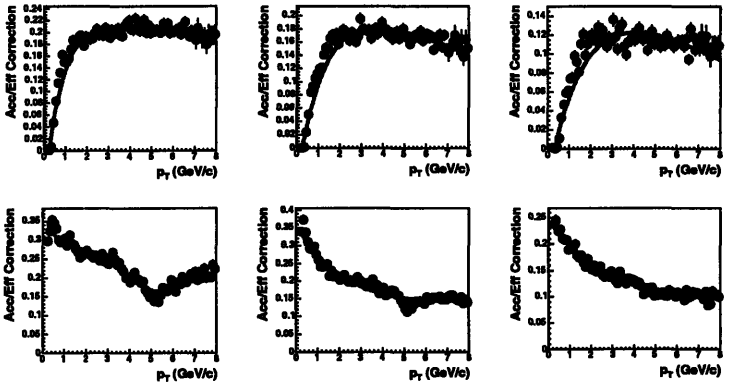

Figure 5-5: Acceptance/efficiency corrections for the η binned d+Au data. The η range for these corrections is $1.0 < \eta < 1.4$. The top row is for tracks bending toward the beam pipe and the bottom row is for tracks bending away from the beam pipe. The columns are for the vertex ranges, from left to right respectively, $-10 < v_z < -5$, $-5 < v_z < 0$, and $0 < v_z < 5$.

$0 < v_z < 5$	$0.14(1 - 0.68e^{-2.29p_T})(1 - 0.043p_T)$
$5 < v_z < 10$	$0.234(1 - 0.78e^{-1.57p_T})(1 - 0.067p_T)$
$0 < v_z < 5$	$0.17 + 0.029p_T - 0.023p_T^2 + 0.0036p_T^3 - 0.00023p_T^4 + 0.0000064p_T^5$
$5 < v_z < 10$	$0.23 + 0.0078p_T - 0.0030p_T^2 - 0.0035p_T^3 + 0.00075p_T^4 - 0.00004p_T^5$

Table 5.6: Acceptance/efficiency correction histograms and functions for the η binned data in the range $0.2 < \eta < 0.6$. The top two rows are for tracks bending toward the beam pipe and away from the spectrometer wing, and the bottom two rows are for tracks bending away from the beam pipe. The first column is the vertex range $0 < v_z < 5$ and the second column is $5 < v_z < 10$.

$-10 < v_z < -5$	$0.094(1 - 64.24e^{-16.89p_T})(1 - 0.0044p_T)$
$-5 < v_z < 0$	$0.23(1 - 8.53e^{-9.25p_T})(1 - 0.014p_T)$
$0 < v_z < 5$	$0.25(1 - 7.21e^{-8.23p_T}(1 - 0.0189p_T)$
$-10 < v_z < -5$	$0.081 + 0.041p_T - 0.025p_T^2 + 0.0067p_T^3 - 0.00081p_T^4 + 0.000037p_T^5$
$-5 < v_z < 0$	$0.21(1 + 0.14exp(-0.32p_T))(1 - 0.083p_T)$
$0 < v_z < 5$	$0.048(1 + 4.39exp(-0.031p_T))(1 - 0.045p_T)$

Table 5.7: Acceptance/efficiency correction histograms and functions for the η binned data in the range $0.6 < \eta < 1.0$. The top three rows are for tracks bending toward the beam pipe and away from the spectrometer wing and the bottom three rows are for tracks bending away from the beam pipe. The first column is the vertex range $-10 < v_z < -5$, the second column is $-5 < v_z < 0$, and the third column is $0 < v_z < 5$

$-10 < v_z < -5$	$0.22(1 - 1.40e^{-1.30p_T})(1 - 0.016p_T)$
$-5 < v_z < 0$	$0.25(1 - 1.22e^{-0.73p_T})(1 - 0.053p_T)$
$0 < v_z < 5$	$0.19(1 - 1.19e^{-0.53p_T})(1 - 0.063p_T)$
$-10 < v_z < -5$	$0.38 - 0.18p_T + 0.13p_T^2 - 0.044p_T^3 + 0.0062p_T^4 - 0.00031p_T^5$
$-5 < v_z < 0$	$0.083 * (1 + 3.28exp(-0.47p_T))(1 + 0.077p_T)$
$0 < v_z < 5$	$0.09(1 + 1.83exp(-0.43p_T))(1 + 0.0036p_T)$

Table 5.8: Acceptance/efficiency correction histograms and functions for the η binned data in the range $1.0 < \eta < 1.4$. The top four rows are for tracks bending toward the beam pipe and away from the spectrometer wing and the bottom three rows are for tracks bending away from the beam pipe. The first column is the vertex range $-10 < v_z < -5$, the second column is $-5 < v_z < 0$, and the third column is $0 < v_z < 5$

$-10 < v_z < -5$	$0.07(1 - 1.44e^{-0.20p_T})(1 - 0.047p_T)$
$-5 < v_z < 0$	$0.065(1 - 10e^{-1.8p_T})(1 - 0.01p_T)$
$0 < v_z < 5$	$0.060(1 - 7.87e^{-2.05p_T})(1 - 0.024p_T)$
$0 < v_z < 5$	$0.048(1 - 24.26e^{-3.71p_T})(1 - 0.099p_T + 0.0047p_T^2)$
$-10 < v_z < -5$	$0.094(1 - 33.98e^{-6.33p_T})(1 - 0.061p_T + 0.0021p_T^2)$
$-5 < v_z < 0$	$0.1(1 - 7.91e^{-3.59p_T})(1 - 0.1p_T + 0.0076p_T^2)$
$0 < v_z < 5$	$0.13(1 - 1.90e^{-1.07p_T})(1 - 0.13p_T + 0.0085p_T^2)$
$0 < v_z < 5$	0

Table 5.9: The fit functions for the plots in Figure 5-6. The top four rows are for tracks bending toward the beam pipe and the bottom four rows are for tracks bending away from the beam pipe.

5.1.1 SpecToF Correction

The SpecToF data relies on a particle being findable in the spectrometer, hitting the SpecTrig, and hitting the ToF. Therefore, the acceptance and efficiencies for this data set is different from the others and separate correction functions were generated. The basic method with which these were generated is the same as the other acceptance/efficiency corrections. MC tracks were generated with flat distributions in $0.0 < \eta < 1.6$, $0 < p_T < 8.0$, $-0.1 < \phi < 0.1$, and $-15 < v_z < 10$.

The resulting correction histograms with the corresponding fit functions are shown in Figure 5-6. The functional forms of the fits are shown in Table 5.9. The acceptance of the spectrometer and ToF together does not cover the same vertex range as the spectrometer alone. For this reason, the vertex range for the SpecToF triggered data is $-10 < v_z < 10$ for tracks bending toward the beam pipe and $-10 < v_z < 5$ for tracks bending toward the outer wing. The reason this range is different than the spectrometer tracks is the limited acceptance of the ToF.

5.2 Momentum Resolution and Bin Width Correction

As seen in Section 4.3, the momentum resolution of the tracking is finite, and therefore must be corrected for. Another correction that is folded in with the momentum

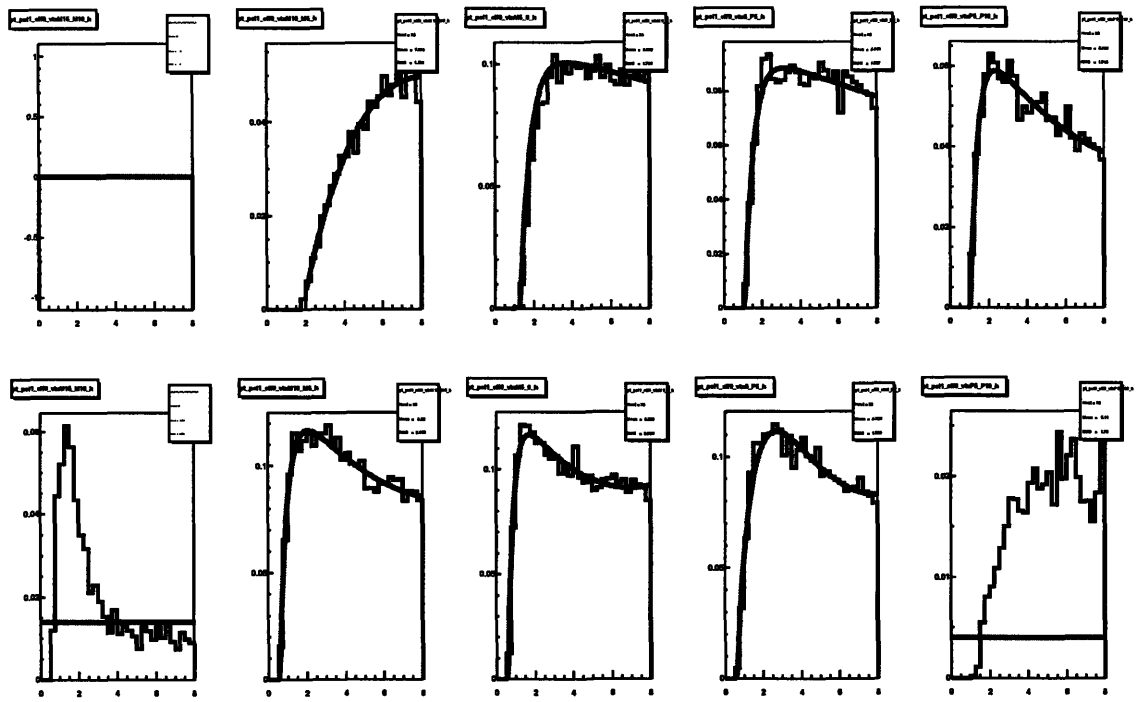

Figure 5-6: Acceptance and efficiency corrections for the SpecTrig d+Au data. The top four rows are for tracks bending toward the beam pipe and the bottom four rows are for tracks bending away from the beam pipe. The columns are the five vertex bins, starting with $-15 < v_z < -10$ and ending with $5 < v_z < 10$.

resolution correction is for the bin width size of the histograms in the spectra. When histogramming the p_T spectra, the points are placed in the center of the bin. After all the tracks are histogrammed and event weighted, the resulting value in a histogram bin is the average of the p_T values of all the tracks. Unless the spectrum is linear in p_T, the average value will not lie in the center of the bin. Since the spectra are generally exponential or power law in shape, the actual average value will be lower in p_T than the bin center. To correct for this, if the point is to remain in the bin center, than it must be lowered such that it lies on the actual physical spectrum. This correction is obviously dependent on the shape of the spectra, and therefore must be calculated separately for different centralities, species, and η acceptances.

To determine the momentum resolution at different p_T values the same reconstructed embedded MC tracks used for the acceptance and efficiency corrections are used. The reconstructed momentum is subtracted from the true embedded momentum at intervals of 500 MeV/c, and these histograms are fit with a gaussian function. These histograms are then normalized such that the integrals are unity and then summed. Figure 4-5 shows the momentum resolution as a function of p.

Next, functions are fit to the corrected $d^2N/dp_Td\eta$ spectra in the centrality, or pseudorapidity, bins, which are denoted $f_i(p_T)$. Each $f_i(p_T)$ is then multiplied by the summed momentum resolution fits. The correction function is then obtained by integrating this function and histogram product over p_T. To translate this to a correction for $1/p_Td^2N/dp_Td\eta$ distributions, the function is weighted by $1/p_T$. Finally, to include the bin width correction, the final correction, the final resolution and bin width correction is found by dividing the function obtained from the integration by the width of each p_T bin. What is applied is the ratio of this correction with the original value of the $1/p_Td^2N/dp_Td\eta$ distribution, which introduces a value for each bin which divides the original value.

This procedure gives correction points for each p_T bin. These points, for each centrality or pseudorapidity bin, are then fit to a smooth function, which the data is divided by as the final step in the correction process. Figure 5-7 and Table 5.10 show these functions and their analytic forms.

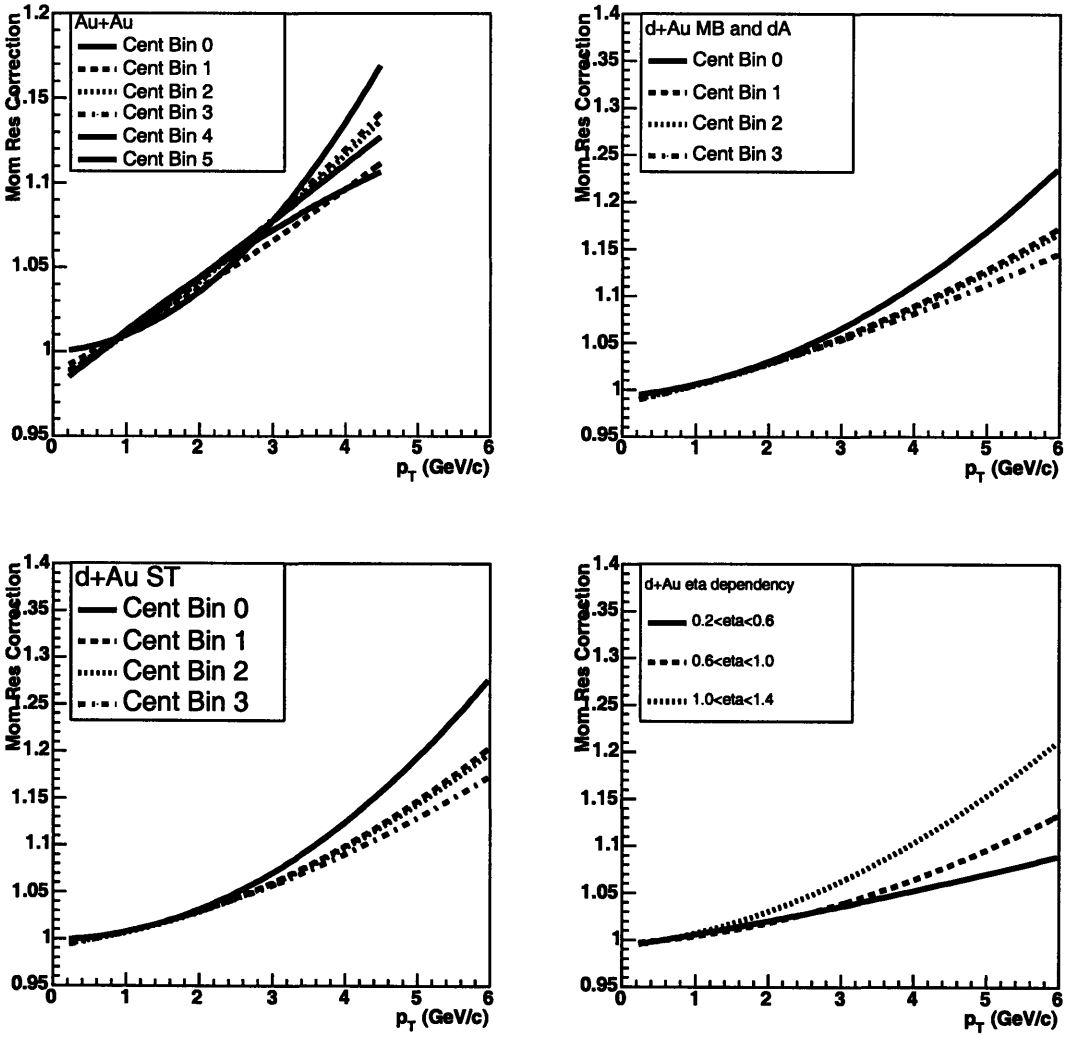

Figure 5-7: The final momentum resolution and bin width correction functions for the different data sets: Au+Au in the top left and d+Au for the min-bias and dAVertex data sets (top right), d+Au for the SpecTof data set (bottom left), and the d+Au in the three η bins (bottom right). The SpecToF were done separately because of the different acceptances between it and the MB and dA data sets (see Figures 4-6 and 4-7). These functions are all parabolas, and their forms are shown in Table 5.10.

Data Set	Bin	Function
Au+Au	Cent Bin = 0	$0.977 + 0.0374p_T - 0.0019p_T^2$
Au+Au	Cent Bin = 1	$0.987 + 0.0233p_T - 0.0010p_T^2$
Au+Au	Cent Bin = 2	$0.982 + 0.0261p_T - 0.0019p_T^2$
Au+Au	Cent Bin = 3	$0.983 + 0.0250p_T - 0.0023p_T^2$
Au+Au	Cent Bin = 4	$1.000 + 0.0019p_T - 0.0080p_T^2$
Au+Au	Cent Bin = 5	$0.978 + 0.0330p_T - 0.00006p_T^2$
d+Au	Cent Bin = 0	$0.993 + 0.00751p_T + 0.00554p_T^2$
d+Au	Cent Bin = 1	$0.989 + 0.01402p_T + 0.00277p_T^2$
d+Au	Cent Bin = 2	$0.987 + 0.01533p_T + 0.00246p_T^2$
d+Au	Cent Bin = 3	$0.985 + 0.01866p_T + 0.00136p_T^2$
d+Au ST	Cent Bin = 0	$0.999 + 0.00114p_T + 0.00756p_T^2$
d+Au ST	Cent Bin = 1	$0.995 + 0.00836p_T + 0.00442p_T^2$
d+Au ST	Cent Bin = 2	$0.993 + 0.00978p_T + 0.00407p_T^2$
d+Au ST	Cent Bin = 3	$0.991 + 0.01355p_T + 0.00282p_T^2$
d+Au	$0.2 < \eta < 0.6$	$0.993 + 0.0124p_T + 0.00061p_T^2$
d+Au	$0.6 < \eta < 1.0$	$0.996 + 0.0053p_T + 0.00294p_T^2$
d+Au	$1.0 < \eta < 1.4$	$0.993 + 0.0097p_T + 0.00447p_T^2$

Table 5.10: The parabolic fits for the momentum resolution and bin width corrections are shown here. These functions are all used to divide the data.

5.3 Feeddown Correction

A correction is made to account for the effects of secondary particles which are formed from interactions of particles with the detector material and from the decay products of parent particles.

5.3.1 Au+Au Correction

To determine the correction function Monte Carlo HIJING events were used. Both true MC tracks that hit the spectrometer and reconstructed tracks are stored in trees. Hijing associates a number with each track that gives information to its origin. This number is called the *parent number*, and is zero for primary tracks, and nonzero for all tracks that result from decays or interactions with the detector. These MC true tracks are taken directly from the event. The tracks reconstructed from the MC event do not have this parent number associated with them.

All of the reconstructed tracks were compared to the true tracks by matching the hits associated with the track. If a reconstructed track shares at least 10 hits with a non-primary track, then it is considered "matched" and is counted as a feeddown or secondary track. Figure 5-8 shows the ratio of non-primary to primary tracks that are accepted by the spectrometer. Using this histogram a correction function is fit which is applied to the data. The correction function is given by:

$$1 - 0.015(3.0 - p_T) \tag{5.1}$$

This is a multiplicative correction.

5.3.2 d+Au Correction

The basic idea of the feeddown correction for d+Au data is the same as the Au+Au data, but the procedure is different. Because the hit information was not stored in this analysis set, another track matching procedure had to be used. For each reconstructed track the distance in η was calculated for each reconstructible MC true

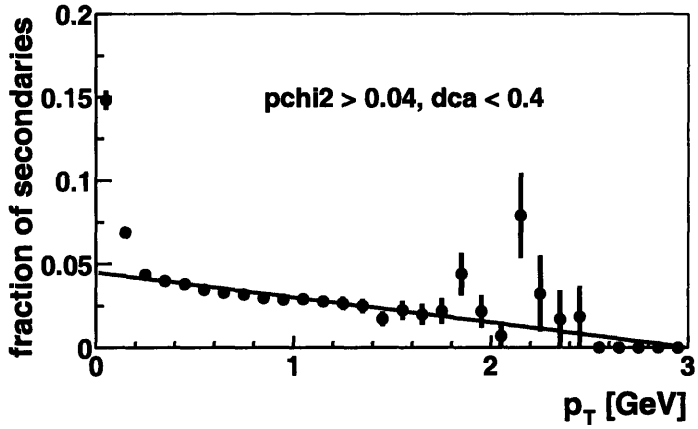

Figure 5-8: Fraction of reconstructed tracks that are not primary. The linear fit shown is the correction function applied to the data.

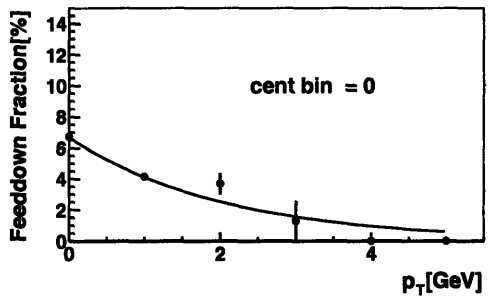

Figure 5-9: Histogram showing the fraction of secondaries reconstructed for the most peripheral bin in d+Au MC events. The histogram has been fit with a function which is applied to the data.

track. The closest true track is taken to be the matched track. Once the track is matched its parent number can be looked up to determine if it is a primary or non-primary track. Once this determination is made the fraction of non-primary tracks is readily determined as a function of p_T. Figures 5-9, 5-10, 5-11, and 5-12, show the four feeddown/secondary corrections for the four centrality bins.

The analytic function for the feeddown/secondary correction is

$$1.0 - 0.0676e^{-0.68p_T} \tag{5.2}$$

This is a multiplicative correction.

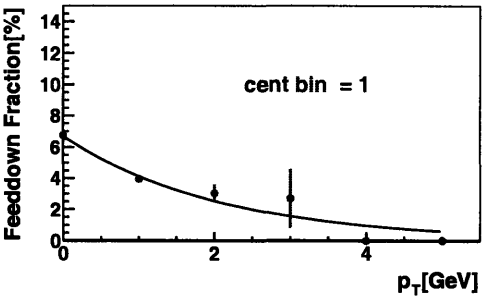

Figure 5-10: Histogram showing the fraction of secondaries reconstructed for the 40-70% bin in d+Au MC events. The histogram has been fit with a function which is applied to the data.

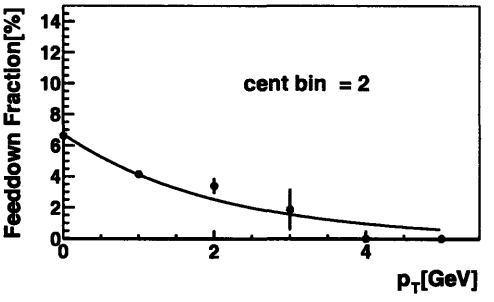

Figure 5-11: Histogram showing the fraction of secondaries reconstructed for the 20-40% bin in d+Au MC events. The histogram has been fit with a function which is applied to the data.

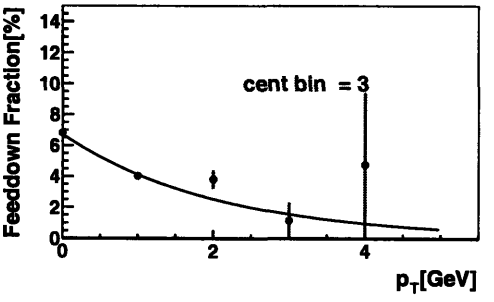

Figure 5-12: Histogram showing the fraction of secondaries reconstructed for the most central bin in d+Au MC events. The histogram has been fit with a function which is applied to the data.

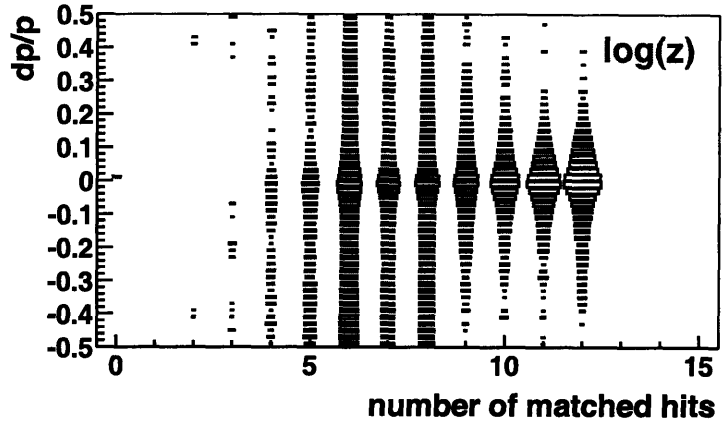

Figure 5-13: Momentum difference versus the number of matched hits for two MC tracks that share hits. This is used to define ghost tracks.

5.4 Ghost Correction

A correction must also be applied for ghost tracks, which are tracks that have been reconstructed but do not correspond to a real track.

5.4.1 Au+Au Correction

Similar to the feeddown/secondary correction, track matching is also used to determine the ghost correction. The tracking reconstruction is run over HIJING events, and found tracks are matched with true MC tracks. To determine what defines a ghost track, Figure 5-13 shows the momentum difference of the reconstructed track with its matched track versus the number of matched hits between the two tracks. Above 10 matched hits, there is a good correlation between the momenta of the found and matched tracks. Below 10 hits, the correlation becomes weaker. Therefore, tracks with less than 10 matched hits are defined to be ghost tracks. Figure 5-14 shows the fraction of ghost tracks with a probability cut greater than 0.04.

The centrality dependent functional form of the correction is

$$1 - 0.01(5.0 - p_T)\frac{N_{part}}{340} \tag{5.3}$$

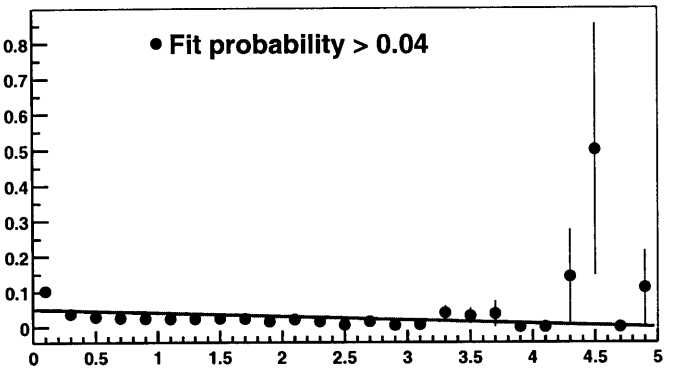

Figure 5-14: The fraction of ghost tracks with a fit probability > 0.04 for Au+Au MC. The fit to this histograms is the correction that is applied to the data.

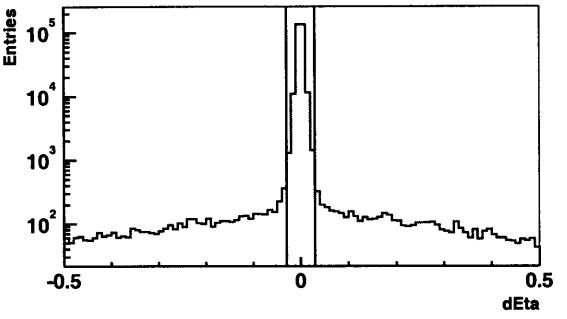

Figure 5-15: The difference in η between reconstructed MC tracks and the closest true MC track match. The horizontal lines denote the ghost cutoff. Tracks outside of the lines are considered to be ghosts.

This is a multiplicative correction.

5.4.2 d+Au Correction

The track matching for the d+Au ghost correction is done the same way as the feeddown/secondary d+Au correction. Figure 5-15 shows the η difference between the reconstructed track and its closest MC true track match. The solid lines show the cuts to signify ghost tracks.

Using these cuts to determine the ghost tracks, the fractions of ghost tracks to real tracks are plotted versus p_T for the four centrality bins in Figures 5-16, 5-17,

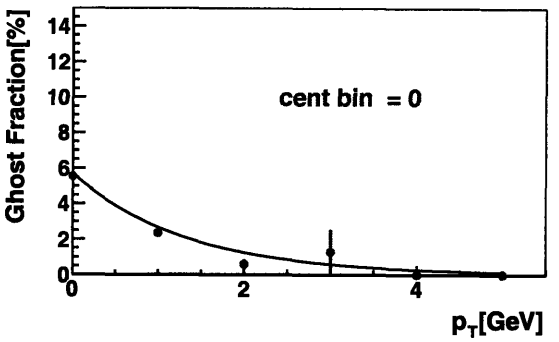

Figure 5-16: Fraction of ghosts in d+Au data for MC events, centrality bin 0.

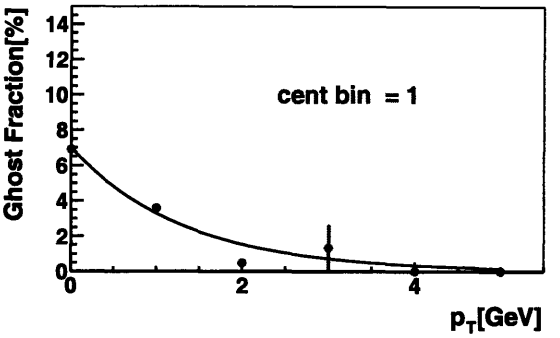

Figure 5-17: Fraction of ghosts in d+Au data for MC events, centrality bin 1.

5-18, and 5-19. The functional form of the fits are shown in Table 5.11.

5.5 Dead Channel Map Correction

Some of the channels have very high noise levels, and others are "broken" and do not give output signals. If a channel is dead or has a noise level higher than a predetermined threshold (10 ADC counts for the spectrometer), then these channels are masked out and the outputs are not used for analyses. Since the tracking algorithm depends on finding 12 hits, dead channels can cause a track to be missed if it hits one of the dead channels.

Monte Carlo events were analyzed with the tracking and the number of tracks was counted. Then the dead channel map was applied to the detector and the tracking was rerun. The ratio of the tracks found with the dead channel map with the number

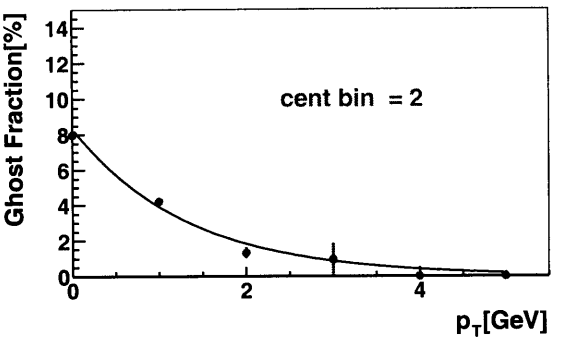

Figure 5-18: Fraction of ghosts in d+Au data for MC events, centrality bin 2.

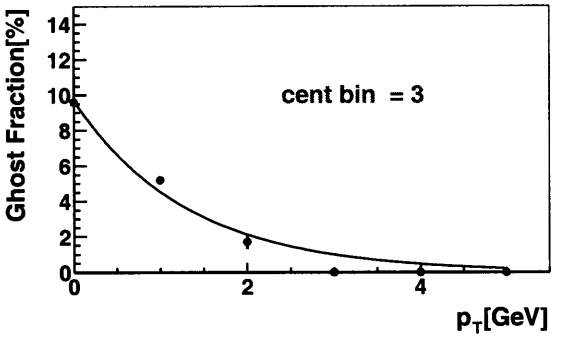

Figure 5-19: Fraction of ghosts in d+Au data for MC events, centrality bin 3.

Centrality bin	Correction function
0	$1 - 0.05e^{-1.125p_T}$
1	$1 - 0.067e^{-1.125p_T}$
2	$1 - 0.083e^{-1.125p_T}$
3	$1 - e^{-1.125p_T}$

Table 5.11: Centrality based correction functions for feeddown and secondary particles in the d+Au data set. These corrections are multiplicative with the data.

of tracks found without the dead channel map gives the percentage correction. This correction is independent of p_T, so this correction is an overall scale factor. For the Au+Au data, the correction is 7.8% and for the d+Au data it is 10.5%.

5.6 OctDeVtx Resolution Event Normalization Correction

As mentioned in Section 3.3.8, the resolution of OctDeVtx varies between 0.8 and 1.3 cm, which gives a much larger spread than RMSSelVertex used in Au+Au events. This wide resolution requires a correction to be made to the event normalization. When running over the events, a cut is made on the event vertex and only events with an OctDeVtx Z-coordinate between -10 and 10 are accepted. Furthermore, since the track vertex is not necessarily the same as the event vertex since they are determined separately, a cut is also made on the individual track vertex such that $-10 < v_z^{track} < 10$.

To see why a correction is needed consider an event that takes place just outside the accepted range of v_z. The resolution of about 1 cm can put the reconstructed vertex just inside the accepted region. The track vertex, however, has a resolution of about 1 mm, so reconstructed tracks in the event can be reconstructed with a vertex outside of the accepted region, and therefore will not be counted. This means that the event count will be over counted and the correction must account for this.

Figure 5-20 shows an illustration of the situation. The rectangle made with the dashed lines shows the v_z distribution of real events, and the solid curve shows the v_z distribution as reconstructed with OctDeVtx. The events that need to be corrected for correspond to the area of the regions a_1 and a_2. The areas a_3 and a_4 are events that are not counted and are simply thrown away without affecting the event normalization. To calculate these areas we use the OctDeVtx resolution σ, the event density $\rho\ cm^{-1}$, and the derivative of the event density $s\ cm^{-2}$.

This is then multiplied by the event density $\rho_i(1 + s_i z)$ and integrated to find the

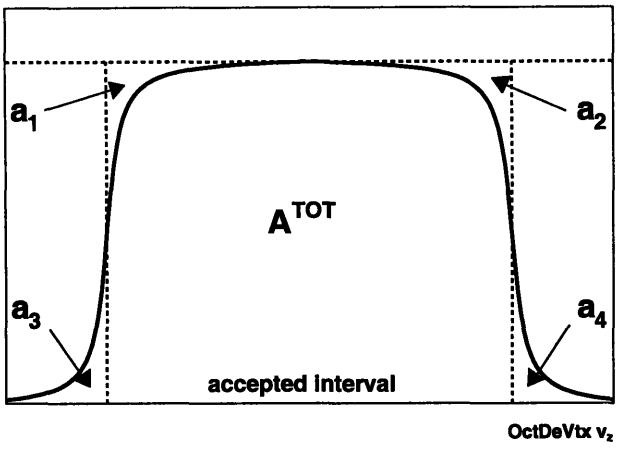

Figure 5-20: An illustration showing the finite resolution of OctDeVtx and the need to apply a correction to the event normalization. The areas a_1 and a_2, when divided by the total rectangular area a^{TOT}, give the percentage correction by which the event normalization must be decreased.

centrality bin	3	2	1	0
$s_1\rho_1$	-1.2	8	21.6	25.5
ρ_1	287	1542	1951	1553
$s_2\rho_2$	-1.2	-15	-15.4	-8
ρ_2	263	1544	2104	1757
σ	1.42	1.12	1.89	0.77
A^{TOT}	5510	32097	42491	34909
a_1	162	691	696	474
a_2	150	694	750	534

Table 5.12: Values for the variables used in the OctDeVtx correction. See the text for details.

areas a_1 and a_2:

A straight line fit to the event distribution gives the approximate slope s and the densities ρ. Since the resolution σ is centrality dependent the event normalization correction will be centrality dependent also. The results are shown in Table 5.12.

These corrections have to be done separately for the SpecToF data and the η dependent spectra. The SpecToF data have different vertex cuts, as seen in the acceptance/efficiency corrections, and the η dependent spectra also have different vertex cuts. The same methodology is applied, and the corrections calculated are shown in Table 5.13. The corrections are give in percentages, which correspond to

centrality bin	3	2	1	0
All η	5.7	4.3	3.4	2.9
SpecToF	2.7	2.2	1.8	1.6

Table 5.13: Correction factors in percentages for the OctDeVtx correction

$(a_1 + a_2)/A^{TOT}$ in Table 5.12. The η dependent data are averaged over centrality, and those corrections are 7.9% for the $0.2 < \eta < 0.6$ data, and 2.9% for the other η bins.

5.7 Centrality Dependence of the Efficiency

Since the efficiency studies described above were done for single tracks, the centrality dependence must be studied. Known MC tracks were embedded into actual data events, and the resulting output tracks were matched to the embedded tracks to see if the MC track was reconstructed. The matching procedure is the same as that described for the Au+Au feeddown and ghost studies.

The tracks were embedded for three different centrality bins: 7-10, 11-14, and 15-17. Figure 4-4 shows the single track efficiency. The ratio of the two is also shown, and is the correction that needs to be applied. Within the errors, the correction is independent of p_T. The centrality dependent correction function is

$$0.963 - 0.00038 N_{part} \tag{5.4}$$

The data must be divided by this correction.

Chapter 6

Data Analysis and Results

6.1 Event Selection

Most of the event selection is discussed in Section 3.2. For the Au+Au data set, the selected events, in addition to the *IsColl* determination discussed earlier, must have a valid RMSSelVertex, and the vertex must have $-10 < v_z < 10$. 6 million events were collected that pass the selection cuts. These events are grouped into six centrality bins. The grouping is shown in Table 6.1.

For the d+Au data set there must be a valid OctDeVtx reconstructed, and again only events with $-10 < v_z < 10$ were used. The total number of triggered events were 29 million MinBias, 54 million dAVertex and Peripheral, and 51 million SpecToF. The number that passed the event cuts is 25.9 million. These events are then separated into four centrality bins, which is shown in Table 6.2

Centrality bins	Percentage cross section	N_{part}	N_{coll}	Events
16 and 17	$0-6\%$	344 ± 11	1040 ± 47	675K
14 and 15	$6-15\%$	276 ± 9	762 ± 35	1057K
12 and 13	$15-25\%$	200 ± 8	483 ± 28	1193K
10 and 11	$25-35\%$	138 ± 6	286 ± 18	1192K
8 and 9	$35-45\%$	93 ± 5	164 ± 12	1196K
7	$45-50\%$	65 ± 4	99 ± 9	593K

Table 6.1: Centrality binning used for the Au+Au data analysis.

Centrality bin	Percentage cross section	N_{part}	N_{coll}	Events
3	$0-20\%$	14.6 ± 0.9	15.5 ± 1.0	9.8M
2	$20-40\%$	9.7 ± 0.8	10.9 ± 0.9	7.3M
1	$40-70\%$	5.4 ± 0.8	6.7 ± 0.9	5.8M
0	$70-100\%$	2.2 ± 0.6	3.3 ± 0.7	3.0M

Table 6.2: Centrality binning used for the d+Au data analysis.

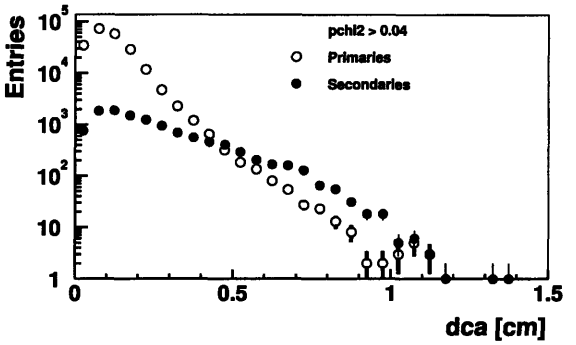

Figure 6-1: *dca* distributions from Monte Carlo for both primary and secondary particles. The secondary distribution dominates after $dca \sim 0.4$, so by cutting on the *dca* distribution that part of the secondary distribution is removed from the data.

6.2 Track Cuts

In addition to the quality cuts hard coded in the tracking algorithm, two more cuts are made on tracks reconstructed in the events. The distance of closest approach, or *dca*, is one of the cuts. The *dca* is the closest distance the track comes to the reconstructed vertex position. This is found by extrapolating the straight part of the track back to the vertex. The purpose of this cut is to reduce the number of secondary particles. Figures 6-2 and 6-3 show the dca distributions for Au+Au and d+Au data. The cuts are $dca < 0.35$ for Au+Au data and $dca < 0.4$ for d+Au. The exponential fits in Figure 6-2 correspond to primary and secondary distributions. The "kink" in the distribution is due to the overlay of two exponential distributions corresponding to primary and secondary tracks. This can be seen more clearly in Figure 6-1, which shows the two distributions separately. By cutting on *dca* we cut out the distribution dominated by secondary tracks.

As the tracks are being analyzed from the trees, only those with pseudorapidity

between 0.2 and 1.4 are used, which is the approximate acceptance of the spectrometer.

Finally, a cut is made on the probability. Figures 6-2 and 6-4 show the probability distributions in Au+Au and d+Au. There is a peak in the distribution at zero, so by cutting around that point the number of tracks that have a very low probability of being real are eliminated from the analysis. This helps make the ghost levels low (although a ghost correction is still made, which includes this probability cut). All tracks with $prob < 0.04$ are discarded from the analysis.

6.3 Assembling the Spectra

6.3.1 Histogramming Spectra

The first step in assembling the spectra is running over the event trees that contain all of the information in the event, including the tracks. The tracks are histogrammed separately by centrality bin, vertex bin, charge, and magnet polarity. The vertex binning is the same as the binning of the acceptance and efficiency corrections: 5 cm intervals between -10 and 10. There are four separate possibilities for the charge and polarity combinations: positive polarity and positive charge, positive polarity and negative charge, negative polarity and positive charge, and negative polarity and negative charge. These are abbreviated PPPC, PPNC, NPPC, and NPNC respectively.

As each track's p_T value is histogrammed, it is weighted individually by the value of the acceptance and efficiency correction function at the track's p_T value. For the Au+Au data, the appropriate correction function is used depending on the track's bending direction (charge and polarity combination) and the event's vertex position. In the d+Au data the track's extrapolated vertex position is used since the resolution of the event vertex is low. Four versions of each histogram are filled. The histograms are also weighted by the p_T value, creating a $(1/p_T)dN/dp_T$ distribution, a histogram is made with no acceptance and efficiency correction, and finally a histogram is filled

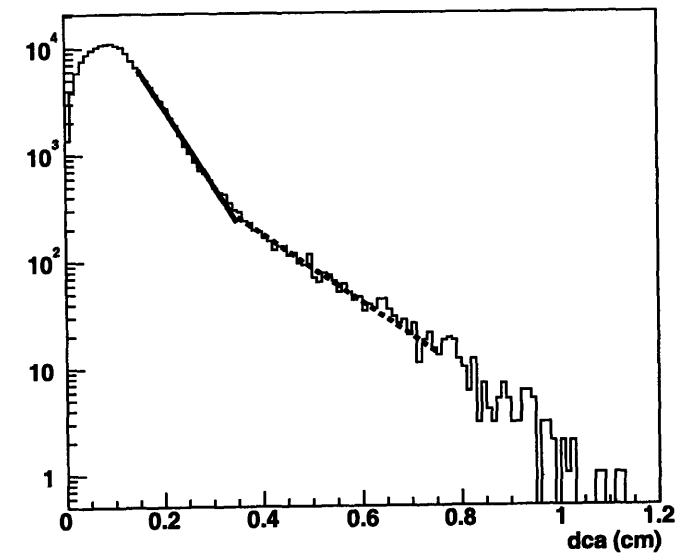

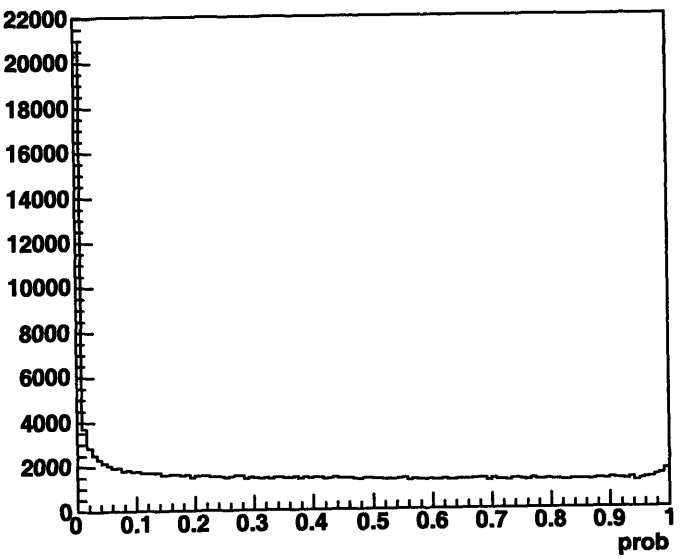

Figure 6-2: Distance of closest approach and probability distributions for Au+Au data. The dca histogram shows two exponential fits to the data, which meet at the cut of dca = 0.35, which is applied to the data. By cutting on tracks with dca > 0.35 the portion of the dca spectrum dominated by secondary tracks is discarded. The probability distribution has a spike at 0, and by cutting on prob > 0.04 a cut on probable ghost tracks is made.

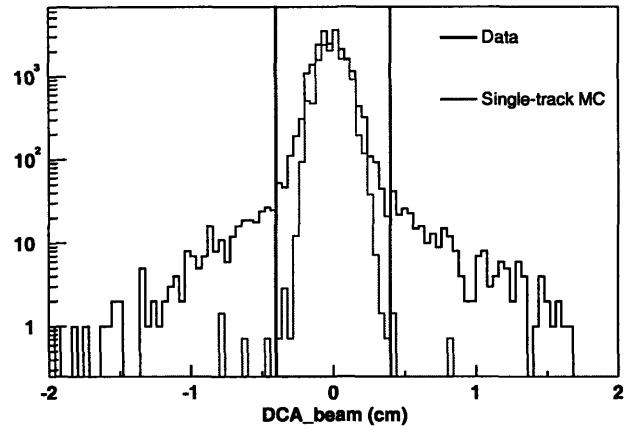

Figure 6-3: *dca* distribution for the d+Au data (along with the MC single tracks). The definition of dca for the d+Au data sets allows for negative values, unlike the Au+Au data.

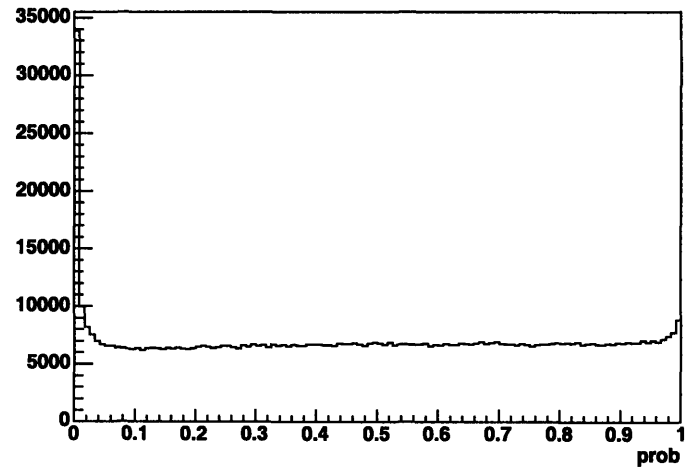

Figure 6-4: Probability distribution for the d+Au data. As in the Au+Au, a cut is made on prob > 0.04 to eliminate the spike at zero, and hence remove tracks that are likely to be ghosts.

with just the number of tracks, with no other operations applied to it. Also, the $(1/p_T)dN/dp_T$ distribution is weighted by the η range and also by the bin width, creating a $(1/p_T)d^2N/dp_Td\eta$ histogram for each centrality, vertex, and charge/polarity combination.

Once the histograms are filled, they must be combined in the correct way to produce the spectra in centrality bins. The histograms for each charge and polarity combination and centrality bin have their four vertex bins added together. These are then weighted by the number of events. The number of accepted events for each centrality and magnet polarity is recorded, and this is used as a scale factor.

The results are four sets of acceptance and efficiency corrected spectra for each centrality bin and charge polarity combination, which amounts to 24 histograms for the Au+Au data and 48 histograms for the d+Au data (four charge polarity combinations, four centrality bins, and three trigger configurations). Since the goal is to produce an $h^+ + h^-$ distribution, the positive charge histograms and the negative charge histograms can be added together. However, the two different bending directions have different acceptances and efficiencies, so simply adding them together is not correct. For this reason, the PPPC and NPNC histograms are added together, and the PPNC and NPPC histograms are added. Since these correspond to the same bending direction, these can be added together to make a valid $h^+ + h^-$ histogram. For the d+Au data, this is done separately for the three different trigger configurations.

To combine these histograms with the different bending directions an averaging procedure is used. For one histogram bin, the yield in that bin is given by

$$Y_1 = \frac{T_1}{N_1\langle\epsilon_1\rangle} \tag{6.1}$$

and the corresponding yield in the second histogram is

$$Y_2 = \frac{T_2}{N_2\langle\epsilon_2\rangle} \tag{6.2}$$

Y_i is the yield, N_i is the event normalization T_i is the raw number of tracks in the bin, and $\langle\epsilon_i\rangle$ is the average acceptance and efficiency correction factor. Since the vertex

bins have been added together at this point, this average correction is an average of the values of the vertex binned correction functions at that p_T value. The total averaged yield for the final histogram is

$$Y = \frac{T_1 + T_2}{N_1\epsilon_1 + N_2\epsilon_2} = \frac{T_1 + T_2}{\frac{T_1}{Y_1} + \frac{T_2}{Y_2}} \tag{6.3}$$

The statistical error assigned to each bin is

$$\frac{Y}{\sqrt{T_1 + T_2}} \tag{6.4}$$

since this is simply the number of tracks produced divided by the square root of the number detected.

For the d+Au data, after the separate bending directions are added together the three different trigger configurations are combined using the same averaging procedure.

Tracks that bend toward the beam pipe, or away from the outer wing, have a much lower acceptance at low p_T. For this reason, the acceptance correction is very high in this region, and the variation of the correction function as a function of p_T is very steep. In this bending direction, only tracks with $p_T > 0.7$ are used. The other bending direction has a low p_T cut of 0.2. This means that in the region $0.2 < p_T < 0.7$ all of the tracks come from tracks that bend into the outer wing. The SpecToF data also have very low acceptances at low p_T. The p_T cutoffs for this data set are 2.2 and 1.5 GeV/c for bending toward the beampipe and toward the outer wing respectively.

6.3.2 Final Corrections

The acceptance and efficiency corrections are applied on a track by track basis, and are the largest of the corrections. The other minor corrections are applied after the final histograms are obtained. The correction functions are then either used to divide or multiply the histograms, and the dead channel scale factor is applied. For the d+Au data, the OctDeVtx correction is applied to the event normalization, so that this effect is taken into account during the averaging procedure. The final correction

applied is the momentum resolution and bin width correction function, which are used to divide the spectra. This must be done as the final step, as these functions are dependent on the shape of the spectra and were derived using an approximation of the final spectra. Since the final shape of the spectra is not known until all corrections are made, this correction is in reality an approximation to a certain degree. However, the effect is small, and a systematic error associated with these functions are included.

6.4 UA1 Reference Spectra

6.4.1 UA1 Correction

One of the goals of this analysis is to compare the spectra from both Au+Au data and d+Au data to a reference from p+p or $p + \bar{p}$ collisions. The UA1 collaboration has published p_T charged hadron spectra at $\sqrt{s_{NN}} = 200$ GeV [47], so this can be used as a suitable $p+\bar{p}$ reference spectrum. However, there is a correction that needs to be made. The UA1 data lies in the range $-2.5 < \eta < 2.5$, whereas the PHOBOS data presented here is in the range $0.2 < \eta < 1.4$. Because these ranges are quite different, this difference must be accounted for.

This correction is done using the PYTHIA [48] event generator. $p+\bar{p}$ events were simulated at $\sqrt{s_{NN}} = 200$ GeV, and the resulting tracks with $-2.5 < \eta < 2.5$ had their p_T values histogrammed. This simulates the UA1 data. The same was done for the PHOBOS acceptance of $0.2 < \eta < 1.4$. No other detector effects are used, so these are the "true" spectra for these η ranges according to the PYTHIA generator. The two histograms are then divided, and the result is fit to a function. This function is then the correction to the functional fit of the UA1 data. The same procedure is done for the η dependent d+Au spectra, so tracks are histogrammed in the ranges $0.2 < \eta < 0.6$, $0.6 < \eta < 1.0$, and $1.0 < \eta < 1.4$.

Figure 6-5 shows the generated distributions for the two acceptances, and Figure 6-6 shows the ratio of the PHOBOS distribution over the UA1 distribution with the corresponding fit function. The functional form of this fit is

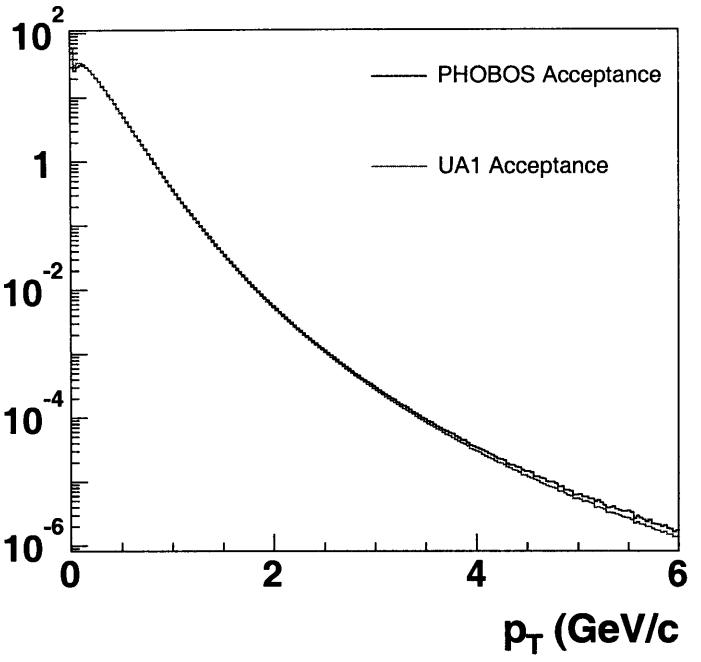

Figure 6-5: Spectra generated with the PYTHIA event generator for tracks in the PHOBOS acceptance and tracks in the UA1 acceptance.

$$(\ln(e^{(1.065+0.004p_T)^{40}}+e^{(0.85+0.07p_T)^{40}})/40.0-0.12e^{-2.0p_T}+0.04e^{-3.66p_T})(p_T/\sqrt{p_T^2+0.00545}) \tag{6.5}$$

6.4.2 UA1 Fit Function

The original UA1 data is fit to a function with a power law form:

$$A(1+\frac{p_T}{p_0})^{-n} \tag{6.6}$$

The parameters determined are A = 50.9, p_0 = 1.59, and n = 11.2. The ratio of the UA1 data with this fit function is shown in Figure 6-7

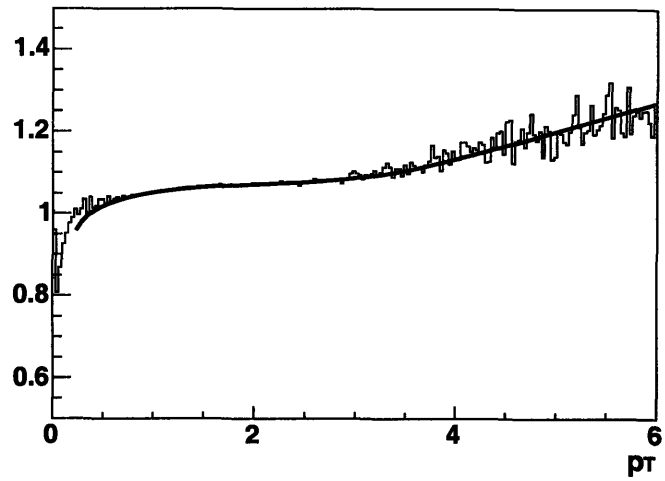

Figure 6-6: Ratio of the PHOBOS PYTHIA distribution with the UA1 PYTHIA distribution. This histogram is then fit to a function, which is used as a correction to the functional fit of the UA1 data.

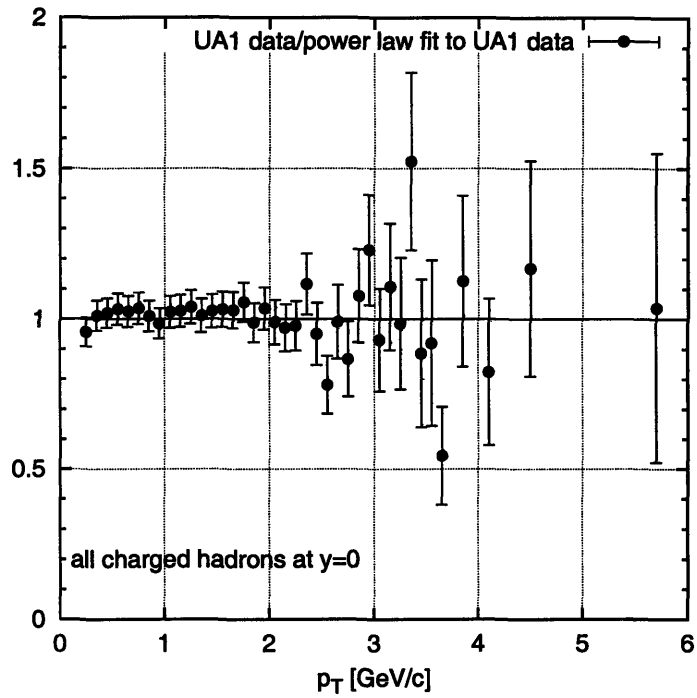

Figure 6-7: Fit quality of the UA1 fit function. This shows the ratio of the UA1 data with the fit function given by Equation 6.6.

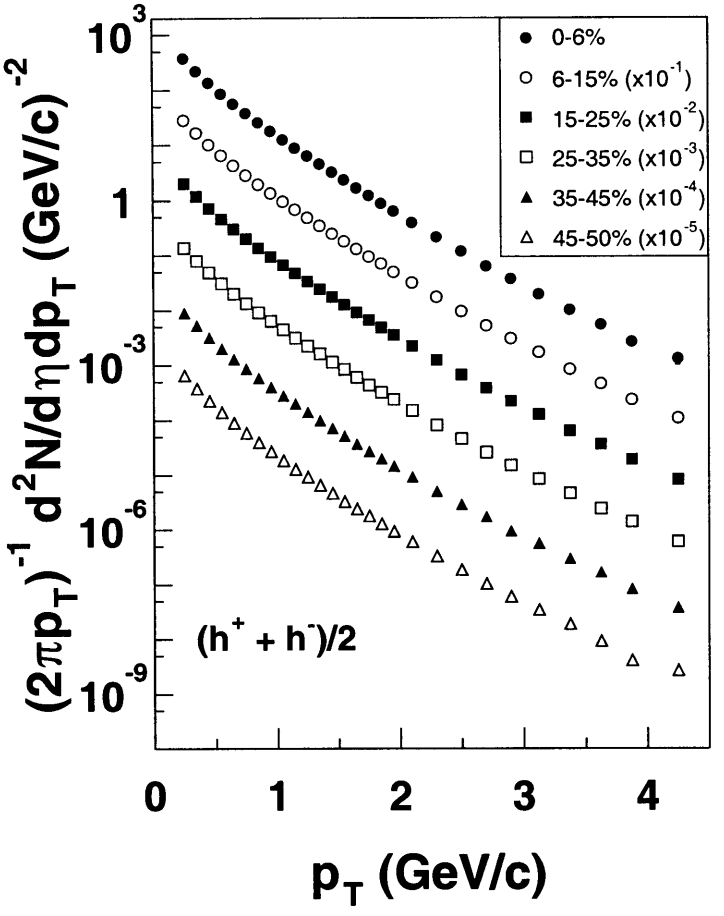

Figure 6-8: $\frac{1}{2\pi p_T}\frac{d^2N}{dp_T d\eta}$ distributions for the six centrality bins in the Au+Au data. The different centralities have been weighted by successive factors of 10 for clarity.

6.5 Centrality Dependence of the Spectra

Once the spectra are properly averaged together and all the corrections have been applied, the evolution as a function of centrality can be studied.

6.5.1 Au+Au Results

Figure 6-8 shows the $(1/2\pi p_T)d^2N/dp_T d\eta$ distributions for the Au+Au data [49].

To study the evolution as a function of centrality the spectra are compared to the UA1 reference spectrum. with the nuclear modification factor R_{AA}, which is given by

$$R_{AA} = \frac{d^2N_{AA}/dp_T d\eta}{\langle N_{coll}\rangle d^2N_{pp}/dp_T d\eta} \tag{6.7}$$

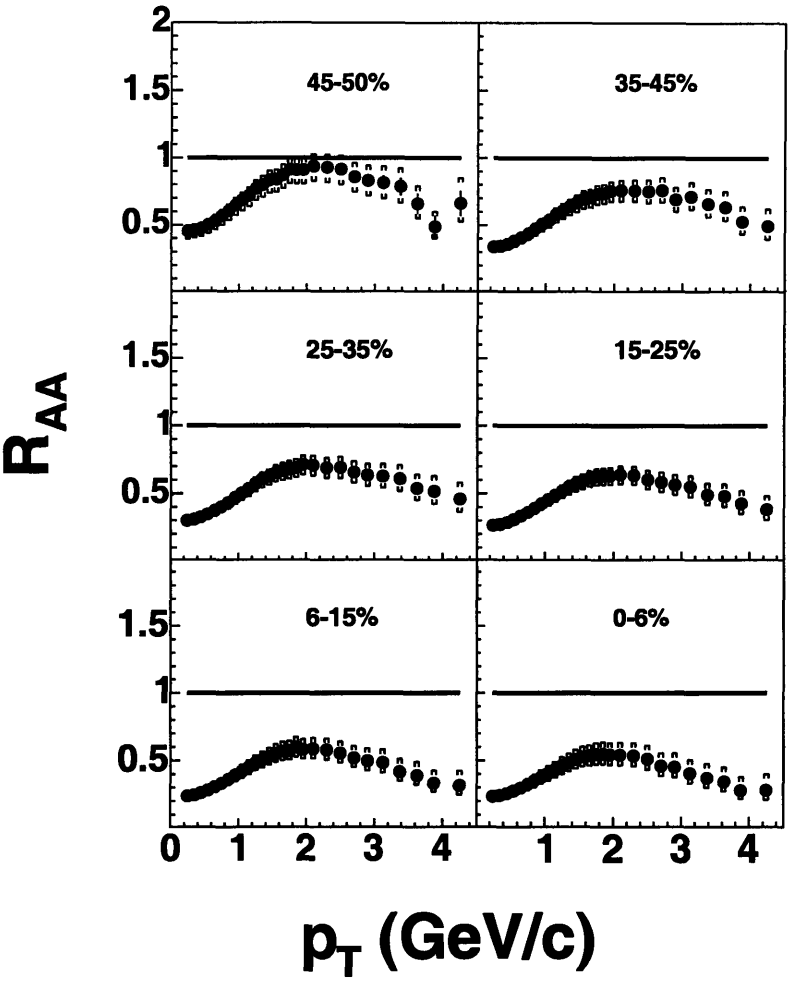

Figure 6-9: R_{AA} as a function of p_T for the six centrality bins. The PHOBOS spectra have been weighted by each centrality's corresponding N_{part} value and the corrected UA1 fit

The spectra are weighted by the N_{coll} value for the given centrality bin and divided by the UA1 fit function. The results are shown in Figure 6-9.

Since the scaling behavior is not known, we also scale the Au+Au spectra by the number of participant pairs $N_{part}/2$. Figure 6-10 shows this quantity $R_{AA}^{N_{part}}$:

$$R_{AA}^{N_{part}} = \frac{d^2N_{AA}/dp_Td\eta}{\langle N_{part}/2\rangle d^2N_{pp}/dp_Td\eta} \tag{6.8}$$

Another method used to look at the centrality evolution is to compare the centrality binned spectra with the most peripheral bin rather than the UA1 reference

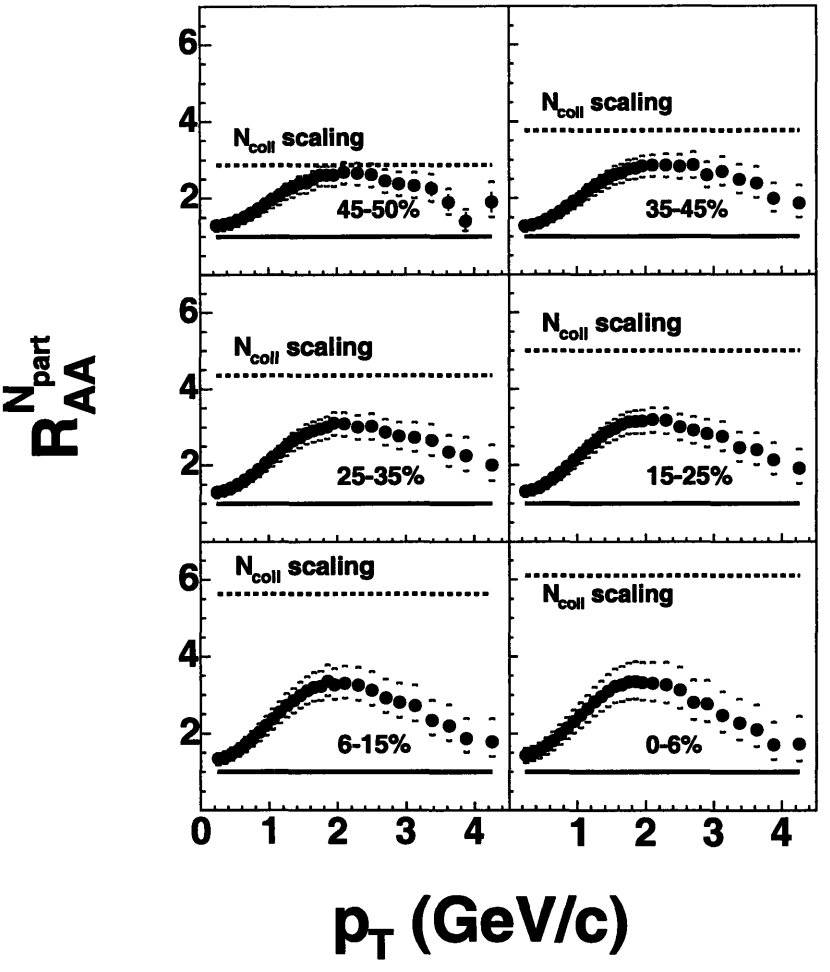

Figure 6-10: $R_{AA}^{N_{part}}$ as a function of p_T for the six centrality bins. This is the same quantity as Figure 6-9, but with the spectra weighted by the appropriate $N_{part}/2$ values rather than N_{coll}.

spectra. This quantity is called $R_{CP}^{N_{part}}$, since all spectra are scaled by their $\langle N_{part} \rangle$ values, and then divided by a fit the most peripheral data:

$$R_{CP}^{N_{part}} = \frac{\langle N_{part} \rangle_P d^2N_C^2/dp_T d\eta}{\langle N_{part} \rangle_C d^2N_P^2/dp_T d\eta} \tag{6.9}$$

This functional fit is:

$$5.0\mathrm{e}^{-3.12p_T} + 58.3(1 + p_T/1.269)^{-9.68} \tag{6.10}$$

Finally, for the Au+Au data $R_{CP}^{N_{part}}$ values have been plotted for six different p_T values versus N_{part}. This is shown in Figure 6-12.

Finally, figure 6-13 shows R_{CP} for the six centrality bins. By comparing this figure with 6-11, it is evident that the scaling with N_{part} is a much better description than scaling with N_{coll}.

6.5.2 d+Au Results

To differentiate between initial state effects and final state effects the nuclear modification factor for d+Au collisions, R_{dAu} is studied. If the suppression was due to the interactions of jets in the medium produced in the collision (a final state effect), the suppression should be absent in d+Au collisions, since the system size produced would be too small to effect the jets. However, an initial state could still effect the d+Au spectra.

Figure 6-14 shows the d+Au invariant yields divided into the four centrality bins [50]. Figure 6-15 shows the nuclear modification factor R_{dAu} for the four centrality bins. Similar to the Au+Au results, four different p_T values were chosen and R_{dAu} plotted for each p_T value as a function of N_{coll}. This is shown in Figure 6-16. Since these p_T points do not correspond to exact bin centers from Figure 6-15, the values are interpolations of functions fit to the data. These are the fits to the invariant yields, which are then divided by the UA1 fit function.

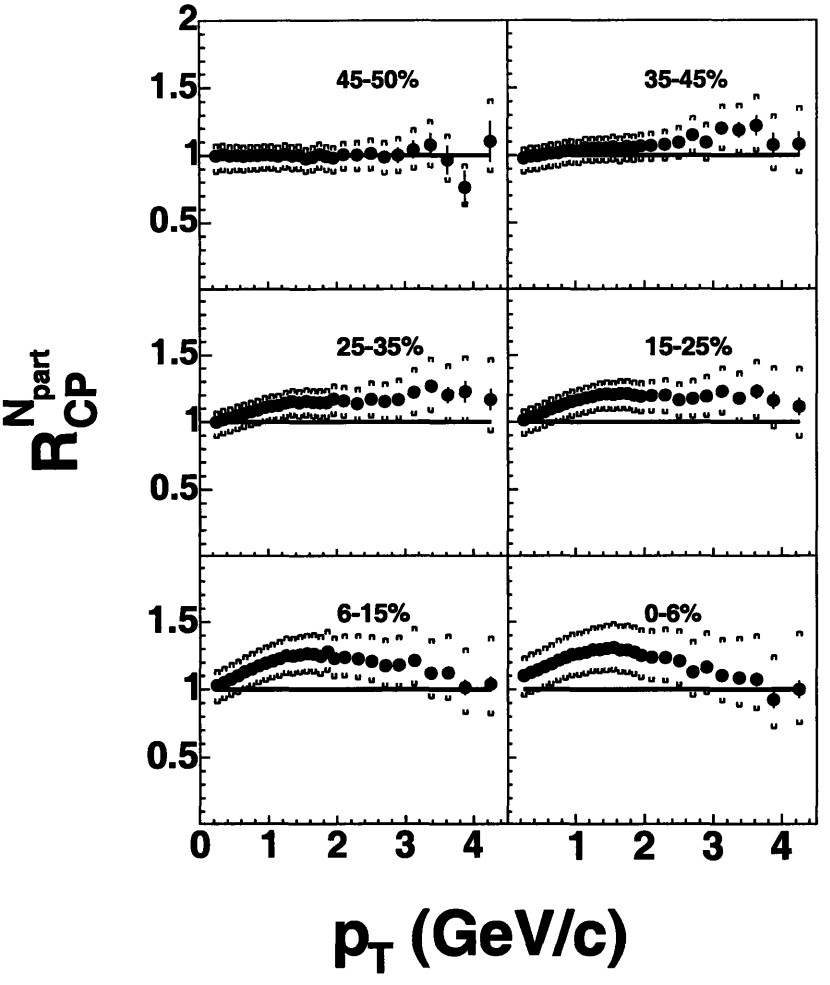

Figure 6-11: $R_{CP}^{N_{part}}$ as a function of p_T for the six centrality bins. Each centrality bin has been weighted by its N_{part} value and divided by a fit to the most peripheral bin. The top left panel, which is the most peripheral bin, has been divided by a fit to itself, which shows the quality of the fit.

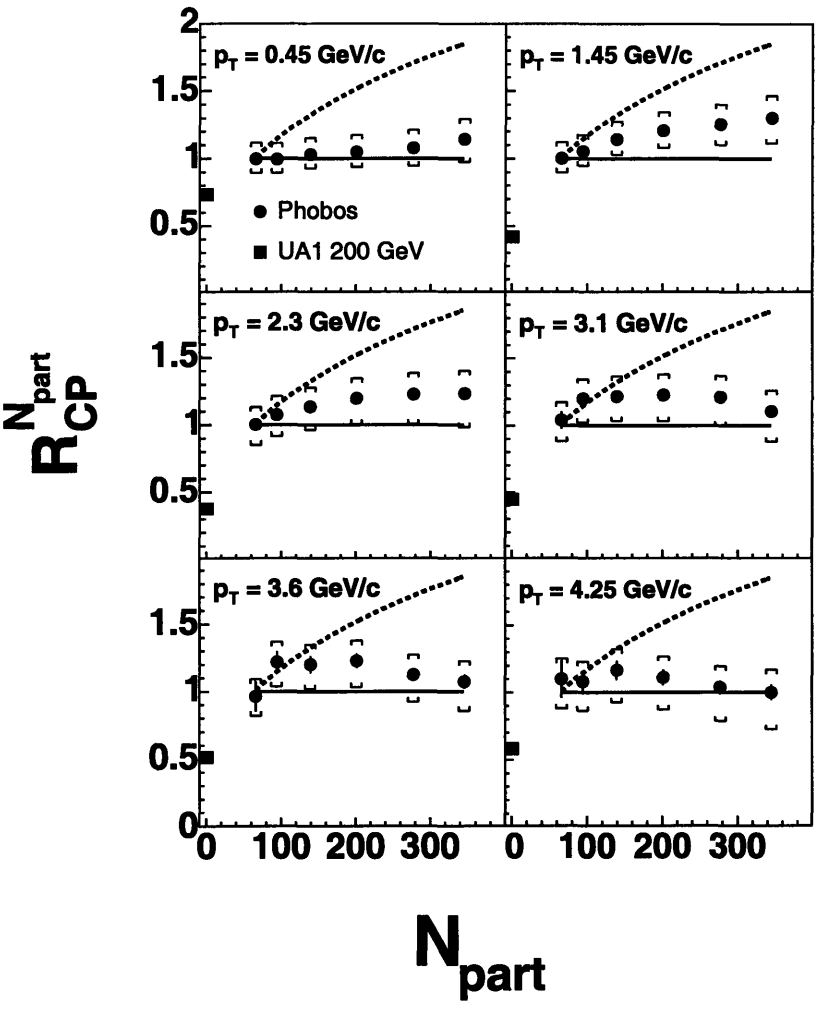

Figure 6-12: $R_{CP}^{N_{part}}$ as a function of N_{part} for six different p_T values. These values for the different p_T's were taken from Figure 6-11 and plotted as a function of N_{part} for each centrality bin. The dashed curve in each panel shows where the points would lie if N_{coll} scaling held.

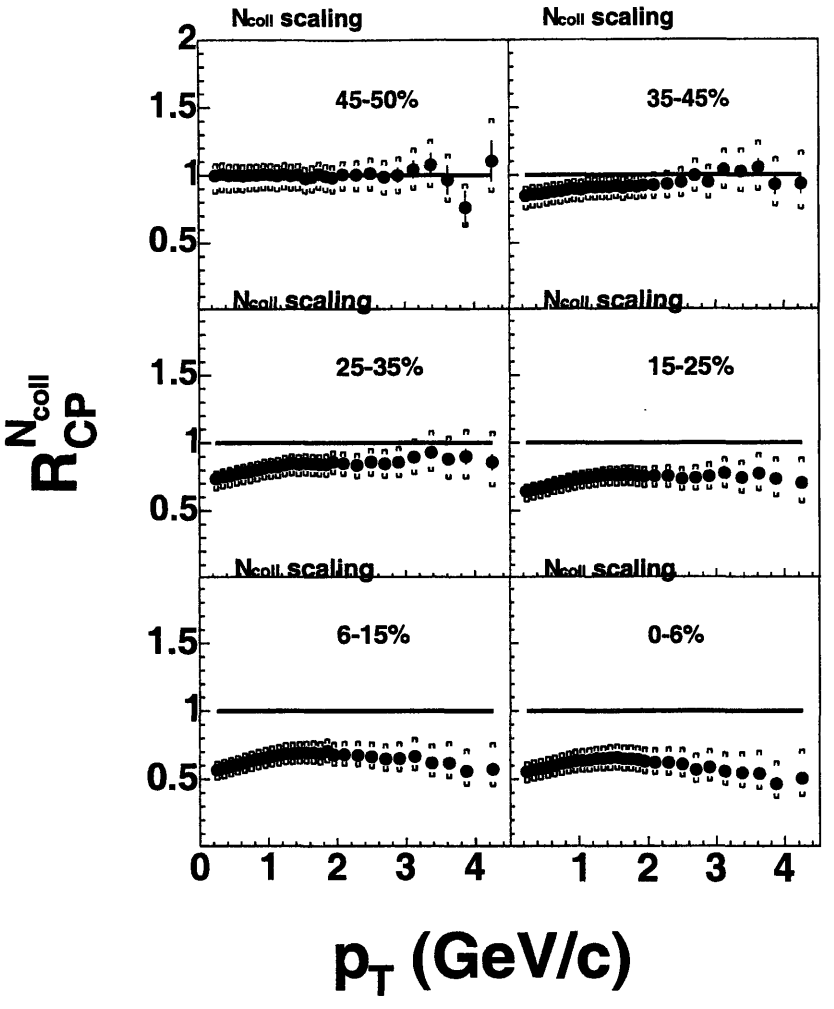

Figure 6-13: $R_{CP}^{N_{coll}}$ as a function of p_T for the six centrality bins. Each centrality bin has been weighted by its N_{coll} value and divided by a fit to the most peripheral bin. The top left panel, which is the most peripheral bin, has been divided by a fit to itself, which shows the quality of the fit.

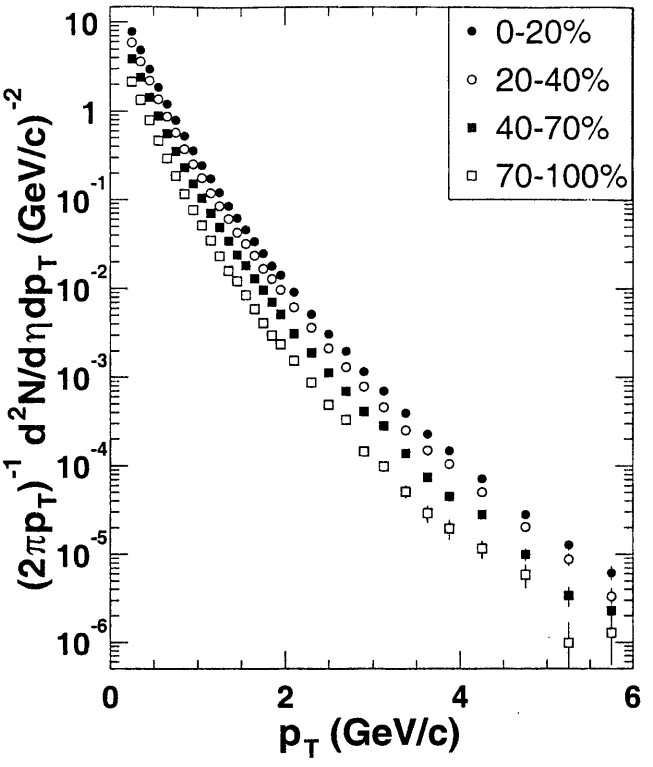

Figure 6-14: d+Au $\frac{1}{2\pi p_T}\frac{d^2N}{dp_T d\eta}$ distributions for the four centrality bins.

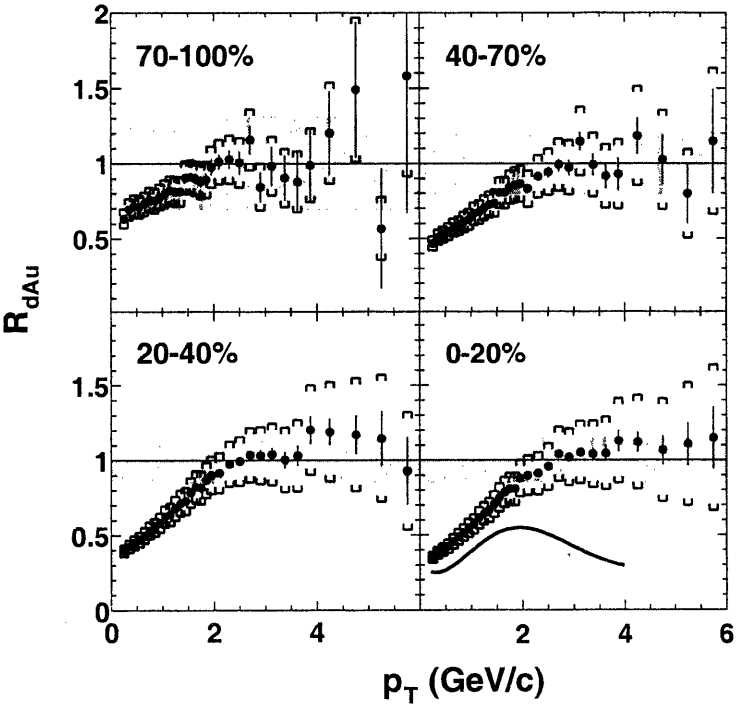

Figure 6-15: Nuclear modification factor R_{dAu} for the four centrality bins. The gray bands show the overall scale error.

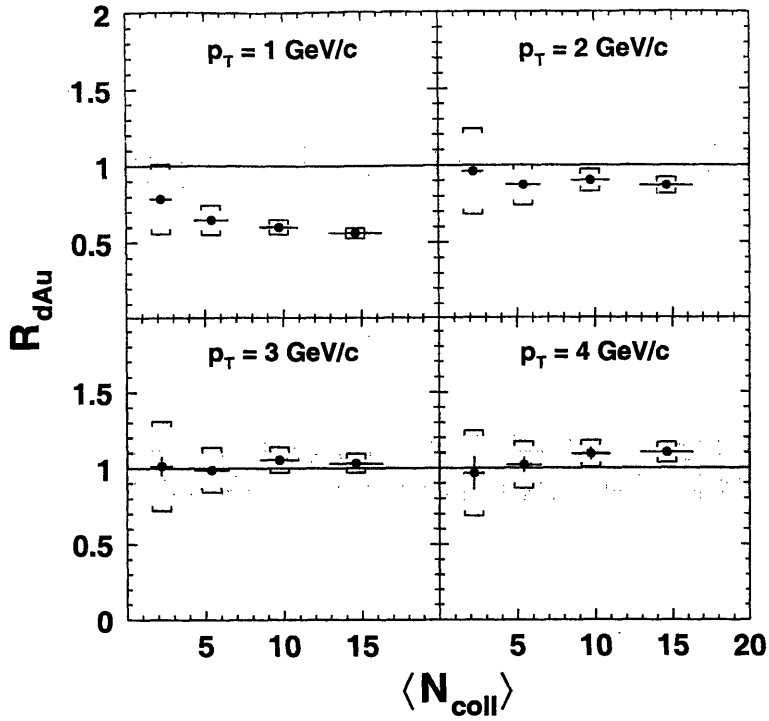

Figure 6-16: Nuclear modification factor R_{dAu} versus N_{coll} for the four centrality bins and at four different p_T values.

6.5.3 Systematic Errors

The brackets and the gray error bands in the Au+Au and d+Au data plots represent the systematic errors on the data. The source of these systematic errors comes from the correction functions applied to the data, as well as, in the case of the d+Au data set, unknown systematic discrepancies seen in the data.

In the Au+Au data error functions were generated that represent the 90% confidence level in the spectra for the given correction function. These errors are representative of the uncertainty due to statistical fluctuations in the Monte Carlo simulations used to generate the corrections, the quality of the function used to fit to the histogram points, and the inherent uncertainty in using MC to apply to data.

Each correction function has an error function associated with it. These error functions are shown in Figures 6-17 and 6-18 for the Au+Au and d+Au data respectively. The final error function is obtained by combining all of the separate error functions in quadrature, and applying the value of that final function to each point

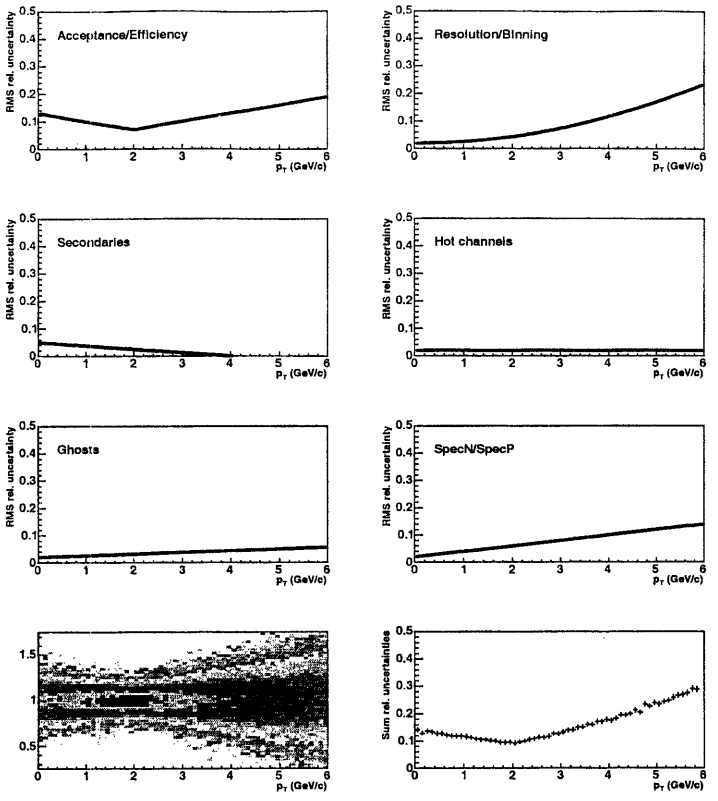

Figure 6-17: Systematic error functions, in percentages, for the correction functions for the Au+Au data. These errors are taken to be Gaussian, and the final error function, in the bottom right, is the quadrature sum of the others.

in the data histograms. In the d+Au data set there is a larger percentage error in the N_{part} and N_{coll} determination, and this error is represented as a gray band. This error will just introduce a scale factor, and is therefore independent of p_T

Since the systematic errors are calculated from the correction functions, it is important to check the data itself to see if the errors applied are realistic. Several cross checks were done comparing different data. In both Au+Au and d+Au data sets spectra from different magnet polarities and charge signs were compared. The ratios B^-h^-/B^+h^- and B^+h^+/B^-h^+ were plotted. This ratio compares different bending directions, which have different acceptances and efficiencies while keeping the charge signs the same. In both cases the ratio was found to be within 10%, and consistent with unity. Another cross check was looking at the ratio of spectra from different spectrometer arms. For the Au+Au data this ratio was within 10% and consistent

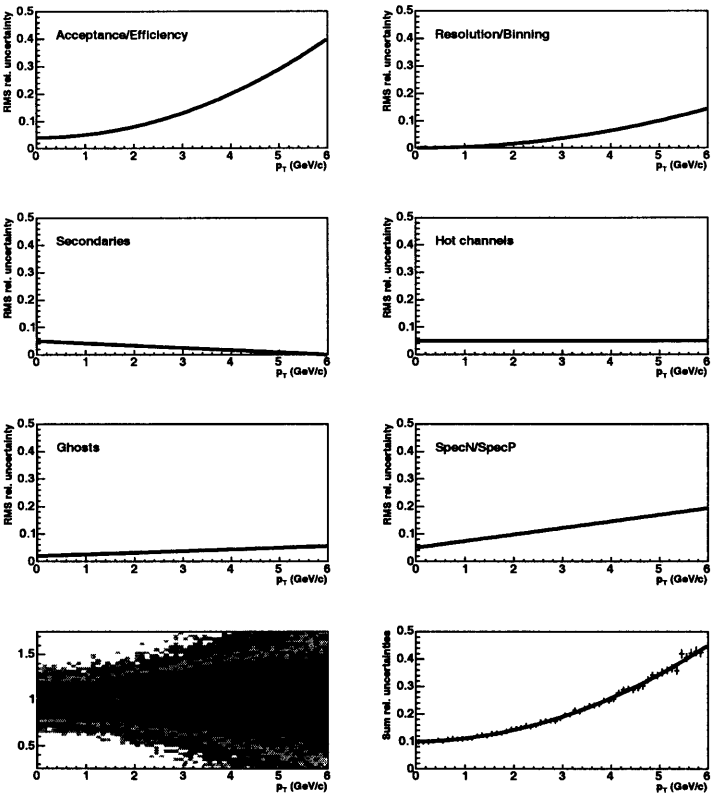

Figure 6-18: Systematic error functions, in percentages, for the correction functions for the d+Au data. These errors are taken to be Gaussian, and the final error function, in the bottom right, is the quadrature sum of the others.

with unity, but in the d+Au data set the ratio SpecN/SpecP was about 90%. The reason for this is not understood, and introduces another source of error included in the systematic error.

6.5.4 Au+Au and d+Au Centrality Dependence Discussion

Figures 6-9 and 6-10 show how the Au+Au spectra scale with respect to $p+\bar{p}$ collisions. While soft particle production is thought to dominate at low p_T ($p_T < 2$ GeV/c) and scale with N_{part}, the high p_T region was thought to be dominated by hard processes and scale with N_{coll}. According to the Glauber model, the ratio $\langle N_{coll}\rangle/\langle N_{part}/2\rangle$ will increase by a factor of six from p+p to central Au+Au collisions. In particular, for Au+Au collisions the Glauber models predict $N_{coll} \sim N_{part}^{4/3}$. Due to this increase if these scaling models were to hold there would be similar changes in the yields at low to high p_T values when compared to p+p spectra.

What we see in the data, in Figures 6-9 and 6-10, is increase in the relative yields up to $p_T = 2$ GeV/c approximately. However, at high p_T the spectra do not scale with N_{coll}. Only in the most peripheral bin at p_T around 2 GeV/c is it close to N_{coll} scaling. At the highest centrality R_{AA} has decreased by almost a factor of two. This decrease in R_{AA} is smaller in $R_{AA}^{N_{part}}$. In fact, at low and high p_T there is a similar scaling behavior at all centralities for $R_{AA}^{N_{part}}$.

To investigate the scaling behavior with N_{part} further $R_{CP}^{N_{part}}$ and $R_{CP}^{N_{coll}}$ are examined, shown in Figures 6-11 and 6-13. In relation to the most peripheral bin, the spectra scale with N_{part} at all p_T, to within 25%. This scaling is most consistent for low p_T and $p_T > 3$ GeV/c. To see this more clearly $R_{CP}^{N_{part}}$ for six different p_T values has been plotted versus N_{part}, as shown in Figure 6-12. The dashed curve shows where the points would be for N_{coll} scaling, and the solid line at unity is N_{part} scaling. The data are more consistent with N_{part} scaling, especially at higher p_T. As can be seen by comparing $R_{CP}^{N_{part}}$ and $R_{CP}^{N_{coll}}$, there is no universal approximate scaling for N_{coll} as there is for N_{part}.

Similar results have been published from the other heavy ion experiments at RHIC. Figure 6-19 shows some comparisons between the STAR [51] and PHENIX [52] data

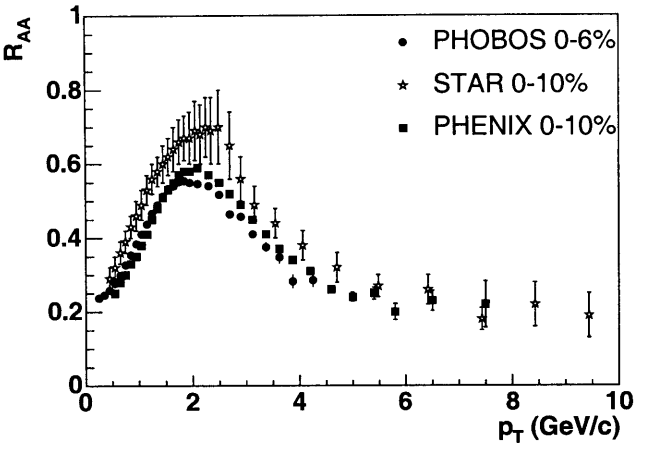

Figure 6-19: Comparison between the central R_{AA} between PHOBOS, STAR, and PHENIX. The STAR and PHENIX data are the centrality bin $0-10\%$. Systematic errors have been removed for clarity. The STAR data are from [51] and the PHENIX data are from [52].

and the PHOBOS data. The PHOBOS data is consistent with that from STAR and PHENIX. The STAR and PHENIX data extend to higher p_T values than the PHOBOS data. However, even past the maximum PHOBOS p_T value of 4.5 GeV/c, their R_{AA} data flatten out at values consistent with N_{part} scaling, to within $\sim 15-20\%$. For this reason, the N_{part} scaling with respect to our most peripheral bin does not appear to be an accident of our particular cutoff value in p_T.

Studying the high p_T spectra can give information of the state of matter created in the collision of the nuclei. Since the leading partons for jet formation are expected to have a high energy loss (quenched), these particles were thought to be a good "hard probe" into the state of the partons very early in the evolution of the system, before hadronization if indeed the partons become deconfined.

The spectra results shown in this thesis show that there is a suppression past $p_T \sim 2$ GeV/c, compared to $p+\bar{p}$ collisions, as predicted by jet quenching theory [30]. This is, however, not the only explanation, and whether or not this suppression is caused by jet quenching in a deconfined medium is not a trivial conclusion. By examining these data and comparing with recent theoretical studies further constraints can be placed on both the mechanism of this energy loss and the magnitude of it. This, in turn, can shed light on the energy density of the medium created in the heavy ion

collision.

Theoretical models have been studied using different magnitudes of energy loss. Salgado and Wiedemann [53] start with the probability that a parton will lose a fraction of its energy ΔE due to interactions with deconfined partons in the medium. The method of this energy loss is gluon radiation, which involves the processes $q \rightarrow qg$ and $g \rightarrow gg$. This is also known as gluon Bremstrahlung radiation, as discussed in [30]. This probability for energy loss is $P(\Delta E)$, which is also called the *quenching weight.* The probability for these multiple scatterings is dependent on the medium the partons traverse, and therefore the effects of these medium-induced energy losses can give information about the medium itself.

The calculations of the quenching weights have been carried out in two approximations: the multiple soft scattering approximation (which produces a Brownian motion for p_T) and the single hard scattering approximation. In the first case the effect of the medium induced energy loss comes from many interactions of the leading parton, with the energy loss from each single interaction being small. In the second case the energy loss comes from a single interaction with the medium and a large energy loss. The multiple scattering energy loss approximation is known as the BDMPS [54] model and the single hard scattering model is known as the GLV [55] model. The effect of the medium on the induced transverse momentum of the particle is characterized with the *transport coefficient* $\hat{q}$:

$$\hat{q} = \langle q_T^2 \rangle / \lambda \tag{6.11}$$

where λ is the path length of the particle in the medium. The transport coefficient of the medium depends on the energy density of the medium: $\hat{q} = c\epsilon^{3/4}$ [56], with c being a constant to be determined. One of the goals is to use the energy loss in the spectrum to determine the transport coefficient, which in turn can give information on the energy density of the medium produced in the collision.

In the multiple soft scattering case the radiated gluon spectrum depends on characteristic gluon frequency:

$$\omega_c = \frac{1}{2}\hat{q}L^2 \tag{6.12}$$

and the dimensionless parameter R:

$$R = \omega_c L \tag{6.13}$$

L in these equations is the path length the hard parton traverses in the medium. In the single hard scattering approximation there are similar parameters:

$$\bar{\omega}_c = \frac{1}{2}\mu^2 L^2 \tag{6.14}$$

and

$$\bar{R} = \bar{\omega}_c L \tag{6.15}$$

where μ is the transverse momentum acquired by the parton after the single hard interaction. In this model the energy loss by the single scattering is modeled after a Yukawa potential with an additional Debye scattering due to the high color density.

It is shown in [53] that within theoretical uncertainties both approximations lead to similar results for the resulting energy loss for both approximations.

Calculations done with the quenching weights have been carried out and used to calculate R_{AA} for RHIC energies [57]. In those calculations the multiple soft scattering approximation was used since the two approximations produce similar numerical results. In addition, the condition that there is also a finite probability that the parton can escape the medium with no interactions is included. The probability for the leading parton to lose energy ΔE then becomes:

$$P(\Delta E/\omega_c, R) = p_0(R)\delta(\Delta E/\omega_c) + p(\Delta E/\omega_c, R) \tag{6.16}$$

This includes both the discrete term (the first term, which corresponds to the probability of the leading parton escaping with no energy loss), and the continuous term (the second term, which corresponds to the probability to lose and energy ΔE due

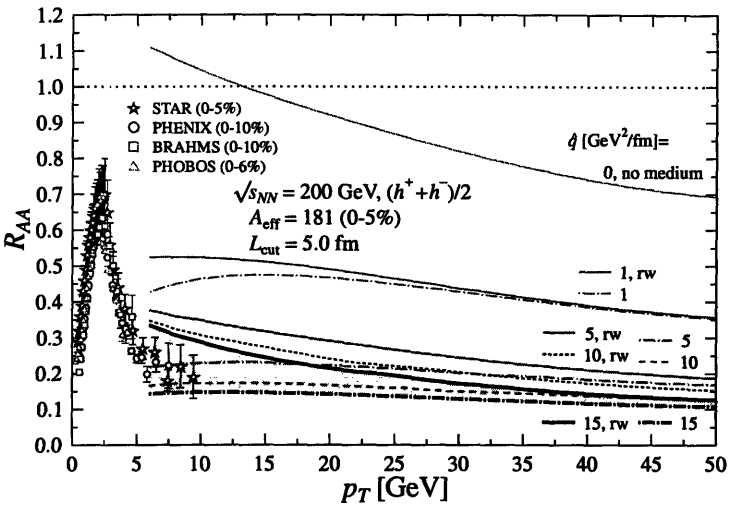

Figure 6-20: Results from the theoretical calculations in [53, 57]. This shows the nuclear modification factor R_{AA} for different quenching weights $\hat{q}$. See the text for a discussion of the different curves.

to the interactions within the medium). The calculations for R_{AA} were carried out using factorized leading order (LO) pQCD, no initial p_T of the leading parton, and N_{part} from the Glauber model. The results are shown in Figure 6-20 along with the PHOBOS data and data from STAR, BRAHMS, and PHENIX. Although the model here starts at $p_T \sim 5$ GeV/c and the PHOBOS data only extends to 4.5 GeV/c, it can still be used as a valid comparison. Results from other experiments show that R_AA flattens out at a p_T value around 4-5 GeV/c.

From Figure 6-20, it is evident that constraints can be placed on the possible values of $\hat{q}$. The different curves show the different values for $\hat{q}$, as labeled in the figure. There are also sets of curves for the normal calculation and the reweighted, or rw calculations. The "normal" calculations are done in the very high initial energy limit for the colliding partons. The rw calculations have kinematic cuts that exclude the possibility of the final energy of the partons being greater than the initial collision energy. The data shows that the model favors $\hat{q}$ between 5 and 15 GeV^2/fm. These values can then be used to extract the proportionality factor of the transport coefficient and the energy density. Calculations have suggested that the energy density at time τ_0

can be as large as $\sim$ 100 GeV/fm^3 [58], from the pQCD+saturation+hydrodynamic model, and the proportionality factor c between $\hat{q}$ and ϵ is then about 4-5 times larger than predicted from perturbative estimates.

Since the leading partons lose a significant fraction of their energy when traversing the medium, it follows that the high p_T particles that are observed in the spectra most likely did not originate from the central regions of the extended medium produced in the collision. Most of these observed high p_T particles are thought to have formed near the surface of the system, thereby having a small path length L through the medium. The analysis of the energy loss with the quenching weights from [53] and [57] supports this idea. The nuclear modification factor R_{AA} was calculated at a fixed $\hat{q} = 10$ GeV^2/fm for different path lengths L, ranging from 3 fm to 6 fm. The results and the data are shown in Figure 6-21. The two sets again show the reweighted and non-reweighted calculations. All four calculations are still in relative reasonable agreement with the PHOBOS data, and in fact change very little with a factor two difference in L. This indicates that particles with a path length greater than 3 fm (compared to an average path length of 5-6 fm) give very little contribution, which means that the high p_T particles observed in the data have short path lengths. The interpretation of this is that they originate on or near the surface, or from the skin, of the medium. This is known as *surface emission.* It should be noted that this is a bit of a misnomer, as the origin of the particles is not strictly the surface, but rather a thin skin surrounding the system.

This approximate surface emission scenario can be understood in very simple terms by examining the expected scaling behavior and the relation between N_{part} and N_{coll}. The spectra at high p_T is expected to scale with N_{coll}, and Glauber studies show that N_{coll} scales approximately with $N_{part}^{4/3}$. Furthermore, the number of participants scales with the volume of the nucleus, or N_{part} (proportional to R^3). Substituting in R for N_{part} the yield is seen to be proportional to R^4. Now, if we assume that the yield at high p_T comes from the surface, or a thin skin at the surface, the density of particles drops from a volume dependence to a surface dependence, meaning a reduction by one power of R. Thus, the yield becomes proportional to R^3, or N_{part}.

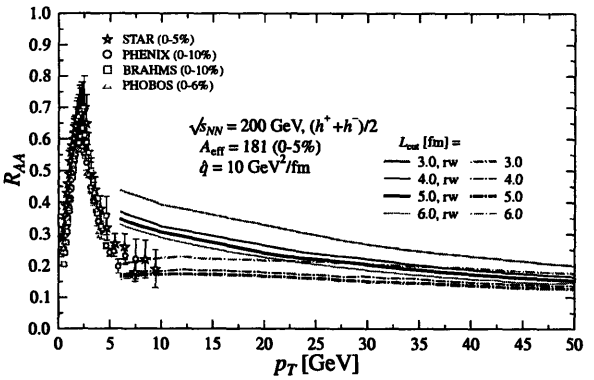

Figure 6-21: Results from the theoretical calculation in [53, 57]. This shows the nuclear modification factor R_{AA} for a quenching weight of $\hat{q} = 10\text{GeV}^2/\text{fm}$ for different path lengths L from 3 to 6 fm.

This scaling behavior is seen in the PHOBOS data at low and high (> 4 GeV/c) p_T, as seen in Figure 6-12.

The above discussion is admittedly very approximate. A more detailed analysis, including more realistic geometrical considerations, has been carried out [59]. In this calculation, the momentum loss of the leading partons is assumed to have the form

$$\Delta p_T = \eta p_T^{\mu} L \tag{6.17}$$

where L is the length of the medium traversed and μ is a scaling exponent. The system shape is assumed to be cylindrical. The quenched spectrum and the non-quenched spectrum are related thus:

$$\frac{dN_q}{d^2p_T} = Q(p_T)\frac{dN}{d^2p_T} \tag{6.18}$$

where $Q(p_T)$ is the quenching factor. If the spectrum is assumed to have a power law form:

$$\frac{dN}{d^2p_T} = A(1 + p_T/p_0)^{-n} \tag{6.19}$$

The quenching factor is then found to be:

$$Q(p_T) = \frac{2(p_0 + p_T)}{\pi R \eta (n-1) p_T^{\mu}} \tag{6.20}$$

Again, this quenching factor reduces the R dependence of the spectra by one power of R, from a volume to a surface dependence.

The p_T and centrality dependencies of the suppression in the spectra can also be used to shed light on the rate of the energy loss in the medium. While pQCD predicts that a given parton will lose energy proportional to the square of the path length [60], this is actually not the quantity that needs to be considered when studying the suppression of the spectra. The important quantity here is how the average energy loss relates to all partons with a given p_T (i.e. how the energy loss of a given bin in the spectra is affected by the medium). There are several predictions for how the energy loss scales with path length and density, three of which were numerically studied in [59]. They are:

$$\Delta p_T = \eta L_{eff} \sqrt{\rho p_T / \nu} \tag{6.21}$$

$$\Delta p_T = \eta p_T (L\rho)_{eff} \tag{6.22}$$

$$\Delta p_T = \eta p_T \sqrt{(L\rho)_{eff}} \tag{6.23}$$

The first is called BDMS, the second BH (Bethe-Heitler), and the third RW.

The results of these models are shown in Figure 6-22, which shows the expected $R_{AA}^{N_{part}}$ for the different models. Only the RW model, which exhibits a scaling of $(L\rho)^{1/2}$, shows a flat dependence of $R_{AA}^{N_{part}}$ as a function of N_{part}. This flat scaling behavior is indeed seen in the PHOBOS data in Figure 6-12, and is an expected consequence of surface emission of jets.

As mentioned earlier, there are nuclear effects that are expected to effect the spectra in heavy ion collisions. Although these effects are more evident in d+Au collisions (the Cronin effect, for example), they are also expected to be present in

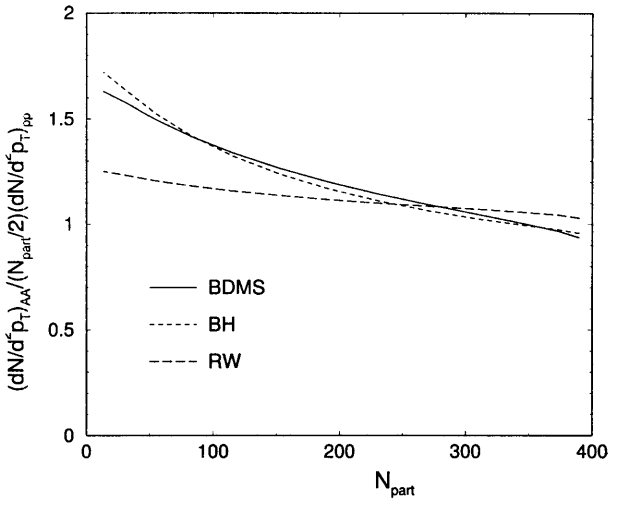

Figure 6-22: Results from the theoretical calculation in [59]. RW shows an approximate N_{part} scaling of the nuclear modification factor that is consistent with surface emission of jets due to jet quenching in a deconfined medium

Au+Au collisions as well. Their effects, however, are likely to be at least partially masked by jet quenching effects. Theoretical studies have been carried out that include not only the medium induced parton energy loss, but also nuclear effects which have the largest impact at intermediate p_T. Wang [61] has developed a model that includes this jet quenching as well as initial p_T broadening (the Cronin effect) and nuclear shadowing. Thus, the effects of the final state induced radiative energy loss as well as the interactions of hadrons with other hadrons before freezout is reached are included in the calculation. These calculations were done in the framework of LO pQCD. The nuclear distribution model used here is the hard sphere model, and the initial p_T of the partons is assumed to be Gaussian. The energy loss, from numerical results [62], is taken to be

$$\langle \frac{dE}{dl} \rangle_{1d} = \epsilon_0 (E/\mu_0 - 1.6)^{1.2}/(7.5 + E/\mu_0) \tag{6.24}$$

The data is shown with the results of this theoretical calculation in Figure 6-23. The parameters that have been fit are $\mu_0 = 1.5$ GeV and $\epsilon_0 = 1.07$ GeV/fm for the HIJING parameterization and $\mu_0 = 1.3$ GeV and $\epsilon_0 = 1.09$ GeV/fm for the EKS parameterization. These values were fit to the STAR data. A 10 GeV quark will

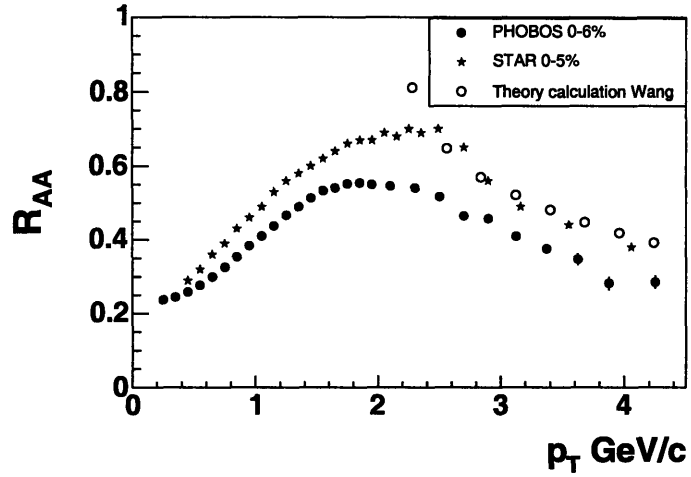

Figure 6-23: R_{AA} fit to the STAR data and shown with the PHOBOS data with several predictions included: pQCD, shadowing, the Cronin effect, and jet quenching.

have an average energy loss of 0.85 ± 0.25 GeV/fm traversing the medium.

Wang also argues that the observed hadron suppression cannot be due to nuclear absorption because of the uncertainty principle [63]. Theoretical calculations show the gluon density to be $\sim$ 30 times the gluon density in nuclear matter, and the energy density to be $\sim$ 100 times the energy density of cold nuclear matter, and under these conditions cold hadronic matter cannot exist. By the uncertainty principle, the formation time of a hadron with size R, energy E, and mass m is given by:

$$\tau \sim R\frac{E}{m} \tag{6.25}$$

A 5 GeV pion with radius 0.5 - 1.0 fm will have, for example, a formation time τ of 17 - 35 fm/c. This is far too large for the pion to form within the deconfined region. This order of magnitude value for the formation time precludes the possibility of partons hadronizing within the medium and then losing energy through nuclear absorption.

The effect of jet quenching was not the only explanation to account for the energy loss at high p_T that has been observed. Another possibility was that it is caused by the initial state effect of parton saturation [35]. The parton saturation model was successful in predicting the multiplicity at midrapidity in the 200 GeV data from RHIC [64]. This model was also used to explain the N_{part} scaling of the Au+Au

spectra with respect to peripheral collisions, which is due to the effects of the Color Glass Condensate. The N_{part} scaling was predicted to extend to a p_T of 6 GeV/c, much higher than a p_T of 2 GeV/c predicted from the pQCD crossover from soft to hard processes. Although this p_T value is beyond the range of the PHOBOS data, the data from STAR and PHENIX are more consistent with continued N_{part} scaling past a p_T of 6 GeV/c. Figure 6-24 shows the predictions of this model at 130 and 200 GeV/c beam energy, which corresponds to Figure 6-12 for the PHOBOS data. Although approximations were made in this model, the same general features are observed: N_{coll} scaling is highly violated, as the yields do not even remotely follow the solid lines, which represent N_{coll} scaling, and the yields are more consistent with N_{part} scaling, although the agreement is only approximate.

The d+Au run at RHIC is pivotal in disentangling these effects and models in the Au+Au data. The collision area is much smaller in the d+Au collisions, and it is not expected to provide an environment that would cause jet quenching. Also, the effects of parton saturation that were used to explain the features of the Au+Au spectra discussed above also lead to predictions for the d+Au spectra. These predictions can be used to test which models are consistent with both sets of data.

In Au+Au collisions there is an obvious turnover in R_{AA} at around 2 GeV/c. This effect is absent in the d+Au data. The PHOBOS d+Au data show that R_{dAu} reaches a maximum value between 2 and 3 GeV/c of unity for all centralities. While at first this may seem like N_{coll} scaling holds for d+Au collisions, the next section will explore this more. In fact, it seems to be an accident for these data. Due to the Cronin effect, an enhancement in R_{dAu} is expected at high p_T.

The other RHIC experiments performed similar measurements, and all four published their findings in the same journal [65, 66, 67]. All experiments show a lack of suppression at high p_T, and instead the spectra show an enhancement at high p_T. The results from the STAR and PHENIX collaborations with the PHOBOS data are shown in Figure 6-25.

Figure 6-16 shows the evolution of R_{dAu} with centrality more clearly. At $p_T = 4$ GeV/c there is a slight rise (with the errors it could also be interpreted as flat). The

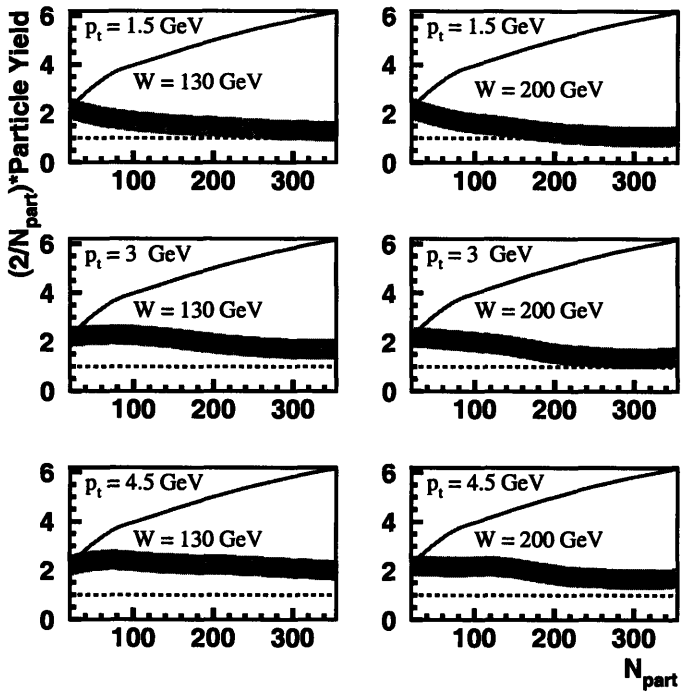

Figure 6-24: Predictions of $R_{CP}^{N_{part}}$ for 130 and 200 GeV beam energy for three different values of p_T. The gray bands show the predicted yields, and the solid lines show the expected yields from N_{coll} scaling.

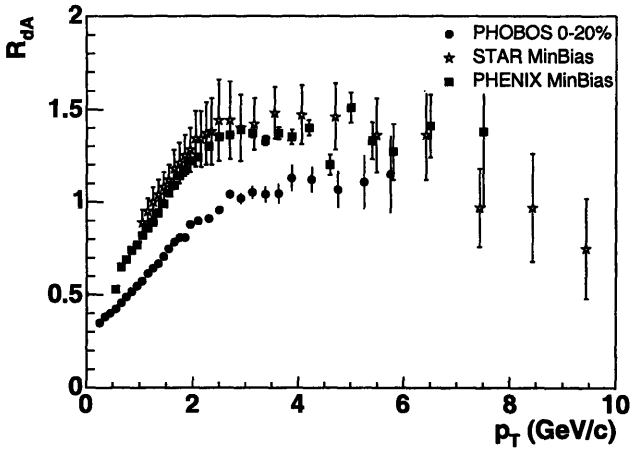

Figure 6-25: Results for R_{dAu} for PHOOBS, STAR [65], and PHENIX [66] data. The STAR and PHENIX data are MinBias, and the PHOBOS data are in the centrality bin $0-20\%$. Also, the STAR and PHENIX data are at midrapidity while the PHOBOS data are centered at $\eta = 0.8$. Errors shown are only statistical for clarity.

parton saturation model predicts a suppression in R_{dAu} as the centrality increases, similar to Au+Au data [36]. In particular, if the suppression effects that lead to N_{part} scaling in the Au+Au spectra are in fact present, then the d+Au spectra is expected to scale as $(N_{part})^{-1/2}$. The saturation effects are not expected to set in until N_{part} is about 6. This corresponds roughly to the $40-70\%$ bin in the PHOBOS data. Thus, from bin 2 to the most central bin there would be a suppression of about $(6/15.5)^{-1/2}$ $= 38\%$. This can be most clearly seen in Figure 6-16, where there is about a 10% rise from bin 2 to the most central bin at $p_T = 4$ GeV/c, which is inconsistent with the predictions from the parton saturation model. Calculations from perturbative QCD predict a Cronin enhancement (resulting from a broadening of the p_T distribution of particles from interactions in the nuclear medium) of 10% when going from peripheral to central collisions [68]. This prediction is consistent with the PHOBOS data. This indicates that the suppression seen in Au+Au collisions is indeed due to the final state interactions, and not initial state effects

By studying the d+Au data, the best explanation for the suppression in the high p_T spectra in Au+Au collisions is that it is caused by the final state effect of interactions with the dense, deconfined medium created by the collision. Further results published by the STAR collaboration give further support to this conclusion. Along

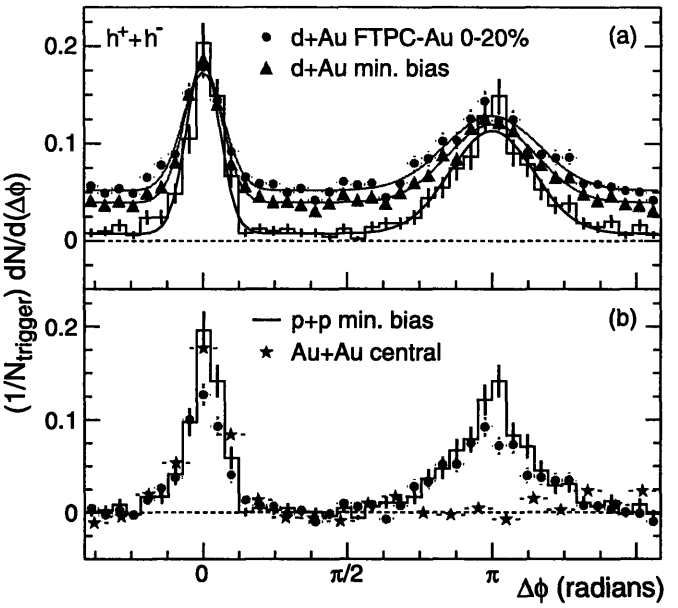

Figure 6-26: Back to back correlations from the STAR collaboration.

with the d+Au spectra from STAR [65], they showed data from back to back jets, Figure 6-26. In these data, the trigger is a high p_T particle with $4 < p_T^{trig} < 6$ GeV/c. These trigger particles are plotted, with the angular difference between the trigger particle and all other particles in the event with $2 < p_T^{trig}$ GeV/c. The p+p data and the d+Au data both show the trigger jet and the corresponding back to back jet in the opposite direction. In the Au+Au data, however, the back to back jet is missing (meaning that there are no particles with a $p_T > 2$ GeV/c in the opposite direction as the trigger jet). This is consistent with the hypothesis of jets being quenched in the final state medium. If a jet is to be detected, then it would have to be created by a hard collision at or near the surface of the medium. In this way, the jet escapes the deconfined medium since its path length through it is minimal at best. The other jet, however, has to traverse the entire distance of the medium to be detected, and hence will have a maximal energy loss.

6.6 Pseudorapidity Dependence of the Spectra

6.6.1 d+Au Versus η Results

Motivated by theoretical work on parton saturation and the CGC, the d+Au spectra has been divided into three η bins, and the R_{dAu} factor is shown for each η bin. These nuclear modification factors are shown in Figure 6-27 [69]. To study the evolution with η of these factors, their values at four different p_T values of 2, 2.6, 3.2, and 3.8 have been plotted versus η, which is shown in Figure 6-28. To decrease the statistical fluctuations in the data, functions were fit to the data in Figure 6-27, and the values of these functions are used as the points in Figure 6-28. The error bars in Figure 6-28 shown the point-to-point systematic error, while the gray band shows the common systematic error between the points.

For these data, the systematic errors shown in Figure 6-28 were calculated differently. Error functions were again used for each correction function, however, these were divided into two groups: errors that are dependent on η and those that are independent of η. The reason for this is that errors that are independent on η will just introduce an overall scale factor. For this plot it is important to know how much the points at each p_T differ from each other, and thus it is important to separate overall scale errors from point to point errors. The errors that are uncorrelated are from the errors in N_{coll}, the UA1 correction function, and the acceptance and efficiency correction. The correlated point to point errors are from the errors in the momentum resolution, the feeddown and secondaries correction, the dead channel correction, and the error from the uncertainty in the two spectrometer arms.

The SpecTof triggered data were omitted in this analysis due to the difference in acceptance of the ToF walls (see Figures 4-6 and 4-7). The phase space acceptance of the ToF walls has a strong p_T and η dependence, and dividing the spectra into the three η bins completely excludes a range of p_T values in each bin. The remaining data were averaged over centrality (weighting each centrality bin's N_{coll} value with the number of events in each bin). This is not strictly a min-bias data set due to the inclusion of the dAVertex triggered data. The average centrality for these data are

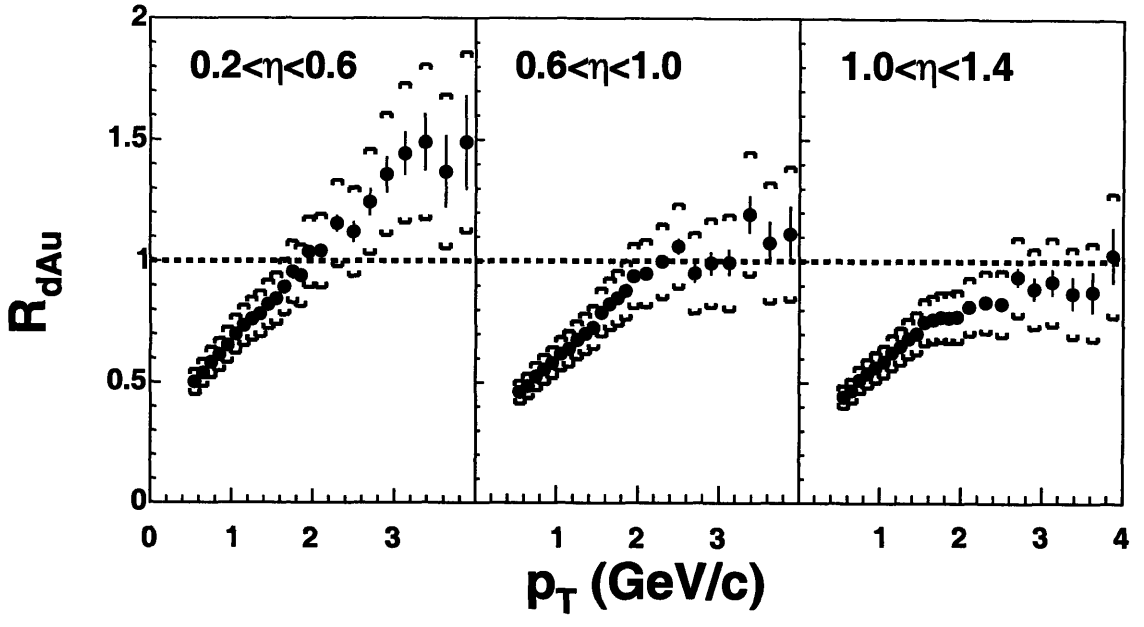

Figure 6-27: Nuclear modification factor R_{dAu} versus p_T for the three η bins, $0.2 < \eta < 0.6$, $0.6 < \eta < 1.0$, $1.0 < \eta < 1.4$.

$\langle N_{coll} \rangle = 9.5 \pm 0.8$.

6.6.2 d+Au Versus η Discussion

As can be seen in Figure 6-15, the PHOBOS results do not seem entirely consistent with the other experiments. R_{dAu} in PHOBOS flattens out at a value consistent with expectations based on binary collision scaling for all centralities, while the other experiments show a value between 1.3 and 1.5 for their min-bias data as seen in Figure 6-25.

Recent theoretical work on parton saturation and the Color Glass Condensate (CGC) predicts that at high pseudorapidities in the deuteron direction there will be a suppression in R_{dAu} relative to midrapidity. Since STAR's data is in the range $|\eta| < 0.5$, PHENIX's in the range $|0.35| < \eta$ and BRAHMS' is centered at $\eta = 0$, they all are at midrapidity, while PHOBOS has an average η of 0.8.

The fact that the CGC model failed to predict a suppression in the d+Au data does not mean that the model is invalid. These η dependent data are consistent with

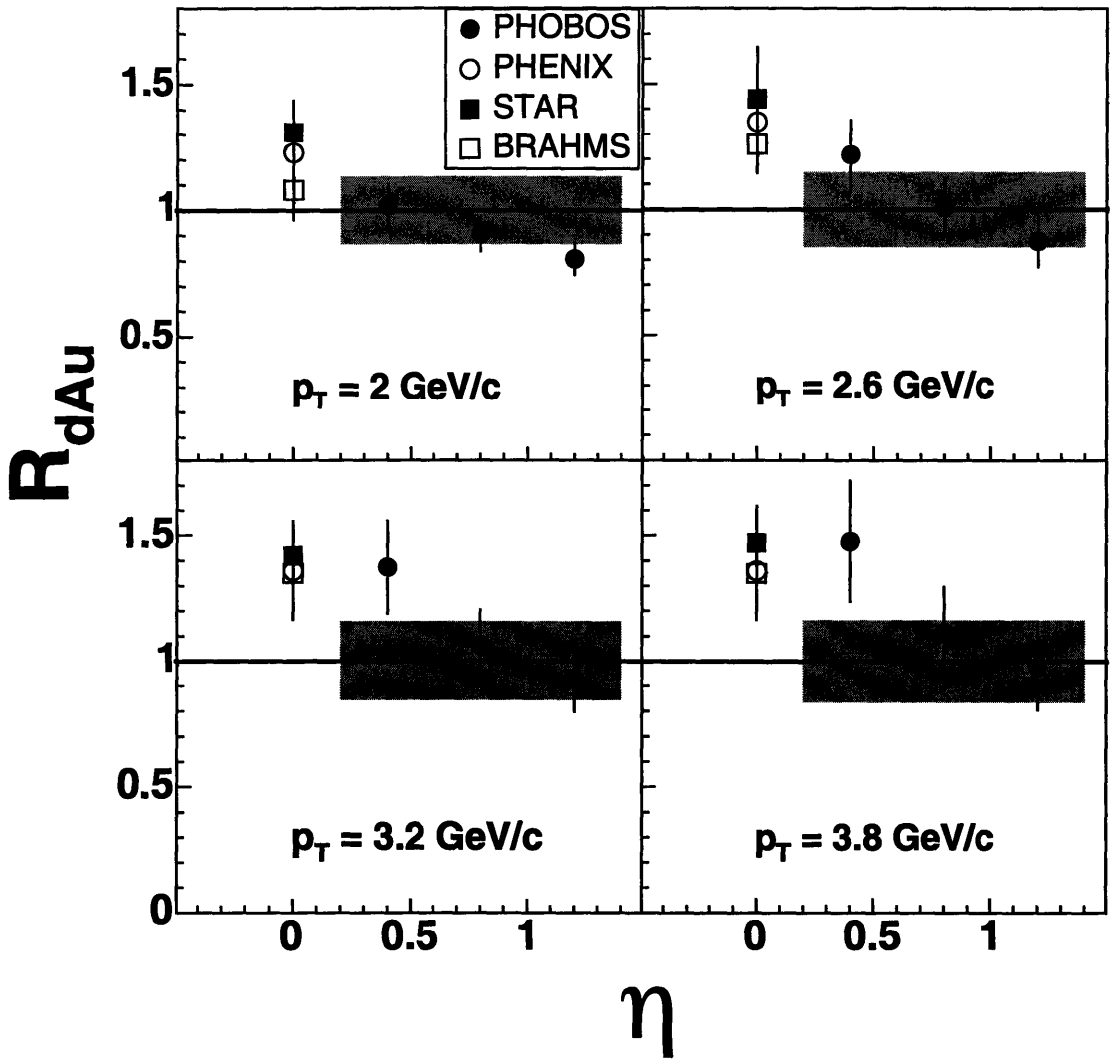

Figure 6-28: Nuclear modification factor R_{dAu} versus η at four different p_T values. Included are the mid-rapidity values from the STAR, PHENIX, and BRAHMS experiments.

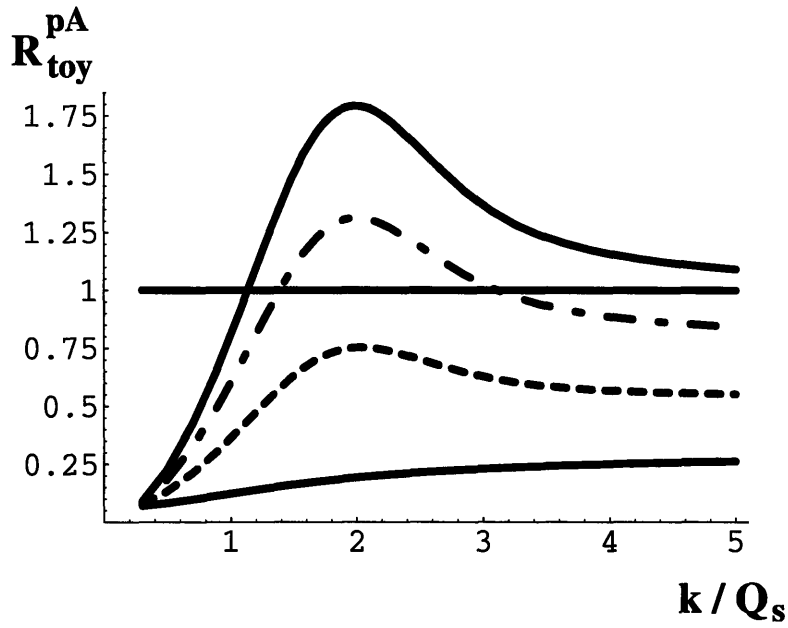

Figure 6-29: Qualitative results from [36] showing the predicted evolution of R_{dAu} vs p_T (with Q_s being the saturation scale) as rapidity increases in the deuteron direction. This shows a decrease in R_{dAu} as the rapidity increases. This decrease is seen in the PHOBOS data.

the predictions of the CGC [36], and show a systematic suppression as η increases. Figure 6-29 shows some theoretical calculations for how R_{pA} evolves with increasing rapidity. The top curve is from the parton saturation model from McLerran and Venugopalan [25], [26]. The bottom solid curve is at high rapidities incorporating suppression from saturation [36]. The middle dashed curves are for intermediate rapidities, and are for illustrative purposes only to show the evolution. Qualitatively, the PHOBOS data, and the BRAHMS data (from [70]), agree with these calculations. Both show a decrease in R_{dAu} at all p_T as η increases.

Other explanations have been offered as the cause of the suppression in R_{dAu} versus η. Capella et. al. [71] argue that energy and momentum conservation from low p_T effects in string models will lead to a suppression in R_{dAu} of about 30% from $\eta^* = 0$ to $\eta^* = 3.2$. This alone is not enough to account for the suppression seen in the PHOBOS data, which extend to a smaller η and show a higher suppression than predicted. However, Capella et. al. also argue that there should be a decrease in the shadowing corrections as η increases in the deuteron fragmentation region.

They again estimate a suppression of 30% in R_{dAu} from $\eta^* = 0$ to $\eta^* = 3.2$. These two results together could explain the PHOBOS data and the results published from BRAHMS. However, since the PHOBOS data extend to $\eta = 1.4$, extrapolation would be necessary to make a quantitative comparison.

Another similar explanation can be found in [72]. Kopeliovich et.al. argue that this suppression can be understood in the simple terms of conservation of energy. They argue that the production of a particle with a high Feynman x, x_F, "does not leave energy for producing anything else". A particle produced at these high η values will, due to this conservation of energy, produce a large rapidity gap (LRG), where no other particles will be produced. The size of this rapidity gap is given by:

$$\Delta y = -\ln(1 - x_F) \tag{6.26}$$

This effect reproduces the BRAHMS results at $\eta = 3.2$ fairly well. Furthermore, this effect appears to be universal, and has been observed in all systems, including the Drell-Yan cross section, J/Ψ production, and heavy charm production, to name a few. Including this conservation of energy effect does not leave room for other effects, such as that from the CGC.

Figure 6-30 shows a prediction of R_{dAu} for mid rapidity and a rapidity of +3 (in the deuteron direction) [68]. These predict the rapidity effects of the Cronin p_T broadening effect, and include results for both shadowing and without shadowing. The theory shows a shift in the Cronin peak from a p_T of about 3.5 GeV/c at midrapidity to about 4.5 GeV/c. The value of R_{dAu} rises by an order of 10% in going out to high rapidity. The PHOBOS data clearly show there is no rise in R_{dAu} in going to forward rapidity, which implies that there is a mechanism working against the enhancement in the yield due to nuclear medium effects at high rapidity.

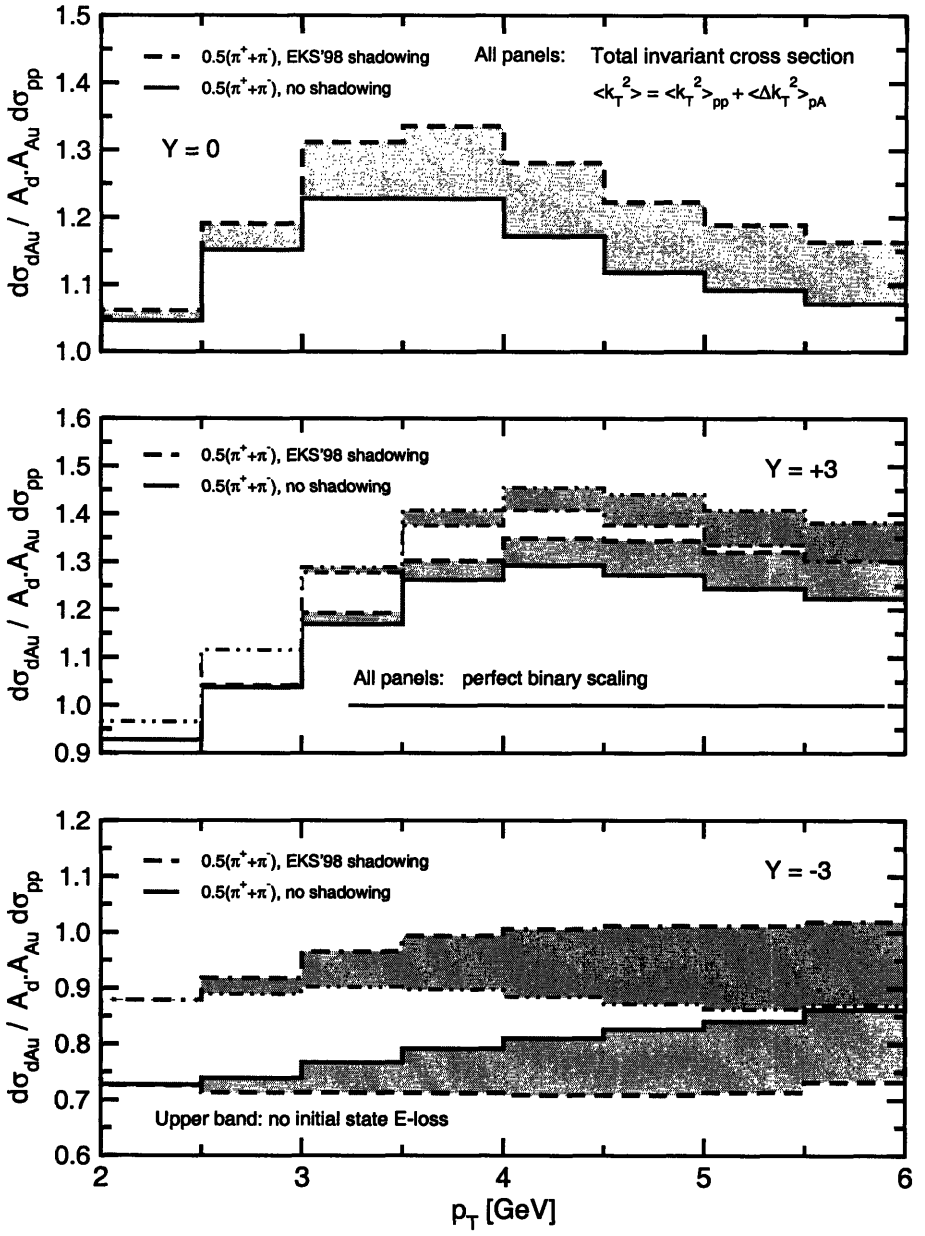

Figure 6-30: Theoretical calculations for the change in R_{dAu} versus rapidity from effects of the nuclear medium only.

Chapter 7

Conclusions

This thesis presents measurements of the transverse momentum spectra of unidentified charged hadrons at a center of mass energy of $\sqrt{s_{NN}} = 200$ GeV for Au+Au and d+Au collisions at the Relativistic Heavy Ion Collider. The data was collected with the PHOBOS detector at two runs from RHIC in 2001 and 2003.

The spectra measured were compared to $p + \bar{p}$ collisions collected from the UA1 experiment. The particle production at high momentum ($p_T \sim> 2$ GeV/c) is expected to scale with the number of binary collisions N_{coll} in heavy ion collisions. The Au+Au spectra presented here show a clear suppression in the nuclear modification factor R_{AA} by a factor of 4 - 5 at high p_T. This result was predicted if the heavy ion collisions produce a deconfined state of quarks and gluons. The PHOBOS data show that the yield at high p_T scales approximately with the number of participants N_{part} as a function of centrality.

This N_{part} scaling result led to a theory that the suppression was caused by the initial state effect of the Color Glass Condensate. The CGC model predicts a high density saturation of gluons in the nuclei before the collision, and this saturation could lead to the N_{part} scaling seen in the PHOBOS data.

To disentangle the effects of the final state QGP and initial state CGC RHIC, in the 2003 run, collided deuterons with gold ions. The d+Au collisions are not thought to produce a QGP due to the much smaller system size. The same work that explained the N_{part} scaling with the CGC model also predicted a suppression in

the nuclear modification factor R_{dA} as the centrality of the collision increases. The results for R_{dA} presented here do not show the expected decrease of $\sim$ 38%, and instead reach a value consistent with expectations based on binary collision scaling for all centralities. These results from Au+Au and d+Au lead to the conclusion that a deconfined state of quarks and gluons is created in Au+Au collisions at the energy of 200 GeV per nucleon.

Another model [53] that uses gluon radiation in a QGP as the mechanism for suppression has been compared to the PHOBOS data, and is consistent with the results in this thesis. Given an average path length of 6 fm for a particle traversing the medium, the data shows that the quenching weight factor $\hat{q}$ is between 5 and 15 GeV^2/fm. Further studies with this model shows that R_{AA} is rather insensitive to the path length L, and for values of L between 3 and 6 fm there is little difference. The interpretation of this result is that the high p_T particles that are observed originate from a thin skin on the outside of the system produced in the collision. This surface emission of particles will lead to N_{part} scaling, which can also be understood from geometrical arguments [59].

The d+Au data do not show a suppression of R_{dA}. However, since a QGP is not thought be form here, the data could exhibit the effects of the CGC. The CGC was predicted to cause a suppression in R_{dA} as η increases in the deuteron fragmentation region. The PHOBOS spectra from the d+Au run were divided into three η bins. At the highest p_T, R_{dA} is seen to decrease from about 1.5 to about 1 as η increases. This decrease is also seen in the BRAHMS data, and is consistent with the predictions of the CGC. However, more work needs to be done to quantify the agreement between data and theory. Other physically simpler models, such as conservation of energy, also reproduce this effect.

The results of p_T spectra from RHIC have provided much information and insight to the state of matter created at high energies and densities. Further information can be gained by studying how the suppression evolves as a function of energy. Results from different energies and species type from RHIC, and the impending LHC data will be very important in putting these results into the bigger picture.

Acknowledgements

There are many people who helped me and guided me in the process of completing this thesis.

First I would like to thank my advisor Gunther Roland. He led me through the analysis for this thesis, and his knowledge and instincts in physics were crucial. It is difficult to overstate how much I have learned while working under Gunther. Bolek Wyslouch was on my thesis committee, and discussions with him were very helpful. Krishna Rajagopal was also on my committee, and his thorough reading of the theory material were crucial in completing this thesis.

There were many people at MIT that I worked with and helped me along the way. Wit Busza led PHOBOS through most of my time in the group. His ability to pose perplexing physics questions helped prepare me for exams, and let me realize how much physics I really did not know. George Stephans worked with me on the spectra, and his attention to detail made me confident in our results.

Christof Roland did a tremendous amount of work on the spectra and advised and guided me along the way. He also helped me keep my sanity when things got rough. It will be hard to forget the Mastic Beach pub crawl. Gerrit van Nieuwenhuizen was on several spectra committees. I learned a lot from working with Gerrit, both physics and hardware issues.

Mark Baker served as both project manager and spokesman of the PHOBOS group. He was a big help in understanding physics ideas, and as a member of one of my committees greatly helped in finalizing the analysis. Peter Steinberg also served as project manager and showed me how much work one person can actually get done in a 24 hour day. Burt Holzman also served on one of my committees, and was

always around to bail me out of a computer crisis. The UIC crew was instrumental in this analysis. Without their extremely hard work there would be no trigger and no centrality determination.

The MIT students before me, Patrick Decowski, Pradeep Sarin, Kris Gulbrandsen, and Carla Vale, were all great friends and colleagues. Their help and guidance during my early years at MIT was instrumental in my education. Conor Henderson, Corey Reed, and I worked closely on many things, from classwork, to studying for exams, and analysis projects. They were also great roommates and friends. A lot of their own work has gone into this thesis. Gabor Veres was a postdoc that came to PHOBOS. His influence on the group, and on my research, was tremendous due to his knowledge of physics and work ethic.

There are many more people in PHOBOS that helped me along and were great friends. So to all of you, thank you.

In addition to my colleages in PHOOBS there are many other friends I'd like to thank. They kept me sane over the years, and provided a life outside of work. In particular, at MIT I'd like to thank the THDA for this. You know who you are.

Lastly, I'd like to thank my parents Jeff and Sue, and my sister Sandy. They in particular supported me during the long road to my degree, and without their endless moral support I'm not sure I would have made it. Whenever things got rough I could always count on them to listen and help me through. Thank you.

Appendix A

Tables of Data A

A.1 Au+Au Invariant Yields

A.2 R_{AA} Data

A.3 $R_{AA}^{N_{part}}$ Data

p_T	Invariant yield	Error up	Error down
0.250	64.594711	5.47673	8.46639
0.350	37.452461	3.10232	4.80418
0.450	22.232103	1.80157	2.79430
0.550	13.886354	1.10238	1.71230
0.650	8.861903	0.69028	1.07351
0.750	5.853603	0.44754	0.69725
0.850	3.928222	0.29557	0.46095
0.950	2.694828	0.19991	0.31201
1.050	1.862970	0.13652	0.21318
1.150	1.291663	0.09371	0.14635
1.250	0.926603	0.06669	0.10413
1.350	0.652656	0.04673	0.07290
1.450	0.469772	0.03354	0.05226
1.550	0.329894	0.02357	0.03664
1.650	0.241710	0.01733	0.02685
1.750	0.179988	0.01298	0.02005
1.850	0.129192	0.00942	0.01447
1.950	0.093832	0.00695	0.01060
2.100	0.060855	0.00449	0.00689
2.300	0.033414	0.00257	0.00389
2.500	0.018814	0.00153	0.00227
2.700	0.010365	0.00091	0.00132
2.900	0.006052	0.00058	0.00082
3.125	0.003454	0.00036	0.00050
3.375	0.001885	0.00023	0.00030
3.625	0.000921	0.00014	0.00017
3.875	0.000410	0.00008	0.00009
4.250	0.000269	0.00005	0.00006

Table A.1: Invariant yield from Figure 6-8, centrality bin 45-50%

p_T	Invariant yield	Error up	Error down
0.250	90.576385	7.16809	10.7099
0.350	52.756279	4.10662	6.10097
0.450	31.719557	2.43126	3.59222
0.550	19.958788	1.50808	2.21657
0.650	12.906556	0.96251	1.40769
0.750	8.523917	0.62789	0.91427
0.850	5.795758	0.42238	0.6124
0.950	3.985322	0.28773	0.4156
1.050	2.743416	0.19650	0.28286
1.150	1.958266	0.13935	0.19999
1.250	1.381826	0.09784	0.14006
1.350	0.985625	0.06955	0.09935
1.450	0.706800	0.04979	0.07100
1.550	0.514638	0.03625	0.05163
1.650	0.367780	0.02596	0.03693
1.750	0.271782	0.01925	0.02738
1.850	0.197347	0.01406	0.01999
1.950	0.146383	0.01051	0.01494
2.100	0.092737	0.00669	0.00956
2.300	0.051381	0.00380	0.00544
2.500	0.029109	0.00222	0.00319
2.700	0.017319	0.00138	0.00198
2.900	0.009475	0.00080	0.00114
3.125	0.005702	0.00050	0.00073
3.375	0.002972	0.00029	0.00041
3.625	0.001667	0.00018	0.00025
3.875	0.000830	0.00010	0.00014
4.250	0.000378	0.00005	0.00007

Table A.2: Invariant yield from Figure 6-8, centrality bin 35-45%

p_T	Invariant yield	Error up	Error down
0.250	137.504745	10.70205	15.90064
0.350	80.520576	6.17046	9.11801
0.450	48.853172	3.69021	5.42473
0.550	30.911774	2.30429	3.37082
0.650	20.094576	1.48005	2.15522
0.750	13.376117	0.97439	1.41315
0.850	9.092636	0.65608	0.94795
0.950	6.319173	0.45225	0.65128
1.050	4.404702	0.31311	0.44961
1.150	3.098040	0.21905	0.31380
1.250	2.226013	0.15679	0.22418
1.350	1.605190	0.11280	0.16106
1.450	1.140237	0.08007	0.11422
1.550	0.829811	0.05832	0.08316
1.650	0.597278	0.04209	0.06001
1.750	0.433208	0.03066	0.04373
1.850	0.316890	0.02256	0.03221
1.950	0.238056	0.01708	0.02441
2.100	0.148855	0.01077	0.01548
2.300	0.080361	0.00596	0.00860
2.500	0.046178	0.00353	0.00513
2.700	0.025733	0.00205	0.00298
2.900	0.014983	0.00125	0.00183
3.125	0.008587	0.00075	0.00111
3.375	0.004710	0.00045	0.00066
3.625	0.002433	0.00025	0.00037
3.875	0.0014027	0.00016	0.00024
4.250	0.000605	0.00008	0.00011

Table A.3: Invariant yield from Figure 6-8, centrality bin 25-35%

p_T	Invariant yield	Error up	Error down
0.250	201.868256	15.71037	23.34270
0.350	118.550262	9.08403	13.42394
0.450	72.072914	5.44361	8.00272
0.550	45.854973	3.41776	5.00002
0.650	30.071833	2.21452	3.22504
0.750	20.059315	1.46101	2.11907
0.850	13.709265	0.98900	1.42912
0.950	9.528029	0.68173	0.98187
1.050	6.659878	0.47326	0.67970
1.150	4.719450	0.33355	0.47794
1.250	3.362221	0.23668	0.33852
1.350	2.424079	0.17022	0.24313
1.450	1.745610	0.12246	0.17477
1.550	1.253631	0.08800	0.12555
1.650	0.915188	0.06438	0.09187
1.750	0.665488	0.04699	0.06711
1.850	0.480867	0.03415	0.04881
1.950	0.350510	0.02507	0.03589
2.100	0.223107	0.01610	0.02317
2.300	0.122829	0.00907	0.01312
2.500	0.066536	0.00506	0.00737
2.700	0.038006	0.00300	0.00439
2.900	0.022158	0.00182	0.00269
3.125	0.012550	0.00108	0.00161
3.375	0.006337	0.00059	0.00088
3.625	0.003606	0.00036	0.00054
3.875	0.001925	0.00022	0.00032
4.250	0.000838	0.00010	0.00015

Table A.4: Invariant yield from Figure 6-8, centrality bin 15-25%

p_T	Invariant yield	Error up	Error down
0.250	283.098663	30.52364	35.56604
0.350	166.264755	17.72722	20.48911
0.450	102.104210	10.77426	12.35802
0.550	64.900070	6.78368	7.72544
0.650	42.738888	4.42898	5.01069
0.750	28.605667	2.94138	3.30785
0.850	19.594679	2.00118	2.23849
0.950	13.598597	1.38072	1.53724
1.050	9.544915	0.96442	1.06951
1.150	6.771625	0.68155	0.75339
1.250	4.864176	0.48816	0.53830
1.350	3.465601	0.34716	0.38219
1.450	2.501448	0.25037	0.27540
1.550	1.813785	0.18159	0.19973
1.650	1.314291	0.13175	0.14503
1.750	0.944045	0.09486	0.10458
1.850	0.707797	0.07137	0.07887
1.950	0.499861	0.05064	0.05613
2.100	0.318135	0.03246	0.03620
2.300	0.173707	0.01799	0.02028
2.500	0.095376	0.01007	0.01150
2.700	0.052496	0.00568	0.00658
2.900	0.030322	0.00338	0.00397
3.125	0.017099	0.00197	0.00236
3.375	0.008333	0.00101	0.00123
3.625	0.004553	0.00059	0.00073
3.875	0.002325	0.00032	0.00041
4.250	0.001078	0.00016	0.00021

Table A.5: Invariant yield from Figure 6-8, centrality bin 6-15%

p_T	Invariant yield	Error up	Error down
0.250	377.453552	47.79411	53.23293
0.350	221.677246	27.80345	30.82030
0.450	135.237030	16.81605	18.55912
0.550	85.800011	10.58668	11.63763
0.650	56.043850	6.86828	7.52335
0.750	37.703026	4.59328	5.01589
0.850	25.705048	3.11627	3.39411
0.950	17.855005	2.15611	2.34338
1.050	12.425210	1.49604	1.62337
1.150	8.765121	1.05332	1.14174
1.250	6.285587	0.75466	0.81756
1.350	4.481295	0.53810	0.58294
1.450	3.234529	0.38884	0.42146
1.550	2.343560	0.28235	0.30635
1.650	1.674614	0.20241	0.21996
1.750	1.218688	0.14794	0.16110
1.850	0.881024	0.10753	0.11739
1.950	0.633727	0.07785	0.08524
2.100	0.396669	0.04921	0.05419
2.300	0.217717	0.02751	0.03055
2.500	0.119068	0.01539	0.01726
2.700	0.062827	0.00835	0.00946
2.900	0.037284	0.00511	0.00586
3.125	0.019411	0.00276	0.00321
3.375	0.010056	0.00151	0.00177
3.625	0.005423	0.00086	0.00103
3.875	0.002641	0.00045	0.00054
4.250	0.001296	0.00024	0.00029

Table A.6: Invariant yield from Figure 6-8, centrality bin 0-6%

p_T	R_{AA}	Statistical Error	Sys. Err.Up	Sys. Err. down
0.250	0.42706	0.00146	0.03636	0.05599
0.350	0.43528	0.00154	0.03638	0.05588
0.450	0.44643	0.00177	0.03672	0.05620
0.550	0.47134	0.00213	0.03826	0.05826
0.650	0.49752	0.00260	0.03997	0.06047
0.750	0.53246	0.00245	0.04246	0.06373
0.850	0.56792	0.00299	0.04509	0.06706
0.950	0.60825	0.00365	0.04822	0.07096
1.050	0.64564	0.00444	0.05126	0.07456
1.150	0.67676	0.00535	0.05397	0.07750
1.250	0.72345	0.00648	0.05813	0.08231
1.350	0.74913	0.00770	0.06082	0.08484
1.450	0.78275	0.00917	0.06441	0.08841
1.550	0.78853	0.01069	0.06595	0.08900
1.650	0.81958	0.01260	0.06988	0.09263
1.750	0.85670	0.01485	0.07468	0.09715
1.850	0.85467	0.01705	0.07638	0.09743
1.950	0.85470	0.01951	0.07852	0.09815
2.100	0.88091	0.01711	0.08475	0.10264
2.300	0.87176	0.02198	0.08997	0.10427
2.500	0.85859	0.02776	0.09592	0.10619
2.700	0.80505	0.03398	0.09814	0.10365
2.900	0.78012	0.04174	0.10450	0.10521
3.125	0.76553	0.04700	0.11483	0.10949
3.375	0.73874	0.05953	0.12656	0.11360
3.625	0.61893	0.06869	0.12180	0.10298
3.875	0.45943	0.07498	0.10428	0.08312
4.250	0.62207	0.08600	0.17570	0.12854

Table A.7: R_{AA} yield from Figure 6-9, centrality bin 45-50%

p_T	R_{AA}	Statistical Error	Sys. Err.Up	Sys. Err. down
0.250	0.36150	0.00074	0.02874	0.04276
0.350	0.37013	0.00078	0.02908	0.04285
0.450	0.38449	0.00090	0.02993	0.04362
0.550	0.40896	0.00109	0.03163	0.04554
0.650	0.43740	0.00134	0.03369	0.04789
0.750	0.46805	0.00127	0.03600	0.05047
0.850	0.50581	0.00156	0.03896	0.05381
0.950	0.54300	0.00190	0.04198	0.05711
1.050	0.57394	0.00231	0.04466	0.05978
1.150	0.61937	0.00282	0.04864	0.06403
1.250	0.65126	0.00340	0.05174	0.06695
1.350	0.68293	0.00407	0.05502	0.06997
1.450	0.71093	0.00483	0.05823	0.07275
1.550	0.74257	0.00574	0.06198	0.07606
1.650	0.75280	0.00668	0.06418	0.07735
1.750	0.78090	0.00784	0.06817	0.08066
1.850	0.78810	0.00906	0.07059	0.08202
1.950	0.80490	0.01048	0.07413	0.08457
2.100	0.81036	0.00909	0.07811	0.08673
2.300	0.80919	0.01172	0.08344	0.08937
2.500	0.80191	0.01487	0.08907	0.09210
2.700	0.81206	0.01889	0.09777	0.09767
2.900	0.73732	0.02248	0.09676	0.09344
3.125	0.76281	0.02601	0.11091	0.10320
3.375	0.70318	0.03212	0.11525	0.10301
3.625	0.67661	0.03988	0.12561	0.10794
3.875	0.56183	0.04586	0.11858	0.09806
4.250	0.52773	0.04351	0.13563	0.10606

Table A.8: R_{AA} yield from Figure 6-9, centrality bin 35-45%

p_T	R_{AA}	Statistical Error	Sys. Err.Up	Sys. Err. down
0.250	0.31469	0.00053	0.02461	0.03641
0.350	0.32394	0.00056	0.02506	0.03672
0.450	0.33957	0.00065	0.02606	0.03778
0.550	0.36320	0.00079	0.02772	0.03972
0.650	0.39051	0.00097	0.02972	0.04205
0.750	0.42117	0.00092	0.03205	0.04474
0.850	0.45504	0.00113	0.03471	0.04777
0.950	0.49372	0.00139	0.03786	0.05132
1.050	0.52841	0.00170	0.04083	0.05450
1.150	0.56188	0.00206	0.04387	0.05763
1.250	0.60160	0.00250	0.04759	0.06148
1.350	0.63778	0.00300	0.05124	0.06509
1.450	0.65766	0.00355	0.05379	0.06717
1.550	0.68658	0.00421	0.05731	0.07032
1.650	0.70104	0.00492	0.05986	0.07217
1.750	0.71376	0.00573	0.06248	0.07402
1.850	0.72567	0.00664	0.06527	0.07597
1.950	0.75060	0.00774	0.06952	0.07949
2.100	0.74588	0.00666	0.07245	0.08068
2.300	0.72573	0.00846	0.07561	0.08130
2.500	0.72948	0.01081	0.08207	0.08526
2.700	0.69187	0.01328	0.08456	0.08492
2.900	0.66854	0.01629	0.08924	0.08668
3.125	0.65882	0.01839	0.09764	0.09141
3.375	0.63908	0.02329	0.10697	0.09621
3.625	0.56606	0.02780	0.10749	0.09296
3.875	0.54418	0.03417	0.11763	0.09789
4.250	0.48390	0.03153	0.12756	0.10034

Table A.9: R_{AA} yield from Figure 6-9, centrality bin 25-35%

p_T	R_{AA}	Statistical Error	Sys. Err.Up	Sys. Err. down
0.250	0.27356	0.00038	0.02139	0.03165
0.350	0.28241	0.00041	0.02185	0.03202
0.450	0.29664	0.00047	0.02276	0.03300
0.550	0.31903	0.00057	0.02435	0.03489
0.650	0.34604	0.00071	0.02633	0.03726
0.750	0.37399	0.00067	0.02846	0.03973
0.850	0.40625	0.00083	0.03099	0.04265
0.950	0.44080	0.00102	0.03380	0.04582
1.050	0.47308	0.00125	0.03656	0.04880
1.150	0.50683	0.00152	0.03958	0.05198
1.250	0.53806	0.00183	0.04256	0.05499
1.350	0.57031	0.00221	0.04582	0.05820
1.450	0.59617	0.00263	0.04876	0.06089
1.550	0.61419	0.00310	0.05127	0.06291
1.650	0.63606	0.00364	0.05431	0.06548
1.750	0.64925	0.00425	0.05684	0.06733
1.850	0.65204	0.00489	0.05865	0.06826
1.950	0.65441	0.00561	0.06061	0.06931
2.100	0.66197	0.00488	0.06430	0.07160
2.300	0.65683	0.00626	0.06843	0.07358
2.500	0.62237	0.00777	0.07002	0.07274
2.700	0.60508	0.00966	0.07395	0.07427
2.900	0.58544	0.01185	0.07815	0.07591
3.125	0.57011	0.01329	0.08449	0.07910
3.375	0.50909	0.01614	0.08521	0.07664
3.625	0.49683	0.02028	0.09435	0.08159
3.875	0.44253	0.02399	0.09566	0.07961
4.250	0.39660	0.02232	0.10454	0.08223

Table A.10: R_{AA} yield from Figure 6-9, centrality bin 15-25%

p_T	R_{AA}	Statistical Error	Sys. Err.Up	Sys. Err. down
0.250	0.24317	0.00030	0.02635	0.03057
0.350	0.25106	0.00033	0.02703	0.03097
0.450	0.26638	0.00038	0.02856	0.03230
0.550	0.28620	0.00046	0.03064	0.03417
0.650	0.31173	0.00057	0.03339	0.03670
0.750	0.33806	0.00055	0.03632	0.03931
0.850	0.36805	0.00067	0.03975	0.04234
0.950	0.39877	0.00083	0.04340	0.04548
1.050	0.42977	0.00102	0.04724	0.04868
1.150	0.46096	0.00124	0.05128	0.05195
1.250	0.49340	0.00151	0.05568	0.05544
1.350	0.51681	0.00180	0.05928	0.05800
1.450	0.54151	0.00215	0.06327	0.06083
1.550	0.56326	0.00255	0.06716	0.06346
1.650	0.57899	0.00299	0.07059	0.06556
1.750	0.58379	0.00346	0.07291	0.06656
1.850	0.60835	0.00406	0.07797	0.06998
1.950	0.59155	0.00459	0.07793	0.06879
2.100	0.59831	0.00399	0.08240	0.07097
2.300	0.58879	0.00509	0.08648	0.07216
2.500	0.56549	0.00636	0.08906	0.07210
2.700	0.52976	0.00777	0.08991	0.07071
2.900	0.50781	0.00949	0.09327	0.07135
3.125	0.49234	0.01060	0.09928	0.07372
3.375	0.42436	0.01263	0.09536	0.06862
3.625	0.39769	0.01548	0.09999	0.06981
3.875	0.33886	0.01792	0.09563	0.06486
4.250	0.32357	0.01713	0.10903	0.07091

Table A.11: R_{AA} yield from Figure 6-9, centrality bin 6-15%

p_T	R_{AA}	Statistical Error	Sys. Err.Up	Sys. Err. down
0.250	0.23755	0.00033	0.03023	0.03352
0.350	0.24525	0.00035	0.03106	0.03414
0.450	0.25850	0.00041	0.03266	0.03555
0.550	0.27723	0.00049	0.03503	0.03771
0.650	0.29951	0.00061	0.03794	0.04037
0.750	0.32647	0.00058	0.04156	0.04367
0.850	0.35376	0.00071	0.04536	0.04704
0.950	0.38363	0.00088	0.04966	0.05080
1.050	0.40991	0.00107	0.05369	0.05413
1.150	0.43717	0.00130	0.05808	0.05768
1.250	0.46715	0.00158	0.06307	0.06169
1.350	0.48964	0.00189	0.06733	0.06483
1.450	0.51304	0.00226	0.07200	0.06821
1.550	0.53324	0.00267	0.07653	0.07133
1.650	0.54052	0.00311	0.07947	0.07286
1.750	0.55218	0.00362	0.08333	0.07513
1.850	0.55482	0.00417	0.08609	0.07633
1.950	0.54950	0.00476	0.08782	0.07656
2.100	0.54660	0.00410	0.09157	0.07784
2.300	0.54070	0.00526	0.09696	0.07970
2.500	0.51725	0.00657	0.09981	0.07936
2.700	0.46453	0.00785	0.09690	0.07456
2.900	0.45750	0.00975	0.10359	0.07717
3.125	0.40953	0.01050	0.10211	0.07341
3.375	0.37519	0.01291	0.10457	0.07232
3.625	0.34700	0.01579	0.10850	0.07226
3.875	0.28199	0.01785	0.09918	0.06367
4.250	0.28506	0.01764	0.12003	0.07304

Table A.12: R_{AA} yield from Figure 6-9, centrality bin 0-6%

p_T	$R_{AA}^{N_{part}}$	Statistical Error	Sys. Err.Up	Sys. Err. down
0.250	1.30090	0.00443	0.11076	0.17056
0.350	1.32594	0.00471	0.11081	0.17023
0.450	1.35988	0.00540	0.11185	0.17118
0.550	1.43579	0.00649	0.11655	0.17746
0.650	1.51551	0.00791	0.12176	0.18419
0.750	1.62195	0.00747	0.12935	0.19414
0.850	1.72997	0.00911	0.13735	0.20426
0.950	1.85281	0.01113	0.14688	0.21616
1.050	1.96671	0.01353	0.15614	0.22712
1.150	2.06152	0.01629	0.16440	0.23608
1.250	2.20373	0.01974	0.17706	0.25073
1.350	2.28196	0.02347	0.18527	0.25844
1.450	2.38438	0.02794	0.19620	0.26932
1.550	2.40198	0.03255	0.20091	0.27112
1.650	2.49657	0.03837	0.21288	0.28216
1.750	2.60964	0.04522	0.22749	0.29592
1.850	2.60345	0.05194	0.23266	0.29679
1.950	2.60354	0.05942	0.23917	0.29897
2.100	2.68339	0.05211	0.25817	0.31267
2.300	2.65550	0.06694	0.27408	0.31762
2.500	2.61539	0.08457	0.29219	0.32346
2.700	2.45231	0.10350	0.29895	0.31573
2.900	2.37637	0.12713	0.31833	0.32048
3.125	2.33192	0.14318	0.34980	0.33354
3.375	2.25030	0.18134	0.38553	0.34606
3.625	1.88534	0.20923	0.37103	0.31368
3.875	1.39950	0.22840	0.31766	0.25321
4.250	1.89491	0.26197	0.53520	0.39156

Table A.13: $R_{AA}^{N_{part}}$ yields from Figure 6-10, centrality bin 45-50%

p_T	$R_{AA}^{N_{part}}$	Statistical Error	Sys. Err.Up	Sys. Err. down
0.250	1.27495	0.00259	0.10137	0.15083
0.350	1.30541	0.00276	0.10257	0.15112
0.450	1.35606	0.00319	0.10557	0.15385
0.550	1.44234	0.00385	0.11155	0.16062
0.650	1.54267	0.00473	0.11883	0.16890
0.750	1.65076	0.00447	0.12698	0.17800
0.850	1.78395	0.00549	0.13740	0.18979
0.950	1.91511	0.00672	0.14807	0.20140
1.050	2.02421	0.00815	0.15752	0.21084
1.150	2.18444	0.00996	0.17153	0.22581
1.250	2.29693	0.01199	0.18247	0.23614
1.350	2.40861	0.01435	0.19405	0.24678
1.450	2.50735	0.01705	0.20537	0.25658
1.550	2.61894	0.02023	0.21860	0.26825
1.650	2.65503	0.02356	0.22637	0.27280
1.750	2.75416	0.02766	0.24041	0.28449
1.850	2.77955	0.03196	0.24895	0.28927
1.950	2.83880	0.03697	0.26143	0.29828
2.100	2.85806	0.03207	0.27548	0.30587
2.300	2.85393	0.04134	0.29427	0.31521
2.500	2.82823	0.05246	0.31415	0.32484
2.700	2.86402	0.06664	0.34484	0.34446
2.900	2.60043	0.07930	0.34126	0.32956
3.125	2.69034	0.09172	0.39118	0.36398
3.375	2.48005	0.11327	0.40647	0.36329
3.625	2.38631	0.14065	0.44301	0.38070
3.875	1.98152	0.16173	0.41820	0.34586
4.250	1.86124	0.15346	0.47834	0.37406

Table A.14: $R_{AA}^{N_{part}}$ yields from Figure 6-10, centrality bin 35-45%

p_T	$R_{AA}^{N_{part}}$	Statistical Error	Sys. Err.Up	Sys. Err. down
0.250	1.30437	0.00218	0.10200	0.15091
0.350	1.34272	0.00232	0.10388	0.15222
0.450	1.40750	0.00270	0.10801	0.15658
0.550	1.50543	0.00326	0.11489	0.16463
0.650	1.61862	0.00402	0.12318	0.17429
0.750	1.74573	0.00381	0.13283	0.18543
0.850	1.88610	0.00468	0.14387	0.19800
0.950	2.04642	0.00576	0.15691	0.21274
1.050	2.19020	0.00703	0.16925	0.22592
1.150	2.32895	0.00853	0.18185	0.23887
1.250	2.49360	0.01035	0.19725	0.25484
1.350	2.64354	0.01245	0.21237	0.26978
1.450	2.72595	0.01473	0.22295	0.27840
1.550	2.84582	0.01747	0.23754	0.29149
1.650	2.90577	0.02041	0.24810	0.29916
1.750	2.95848	0.02375	0.25898	0.30681
1.850	3.00786	0.02750	0.27055	0.31489
1.950	3.11120	0.03207	0.28814	0.32949
2.100	3.09161	0.02758	0.30029	0.33442
2.300	3.00809	0.03508	0.31338	0.33699
2.500	3.02364	0.04481	0.34016	0.35339
2.700	2.86775	0.05505	0.35051	0.35199
2.900	2.77105	0.06754	0.36991	0.35929
3.125	2.73074	0.07621	0.40471	0.37889
3.375	2.64893	0.09652	0.44339	0.39880
3.625	2.34627	0.11521	0.44556	0.38533
3.875	2.25557	0.14163	0.48759	0.40576
4.250	2.00572	0.13071	0.52871	0.41588

Table A.15: $R_{AA}^{N_{part}}$ yields from Figure 6-10, centrality bin 25-35%

0.250	1.32129	0.00183	0.10333	0.15287
0.350	1.36405	0.00196	0.10553	0.15463
0.450	1.43277	0.00228	0.10994	0.15940
0.550	1.54089	0.00277	0.11759	0.16850
0.650	1.67138	0.00342	0.12719	0.17997
0.750	1.80639	0.00325	0.13745	0.19187
0.850	1.96218	0.00400	0.14968	0.20599
0.950	2.12905	0.00492	0.16325	0.22133
1.050	2.28498	0.00602	0.17657	0.23570
1.150	2.44801	0.00733	0.19115	0.25108
1.250	2.59881	0.00886	0.20557	0.26559
1.350	2.75457	0.01066	0.22129	0.28111
1.450	2.87951	0.01270	0.23551	0.29408
1.550	2.96652	0.01496	0.24761	0.30385
1.650	3.07216	0.01761	0.26231	0.31629
1.750	3.13589	0.02051	0.27451	0.32521
1.850	3.14936	0.02362	0.28327	0.32970
1.950	3.16081	0.02711	0.29274	0.33474
2.100	3.19731	0.02355	0.31056	0.34585
2.300	3.17246	0.03022	0.33050	0.35541
2.500	3.00606	0.03753	0.33818	0.35133
2.700	2.92252	0.04668	0.35720	0.35871
2.900	2.82769	0.05725	0.37747	0.36663
3.125	2.75365	0.06421	0.40811	0.38207
3.375	2.45889	0.07793	0.41158	0.37019
3.625	2.39967	0.09794	0.45570	0.39410
3.875	2.13741	0.11586	0.46204	0.38450
4.250	1.91557	0.10781	0.50495	0.39719

Table A.16: $R_{AA}^{N_{part}}$ yields from Figure 6-10, centrality bin 15-25%

p_T	$R_{AA}^{N_{part}}$	Statistical Error	Sys. Err.Up	Sys. Err. down
0.250	1.43637	0.00198	0.18278	0.20269
0.350	1.48293	0.00212	0.18780	0.20642
0.450	1.56305	0.00246	0.19749	0.21492
0.550	1.67627	0.00299	0.21181	0.22803
0.650	1.81098	0.00369	0.22941	0.24411
0.750	1.97399	0.00351	0.25128	0.26407
0.850	2.13902	0.00432	0.27427	0.28444
0.950	2.31961	0.00531	0.30028	0.30714
1.050	2.47852	0.00648	0.32467	0.32733
1.150	2.64333	0.00788	0.35115	0.34878
1.250	2.82466	0.00955	0.38138	0.37301
1.350	2.96062	0.01143	0.40712	0.39197
1.450	3.10209	0.01364	0.43535	0.41246
1.550	3.22422	0.01614	0.46271	0.43128
1.650	3.26828	0.01881	0.48054	0.44056
1.750	3.33876	0.02191	0.50386	0.45430
1.850	3.35473	0.02524	0.52055	0.46154
1.950	3.32255	0.02879	0.53098	0.46293
2.100	3.30500	0.02482	0.55369	0.47068
2.300	3.26934	0.03182	0.58627	0.48192
2.500	3.12757	0.03970	0.60350	0.47985
2.700	2.80879	0.04747	0.58592	0.45083
2.900	2.76626	0.05894	0.62636	0.46663
3.125	2.47622	0.06347	0.61744	0.44387
3.375	2.26858	0.07808	0.63231	0.43731
3.625	2.09817	0.09545	0.65605	0.43693
3.875	1.70506	0.10794	0.59971	0.38497
4.250	1.72365	0.10664	0.72577	0.44164

Table A.17: $R_{AA}^{N_{part}}$ yields from Figure 6-10, centrality bin 0-6%

Appendix B

Data Tables B

B.1 $R_{CP}^{N_{part}}$ Data

B.2 $R_{CP}^{N_{coll}}$ Data

B.3 d+Au Invariant Yields Data

p_T	$R_{CP}^{N_{part}}$	Statistical Error	Sys. Err.Up	Sys. Err. down
0.250	0.99762	0.00340	0.08494	0.13079
0.350	1.00644	0.00357	0.08411	0.12921
0.450	0.99579	0.00395	0.08190	0.12535
0.550	0.99972	0.00452	0.08115	0.12356
0.650	0.99483	0.00520	0.07993	0.12091
0.750	0.99931	0.00460	0.07970	0.11961
0.850	0.99907	0.00526	0.07932	0.11796
0.950	1.00402	0.00603	0.07959	0.11714
1.050	1.00286	0.00690	0.07962	0.11582
1.150	0.99330	0.00785	0.07921	0.11375
1.250	1.00842	0.00903	0.08102	0.11473
1.350	0.99730	0.01026	0.08097	0.11295
1.450	1.00120	0.01173	0.08238	0.11309
1.550	0.97501	0.01321	0.08155	0.11005
1.650	0.98568	0.01515	0.08405	0.11140
1.750	1.00818	0.01747	0.08789	0.11432
1.850	0.98993	0.01975	0.08847	0.11285
1.950	0.97979	0.02236	0.09001	0.11251
2.100	1.00406	0.01950	0.09660	0.11700
2.300	1.00233	0.02527	0.10345	0.11989
2.500	1.01175	0.03272	0.11303	0.12513
2.700	0.98461	0.04156	0.12003	0.12677
2.900	0.99950	0.05347	0.13389	0.13480
3.125	1.04071	0.06390	0.15611	0.14885
3.375	1.07621	0.08673	0.18438	0.16550
3.625	0.96409	0.10699	0.18973	0.16040
3.875	0.75962	0.12397	0.17242	0.13744
4.250	1.10150	0.15228	0.31111	0.22761

Table B.1: $R_{CP}^{N_{part}}$ yields from Figure 6-11, centrality bin 45-50%

p_T	$R_{CP}^{N_{part}}$	Statistical Error	Sys. Err.Up	Sys. Err. down
0.250	0.97771	0.00199	0.07774	0.11566
0.350	0.99086	0.00210	0.07786	0.11471
0.450	0.99299	0.00234	0.07731	0.11266
0.550	1.00428	0.00268	0.07767	0.11184
0.650	1.01266	0.00311	0.07801	0.11087
0.750	1.01706	0.00275	0.07824	0.10967
0.850	1.03024	0.00317	0.07935	0.10961
0.950	1.03778	0.00364	0.08024	0.10914
1.050	1.03219	0.00416	0.08032	0.10751
1.150	1.05253	0.00480	0.08265	0.10880
1.250	1.05106	0.00548	0.08350	0.10806
1.350	1.05265	0.00627	0.08481	0.10785
1.450	1.05284	0.00716	0.08623	0.10774
1.550	1.06308	0.00821	0.08873	0.10889
1.650	1.04824	0.00930	0.08937	0.10770
1.750	1.06401	0.01069	0.09288	0.10991
1.850	1.05689	0.01215	0.09466	0.10999
1.950	1.06833	0.01391	0.09839	0.11225
2.100	1.06942	0.01200	0.10308	0.11445
2.300	1.07722	0.01560	0.11107	0.11898
2.500	1.09409	0.02029	0.12153	0.12566
2.700	1.14991	0.02675	0.13845	0.13830
2.900	1.09374	0.03335	0.14353	0.13861
3.125	1.20067	0.04094	0.17458	0.16244
3.375	1.18609	0.05417	0.19439	0.17375
3.625	1.22026	0.07192	0.22653	0.19467
3.875	1.07553	0.08779	0.22699	0.18773
4.250	1.08193	0.08921	0.27806	0.21744

Table B.2: $R_{CP}^{N_{part}}$ yields from Figure 6-11, centrality bin 35-45%

p_T	$R_{CP}^{N_{part}}$	Statistical Error	Sys. Err.Up	Sys. Err. down
0.250	1.00027	0.00167	0.07822	0.11573
0.350	1.01918	0.00176	0.07885	0.11554
0.450	1.03066	0.00197	0.07909	0.11466
0.550	1.04821	0.00227	0.07999	0.11463
0.650	1.06251	0.00264	0.08086	0.11441
0.750	1.07557	0.00235	0.08184	0.11425
0.850	1.08924	0.00270	0.08309	0.11435
0.950	1.10894	0.00312	0.08503	0.11528
1.050	1.11683	0.00358	0.08630	0.11520
1.150	1.12216	0.00411	0.08762	0.11509
1.250	1.14106	0.00474	0.09026	0.11661
1.350	1.15532	0.00544	0.09281	0.11790
1.450	1.14463	0.00618	0.09362	0.11690
1.550	1.15517	0.00709	0.09642	0.11832
1.650	1.14724	0.00806	0.09795	0.11811
1.750	1.14295	0.00917	0.10005	0.11853
1.850	1.14370	0.01046	0.10287	0.11973
1.950	1.17084	0.01207	0.10844	0.12400
2.100	1.15681	0.01032	0.11236	0.12513
2.300	1.13541	0.01324	0.11829	0.12720
2.500	1.16968	0.01733	0.13159	0.13671
2.700	1.15141	0.02210	0.14073	0.14132
2.900	1.16551	0.02841	0.15558	0.15112
3.125	1.21870	0.03401	0.18062	0.16910
3.375	1.26686	0.04616	0.21205	0.19073
3.625	1.19978	0.05892	0.22784	0.19704
3.875	1.22428	0.07688	0.26465	0.22024
4.250	1.16592	0.07598	0.30734	0.24175

Table B.3: $R_{CP}^{N_{part}}$ yields from Figure 6-11, centrality bin 25-35%

p_T	$R_{CP}^{N_{part}}$	Statistical Error	Sys. Err.Up	Sys. Err. down
0.250	1.01325	0.00141	0.07924	0.11723
0.350	1.03537	0.00149	0.08010	0.11737
0.450	1.04916	0.00167	0.08051	0.11672
0.550	1.07290	0.00193	0.08188	0.11733
0.650	1.09715	0.00225	0.08349	0.11814
0.750	1.11295	0.00200	0.08468	0.11822
0.850	1.13317	0.00231	0.08644	0.11896
0.950	1.15372	0.00267	0.08846	0.11993
1.050	1.16516	0.00307	0.09004	0.12019
1.150	1.17953	0.00353	0.09210	0.12098
1.250	1.18920	0.00405	0.09407	0.12153
1.350	1.20384	0.00466	0.09671	0.12285
1.450	1.20911	0.00533	0.09889	0.12348
1.550	1.20417	0.00607	0.10051	0.12334
1.650	1.21293	0.00695	0.10356	0.12488
1.750	1.21149	0.00792	0.10605	0.12564
1.850	1.19751	0.00898	0.10771	0.12537
1.950	1.18951	0.01020	0.11017	0.12597
2.100	1.19636	0.00881	0.11620	0.12941
2.300	1.19746	0.01141	0.12475	0.13415
2.500	1.16288	0.01452	0.13082	0.13591
2.700	1.17340	0.01874	0.14342	0.14402
2.900	1.18933	0.02408	0.15876	0.15421
3.125	1.22892	0.02865	0.18213	0.17051
3.375	1.17597	0.03727	0.19684	0.17704
3.625	1.22709	0.05008	0.23303	0.20153
3.875	1.16015	0.06288	0.25079	0.20870
4.250	1.11351	0.06267	0.29352	0.23088

Table B.4: $R_{CP}^{N_{part}}$ yields from Figure 6-11, centrality bin 15-25%

p_T	$R_{CP}^{N_{part}}$	Statistical Error	Sys. Err.Up	Sys. Err. down
0.250	1.02970	0.00129	0.11157	0.12944
0.350	1.05224	0.00137	0.11328	0.12982
0.450	1.07705	0.00154	0.11548	0.13061
0.550	1.10037	0.00178	0.11779	0.13137
0.650	1.12992	0.00208	0.12103	0.13302
0.750	1.15009	0.00186	0.12356	0.13373
0.850	1.17366	0.00215	0.12677	0.13503
0.950	1.19319	0.00248	0.12987	0.13608
1.050	1.21008	0.00286	0.13301	0.13705
1.150	1.22639	0.00330	0.13645	0.13821
1.250	1.24669	0.00381	0.14069	0.14007
1.350	1.24716	0.00435	0.14306	0.13997
1.450	1.25554	0.00499	0.14669	0.14105
1.550	1.26248	0.00571	0.15053	0.14224
1.650	1.26223	0.00652	0.15389	0.14292
1.750	1.24536	0.00738	0.15553	0.14199
1.850	1.27727	0.00852	0.16370	0.14693
1.950	1.22924	0.00953	0.16194	0.14294
2.100	1.23618	0.00823	0.17024	0.14662
2.300	1.22715	0.01062	0.18024	0.15040
2.500	1.20791	0.01359	0.19025	0.15401
2.700	1.17447	0.01724	0.19933	0.15675
2.900	1.17936	0.02205	0.21662	0.16570
3.125	1.21328	0.02612	0.24465	0.18166
3.375	1.12064	0.03334	0.25183	0.18120
3.625	1.12290	0.04371	0.28234	0.19712
3.875	1.01561	0.05370	0.28661	0.19438
4.250	1.03857	0.05498	0.34995	0.22761

Table B.5: $R_{CP}^{N_{part}}$ yields from Figure 6-11, centrality bin 6-15%

p_T	$R_{CP}^{N_{part}}$	Statistical Error	Sys. Err.Up	Sys. Err. down
0.250	1.10150	0.00152	0.14016	0.15544
0.350	1.12560	0.00161	0.14255	0.15668
0.450	1.14456	0.00180	0.14461	0.15738
0.550	1.16716	0.00208	0.14748	0.15878
0.650	1.18879	0.00242	0.15059	0.16024
0.750	1.21621	0.00216	0.15482	0.16270
0.850	1.23530	0.00249	0.15839	0.16427
0.950	1.25698	0.00288	0.16272	0.16644
1.050	1.26385	0.00331	0.16555	0.16691
1.150	1.27364	0.00380	0.16920	0.16805
1.250	1.29255	0.00437	0.17452	0.17069
1.350	1.29389	0.00500	0.17793	0.17130
1.450	1.30257	0.00573	0.18280	0.17319
1.550	1.30877	0.00655	0.18782	0.17507
1.650	1.29036	0.00742	0.18972	0.17394
1.750	1.28987	0.00847	0.19466	0.17551
1.850	1.27559	0.00960	0.19793	0.17549
1.950	1.25038	0.01084	0.19982	0.17421
2.100	1.23666	0.00929	0.20718	0.17612
2.300	1.23402	0.01201	0.22129	0.18190
2.500	1.20989	0.01536	0.23346	0.18563
2.700	1.12773	0.01906	0.23525	0.18101
2.900	1.16349	0.02479	0.26345	0.19626
3.125	1.10511	0.02833	0.27555	0.19810
3.375	1.08496	0.03734	0.30240	0.20915
3.625	1.07291	0.04881	0.33548	0.22343
3.875	0.92547	0.05859	0.32551	0.20896
4.250	1.00195	0.06199	0.42189	0.25672

Table B.6: $R_{CP}^{N_{part}}$ yields from Figure 6-11, centrality bin 0-6%

p_T	$R_{CP}^{N_{coll}}$	Statistical Error	Sys. Err.Up	Sys. Err. down
0.250	0.99762	0.00340	0.08494	0.13079
0.350	1.00644	0.00357	0.08411	0.12921
0.450	0.99579	0.00395	0.08190	0.12535
0.550	0.99972	0.00452	0.08115	0.12356
0.650	0.99483	0.00520	0.07993	0.12091
0.750	0.99931	0.00460	0.07970	0.11961
0.850	0.99907	0.00526	0.07932	0.11796
0.950	1.00402	0.00603	0.07959	0.11714
1.050	1.00286	0.00690	0.07962	0.11582
1.150	0.99330	0.00785	0.07921	0.11375
1.250	1.00842	0.00903	0.08102	0.11473
1.350	0.99730	0.01026	0.08097	0.11295
1.450	1.00120	0.01173	0.08238	0.11309
1.550	0.97501	0.01321	0.08155	0.11005
1.650	0.98568	0.01515	0.08405	0.11140
1.750	1.00818	0.01747	0.08789	0.11432
1.850	0.98993	0.01975	0.08847	0.11285
1.950	0.97979	0.02236	0.09001	0.11251
2.100	1.00406	0.01950	0.09660	0.11700
2.300	1.00233	0.02527	0.10345	0.11989
2.500	1.01175	0.03272	0.11303	0.12513
2.700	0.98461	0.04156	0.12003	0.12677
2.900	0.99950	0.05347	0.13389	0.13480
3.125	1.04071	0.06390	0.15611	0.14885
3.375	1.07621	0.08673	0.18438	0.16550
3.625	0.96409	0.10699	0.18973	0.16040
3.875	0.75962	0.12397	0.17242	0.13744
4.250	1.10150	0.15228	0.31111	0.22761

Table B.7: $R_{CP}^{N_{part}}$ yields from Figure 6-13, centrality bin 45-50%

p_T	$R_{CP}^{N_{coll}}$	Statistical Error	Sys. Err.Up	Sys. Err. down
0.250	0.84445	0.00172	0.06714	0.09990
0.350	0.85580	0.00181	0.06724	0.09907
0.450	0.85764	0.00202	0.06677	0.09730
0.550	0.86739	0.00232	0.06708	0.09659
0.650	0.87463	0.00268	0.06737	0.09576
0.750	0.87843	0.00238	0.06757	0.09472
0.850	0.88982	0.00274	0.06853	0.09467
0.950	0.89633	0.00314	0.06930	0.09426
1.050	0.89150	0.00359	0.06938	0.09286
1.150	0.90907	0.00415	0.07139	0.09397
1.250	0.90780	0.00474	0.07211	0.09333
1.350	0.90917	0.00542	0.07325	0.09315
1.450	0.90933	0.00618	0.07448	0.09305
1.550	0.91818	0.00709	0.07664	0.09405
1.650	0.90536	0.00804	0.07719	0.09302
1.750	0.91899	0.00923	0.08022	0.09493
1.850	0.91283	0.01050	0.08176	0.09500
1.950	0.92271	0.01202	0.08497	0.09695
2.100	0.92366	0.01036	0.08903	0.09885
2.300	0.93039	0.01348	0.09593	0.10276
2.500	0.94496	0.01753	0.10496	0.10853
2.700	0.99317	0.02311	0.11958	0.11945
2.900	0.94466	0.02881	0.12397	0.11972
3.125	1.03701	0.03536	0.15078	0.14030
3.375	1.02442	0.04679	0.16790	0.15006
3.625	1.05393	0.06212	0.19566	0.16814
3.875	0.92893	0.07582	0.19605	0.16214
4.250	0.93446	0.07705	0.24016	0.18780

Table B.8: $R_{CP}^{N_{part}}$ yields from Figure 6-13, centrality bin 35-45%

p_T	$R_{CP}^{N_{coll}}$	Statistical Error	Sys. Err.Up	Sys. Err. down
0.250	0.73511	0.00123	0.05749	0.08505
0.350	0.74901	0.00130	0.05795	0.08491
0.450	0.75744	0.00145	0.05812	0.08427
0.550	0.77034	0.00167	0.05879	0.08424
0.650	0.78085	0.00194	0.05942	0.08408
0.750	0.79045	0.00173	0.06014	0.08396
0.850	0.80049	0.00199	0.06106	0.08403
0.950	0.81497	0.00229	0.06249	0.08472
1.050	0.82077	0.00263	0.06343	0.08466
1.150	0.82469	0.00302	0.06439	0.08458
1.250	0.83858	0.00348	0.06633	0.08570
1.350	0.84906	0.00400	0.06821	0.08665
1.450	0.84120	0.00454	0.06880	0.08591
1.550	0.84895	0.00521	0.07086	0.08696
1.650	0.84312	0.00592	0.07199	0.08680
1.750	0.83997	0.00674	0.07353	0.08711
1.850	0.84052	0.00769	0.07560	0.08799
1.950	0.86046	0.00887	0.07969	0.09113
2.100	0.85015	0.00759	0.08258	0.09196
2.300	0.83443	0.00973	0.08693	0.09348
2.500	0.85961	0.01274	0.09671	0.10047
2.700	0.84618	0.01624	0.10342	0.10386
2.900	0.85654	0.02088	0.11434	0.11106
3.125	0.89564	0.02500	0.13274	0.12427
3.375	0.93103	0.03392	0.15584	0.14017
3.625	0.88173	0.04330	0.16744	0.14481
3.875	0.89974	0.05650	0.19450	0.16186
4.250	0.85685	0.05584	0.22587	0.17767

Table B.9: $R_{CP}^{N_{part}}$ yields from Figure 6-13, centrality bin 25-35%

p_T	$R_{CP}^{N_{coll}}$	Statistical Error	Sys. Err.Up	Sys. Err. down
0.250	0.63903	0.00089	0.04997	0.07393
0.350	0.65298	0.00094	0.05052	0.07402
0.450	0.66168	0.00105	0.05077	0.07361
0.550	0.67665	0.00122	0.05164	0.07399
0.650	0.69194	0.00142	0.05266	0.07451
0.750	0.70191	0.00126	0.05341	0.07456
0.850	0.71466	0.00146	0.05451	0.07502
0.950	0.72762	0.00168	0.05579	0.07564
1.050	0.73484	0.00194	0.05679	0.07580
1.150	0.74390	0.00223	0.05809	0.07630
1.250	0.75000	0.00256	0.05933	0.07665
1.350	0.75923	0.00294	0.06099	0.07748
1.450	0.76255	0.00336	0.06237	0.07788
1.550	0.75944	0.00383	0.06339	0.07779
1.650	0.76496	0.00438	0.06531	0.07876
1.750	0.76406	0.00500	0.06688	0.07924
1.850	0.75524	0.00566	0.06793	0.07907
1.950	0.75019	0.00643	0.06948	0.07945
2.100	0.75451	0.00556	0.07329	0.08161
2.300	0.75520	0.00719	0.07868	0.08460
2.500	0.73340	0.00916	0.08251	0.08572
2.700	0.74003	0.01182	0.09045	0.09083
2.900	0.75008	0.01519	0.10013	0.09725
3.125	0.77505	0.01807	0.11487	0.10754
3.375	0.74165	0.02351	0.12414	0.11166
3.625	0.77389	0.03159	0.14696	0.12710
3.875	0.73168	0.03966	0.15817	0.13162
4.250	0.70226	0.03952	0.18512	0.14561

Table B.10: $R_{CP}^{N_{part}}$ yields from Figure 6-13, centrality bin 15-25%

p_T	$R_{CP}^{N_{coll}}$	Statistical Error	Sys. Err.Up	Sys. Err. down
0.250	0.56805	0.00071	0.06155	0.07141
0.350	0.58048	0.00075	0.06249	0.07162
0.450	0.59417	0.00085	0.06371	0.07206
0.550	0.60704	0.00098	0.06498	0.07247
0.650	0.62334	0.00115	0.06677	0.07338
0.750	0.63447	0.00103	0.06817	0.07377
0.850	0.64747	0.00119	0.06994	0.07449
0.950	0.65824	0.00137	0.07164	0.07507
1.050	0.66756	0.00158	0.07338	0.07561
1.150	0.67656	0.00182	0.07527	0.07625
1.250	0.68776	0.00210	0.07761	0.07727
1.350	0.68802	0.00240	0.07892	0.07722
1.450	0.69264	0.00275	0.08092	0.07781
1.550	0.69646	0.00315	0.08304	0.07847
1.650	0.69633	0.00359	0.08489	0.07884
1.750	0.68702	0.00407	0.08580	0.07833
1.850	0.70463	0.00470	0.09030	0.08105
1.950	0.67813	0.00526	0.08934	0.07886
2.100	0.68196	0.00454	0.09392	0.08089
2.300	0.67698	0.00586	0.09943	0.08297
2.500	0.66636	0.00750	0.10495	0.08496
2.700	0.64791	0.00951	0.10996	0.08648
2.900	0.65061	0.01216	0.11950	0.09141
3.125	0.66932	0.01441	0.13496	0.10022
3.375	0.61822	0.01839	0.13893	0.09996
3.625	0.61947	0.02411	0.15576	0.10874
3.875	0.56028	0.02962	0.15811	0.10723
4.250	0.57294	0.03033	0.19305	0.12556

Table B.11: $R_{CP}^{N_{part}}$ yields from Figure 6-13, centrality bin 6-15%

p_T	$R_{CP}^{N_{coll}}$	Statistical Error	Sys. Err.Up	Sys. Err. down
0.250	0.55492	0.00077	0.07061	0.07831
0.350	0.56706	0.00081	0.07182	0.07893
0.450	0.57661	0.00091	0.07285	0.07929
0.550	0.58800	0.00105	0.07430	0.07999
0.650	0.59890	0.00122	0.07587	0.08073
0.750	0.61271	0.00109	0.07800	0.08196
0.850	0.62233	0.00126	0.07980	0.08276
0.950	0.63325	0.00145	0.08198	0.08385
1.050	0.63671	0.00167	0.08340	0.08409
1.150	0.64164	0.00191	0.08524	0.08466
1.250	0.65117	0.00220	0.08792	0.08599
1.350	0.65185	0.00252	0.08964	0.08630
1.450	0.65622	0.00288	0.09209	0.08725
1.550	0.65934	0.00330	0.09462	0.08820
1.650	0.65007	0.00374	0.09558	0.08763
1.750	0.64982	0.00426	0.09807	0.08842
1.850	0.64263	0.00484	0.09972	0.08841
1.950	0.62992	0.00546	0.10067	0.08777
2.100	0.62301	0.00468	0.10437	0.08873
2.300	0.62169	0.00605	0.11148	0.09164
2.500	0.60953	0.00774	0.11761	0.09352
2.700	0.56814	0.00960	0.11851	0.09119
2.900	0.58615	0.01249	0.13272	0.09888
3.125	0.55674	0.01427	0.13882	0.09980
3.375	0.54659	0.01881	0.15235	0.10536
3.625	0.54052	0.02459	0.16901	0.11256
3.875	0.46624	0.02952	0.16399	0.10527
4.250	0.50477	0.03123	0.21254	0.12933

Table B.12: $R_{CP}^{N_{part}}$ yields from Figure 6-13, centrality bin 0-6%

p_T	Invariant Yield	Stat. Err.	Sys. Err.
0.250	2.1281896	0.0132825	0.2138572
0.350	1.3279155	0.0082221	0.1345149
0.450	0.7898048	0.0053893	0.0807927
0.550	0.4654942	0.0036309	0.0481685
0.650	0.2896210	0.0026141	0.0303663
0.750	0.1848910	0.0019441	0.0196734
0.850	0.1154301	0.0014314	0.0124837
0.950	0.0764551	0.0011011	0.0084162
1.050	0.0512640	0.0008591	0.0057517
1.150	0.0348292	0.0006748	0.0039880
1.250	0.0231107	0.0005306	0.0027038
1.350	0.0157638	0.0004169	0.0018865
1.450	0.0120732	0.0003566	0.0014794
1.550	0.0084534	0.0002673	0.0010616
1.650	0.0058885	0.0002153	0.0007586
1.750	0.0041126	0.0001746	0.0005439
1.850	0.0029981	0.0001456	0.0004073
1.950	0.0023831	0.0001277	0.0003328
2.100	0.0015513	0.0000705	0.0002260
2.300	0.0008746	0.0000505	0.0001351
2.500	0.0004892	0.0000364	0.0000802
2.700	0.0003313	0.0000272	0.0000577
2.900	0.0001453	0.0000172	0.0000269
3.125	0.0000985	0.0000127	0.0000195
3.375	0.0000513	0.0000084	0.0000110
3.625	0.0000291	0.0000063	0.0000067
3.875	0.0000196	0.0000049	0.0000049
4.250	0.0000116	0.0000027	0.0000032
4.750	0.0000059	0.0000018	0.0000019
5.250	0.0000010	0.0000007	0.0000004
5.750	0.0000013	0.0000007	0.0000005

Table B.13: Invariant yields from Figure ??, centrality bin 70-100%

p_T	Invariant Yield	Stat. Err.	Sys. Err.
0.250	3.8409917	0.0149919	0.3859729
0.350	2.3855696	0.0092568	0.2416530
0.450	1.4272387	0.0060767	0.1459988
0.550	0.8776131	0.0042538	0.0908137
0.650	0.5555336	0.0030731	0.0582468
0.750	0.3505612	0.0022551	0.0373016
0.850	0.2300270	0.0017052	0.0248773
0.950	0.1518575	0.0013093	0.0167165
1.050	0.1046775	0.0010320	0.0117445
1.150	0.0705218	0.0008094	0.0080748
1.250	0.0491010	0.0006487	0.0057444
1.350	0.0344969	0.0005238	0.0041282
1.450	0.0240675	0.0004209	0.0029491
1.550	0.0183617	0.0002909	0.0023060
1.650	0.0129405	0.0002366	0.0016670
1.750	0.0096319	0.0001982	0.0012738
1.850	0.0070618	0.0001655	0.0009594
1.950	0.0051778	0.0001378	0.0007231
2.100	0.0031318	0.0000733	0.0004563
2.300	0.0019091	0.0000547	0.0002948
2.500	0.0011263	0.0000408	0.0001846
2.700	0.0006957	0.0000272	0.0001211
2.900	0.0004115	0.0000202	0.0000761
3.125	0.0002824	0.0000145	0.0000560
3.375	0.0001379	0.0000099	0.0000295
3.625	0.0000742	0.0000068	0.0000172
3.875	0.0000452	0.0000053	0.0000113
4.250	0.0000280	0.0000028	0.0000078
4.750	0.0000099	0.0000016	0.0000032
5.250	0.0000034	0.0000008	0.0000013
5.750	0.0000023	0.0000007	0.0000010

Table B.14: Invariant yields from Figure ??, centrality bin 40-70%

p_T	Invariant Yield	Stat. Err.	Sys. Err.
0.250	5.8572125	0.0182402	0.5885786
0.350	3.5793073	0.0111206	0.3625760
0.450	2.1932232	0.0074240	0.2243548
0.550	1.3573574	0.0051797	0.1404568
0.650	0.8703532	0.0037821	0.0912551
0.750	0.5721061	0.0028417	0.0608752
0.850	0.3742545	0.0021459	0.0404754
0.950	0.2528087	0.0016662	0.0278292
1.050	0.1769018	0.0013259	0.0198479
1.150	0.1193671	0.0010403	0.0136677
1.250	0.0853065	0.0008463	0.0099802
1.350	0.0609223	0.0006880	0.0072906
1.450	0.0427719	0.0005576	0.0052410
1.550	0.0321276	0.0003817	0.0040348
1.650	0.0237504	0.0003181	0.0030596
1.750	0.0168223	0.0002599	0.0022247
1.850	0.0128629	0.0002211	0.0017476
1.950	0.0096888	0.0001872	0.0013531
2.100	0.0061963	0.0001024	0.0009028
2.300	0.0036645	0.0000755	0.0005659
2.500	0.0021331	0.0000556	0.0003496
2.700	0.0013067	0.0000375	0.0002275
2.900	0.0007846	0.0000279	0.0001452
3.125	0.0004592	0.0000186	0.0000910
3.375	0.0002506	0.0000129	0.0000537
3.625	0.0001503	0.0000097	0.0000347
3.875	0.0001050	0.0000080	0.0000262
4.250	0.0000505	0.0000037	0.0000141
4.750	0.0000204	0.0000022	0.0000066
5.250	0.0000088	0.0000014	0.0000032
5.750	0.0000033	0.0000008	0.0000014

Table B.15: Invariant yields from Figure ??, centrality bin 20-40%

p_T	Invariant Yield	Stat. Err.	Sys. Err.
0.250	7.7993670	0.0198181	0.7837415
0.350	4.8347206	0.0121821	0.4897467
0.450	2.9492018	0.0080813	0.3016873
0.550	1.8436669	0.0056998	0.1907791
0.650	1.1988274	0.0041754	0.1256951
0.750	0.7910870	0.0031565	0.0841760
0.850	0.5265644	0.0024065	0.0569476
0.950	0.3579750	0.0018743	0.0394059
1.050	0.2440567	0.0014714	0.0273825
1.150	0.1729207	0.0011826	0.0197997
1.250	0.1214552	0.0009532	0.0142093
1.350	0.0855573	0.0007696	0.0102386
1.450	0.0624925	0.0006377	0.0076575
1.550	0.0462011	0.0004356	0.0058022
1.650	0.0340975	0.0003639	0.0043926
1.750	0.0250352	0.0003017	0.0033109
1.850	0.0180046	0.0002496	0.0024461
1.950	0.0142281	0.0002163	0.0019871
2.100	0.0091472	0.0001187	0.0013328
2.300	0.0051520	0.0000852	0.0007956
2.500	0.0030893	0.0000636	0.0005063
2.700	0.0019761	0.0000437	0.0003440
2.900	0.0011664	0.0000325	0.0002159
3.125	0.0007003	0.0000216	0.0001389
3.375	0.0003914	0.0000155	0.0000838
3.625	0.0002295	0.0000114	0.0000530
3.875	0.0001485	0.0000090	0.0000370
4.250	0.0000715	0.0000043	0.0000199
4.750	0.0000280	0.0000025	0.0000090
5.250	0.0000128	0.0000016	0.0000047
5.750	0.0000062	0.0000011	0.0000026

Table B.16: Invariant yields from Figure ??, centrality bin 0-20%

Appendix C

Data Tables C

C.1 R_{dAu} Data

C.2 R_{dAu} vs N_{coll} Data

C.3 R_{dA} as a Function of η

C.4 R_{dAu} vs η Data

p_T	R_{dAu}	Stat. Err.	Sys. Err.
0.250	0.6331685	0.0039517	0.0636257
0.350	0.6945042	0.0043002	0.0703518
0.450	0.7136781	0.0048698	0.0730054
0.550	0.7110133	0.0055460	0.0735743
0.650	0.7316828	0.0066041	0.0767158
0.750	0.7568155	0.0079577	0.0805293
0.850	0.7509679	0.0093125	0.0812167
0.950	0.7765474	0.0111841	0.0854823
1.050	0.7994794	0.0133974	0.0896994
1.150	0.8211882	0.0159102	0.0940272
1.250	0.8119693	0.0186426	0.0949942
1.350	0.8142290	0.0215317	0.0974388
1.450	0.9052525	0.0267410	0.1109247
1.550	0.9092513	0.0287531	0.1141890
1.650	0.8984919	0.0328521	0.1157471
1.750	0.8808853	0.0373915	0.1164958
1.850	0.8925386	0.0433455	0.1212604
1.950	0.9768248	0.0523633	0.1364218
2.100	1.0105052	0.0459321	0.1472368
2.300	1.0268246	0.0592837	0.1585657
2.500	1.0045466	0.0746674	0.1646329
2.700	1.1579658	0.0951842	0.2016009
2.900	0.8430302	0.1000493	0.1560093
3.125	0.9821837	0.1267994	0.1947465
3.375	0.9039549	0.1486093	0.1935172
3.625	0.8788617	0.1917834	0.2030566
3.875	0.9893041	0.2473260	0.2465138
4.250	1.2010319	0.2755356	0.3345699
4.750	1.4902130	0.4493161	0.4796110
5.250	0.5667579	0.4007583	0.2095767
5.750	1.5809313	0.9127511	0.6677730

Table C.1: R_{dAu} from Figure 6-15, centrality bin 70-100%. The grey band shows the overall scale uncertainty at 0.31.

p_T	R_{dAu}	Stat. Err.	Sys. Err.
0.250	0.4655660	0.0018172	0.0467837
0.350	0.5083063	0.0019724	0.0514903
0.450	0.5254219	0.0022371	0.0537478
0.550	0.5461292	0.0026471	0.0565124
0.650	0.5717841	0.0031630	0.0599506
0.750	0.5846109	0.0037607	0.0622058
0.850	0.6096917	0.0045196	0.0659377
0.950	0.6283860	0.0054179	0.0691727
1.050	0.6650845	0.0065571	0.0746207
1.150	0.6774094	0.0077750	0.0775644
1.250	0.7028213	0.0092847	0.0822247
1.350	0.7259285	0.0110230	0.0868719
1.450	0.7352068	0.0128588	0.0900882
1.550	0.8046327	0.0127463	0.1010504
1.650	0.8044349	0.0147090	0.1036303
1.750	0.8405065	0.0172979	0.1111558
1.850	0.8564805	0.0200707	0.1163615
1.950	0.8646651	0.0230107	0.1207578
2.100	0.8311259	0.0194445	0.1211001
2.300	0.9131396	0.0261538	0.1410101
2.500	0.9423376	0.0341373	0.1544376
2.700	0.9906700	0.0387976	0.1724748
2.900	0.9724035	0.0477910	0.1799508
3.125	1.1473080	0.0590112	0.2274871
3.375	0.9910724	0.0709722	0.2121672
3.625	0.9149360	0.0835218	0.2113914
3.875	0.9292773	0.1087637	0.2315564
4.250	1.1838287	0.1195848	0.3297776
4.750	1.0243517	0.1640276	0.3296780
5.250	0.7978880	0.1994720	0.2950444
5.750	1.1484909	0.3462830	0.4851136

Table C.2: R_{dAu} from Figure 6-15, centrality bin 40-70%. The grey band shows the overall scale uncertainty at 0.21.

p_T	R_{dAu}	Stat. Err.	Sys. Err.
0.250	0.3952309	0.0012308	0.0397159
0.350	0.4245750	0.0013191	0.0430085
0.450	0.4494863	0.0015215	0.0459800
0.550	0.4702280	0.0017944	0.0486583
0.650	0.4986999	0.0021671	0.0522879
0.750	0.5311311	0.0026382	0.0565153
0.850	0.5522305	0.0031664	0.0597233
0.950	0.5823770	0.0038382	0.0641080
1.050	0.6257167	0.0046898	0.0702037
1.150	0.6383145	0.0055628	0.0730879
1.250	0.6797652	0.0067439	0.0795273
1.350	0.7136953	0.0080604	0.0854080
1.450	0.7273753	0.0094833	0.0891286
1.550	0.7837623	0.0093120	0.0984294
1.650	0.8219250	0.0110070	0.1058835
1.750	0.8172115	0.0126234	0.1080751
1.850	0.8684930	0.0149275	0.1179936
1.950	0.9007327	0.0174024	0.1257949
2.100	0.9154472	0.0151215	0.1333863
2.300	0.9757622	0.0201113	0.1506805
2.500	0.9935411	0.0258960	0.1628292
2.700	1.0358542	0.0297541	0.1803414
2.900	1.0322357	0.0367486	0.1910232
3.125	1.0386682	0.0420890	0.2059461
3.375	1.0026979	0.0517102	0.2146560
3.625	1.0310825	0.0664179	0.2382265
3.875	1.2018521	0.0913751	0.2994763
4.250	1.1902281	0.0877448	0.3315603
4.750	1.1717206	0.1278452	0.3771073
5.250	1.1460662	0.1812090	0.4237943
5.750	0.9285657	0.2252103	0.3922189

Table C.3: R_{dAu} from Figure 6-15, centrality bin 20-40%. The grey band shows the overall scale uncertainty at 0.16.

p_T	R_{dAu}	Stat. Err.	Sys. Err.
0.250	0.3496537	0.0008885	0.0351359
0.350	0.3810182	0.0009601	0.0385963
0.450	0.4015660	0.0011004	0.0410780
0.550	0.4243416	0.0013119	0.0439101
0.650	0.4563723	0.0015895	0.0478499
0.750	0.4879421	0.0019469	0.0519197
0.850	0.5162069	0.0023591	0.0558274
0.950	0.5478780	0.0028686	0.0603104
1.050	0.5735286	0.0034578	0.0643484
1.150	0.6143501	0.0042016	0.0703440
1.250	0.6430017	0.0050461	0.0752263
1.350	0.6659048	0.0059902	0.0796889
1.450	0.7060682	0.0072052	0.0865177
1.550	0.7488183	0.0070609	0.0940409
1.650	0.7839767	0.0083663	0.1009949
1.750	0.8080145	0.0097379	0.1068588
1.850	0.8076612	0.0111949	0.1097289
1.950	0.8788060	0.0133629	0.1227327
2.100	0.8978518	0.0116506	0.1308225
2.300	0.9114270	0.0150778	0.1407457
2.500	0.9559695	0.0196867	0.1566717
2.700	1.0407728	0.0230262	0.1811977
2.900	1.0195380	0.0283973	0.1886734
3.125	1.0524228	0.0324322	0.2086734
3.375	1.0403616	0.0410918	0.2227190
3.625	1.0463599	0.0518025	0.2417563
3.875	1.1291494	0.0680903	0.2813604
4.250	1.1206844	0.0670936	0.3121876
4.750	1.0675490	0.0970499	0.3435806
5.250	1.1071848	0.1429369	0.4094167
5.750	1.1495026	0.2064568	0.4855409

Table C.4: R_{dAu} from Figure 6-15, centrality bin 0-20%. The grey band shows the overall scale uncertainty at 0.15.

N_{coll}	R_{dAu}	Stat. Err.	Sys. Err.
2.200	0.784	0.0043	0.227
5.400	0.646	0.0020	0.0969
9.700	0.601	0.0014	0.0481
14.600	0.562	0.0011	0.0337

Table C.5: R_{dAu} vs N_{coll} from Figure 6-16 for $p_T = 1$ GeV/c. The overall scale error, the gray band, = 0.141.

N_{coll}	R_{dAu}	Stat. Err.	Sys. Err.
2.200	0.960	0.0199	0.278
5.400	0.871	0.0091	0.131
9.700	0.900	0.0067	0.072
14.600	0.868	0.0051	0.052

Table C.6: R_{dAu} vs N_{coll} from Figure 6-16 for $p_T = 2$ GeV/c. The overall scale error, the gray band, = 0.149.

N_{coll}	R_{dAu}	Stat. Err.	Sys. Err.
2.200	1.015	0.0598	0.294
5.400	0.989	0.0271	0.1483
9.700	1.055	0.0204	0.0844
14.600	1.033	0.0158	0.0620

Table C.7: R_{dAu} vs N_{coll} from Figure 6-16 for $p_T = 3$ GeV/c. The overall scale error, the gray band, = 0.173.

N_{coll}	R_{dAu}	Stat. Err.	Sys. Err.
2.200	0.966	0.109	0.280
5.400	1.021	0.0476	0.153
9.700	1.093	0.0367	0.0874
14.600	1.102	0.0283	0.0661

Table C.8: R_{dAu} vs N_{coll} from Figure 6-16 for $p_T = 4$ GeV/c. The overall scale error, the gray band, = 0.215.

p_T	R_{dAu}	Stat. Err.	Sys. Err
0.550	0.5019	0.0022	0.0519
0.650	0.5381	0.0027	0.0564
0.750	0.5822	0.0034	0.0619
0.850	0.6143	0.0041	0.0664
0.950	0.6535	0.0050	0.0719
1.050	0.6984	0.0060	0.0784
1.150	0.7345	0.0073	0.0841
1.250	0.7622	0.0087	0.0892
1.350	0.7822	0.0103	0.0936
1.450	0.8218	0.0123	0.1007
1.550	0.8446	0.0144	0.1061
1.650	0.8923	0.0172	0.1149
1.750	0.9556	0.0205	0.1264
1.850	0.9406	0.0233	0.1278
1.950	1.0381	0.0282	0.1450
2.100	1.0425	0.0244	0.1519
2.300	1.1572	0.0335	0.1787
2.500	1.1217	0.0422	0.1838
2.700	1.2447	0.0562	0.2167
2.900	1.3587	0.0737	0.2514
3.125	1.4455	0.0885	0.2866
3.375	1.4906	0.1171	0.3191
3.625	1.3703	0.1478	0.3166
3.875	1.4897	0.1939	0.3712

Table C.9: R_{dAu} for $0.2 < \eta < 0.6$

p_T	R_{dAu}	Stat. Err.	Sys. Err
0.550	0.4587	0.0016	0.0475
0.650	0.4844	0.0020	0.0508
0.750	0.5241	0.0025	0.0558
0.850	0.5533	0.0030	0.0598
0.950	0.5812	0.0036	0.0640
1.050	0.6180	0.0044	0.0693
1.150	0.6385	0.0053	0.0731
1.250	0.6752	0.0064	0.0790
1.350	0.7009	0.0076	0.0839
1.450	0.7269	0.0090	0.0891
1.550	0.7894	0.0110	0.0991
1.650	0.8245	0.0130	0.1062
1.750	0.8498	0.0151	0.1124
1.850	0.8789	0.0176	0.1194
1.950	0.9396	0.0209	0.1312
2.100	0.9495	0.0181	0.1384
2.300	0.9982	0.0240	0.1541
2.500	1.0616	0.0314	0.1740
2.700	0.9513	0.0368	0.1656
2.900	0.9920	0.0472	0.1836
3.125	0.9952	0.0528	0.1973
3.375	1.1957	0.0767	0.2560
3.625	1.0768	0.0879	0.2488
3.875	1.1139	0.1137	0.2776

Table C.10: R_{dAu} for $0.6 < \eta < 1.0$

p_T	R_{dAu}	Stat. Err.	Sys. Err
0.550	0.4415	0.0017	0.0457
0.650	0.4672	0.0020	0.0490
0.750	0.5117	0.0026	0.0545
0.850	0.5381	0.0031	0.0582
0.950	0.5635	0.0038	0.0620
1.050	0.5878	0.0045	0.0659
1.150	0.6258	0.0055	0.0717
1.250	0.6501	0.0065	0.0761
1.350	0.6818	0.0078	0.0816
1.450	0.7035	0.0092	0.0862
1.550	0.7503	0.0110	0.0942
1.650	0.7620	0.0128	0.0982
1.750	0.7716	0.0148	0.1020
1.850	0.7701	0.0169	0.1046
1.950	0.7739	0.0194	0.1081
2.100	0.8146	0.0172	0.1187
2.300	0.8335	0.0222	0.1287
2.500	0.8272	0.0278	0.1356
2.700	0.9384	0.0376	0.1634
2.900	0.8880	0.0459	0.1643
3.125	0.9167	0.0525	0.1818
3.375	0.8707	0.0660	0.1864
3.625	0.8754	0.0831	0.2023
3.875	1.0265	0.1134	0.2558

Table C.11: R_{dAu} for $1.0 < \eta < 1.4$

η	R_{dAu}	Systematic Error
0.4	1.0189	0.0848
0.8	0.9066	0.0725
1.2	0.8081	0.0655

Table C.12: R_{dAu} vs η for $p_T = 2$ GeV/c. The gray error band is the systematic scale error at 13.4%.

η	R_{dAu}	Systematic Error
0.4	1.2186	0.1414
0.8	1.0097	0.1161
1.2	0.8730	0.1039

Table C.13: R_{dAu} vs η for $p_T = 2.6$ GeV/c. The gray error band is the systematic scale error at 14.8%.

η	R_{dAu}	Systematic Error
0.4	1.3740	0.1869
0.8	1.0637	0.1436
1.2	0.9260	0.1315

Table C.14: R_{dAu} vs η for $p_T = 3.2$ GeV/c. The gray error band is the systematic scale error at 15.6%.

η	R_{dAu}	Systematic Error
0.4	1.4773	0.2438
0.8	1.1150	0.1851
1.2	0.9761	0.1738

Table C.15: R_{dAu} vs η for $p_T = 3.8$ GeV/c. The gray error band is the systematic scale error at 16.4%.

List of Figures

1-1 Vertices for quark-quark-gluon, 3-gluon, and 4-gluon interactions. . . 16

1-2 Two electrons interacting via the exchange of a virtual photon. 17

1-3 Two electrons interacting via the exchange of a virtual photon, and the photon briefly splits into an electron-positron pair 18

1-4 Two quarks interacting via the exchange of a virtual gluon, which in turn has a gluon bubble, which is a result of the fact that gluons are self-interacting. 19

1-5 The strength of the running coupling constant α_s as a function of momentum transfer. The points are gathered from many different experiments, and are compared to theoretical prediction (lines). Figure is taken from [15]. 20

1-6 Illustration of a quark and antiquark separating. The strong force field lines form a tube shape, and as they get farther apart the energy in the strong force field increases. Eventually, there is enough energy in the field to create another quark/antiquark pair and now there are two mesons. The original quark and antiquark are never freed. 22

1-7 Energy density as a function of temperature for a hadronic system. At the critical temperature T_c there is a rapid rise in the energy density, corresponding to the expected phase transition. From [17]. 23

1-8 Pressure of a hadronic system as a function of temperature. At a temperature of about 170 MeV there is a rapid rise. This is similar to the rise in energy density seen in Figure 1-7. From [17]. 23

1-9 QCD phase diagram as discussed in the text. 26

1-10 Gluon distributions from [23] 28

1-11 Illustration of a heavy ion collision. The illustration on the left shows a collision looking down the Z-axis, or in the beam direction. The illustration on the right shows the collision side view. The two nuclei are Lorentz contracted. 30

2-1 The PHOBOS detector for the PR01 Au+Au run. 36

2-2 The PHOBOS detector for the PR03 d+Au run. 36

2-3 Four Silicon modules used in PHOBOS. Clockwise from top left: a sensor from the ring counters, a sensor from the octagon barrel, sensors from the vertex detector, and two sensors from one of the first four planes of the spectrometer. 38

2-4 The Octagon, Ring, Vertex, and Spectrometer detectors. 40

2-5 The PHOBOS Spectrometer 43

2-6 The magnetic field strength as it varies over the spectrometer. 43

2-7 One of the set of paddle counters 44

2-8 The Cerenkov counters and part of the beryllium beam pipe 45

2-9 Position of the ZDC calorimeters in relation to PHOBOS and RHIC. The top figure shows a top view of the position of the ZDC's, with the interaction point being the position of PHOBOS. The bottom figure shows the view looking down the beam pipe. In this view, the DX dipole magnets shown in the top figure have separated the two beams into two different beam pipes. These DX magnets will sweep spectator protons out of the path of the ZDC's, leaving just the neutrons to hit the ZDC's. 46

2-10 One of the ToF walls 49

2-11 Trigger logic for PR01 52

2-12 Trigger logic for the SpecTrig used in PR03 53

2-13 Schematic drawing of the VA chip 54

2-14 Electronics system for reading data from the silicon detectors 55

2-15 RHIC facility. 57

3-1 The top figure shows the pedestals for the chips of a given spectrometer sensor. The middle histogram shows the common mode noise (CMN), and the bottom figure shows the random noise. 63

3-2 A plot showing the difference in paddle timing signals for data in Au+Au collisions. The central peak corresponds to collisions that occur in the interaction region. 65

3-3 The negative ZDC timing signal versus the positive ZDC timing signal. These are used to make further event cuts. The enclosed triangle region are the events that pass the cuts. 66

3-4 Average energy deposited in the paddle detectors. This average is calculated from the 12 lowest signals from each paddle. 70

3-5 Truncated mean paddle signal in Monte Carlo versus N_{part} calculated from the Glauber model. 70

3-6 Comparison of the number of paddles hit for data and MC. In the central region, between about 16 and 23 paddles hit, there is good agreement. When the number of paddles hit is low (low centrality) the data falls well short of MC. This is assumed to be due to low efficiencies in the detectors at these low centralities. 71

3-7 Paddle signal divided up into percentages of the total cross section. Although 17 bins in total were calculated, this plot shows only the top 11, which were used in the data analysis. 72

3-8 Paddle signal vs the signal from the ZDC's. 74

3-9 Energy deposited in the six silicon ring counters for MC events versus N_{part} calculated with the Glauber model. The vertical structure seen is a histogramming effect with the quantized N_{part} values. 75

3-10 Energy spectrum for the ring counters, divided into the four centrality bins. This is for monte carlo events that go through the same event selection procedure as the data. 76

3-11 Vertex resolution for RMSSelVertex. These results are from MC and are averaged over centrality and vertex position. 81

3-12 Resolutions for the spectrometer vertices, the vertex vertex, and the octagon vertex, all for the Z coordinate. 82

3-13 Resolutions for OctDeVtx by centrality bin for MC. The most most peripheral is the top row and the most central is the bottom row. The plots on the left show the true vertex versus the difference in the true and found vertex. The plots on the right show the difference in true and found vertices. 84

4-1 Spectrometer layers used for the different sections of the tracking. The layers drawn in black are used in both the central and outer wing algorithms, the red layers are not used in either, the blue layer is used just in the central region, and the green layer is used just in the outer wing section. 88

4-2 Monte Carlo Au+Au event with the tracking run on it. The hits are drawn on the spectrometer with the track hits connected to show the found tracks. 91

4-3 Monte Carlo d+Au event with the tracking run on it. The hits are drawn on the spectrometer with the track hits connected to show the found tracks. 93

4-4 Tracking efficiency for single MC tracks. This efficiency has the track cuts $prob > 0.04$ and $dca < 0.35$ applied. 94

4-5 Tracking momentum resolution for the PR01 Au+Au tracking. 95

4-6 The acceptance of the tracking within the spectrometer as a function of p_T and η. 95

4-7 The acceptance of the tracking within the spectrometer and the ToF wall as a function of p_T and η. 96

5-1 Acceptance and efficiency corrections for the Au+Au data. The left column is the correction functions for the charge/polarity combination of tracks bending toward the beam pipe, and the right hand side is the corrections for tracks that bend into the wing. 100

5-2 Acceptance and efficiency corrections for the d+Au data. The left column is the correction functions for the charge/polarity combination of tracks bending toward the beam pipe, and the right hand side is the corrections for tracks that bend into the wing. 101

5-3 Acceptance/efficiency corrections for the η binned d+Au data. The η range for these corrections is $0.2 < \eta < 0.6$. The top row is for tracks bending toward the beam pipe and the bottom row is for tracks bending away from the beam pipe. The columns are for the vertex ranges, from left to right, $0 < v_z < 5$ and $5 < v_z < 10$. 103

5-4 Acceptance/efficiency corrections for the η binned d+Au data. The η range for these corrections is $0.6 < \eta < 1.0$. The top row is for tracks bending toward the beam pipe, in the vertex ranges $0 < v_z < 5$ and $5 < v_z < 10$ respectively. The bottom row is for tracks bending away from the beam pipe. 104

5-5 Acceptance/efficiency corrections for the η binned d+Au data. The η range for these corrections is $1.0 < \eta < 1.4$. The top row is for tracks bending toward the beam pipe and the bottom row is for tracks bending away from the beam pipe. The columns are for the vertex ranges, from left to right respectively, $-10 < v_z < -5$, $-5 < v_z < 0$, and $0 < v_z < 5$. 104

5-6 Acceptance and efficiency corrections for the SpecTrig d+Au data. The top four rows are for tracks bending toward the beam pipe and the bottom four rows are for tracks bending away from the beam pipe. The columns are the five vertex bins, starting with $-15 < v_z < -10$ and ending with $5 < v_z < 10$. 107

5-7 The final momentum resolution and bin width correction functions for the different data sets: Au+Au in the top left and d+Au for the min-bias and dAVertex data sets (top right), d+Au for the SpecTof data set (bottom left), and the d+Au in the three η bins (bottom right). The SpecToF were done separately because of the different acceptances between it and the MB and dA data sets (see Figures 4-6 and 4-7). These functions are all parabolas, and their forms are shown in Table 5.10. 109

5-8 Fraction of reconstructed tracks that are not primary. The linear fit shown is the correction function applied to the data. 112

5-9 Histogram showing the fraction of secondaries reconstructed for the most peripheral bin in d+Au MC events. The histogram has been fit with a function which is applied to the data. 112

5-10 Histogram showing the fraction of secondaries reconstructed for the 40-70% bin in d+Au MC events. The histogram has been fit with a function which is applied to the data. 113

5-11 Histogram showing the fraction of secondaries reconstructed for the 20-40% bin in d+Au MC events. The histogram has been fit with a function which is applied to the data. 113

5-12 Histogram showing the fraction of secondaries reconstructed for the most central bin in d+Au MC events. The histogram has been fit with a function which is applied to the data. 113

5-13 Momentum difference versus the number of matched hits for two MC tracks that share hits. This is used to define ghost tracks. 114

5-14 The fraction of ghost tracks with a fit probability > 0.04 for Au+Au MC. The fit to this histograms is the correction that is applied to the data. 115

5-15 The difference in η between reconstructed MC tracks and the closest true MC track match. The horizontal lines denote the ghost cutoff. Tracks outside of the lines are considered to be ghosts. 115

5-16 Fraction of ghosts in d+Au data for MC events, centrality bin 0. . . . 116

5-17 Fraction of ghosts in d+Au data for MC events, centrality bin 1. . . . 116

5-18 Fraction of ghosts in d+Au data for MC events, centrality bin 2. . . . 117

5-19 Fraction of ghosts in d+Au data for MC events, centrality bin 3. . . . 117

5-20 An illustration showing the finite resolution of OctDeVtx and the need to apply a correction to the event normalization. The areas a_1 and a_2, when divided by the total rectangular area a^{TOT}, give the percentage correction by which the event normalization must be decreased. . . . 119

6-1 *dca* distributions from Monte Carlo for both primary and secondary particles. The secondary distribution dominates after $dca \sim 0.4$, so by cutting on the *dca* distribution that part of the secondary distribution is removed from the data. 122

6-2 Distance of closest approach and probability distributions for Au+Au data. The dca histogram shows two exponential fits to the data, which meet at the cut of dca = 0.35, which is applied to the data. By cutting on tracks with dca > 0.35 the portion of the dca spectrum dominated by secondary tracks is discarded. The probability distribution has a spike at 0, and by cutting on prob > 0.04 a cut on probable ghost tracks is made. 124

6-3 *dca* distribution for the d+Au data (along with the MC single tracks). The definition of dca for the d+Au data sets allows for negative values, unlike the Au+Au data. 125

6-4 Probability distribution for the d+Au data. As in the Au+Au, a cut is made on prob > 0.04 to eliminate the spike at zero, and hence remove tracks that are likely to be ghosts. 125

6-5 Spectra generated with the PYTHIA event generator for tracks in the PHOBOS acceptance and tracks in the UA1 acceptance. 129

6-6 Ratio of the PHOBOS PYTHIA distribution with the UA1 PYTHIA distribution. This histogram is then fit to a function, which is used as a correction to the functional fit of the UA1 data. 130

6-7 Fit quality of the UA1 fit function. This shows the ratio of the UA1 data with the fit function given by Equation 6.6. 130

6-8 $\frac{1}{2\pi p_T}\frac{d^2N}{dp_T d\eta}$ distributions for the six centrality bins in the Au+Au data. The different centralities have been weighted by successive factors of 10 for clarity. 131

6-9 R_{AA} as a function of p_T for the six centrality bins. The PHOBOS spectra have been weighted by each centrality's corresponding N_{part} value and the corrected UA1 fit 132

6-10 $R_{AA}^{N_{part}}$ as a function of p_T for the six centrality bins. This is the same quantity as Figure 6-9, but with the spectra weighted by the appropriate $N_{part}/2$ values rather than N_{coll}. 133

6-11 $R_{CP}^{N_{part}}$ as a function of p_T for the six centrality bins. Each centrality bin has been weighted by its N_{part} value and divided by a fit to the most peripheral bin. The top left panel, which is the most peripheral bin, has been divided by a fit to itself, which shows the quality of the fit. 135

6-12 $R_{CP}^{N_{part}}$ as a function of N_{part} for six different p_T values. These values for the different p_T's were taken from Figure 6-11 and plotted as a function of N_{part} for each centrality bin. The dashed curve in each panel shows where the points would lie if N_{coll} scaling held. 136

6-13 $R_{CP}^{N_{coll}}$ as a function of p_T for the six centrality bins. Each centrality bin has been weighted by its N_{coll} value and divided by a fit to the most peripheral bin. The top left panel, which is the most peripheral bin, has been divided by a fit to itself, which shows the quality of the fit. 137

6-14 d+Au $\frac{1}{2\pi p_T}\frac{d^2N}{dp_T d\eta}$ distributions for the four centrality bins. 138

6-15 Nuclear modification factor R_{dAu} for the four centrality bins. The gray bands show the overall scale error. 138

6-16 Nuclear modification factor R_{dAu} versus N_{coll} for the four centrality bins and at four different p_T values. 139

6-17 Systematic error functions, in percentages, for the correction functions for the Au+Au data. These errors are taken to be Gaussian, and the final error function, in the bottom right, is the quadrature sum of the others. 140

6-18 Systematic error functions, in percentages, for the correction functions for the d+Au data. These errors are taken to be Gaussian, and the final error function, in the bottom right, is the quadrature sum of the others. 141

6-19 Comparison between the central R_{AA} between PHOBOS, STAR, and PHENIX. The STAR and PHENIX data are the centrality bin $0-10\%$. Systematic errors have been removed for clarity. The STAR data are from [51] and the PHENIX data are from [52]. 143

6-20 Results from the theoretical calculations in [53, 57]. This shows the nuclear modification factor R_{AA} for different quenching weights $\hat{q}$. See the text for a discussion of the different curves. 146

6-21 Results from the theoretical calculation in [53, 57]. This shows the nuclear modification factor R_{AA} for a quenching weight of $\hat{q} = 10\text{GeV}^2/\text{fm}$ for different path lengths L from 3 to 6 fm. 148

6-22 Results from the theoretical calculation in [59]. RW shows an approximate N_{part} scaling of the nuclear modification factor that is consistent with surface emission of jets due to jet quenching in a deconfined medium 150

6-23 R_{AA} fit to the STAR data and shown with the PHOBOS data with several predictions included: pQCD, shadowing, the Cronin effect, and jet quenching. 151

6-24 Predictions of $R_{CP}^{N_{part}}$ for 130 and 200 GeV beam energy for three different values of p_T. The gray bands show the predicted yields, and the solid lines show the expected yields from N_{coll} scaling. 153

6-25 Results for R_{dAu} for PHOOBS, STAR [65], and PHENIX [66] data. The STAR and PHENIX data are MinBias, and the PHOBOS data are in the centrality bin $0 - 20\%$. Also, the STAR and PHENIX data are at midrapidity while the PHOBOS data are centered at $\eta = 0.8$. Errors shown are only statistical for clarity. 154
6-26 Back to back correlations from the STAR collaboration. 155
6-27 Nuclear modification factor R_{dAu} versus p_T for the three η bins, $0.2 < \eta < 0.6$, $0.6 < \eta < 1.0$, $1.0 < \eta < 1.4$. 157
6-28 Nuclear modification factor R_{dAu} versus η at four different p_T values. Included are the mid-rapidity values from the STAR, PHENIX, and BRAHMS experiments. 158
6-29 Qualitative results from [36] showing the predicted evolution of R_{dAu} vs p_T (with Q_s being the saturation scale) as rapidity increases in the deuteron direction. This shows a decrease in R_{dAu} as the rapidity increases. This decrease is seen in the PHOBOS data. 159
6-30 Theoretical calculations for the change in R_{dAu} versus rapidity from effects of the nuclear medium only. 161

List of Tables

1.1 Charges and masses for the six flavors of quarks [4]. 12

2.1 Characteristics for the different silicon sensors in the PHOBOS detectors 39

3.1 The event cuts for Au+Au events, which involve paddle timing and energy deposition and ZDC timing cuts. 67

3.2 Percentage cross section, bin number, and N_{part} values for the centrality bins used in this analysis. 73

3.3 Percentage cross section, bin number, N_{part}, and N_{coll} values for the centrality bins used in this analysis and the efficiency of the event selection. 77

4.1 Maximum angle differences for hits in adjacent layers of the spectrometer to be considered as track candidates. Layer refers to the starting layer when comparing two hits from consecutive layers. 86

4.2 Layer pairs used in the Hough stick finding algorithm for the different parts of the spectrometer. Due to the spectrometer design, not all layers are present in the two sections used. 88

5.1 Vertex ranges for the three different η bins. 99

5.2 Acceptance/efficiency correction functions for the Au+Au tracking divided into 5 cm wide event vertex bins. These functions correspond to particles bending toward the beam pipe, or away from the outer wing. These have a much smaller acceptance at low p_T due to the fact that the low momentum particles will bend out of the accepted region of the spectrometer. 99

5.3 Acceptance/efficiency correction functions for the Au+Au tracking divided into 5 cm wide event vertex bins. These functions are for the particles that bend away from the beam pipe and into the outer wing. This gives a higher acceptance at low p_T. 99

5.4 Acceptance/efficiency correction histograms and functions for the d+Au tracking divided into 5 cm wide event vertex bins. These functions correspond to particles bending toward the beam pipe, or away from the outer wing. These have a much smaller acceptance at low p_T due to the fact that the low momentum particles will bend out of the accepted region of the spectrometer. 102

5.5 Acceptance/efficiency correction histograms and functions for the d+Au tracking divided into 5 cm wide event vertex bins. These functions are for the particles that bend away from the beam pipe and into the outer wing. This gives a higher acceptance at low p_T. 102

5.6 Acceptance/efficiency correction histograms and functions for the η binned data in the range $0.2 < \eta < 0.6$. The top two rows are for tracks bending toward the beam pipe and away from the spectrometer wing, and the bottom two rows are for tracks bending away from the beam pipe. The first column is the vertex range $0 < v_z < 5$ and the second column is $5 < v_z < 10$. 104

5.7 Acceptance/efficiency correction histograms and functions for the η binned data in the range $0.6 < \eta < 1.0$. The top three rows are for tracks bending toward the beam pipe and away from the spectrometer wing and the bottom three rows are for tracks bending away from the beam pipe. The first column is the vertex range $-10 < v_z < -5$, the second column is $-5 < v_z < 0$, and the third column is $0 < v_z < 5$ . . 105

5.8 Acceptance/efficiency correction histograms and functions for the η binned data in the range $1.0 < \eta < 1.4$. The top four rows are for tracks bending toward the beam pipe and away from the spectrometer wing and the bottom three rows are for tracks bending away from the beam pipe. The first column is the vertex range $-10 < v_z < -5$, the second column is $-5 < v_z < 0$, and the third column is $0 < v_z < 5$ . . 105

5.9 The fit functions for the plots in Figure 5-6. The top four rows are for tracks bending toward the beam pipe and the bottom four rows are for tracks bending away from the beam pipe. 106

5.10 The parabolic fits for the momentum resolution and bin width corrections are shown here. These functions are all used to divide the data. 110

5.11 Centrality based correction functions for feeddown and secondary particles in the d+Au data set. These corrections are multiplicative with the data. 117

5.12 Values for the variables used in the OctDeVtx correction. See the text for details. 119

5.13 Correction factors in percentages for the OctDeVtx correction 120

6.1 Centrality binning used for the Au+Au data analysis. 121

6.2 Centrality binning used for the d+Au data analysis. 122

A.1 Invariant yield from Figure 6-8, centrality bin 45-50% 168

A.2 Invariant yield from Figure 6-8, centrality bin 35-45% 169

A.3 Invariant yield from Figure 6-8, centrality bin 25-35% 170

A.4 Invariant yield from Figure 6-8, centrality bin 15-25% 171
A.5 Invariant yield from Figure 6-8, centrality bin 6-15% 172
A.6 Invariant yield from Figure 6-8, centrality bin 0-6% 173
A.7 R_{AA} yield from Figure 6-9, centrality bin 45-50% 174
A.8 R_{AA} yield from Figure 6-9, centrality bin 35-45% 175
A.9 R_{AA} yield from Figure 6-9, centrality bin 25-35% 176
A.10 R_{AA} yield from Figure 6-9, centrality bin 15-25% 177
A.11 R_{AA} yield from Figure 6-9, centrality bin 6-15% 178
A.12 R_{AA} yield from Figure 6-9, centrality bin 0-6% 179
A.13 $R_{AA}^{N_{part}}$ yields from Figure 6-10, centrality bin 45-50% 180
A.14 $R_{AA}^{N_{part}}$ yields from Figure 6-10, centrality bin 35-45% 181
A.15 $R_{AA}^{N_{part}}$ yields from Figure 6-10, centrality bin 25-35% 182
A.16 $R_{AA}^{N_{part}}$ yields from Figure 6-10, centrality bin 15-25% 183
A.17 $R_{AA}^{N_{part}}$ yields from Figure 6-10, centrality bin 0-6% 184

B.1 $R_{CP}^{N_{part}}$ yields from Figure 6-11, centrality bin 45-50% 186
B.2 $R_{CP}^{N_{part}}$ yields from Figure 6-11, centrality bin 35-45% 187
B.3 $R_{CP}^{N_{part}}$ yields from Figure 6-11, centrality bin 25-35% 188
B.4 $R_{CP}^{N_{part}}$ yields from Figure 6-11, centrality bin 15-25% 189
B.5 $R_{CP}^{N_{part}}$ yields from Figure 6-11, centrality bin 6-15% 190
B.6 $R_{CP}^{N_{part}}$ yields from Figure 6-11, centrality bin 0-6% 191
B.7 $R_{CP}^{N_{part}}$ yields from Figure 6-13, centrality bin 45-50% 192
B.8 $R_{CP}^{N_{part}}$ yields from Figure 6-13, centrality bin 35-45% 193
B.9 $R_{CP}^{N_{part}}$ yields from Figure 6-13, centrality bin 25-35% 194
B.10 $R_{CP}^{N_{part}}$ yields from Figure 6-13, centrality bin 15-25% 195
B.11 $R_{CP}^{N_{part}}$ yields from Figure 6-13, centrality bin 6-15% 196
B.12 $R_{CP}^{N_{part}}$ yields from Figure 6-13, centrality bin 0-6% 197
B.13 Invariant yields from Figure ??, centrality bin 70-100% 198
B.14 Invariant yields from Figure ??, centrality bin 40-70% 199
B.15 Invariant yields from Figure ??, centrality bin 20-40% 200

B.16 Invariant yields from Figure ??, centrality bin 0-20% 201

C.1 R_{dAu} from Figure 6-15, centrality bin 70-100%. The grey band shows the overall scale uncertainty at 0.31. 204

C.2 R_{dAu} from Figure 6-15, centrality bin 40-70%. The grey band shows the overall scale uncertainty at 0.21. 205

C.3 R_{dAu} from Figure 6-15, centrality bin 20-40%. The grey band shows the overall scale uncertainty at 0.16. 206

C.4 R_{dAu} from Figure 6-15, centrality bin 0-20%. The grey band shows the overall scale uncertainty at 0.15. 207

C.5 R_{dAu} vs N_{coll} from Figure 6-16 for $p_T = 1$ GeV/c. The overall scale error, the gray band, = 0.141. 208

C.6 R_{dAu} vs N_{coll} from Figure 6-16 for $p_T = 2$ GeV/c. The overall scale error, the gray band, = 0.149. 208

C.7 R_{dAu} vs N_{coll} from Figure 6-16 for $p_T = 3$ GeV/c. The overall scale error, the gray band, = 0.173. 208

C.8 R_{dAu} vs N_{coll} from Figure 6-16 for $p_T = 4$ GeV/c. The overall scale error, the gray band, = 0.215. 208

C.9 R_{dAu} for $0.2 < \eta < 0.6$ 209

C.10 R_{dAu} for $0.6 < \eta < 1.0$ 210

C.11 R_{dAu} for $1.0 < \eta < 1.4$ 211

C.12 R_{dAu} vs η for $p_T = 2$ GeV/c. The gray error band is the systematic scale error at 13.4%. 211

C.13 R_{dAu} vs η for $p_T = 2.6$ GeV/c. The gray error band is the systematic scale error at 14.8%. 211

C.14 R_{dAu} vs η for $p_T = 3.2$ GeV/c. The gray error band is the systematic scale error at 15.6%. 212

C.15 R_{dAu} vs η for $p_T = 3.8$ GeV/c. The gray error band is the systematic scale error at 16.4%. 212

Acknowledgments

Bibliography

[1] Y. Ne'eman. Derivation of strong interactions from a gauge invariance. *Nucl. Phys.*, 26:222–229, 1961.

[2] M. Gell-Mann. The eightfold way: A theory of strong interaction symmetry. *California Institute of Technology Laboratory Report CTSL-20*, 1961.

[3] M. Gell-Mann. A schematic model of mesons and baryons. *Phys. Lett.*, 8:214–215, 1964.

[4] *Eur. Phys. J. C*, 15, 2000. Review of Particle Physics.

[5] O.W.Greenberg. *Phys.Rev.Lett.*, 13, 1964.

[6] E.D.Bloom et.al. High-energy inelastic eP scattering at 6-degrees and 10-degrees. *Phys.Rev.Lett.*, 23:930–934, 1969.

[7] H.W.Kendall E.D.Bloom D.H.Coward H.C.DeStaebler J.Drees L.W.Mo R.E.Taylor M.Breidenbach, J.I.Friedman. Observed behavior of highly inelastic electron-proton scattering. *Phys.Rev.Lett.*, 23:935–939, 1969.

[8] D.L.Dubin J.E.Elias J.I.Friedman H.W.Kendall J.S.Poucher E.M.Riordan M.R.Sogard D.H.Coward A.Bodek, M.Breidenbach. Comparisons of deep inelastic eP and eN cross-sections. *Phys.Rev.Lett.*, 30:1087–1091, 1973.

[9] J.S.Poucher et.al. High-energy single arm inelastic e-P and e-D scattering at 6-degrees and 10-degrees. *Phys.Rev.Lett.*, 32:118–144, 1973.

[10] F.Wilczek D.Gross. Ultraviolet behavior of non-abelian gauge theories. *Phys.Rev.Lett.*, 30:1343, 1973.

[11] H.David Politzer. Reliable perturbative results for strong interactions? *Phys.Rev.Lett.*, 30:1346–1349, 1973.

[12] David J. Griffiths. *Introduction to Elementary Particles.* John Wiley & Sons, Inc.

[13] D.Gross F.Wilczek. Asymptotically free gauge theories, I. *Phys.Rev.D*, 8:3633–3652, 1973.

[14] D.Gross F.Wilczek. Asymptotically free gauge theories, II. *Phys.Rev.D*, 9:980–993, 1974.

[15] *M. Schmelling, Status of the Strong Coupling Constant*, Warsaw, Poland, 1996. Plenary talk given at the XXVIII Intern. Conf. on High Energy Physics.

[16] K.G.Wilson. Confinement of quarks. *Phys.Rev.D*, 10,8:2445, 1974.

[17] F.Karsch. Lattice QCD at high temperature and density. *hep-lat/0106019*, 2001.

[18] L.McLerran M.Gyulassy. New forms of QCD matter discovered at RHIC. *nucl-th/0405013*, 2004.

[19] Michael E. Peskin and Daniel V. Schroeder. *An Introduction to Quantum Field Theory.* Perseus Books Publishing, L.L.C, 1995.

[20] K.Rajagopal. Mapping the QCD phase diagram. *Nucl.Phys.A*, 661:150c–161c, 1999.

[21] M.J.Perry J.C.Collins. Superdense matter: Neutrons or asymptotically free quarks? *Phys.Rev.Lett.*, 34:1353, 1975.

[22] J.D.Bjorken. Fermilab-Pub-82/59-THY, 1982. and erratum (unpublished).

[23] J.Breitweg et.al. "Zeus results on the measurement and phenomenology of f_2 at low x and low q^2". *Eur.Phys.J.C*, 7:609–630, 1999.

[24] M.G.Ryskin L.V.Gribov, E.M.Levin. Semihard proceses in QCD. *Phys.Rept.*, 100:1–150, 1983.

[25] R.Venugopalan L.D.McLerran. Computing quark and gluon distribution functions for very large nuclei. *Phys.Rev.D*, 49:2233–2241, 1994.

[26] R.Venugopalan L.D.McLerran. Gluon distribution functions for very large nuclei at small tranverse momentum. *Phys.Rev.D*, 49:3352–3355, 1994.

[27] J.Qiu A.H.Mueller. Gluon recombination and shadowing at small values of x. *Nucl.Phys.B*, 268:427–476, 1986.

[28] E.Levin. CGC, QCD saturation and RHIC data. hep-ph/0408039, August 2004.

[29] J.F.Owens et.al. Detailed quantum chromodynamic predictions for high p_T processes. *Phys.Rev.D*, 18:1501, 1978.

[30] M.Plumer M.Gyulassy. Jet quenching in dense matter. *Phys.Lett.B*, 1990.

[31] M.Gyulassy X.-N.Wang. Gluon shadowing and jet quenching in A+A collisions at $\sqrt{s} = 200$A GeV. *Phys.Rev.Lett.*, 68:1480–1483, 1992.

[32] J.W.Cronin et.al. Production of hadrons at large transverse momentum at 200, 300, and 400 GeV. *Phys.Rev.D*, 11:3105–3134, 1975.

[33] B.Petersson M.Lev. Nuclear effects at large at large transverse momentum in a QCD parton model. *Z.Phys.C*, 21:155–172, 1983.

[34] X.-N.Wang. Systematic study of high p_t hadron spectra in pp, pA, and AA collisions at ultrarelativistic energies. *Phys.Rev.C*, 61:064910–1 – 13, 2000.

[35] L.McLerran D.Kharzeev, E.Levin. Parton saturation and N_{part} scaling of semihard processes in QCD. hep-ph/0210332, 2002.

[36] K.Tuchin D.Kharzeev, Y.V.Kovchegov. Cronin effect and high-p_T suppression in pA collisions. *Phys.Rev.D*, 68:094913–1 – 23, 2003.

[37] L.D.McLerran A.Dumitru. How protons shatter colored glass. *Nucl.Phys.A*, 700:492–508, 2002.

[38] J.Jalilian-Marian A.Dumitru. Forward quark jets from protons shattering the colored glass. *Phys.Rev.Lett.*, 89, 2002.

[39] R.Noucier et.al. Silicon pad detectors for the PHOBOS experiment at RHIC. *Nucl.Instr.Meth.A*, 461:143–149, 2001.

[40] W.T.Lin et.al. Development of a double metal, AC-coupled silicon pad detector, the silicon detector for the PHOBOS experiment at RHIC. *Nucl.Instr.Meth.A*, 389:415, 1997.

[41] R.Bindel et.al. Array of scintillator counters for PHOBOS at RHIC. *Nucl.Instr.Meth.A*, 474:38–45, 2001.

[42] R.Bindel et.al. Array of cerenkov radiators for PHOBOS at RHIC. *Nucl.Instr.Meth.A*, 488:94, 2002.

[43] C.Adler et.al. The RHIC zero degree calorimeters. *Nucl.Instr.Meth.A*, 470:488, 2001.

[44] B.Back et.al. PHOBOS Collaboration. The PHOBOS detector at RHIC. *Nucl.Instr.Meth.A*, 499:603–623, 2003.

[45] T.Ludlam M.Harrison and S.Ozaki. The RHIC project overview. *Nucl.Instr.Meth.A*, 499:235–244, 2003.

[46] R.J.Glauber. Lectures in theoretical physics, vol 1, 315. Interscine, NY, 1959.

[47] Cronin et.al. Production of hadrons at large transverse momentum at 200, 300, and 400 GeV. *Phys.Rev.D*, 11:3105–3122, 1975.

[48] T.Sjostrand. PYTHIA manual. *Computational Physics Communications*, 82, 1994.

[49] B.Back et.al. PHOBOS Collaboration. Charged hadron transverse momentum distributions in au+au collisions at $\sqrt{s_{NN}} = 200$ GeV. *Phys.Lett.B*, 2004.

[50] B.Back et.al. PHOBOS Collaboration. Centrality dependence of the charged hadron transverse momentum spectra in d+au collisions at $\sqrt{s_{NN}} = 200$ GeV. *Phys.Rev.Lett.*, 2003.

[51] STAR Collaboration J.Adams et.al. Transverse momentum and collision energy dependence of high p_T hadron suppression in Au+Au collisions at ultrarelativistic energies. *Phys.Rev.Lett.*, 91:172302, 2003.

[52] PHENIX Collaboration S.S.Adler et.al. High-p_t charged hadron suppression in au+au collisions at $\sqrt{s_{NN}}$ - 200 gev. *Phys.Rev.C*, 69:034910, 2004.

[53] Urs Achim Wiedemann Carlos A. Salgado. Calculating quenching weights. *Phys.Rev.D*, 68, 2003.

[54] A.H.Mueller S.Peigne D.Schiff R.Baier, Y.L.Dokshitzer. Radiative energy loss and p_t broadening of high energy partons in nuclei. *Nucl.Phys.B*, 484:265, 1997.

[55] I.Vitev M.Gyulassy, P.Levai. Jet quenching in thin plasmas. *Nucl.Phys.A*, 661:637–640, 1999.

[56] R.Baier. Jet quenching. *Nucl.Phys.A*, 715:209, 2003.

[57] C.A.Salgado U.A.Wiedemann K.J.Eskola, H.Honkanen. The fragility of high p_t hadron spectra as a hard probe. *Nucl.Phys.A*, 747:511–529, 2005.

[58] P.V.Ruuskanen K.Tuominen K.J.Eskola, K.Kajantie. Scaling of tranverse energies and multiplicities with atomic number and energy in ultrarelativistic nuclear collisions. *Nucl.Phys.B*, 570:379–389, 2000.

[59] Berndt Müller. Phenomenology of jet quenching in heavy ion collisions. *Phys.Rev.C*, 67, 2003.

[60] A.H.Mueller S.Peigne D.Schiff R.Baier, Y.L.Dokshitzer. Radiative energy loss of high-energy quarks and gluons in a finte volume quark-gluon plasma. *Nucl.Phys.B*, 483:291–320, 1997.

[61] Xin-Nian Wang. High-p_T spectra, azimuthal anisotropy and back-to-back correlations in high-energy heavy-ion collisions. *Phys.Lett.B*, 595:165–170, 2004.

[62] X.N.Wang E.Wang. Parton energy loss with detailed balance. *Phys.Rev.Lett.*, 87, 2001.

[63] Xin-Nian Wang. Why the observed jet quenching at RHIC is due to parton energy loss. *Phys.Lett.B*, 579:299–308, 2004.

[64] E.Levin D.Kharzeev. Manifestations of high density QCD in the first rhic data. *Phys.Lett.B*, 523:79–87, 2001.

[65] J.Adams et.al. STAR Collaboration. Evidence from d+Au measurements for final-state suppression of high p_T hadrons in Au+Au collisions at RHIC. *Phys.Rev.Lett.*, 91:072304, 2003.

[66] S.S.Adler et.al. PHENIX Collaboration. Absence of suppression in particle production at large transverse momentum in $sqrts_{NN}$ = 200GeV d+Au collisions. *Phys.Rev.Lett.*, 91:072303, 2003.

[67] I.Arsene et.al. BRAHMS Collaboration. Tranverse momentum spectra in Au+Au and d+Au collisions at $sqrts_{NN}$ and the pseudorapidity dependence of high-p_T suppression. *Phys.Rev.Lett.*, 91:072305, 2003.

[68] I.Vitev. Initial state parton broadening and energy loss probed in d+Au at RHIC. *Phys.Lett.B*, 562:36–44, 2003.

[69] et.al. B.B.Back. Pseudorapidity dependence of charged hadron transverse momentum spectra in d+Au collisions at $\sqrt{s_{NN}}$ = 200 GeV. *Phys.Rev.C*, 2004.

[70] I.Arsene et.al. BRAHMS Collaboration. Evolution of the nuclear modification factors with rapidity and centrality in d+Au collisions at $\sqrt{s_{NN}} = 200$ GeV. *Phys.Rev.Lett.*, 93:242303, 2004.

[71] A.B.Kaidalov D.Sousa A.Capella, E.G.Ferreiro. Large transverse momentum suppression of π^0's in Au+Au and d+Au collisions at $\sqrt{s} = 200$ GeV. *nucl-th/0405067.*

[72] I.K.Potashnikova M.B.Johnson Ivan Schmidt B.Z.Kopelioich, J.Nemchik. Breakdown of QCD factorization at large Feynman x. *hep-ph/0501260.*